GEOSCIENCE AUSTRALIA

Australian Government
Geoscience Australia

Natural Fields EM Forum 2012:

Abstracts from the ASEG Natural Fields EM Forum 2012

Edited by Richard Lane

Record
2012/04

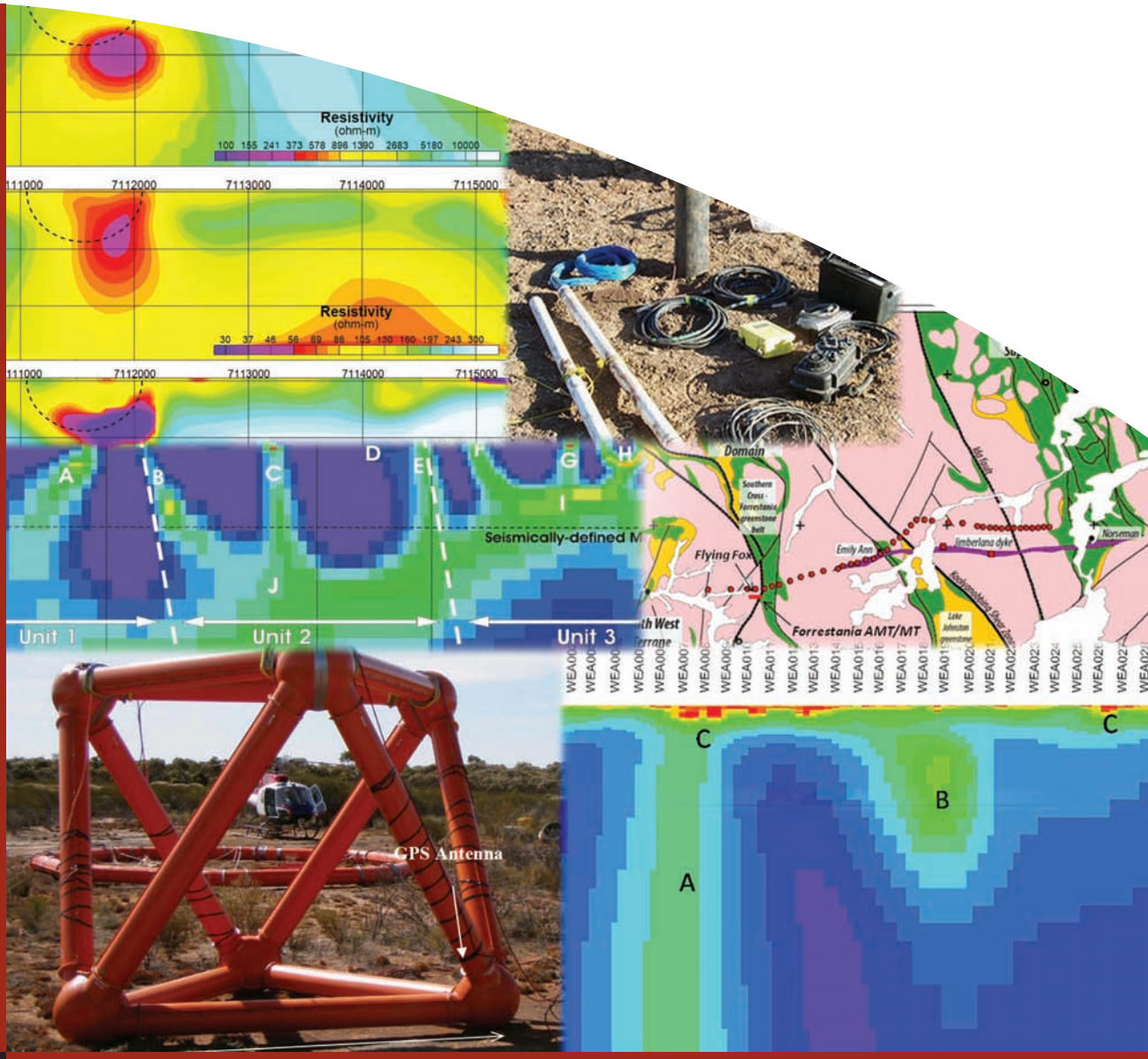

Natural Fields EM Forum 2012:

Abstracts from the ASEG Natural Fields EM Forum 2012

GEOSCIENCE AUSTRALIA RECORD 2012/04

By

Richard Lane[1] (editor)

Australian Government
Geoscience Australia

1. Minerals and Natural Hazards Division, Geoscience Australia, GPO Box 387 Canberra ACT 2601 Australia.

Department of Resources, Energy and Tourism
Minister for Resources and Energy: The Hon. Martin Ferguson, AM MP
Secretary: Mr Drew Clarke

Geoscience Australia
Chief Executive Officer: Dr Chris Pigram

ISSN 1448-2177
ISBN 978-1-921954-68-9 print
ISBN 978-1-921954-67-2 web
GeoCat # 73374

Bibliographic reference:

a) For the entire publication

Lane, R. J. L. (editor), 2012, Natural Fields EM Forum 2012: Abstracts from the ASEG Natural Fields EM Forum 2012: Published by Geoscience Australia, Geoscience Australia Record 2012/04.

b) For an individual paper

Author, I., 2012, Title of paper, In R. J. L. Lane (editor), Natural Fields EM Forum 2012: Abstracts from the ASEG Natural Fields EM Forum 2012: Published by Geoscience Australia, Geoscience Australia Record 2012/04.

N.B. Credits and a short description of the images shown on the front cover are given in the first paper (Introduction to the Natural Fields EM Forum Record).

CONTENTS

Introduction to the "Natural Fields EM Forum" Record

Richard Lane [1], Andrew Mutton [2], Terry Ritchie [3] , and Bob Smith [4]

[1] *Geoscience Australia (richard.lane@ga.gov.au)*
[2] *GeoDiscovery (andrew.mutton@bigpond.com)*
[3] *GRS (tjritchie@consultgrs.com.au)*
[4] *Greenfields Geophysics (greengeo@bigpond.net.au)*

Introduction

As members of the "Natural Fields EM Forum" Organising Committee, we provide this short introduction to the published record of proceedings of the forum which was held in Brisbane, Queensland, Australia, on February 26, 2012, in conjunction with the ASEG 22nd International Geophysical Conference & Exhibition 2012. The forum was organised to review the current state of development of natural field EM methods (NFEM), being those methods that utilise the ambient electromagnetic field rather than deploying an additional active source as an element of a survey. NFEM methods are used to acquire data from which various parameters can be obtained to help interpret the electrical characteristics of the subsurface.

A number of distinguished and knowledgeable speakers were assembled to present papers, and to lead discussions in panel sessions where delegates had an opportunity to ask questions and to contribute directly to the discussions. To provide a lasting record of the event, and to promote the dissemination of geophysical knowledge, the speakers were invited to submit papers for inclusion in a forum volume. These contributions were reviewed and assembled for publication in this Geoscience Australia Record. Participants received a copy at the forum, and additional copies of the Record are available on an ongoing basis from Geoscience Australia (www.ga.gov.au).

The forum was structured to cover a wide range of applications of natural EM fields that are used in the search for minerals and energy resources, from the development of broad-scale regional models to direct detection of drill targets. Principally, these applications involved aspects of ground-based MT and AMT methods, but they also included airborne techniques (e.g., ZTEM) which use only natural EM fields as an energy source. Although the basic principles of these methods are not new, there have been significant developments in acquisition, processing and interpretation methods in recent years, many of which have been made possible through ready access to increased computing power both in the field and in post-acquisition processing facilities. New instrument developments and the availability of contract services have helped to bring about an increase in the use of these methods in a variety of applications, and it seemed timely to review them, to consider the successes which had been achieved, and to speculate on future developments.

The morning session focussed on general principles, instrumentation and data acquisition. A number of equipment manufacturers and service providers gave brief introductions to their capabilities and attendees were invited to refer to this publication or to contact the suppliers directly for further information. The final session of the morning was a panel discussion addressing the subject of data acquisition and quality control. This provided an opportunity for all of the delegates to contribute and to ask questions of the speakers from the earlier presentations.

The presenters in the afternoon session focussed on data processing and interpretation aspects of NFEM methods, and their contributions included a number of case histories. The final session of the day was a second panel discussion that had panellists gazing into possible future aspects of NFEM methods, aided and questioned through contributions from the attendees.

Images on the front cover

The images on the cover of this publication (Figure 1), Geoscience Australia Record 2012/04, were sourced from papers within this volume to illustrate various aspects of natural fields EM methods.

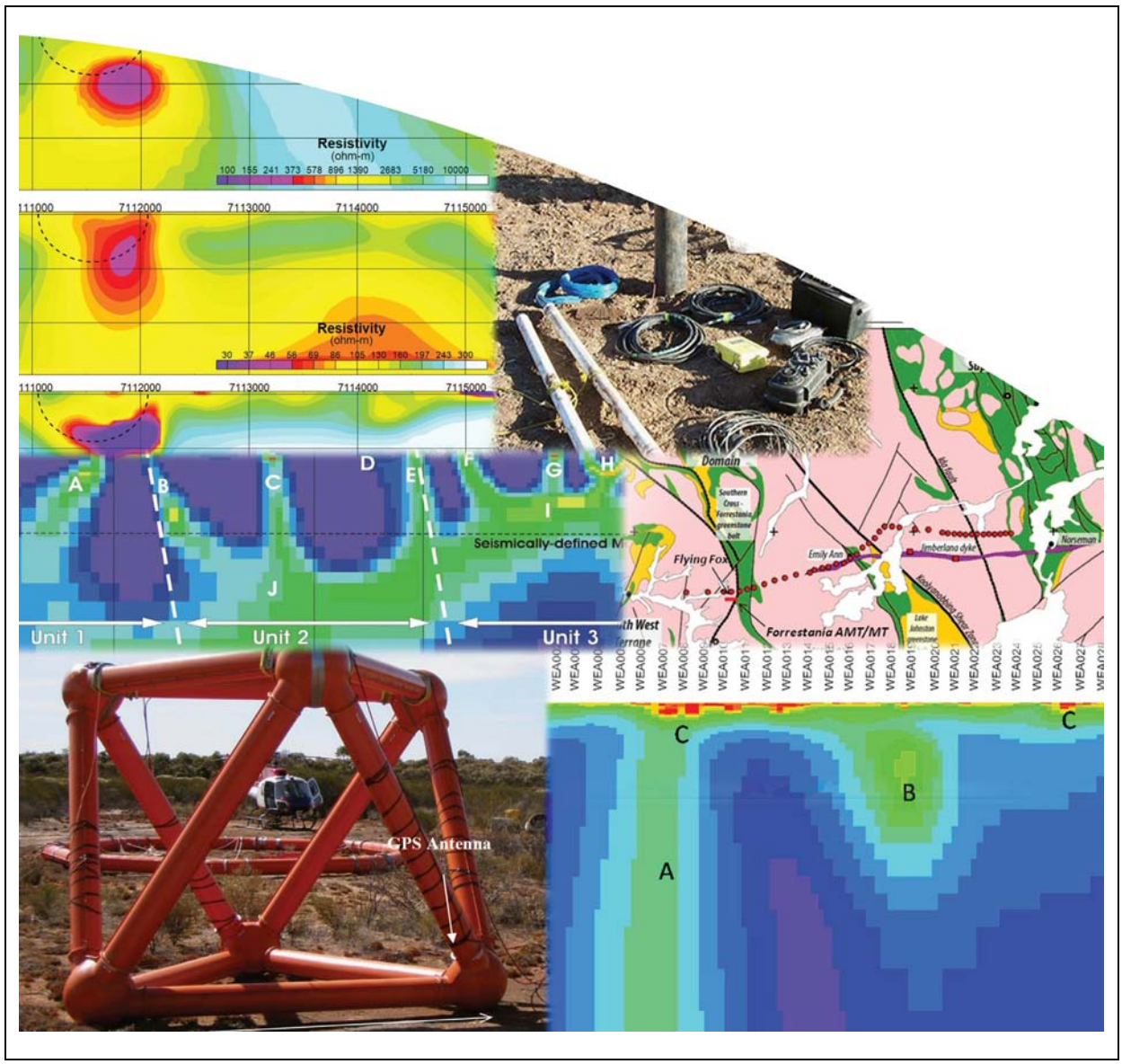

Figure 1. Montage of images and photographs used on the front cover of this publication, Geoscience Australia Record 2012/04.

Left to right across the top row; A comparison of resistivity cross sections looking at the differences related to (a) the airborne system that was used to acquire the data, and (b) the modelling method used to convert the system response into a 3D model of subsurface resistivity (from Legault et al. (2012), this volume); A photograph showing equipment that would be used to acquire ground magnetotelluric data (Retallick et al. (2012), this volume).

Left to right across the middle row; A conductivity cross section, approximately 200 km in length and 70 km in depth extent, across a portion of the Yilgarn Craton in Western Australia, that was derived by modelling ground magnetotelluric data (Evans et al. (2012), this volume); Regional geological map of the southern Yilgarn Craton showing the location of the ground magnetotelluric data acquisition points used as input for the conductivity cross section shown to the left (Evans et al. (2012), this volume).

Left to right across the bottom row; ZTEM magnetic field sensor loop and AirMt base station sensor coil assembly in front of a helicopter used with the airborne ZTEM magnetovariational system (Legault

et al. (2012), this volume); Resistivity cross section, approximately 8 km in length and 4 km in depth extent, across a portion of the Forrestania Greenstone Belt of Western Australia, derived from audio-magnetotelluric and magnetotelluric survey data (Evans et al. (2012), this volume).

Acknowledgments

The Natural Fields EM Forum Organising Committee would like to acknowledge the support of the ASEG 2012 Conference Organising Committee and Geoscience Australia for this forum. Editing of the papers in this volume was the responsibility of Richard Lane (Geoscience Australia), and printing was funded and managed by Geoscience Australia. A large number of people at Geoscience Australia assisted with the reviewing, authorizing, publishing, and printing tasks, including Andy Barnicoat, Marina Costelloe, Andy Marshall, Peter Milligan, Daniel Rawson, Murray Richardson, Ian Roach, Ned Stolz and Robin Swindell. We thank the presenters who contributed their time and energy to the forum, both in the lead-up to the event and on the day itself, and particularly thank the authors for preparing the papers that are included in this volume. Finally, we thank all of the delegates for the support that they provided through attendance at the forum and their contributions to both formal and informal discussions. Richard Lane publishes with the permission of the Chief Executive Officer, Geoscience Australia.

Statement of Capability - EMpulse Geophysics Ltd.

David Goldak [1]

[1] *EMpulse Geophysics Ltd. (empulse@sasktel.net)*

Introduction

EMpulse was formed in 2001 and recently celebrated ten years in business. Led by David Goldak M.Sc. (Engineering Physics), our SFERIC-EM instrumentation and Adaptive Polarization Stacking (APS) algorithm are the result of research and development by EMpulse, building on the foundation laid by Peter Kosteniuk and Ken Paulson in the 1980's at the University of Saskatchewan.

Products and services

Our sole activity is the collection, processing and interpretation of “transient” AMT data with hardware and software of our own design. We offer clients a complete service including report generation with integrated interpretation.

To ensure that the best possible data are collected, contact resistance and self-potentials are measured at every station, and if necessary, pots are moved or re-watered to improve electrical contact with the ground. Prior to automatic triggering, manual recordings are performed to make sure that everything is working properly. Parallel sensor tests are conducted if anything suspicious is noted. Near-field activity is detected and monitored in real-time with a hand-held lightning detector that has approximately 80 km range (see references for the Lightning Detector Company). If strikes are detected, survey activity is suspended for at least two hours until no further near-field events are detected. We also measure the vertical electric field to provide a much improved method of near-field detection and dead-band reduction, but this detection capability is presently only available post-recording when data are processed back in camp. If possible, thunderstorm activity is also monitored via lightning detection networks displayed on the internet.

Time series records are processed in the field every evening in order to inspect Earth response curve quality, and if necessary, data for substandard stations are re-collected. At home base, prior to inversion, error bars are inspected and expanded where deemed necessary. Earth response curves are then further inspected and fit with a spline constrained by the error bars.

EMPulse have several active research and development projects. The first project-scale application of the company’s vertical electric field measurement method was carried out in 2010, and the deployment of a third generation receiver with extended bandwidth is planned for 2012.

Contact information

Canada

EMpulse Geophysics Ltd.
P.O. Box 968, Dalmeny, SK, Canada, S0K 1E0
P: +11-306-254-4844
www.empulse.ca

David Goldak
empulse@sasktel.net

References

Lightning Detector Company website - ThunderBolt Pro Handheld Lightning Detector. Accessed 11 January 2012. http://www.lightningdetector.co/lightning-detector-pages/thunderbolt-pro-lightning-detector.html

Statement of Capability - Fugro ElectroMagnetics Italy Srl

Stephen Hallinan [1]

[1] *Fugro Electro Magnetics Italy Srl (s.hallinan@fugro.com)*

Introduction

Fugro EM Italy (FEMI) was established recently to provide comprehensive, onshore magnetotellurics (MT) services as a natural field EM complement to the established airborne and ground geophysics services offered by Fugro. The FEMI management and geophysics personnel have an average of 20 years of global experience of applying MT technology to the oil and gas, mining, and geothermal industries.

Products and services

FEMI provides a full suite of MT data acquisition, processing, 3D inversion modelling, and interpretation services.

MT data acquisition

Broadband, full tensor, stand-alone Metronix ADU-07e data acquisition units are used. These units have 24-bit A/D, GPS-synchronization, and low noise characteristics that permit deployment in remote reference mode, in small to large synchronized spreads, with a capacity in excess of 200 receiver channels. The acquisition arrays may be 2D or 3D as required to suit the target and environmental constraints, with sparse or dense coverage as required.

Broadband MFS-06e/07e magnetic induction coils are used, thereby avoiding the need to deploy both high frequency and low frequency coils to acquire broadband measurements. Non-polarizable porous pots are used as electric field sensors, providing low noise electrical field data at both high and low frequencies. Data for the frequency range from 0.0003 to 20,000 Hz are recorded for broadband MT measurements, providing information from near surface to depths of 10's of kilometres (i.e., well into basement below even the deepest basins).

The use of portable, stand-alone systems allows crews to record data from arrays that might be full tensor, partial tensor, or a mix of these where sparse Hx and Hy data acquisition is judged to be suitable for both target delineation and/or to lower the impact of the survey on the environmental.

MT data processing

Robust, remote-reference processing of time series data files is carried out at the field office, usually producing EDI files as an intermediate deliverable within 24 hours of acquisition. The robust processing code includes pre-filtering to remove harmonic noise (i.e., frequencies from powerlines) and de-spiking to remove the effects of very close, non-plane wave lightning events.

Data QC is carried out at the measurement site in the form of system status checks and viewing of time series records. QC during data processing at the field office involves examination of time series records and processed data files. In-survey QC is also carried out at HQ by modelling and inspection of e-mailed EDI files. A key element of the QC process is the employment of suitably experienced MT geophysicists as part of every field crew.

Processing of third-party MT data is also offered as a service.

3D modelling

FEMI uses 3D inversion code that has been written by staff with over 20 years experience in developing and running commercial 3D inversions. We offer, as standard products:

- 3D feasibility modelling studies for use when designing survey parameters, and
- 3D inversion modelling:
    - in-survey on constantly updated data sets,
    - post-survey on final MT data sets, and for
    - third-party data.

The efficiency of the FEMI parallelized 3D code means that models with sufficiently detailed topography and cell dimensions are run without incurring unnecessarily high computing costs, whilst modelling the full MT response.

Ancillary information including geological data and surface, airborne and downhole geophysical data are integrated into the modelling procedure to provide 3D *a priori* model constraints. This is considered to be crucial in providing geologically-reliable rather than solely numerically-driven solutions.

Contact information

Italy

Fugro ElectroMagnetics Italy Srl (FEMI)
Via Cardinale Mezzofanti, 34
Milan 20133, ITALY
P: +39 (02) 3675 0150
F: +39 (02) 3675 0151

Stephen Hallinan
s.hallinan@fugro.com

Australia

Fugro Ground Geophysics (FGG) Pty Ltd.
435 Scarborough Beach Road
Osborne Park, WA 6017
P: +61 8 9273 6400
F: +61 8 9273 6466
www.fugroground.com

Kathlene Oliver
Kathlene.Oliver@fugroground.com

Statement of Capability - Geophysical Resources and Services Pty Ltd

Terry Ritchie [1]

[1] *Geophysical Resources and Services Pty Ltd (tjritchie@consultgrs.com.au)*

Introduction

Geophysical Resources and Services (GRS) operates from offices in Australia and Chile and has offered contracting and consulting services in electrical geophysical exploration methods including magnetotellurics (MT) since 2004.

Products and services

MIMDAS distributed acquisition system hardware is used. Up to 200 channels are available but the system is routinely used with 70-90 channels. The system employs 24 bit sampling from 200 seconds to 200 Hz using the EMI BF-4 or Zonge ANT-4 coils.

Although any configuration is possible, GRS promote EMAP (continuous profiling) surveys either by themselves or more usually as part of a 2D or 3D IP survey because of their superior protection from static shifts. Common practice is to use a pair of magnetic coils remote from the survey site (approximately 50 km away) which are linked in real time via satellite internet. These data are combined with the local data, processed in the field, and converted into apparent resistivity and phase for QC purposes. A final step requires that the derived quantities both fit the same 1D Earth model.

Software that is used in the field for data acquisition and QC is the same as that is used in the office. A screen shot of the operator's screen appears below (Figure 1).

Figure 1. An image from the field operator's QC screen showing processed apparent resistivity and phase data with error bars for a single data event against a backdrop of data acquisition records. Also shown is the best fit (rhoplus) 1D model response.

GRS support selected R&D projects and are able to offer 2D and 3D inversion software from Scripps and UBC respectively. The example below is from a combined 3D IP/MT survey in China (Figure 2).

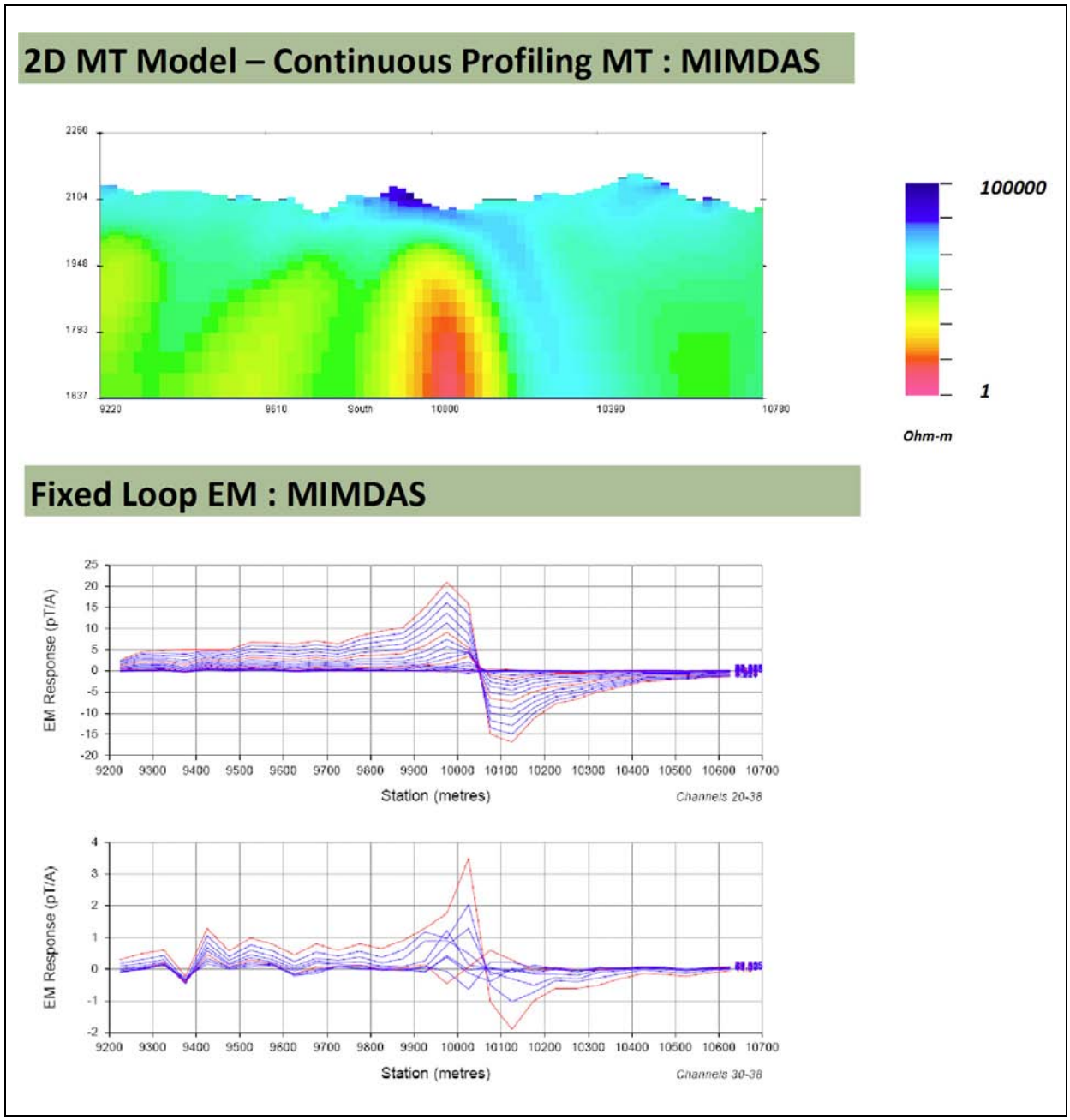

Figure 2. The 2D MT (Occam) inversion model with topography (top) indicates a conductive feature towards the centre of the line. The presence of this feature is supported (bottom) by data from a fixed loop TEM survey on the same line.

Contact information

Australia

Geophysical Resources and Services Pty Ltd
Unit 1, 80 Ebbern Street, Darra, QLD 4076
PO Box 549, Sumner Park, QLD 4074

P: +61 (0)7 3279 0111
F: +61 (0)7 3279 0145
M:+61 (0)419 647 595

www.consultgrs.com.au

Terry Ritchie - Director
tjritchie@consultgrs.com.au

Chile

GRS Chile Ltda.
Encomenderos 231, Of. 602
Las Condes
Santiago, Chile
P: +56 (2) 335 4489

Jimena Vargas
jimena@grschile.com

Statement of Capability - Geotech Airborne Ltd.

Jean Legault [1] and Keith Fisk [2]

[1] *Geotech (jean@geotech.ca)*
[2] *Geotech Airborne (keith@geotechairborne.com)*

Introduction

Geotech Ltd. (Geotech) began to revisit the airborne Audio Frequency Magnetic method (AFMAG) in 2000, updating the technology using digital electronics and modern signal processing tools (Kuzmin et al., 2005). The first airborne passive EM survey results were shown at the Australian Earth Sciences Convention (AESC) in Melbourne, Australia, in 2006 (Lo et al., 2006). Geotech released the ZTEM (z-axis tipper electromagnetic) system in 2006, making it the first commercially-available passive airborne AFMAG (Audio Frequency Magnetics) EM system to be used for mineral exploration in more than 30 years. Since then, Geotech has remained the lone industry supplier of a complete range of airborne AFMAG instrumentation, surveying, processing and interpretation services. Geotech has continued to develop the technology, introducing the Airborne Magnetic Tensor system (AirMt) in 2009 and the Fixed Wing ZTEM system (FW-ZTEM) in 2011.

The company, based in Aurora, Ontario, Canada, was established nearly 30 years ago as a geophysical instrument manufacturer that specialized in building advanced airborne electromagnetic and magnetic equipment for the exploration industry. Its first instrument in 1982 was a 4 frequency helicopter EM (HFEM) system. The Hummingbird digital HFEM system was introduced in 1996, and this was followed by the HAWK digital fixed wingtip frequency (FFEM) system in 1997 (Thompson et al., 2007). It is perhaps best known for its VTEM (versatile time-domain electromagnetic) helicopter EM (HTEM) system that was developed in 2002 (Witherly et al., 2004) and now counts 30 systems worldwide. However, it is becoming more widely known for its passive EM systems, in particular ZTEM, that have now also been used around the world and number 10 systems, including AirMt and FW-ZTEM.

Geotech is presently a full service airborne EM survey provider and among the largest helicopter EM companies in the world, with its head office in Canada and main offices in South Africa and Australia, where it operates under the Geotech Airborne Ltd. banner. Geotech designs, builds, operates and maintains its own airborne geophysical systems, as well as its own fleet of helicopters and fixed-wing aircraft, while providing full survey design, acquisition, data processing and interpretation support for the mining, hydrogeology, oil and gas sectors.

Products and services

Data acquisition

Geotech offers 3 types of airborne passive AFMAG EM survey technologies. The ZTEM, (Z Tipper Electro Magnetic) is a helicopter-borne natural field electromagnetic system (Figure 1) that was developed in 2005 and has been in commercial service since 2007. It provides the deepest penetration of any proven airborne EM system, and it has consequently been used for deep resistivity mapping of lithology, structure and alteration, particularly in porphyry copper exploration applications (Lo and Zang, 2008; Pare and Legault, 2010; Izarra et al., 2011). It is notable that a combination of measuring a single component of the AFMAG field in the airborne receiver and the horizontal fields at the fixed base-station in ZTEM has produced a ten-fold improvement in signal to noise over standard AFMAG (Lo and Kuzmin, 2008).

The continued success of the helicopter ZTEM system has spurred the development of a new FW-ZTEM fixed wing system (Figure 2) for regional geologic exploration and mapping programs. The FW-ZTEM system, which features a newly redesigned, retractable airborne sensor, has been fitted onto a Cessna Caravan and was successfully flight-tested in 2011. The new FW-ZTEM system is designed to be deployed with multi-parameter sensors (including magnetics, gravity/gravity-gradiometry, spectrometric), and will be available for survey in North America in 2012.

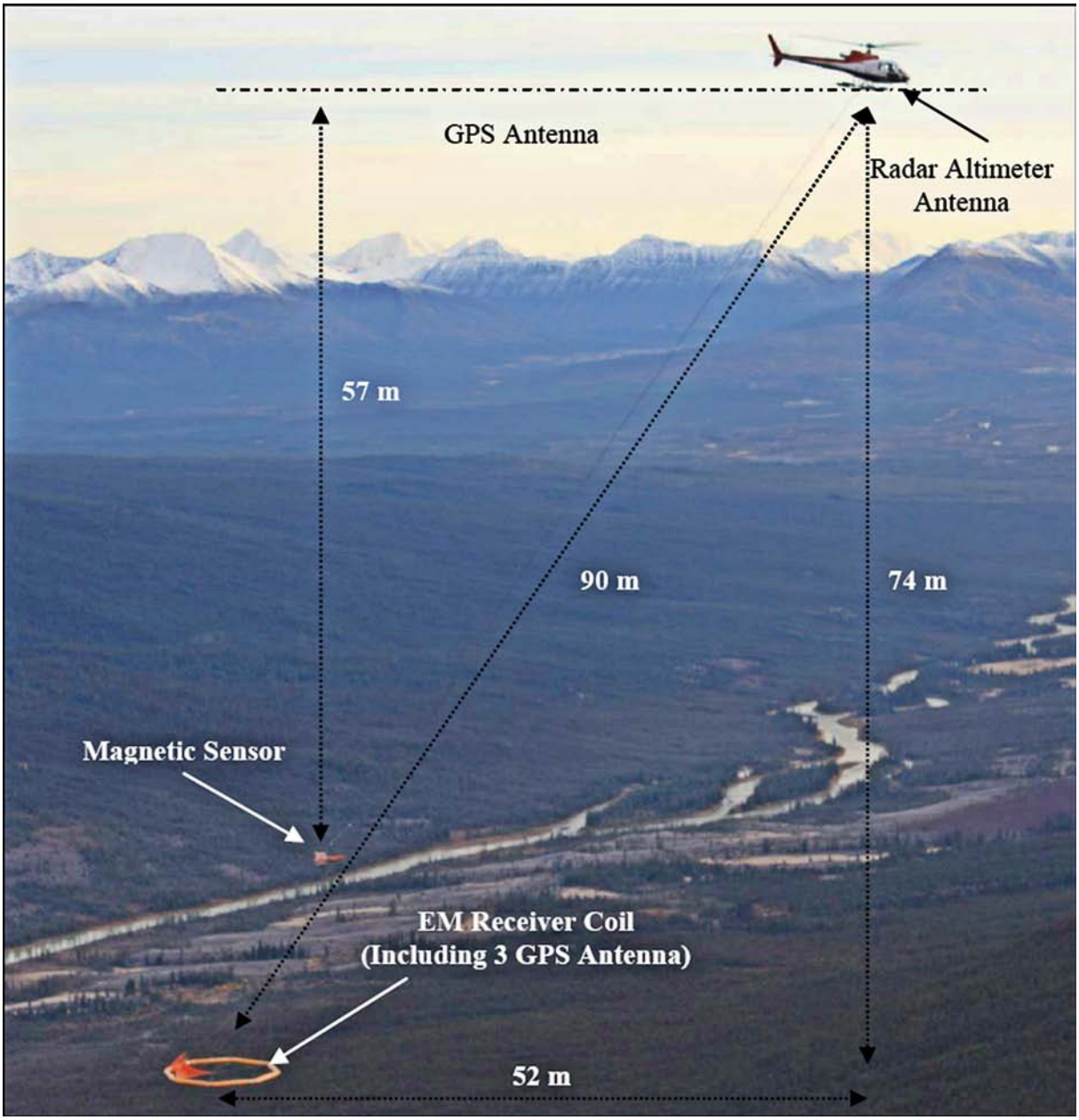

Figure 1. ZTEM (Z-Axis Tipper ElectroMagnetic) system configuration.

Geotech's ongoing research and development efforts have seen the introduction of the helicopter AirMt (Airborne Magnetic Tensor) AFMAG system (Kaminski et al., 2010; Kuzmin et al., 2010) to the market in 2011 (Figure 3). AirMt uses a 3-axis total field (XYZ) EM sensor that measures the magnetic field Amplitude Parameter (AP), which is a rotationally invariant measurement that produces results with an even higher signal-to-noise ratio than the standard tipper measurement recorded in ZTEM. The improved S/N is achieved because the AP does not require an attitude correction to remove the added effect of horizontal fields to vertical field components. AirMt is still at an R&D testing stage and is only available for limited commercial use.

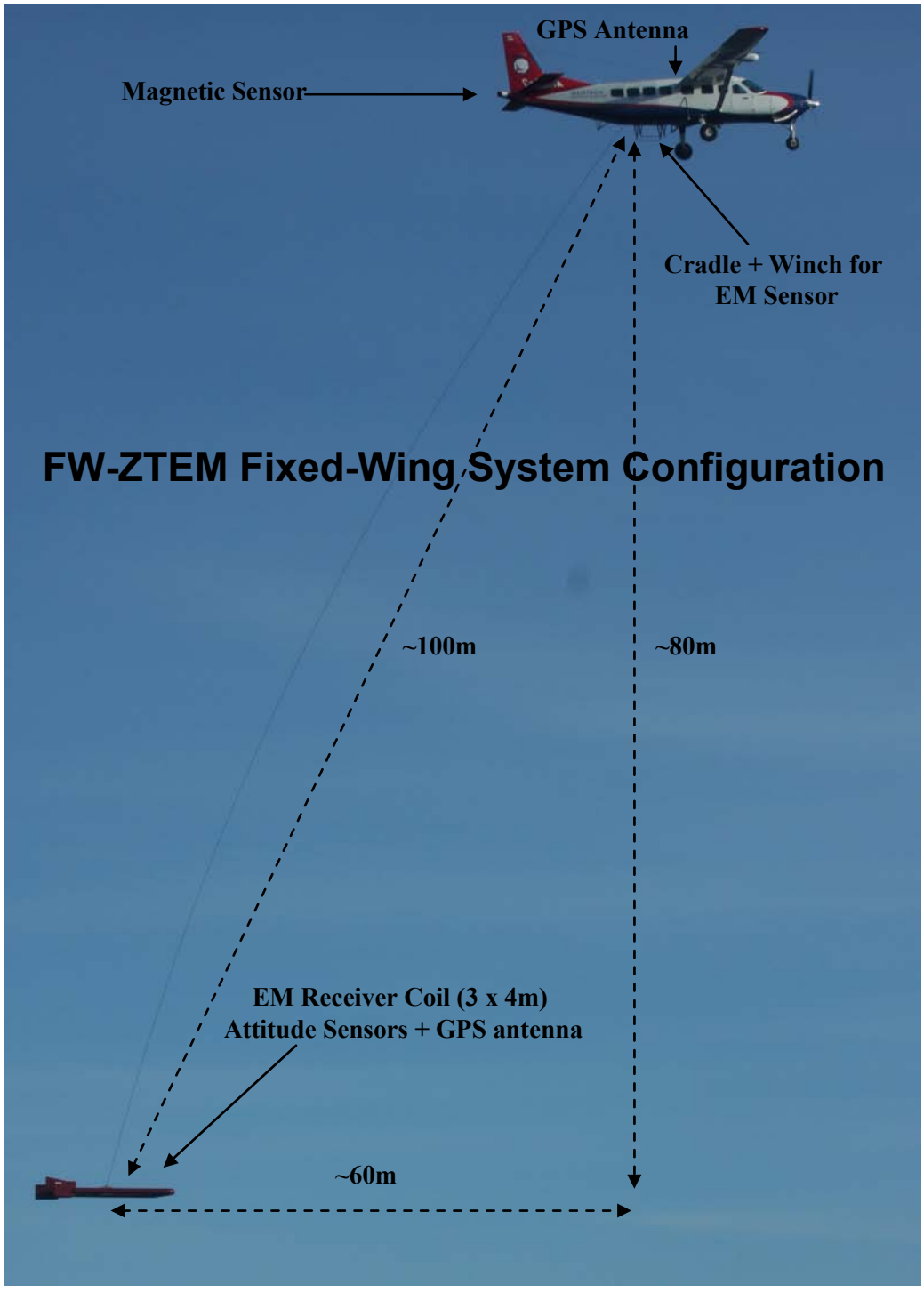

Figure 2. Fixed-wing ZTEM (FW-ZTEM) system configuration.

For helicopter surveys, the ZTEM and AirMt sensors are carried as an external sling load, and are independent of the helicopter (Figure 1 and Figure 2). The new fixed-wing ZTEM system is mounted on a Cessna Grand Caravan and is retractable, using a cradle and winch assembly (Figure 3). The helicopter ZTEM receiver coil measures the vertical magnetic field from a 7.4 m diameter air-core loop sensor, whereas the FW-ZTEM system uses a rectangular receiver coil with dimensions are 3 by 4 m. The AirMt receiver coil assembly simultaneously measures all three components of the magnetic field using three mutually-perpendicular 3.04 m diameter air-core loops. The ZTEM and AirMt receiver coils are encased in a fibreglass shell that is isolated from most vibrations by a patented suspension

system. The ZTEM and AirMt receiver coil assemblies are towed beneath the aircraft using a 90 m cable, and are flown with a nominal ground clearance of 50 to 100 m. Elevation, attitude and terrain clearance positioning of the receiver coil assembly is provided by GPS antennas on the assembly and attitude-sensors mounted on the sensor frame, in combination with GPS and radar onboard the helicopter. For both ZTEM and AirMt systems, the magnetic field time-series are recorded at 2 kHz sampling frequency using 24 bit ADC's. The bandwidths are typically 20 to 800 Hz.

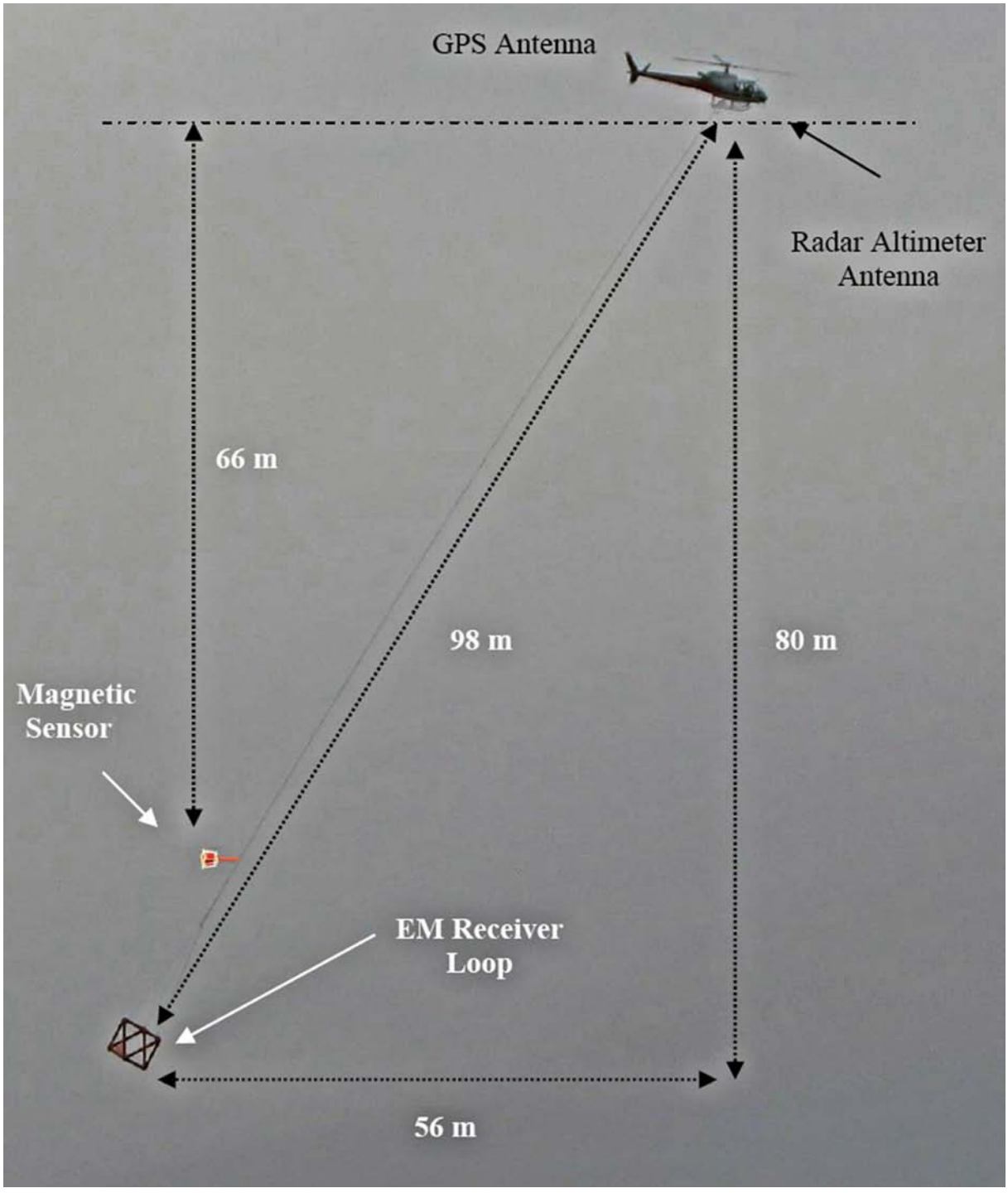

Figure 3. AirMt (Airborne Magnetic Tensor) system configuration.

The base station for these systems are typically the standard two-orthogonal air-core (3.2 by 3.2 m) sensors (Figure 4), but the AirMt sensor, consisting of three mutually-perpendicular 3.04 m diameter air-core loops, can also be used, as shown in Figure 5. The base station provides a reference field which when processed with the airborne receiver data produces the appropriate transfer functions which are output at 2.5 Hz, or approximately 10 m intervals per sample.

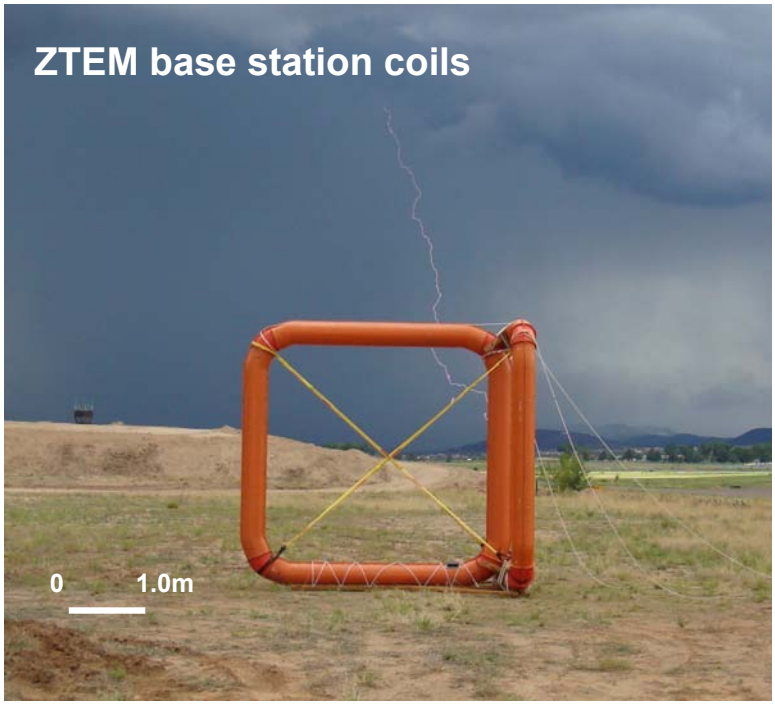

Figure 4. Standard ZTEM base station multi-coil sensors.

Figure 5. AirMt 3-axis sensor for ZTEM and AirMt base station configurations.

Specifications for all three systems are summarised in Table 1.

Table 1. Geotech passive EM system specifications.

Parameter	ZTEM	FW-ZTEM	AirMt
Transmitter	None required	None required	None required
Sampling frequency	A/D = 2000 Hz (0.0005 s) Output = 2.5 Hz (0.4 s)	A/D = 2000 Hz (0.0005 s) Output = 2.5 Hz (0.4 s)	A/D = 2000 Hz (0.0005 s) Output = 2.5 Hz (0.4 s)
Receiver coils (Rx)	Airborne: H_Z Base: $H_X + H_Y$	Airborne: H_Z Base: $H_X + H_Y$	Airborne: $H_X + H_Y + H_Z$ Base: $H_X + H_Y + H_Z$
Survey speed	80-90 km/hr	180-200 km/hr	70-80 km/hr
Rx clearance	50-100 m (nominal)	150 m (nominal)	50-100 m (nominal)
Rx dimensions	Mobile = 7.2 m diameter Base = 3.2 x 3.2 m	Mobile = 3.0 x 4.0 m Base = 3.2 x 3.2 m	Mobile: 3.0 x 3.0 m Base: 3.0 x 3.0 m
Rx Frequency bandwidth	5-6 frequencies 30-720 Hz or 25-600 Hz	5-6 frequencies 30-720 Hz or 25-600 Hz	4-5 frequencies 45-720 Hz or 37-600 Hz
Rx derived measurements	Tzx (in-line) tipper Tzy (cross-line) tipper	Tzx (in-line) tipper Tzy (cross-line) tipper	Amplitude parameter (AP)
Rx transfer functions	In-Phase and Quadrature	In-Phase and Quadrature	In-Phase and Quadrature
Other sensors: **Radar:** **Magnetometer**	GPS on Rx (3) & base (1) Onboard aircraft 15 m above EM bird	GPS on Rx (3) & base (1) Onboard aircraft Stinger-mounted	GPS on Rx (1) & base (1) Onboard aircraft 15 m above EM bird
Optional sensors	Spectrometer	Spectrometer Gravimeter or Gravity gradiometer	Spectrometer

Data Processing, QC, Presentation and Interpretation

All of the data processing and interpretation of Geotech's passive EM survey data are carried out from its offices in Aurora, Ontario, Canada. At the end of each survey day, the raw airborne and base station data are pre-processed and then uploaded via the internet to a central FTP server for initial data QC and further processing. Tipper estimates are obtained from time-series data using spectral FFT algorithms that are analogous to those used for ground tipper data in magnetotellurics (Labson et al., 1985). From these processes, the resulting xyz files contain 20-24 channels of tipper data, at 0.4 s/2.5 Hz intervals (~10 m). These include In-phase and Quadrature transfer functions of the Tzx in-line and Tzy cross-line ZTEM tipper data or the AP parameter for AirMt data, as well as other geophysical and related positional information. These xyz files are then treated with Geosoft-based GX processing, in order to apply, in the case of ZTEM, the attitude correction that removes the influence of the horizontal fields on the vertical field measurement. In the case of AirMt data, no such compensation is required. Following this step, small non-linear spike and low pass smoothing filters are applied to the final processed database. Final geo-referenced databases are delivered in Geosoft gdb format.

Initial field data QC focuses on signal-strength/signal-noise and other system-related issues, according to contract specifications, on a daily, per flight basis. Final data QC reviews the compensation and filtering of all the database channels and related grids of the tipper, magnetic and positional data channels, prior to final map creation and report compilation.

ZTEM tipper and AirMt data are typically presented in the form of profiles (Figure 6) and grid-contoured plan maps. Because ZTEM tipper data produce cross-over anomalies across conductors, resistors and along contacts, it is desirable for plan-view interpretation to combine the two components into one single parameter which has peaks or troughs centred over the conductive or resistive anomalies instead of a cross-over type anomaly. In order to combine the two components and to transform the cross-overs into peaks, the ZTEM data are presented in terms of the DT (Total Divergence) which is defined as the divergence of tipper relations (i.e., DT = div (Tzx, Tzy) = d(Tzx)/dx + d(Tzy)/dy) (Figure 7). It is analogous to the Peaker parameter used in VLF EM (Pedersen, 1998; Lo et al., 2008). Rotated phase grids (i.e., rotated by 90 degrees) of the ZTEM tipper data exhibit maxima

over conductors and are also used in conjunction with DT. They preserve longer wavelength information but have the disadvantage of favouring one direction (X or Y) only (Lo and Zang, 2008).

Typically, grids of both phase-rotated ZTEM components are added to produce a total phase-rotated (TPR) grid contour (Figure 8). AirMt amplitude parameter (AP) data are presented as grid contours and do not required additional grid-processing (Figure 9).

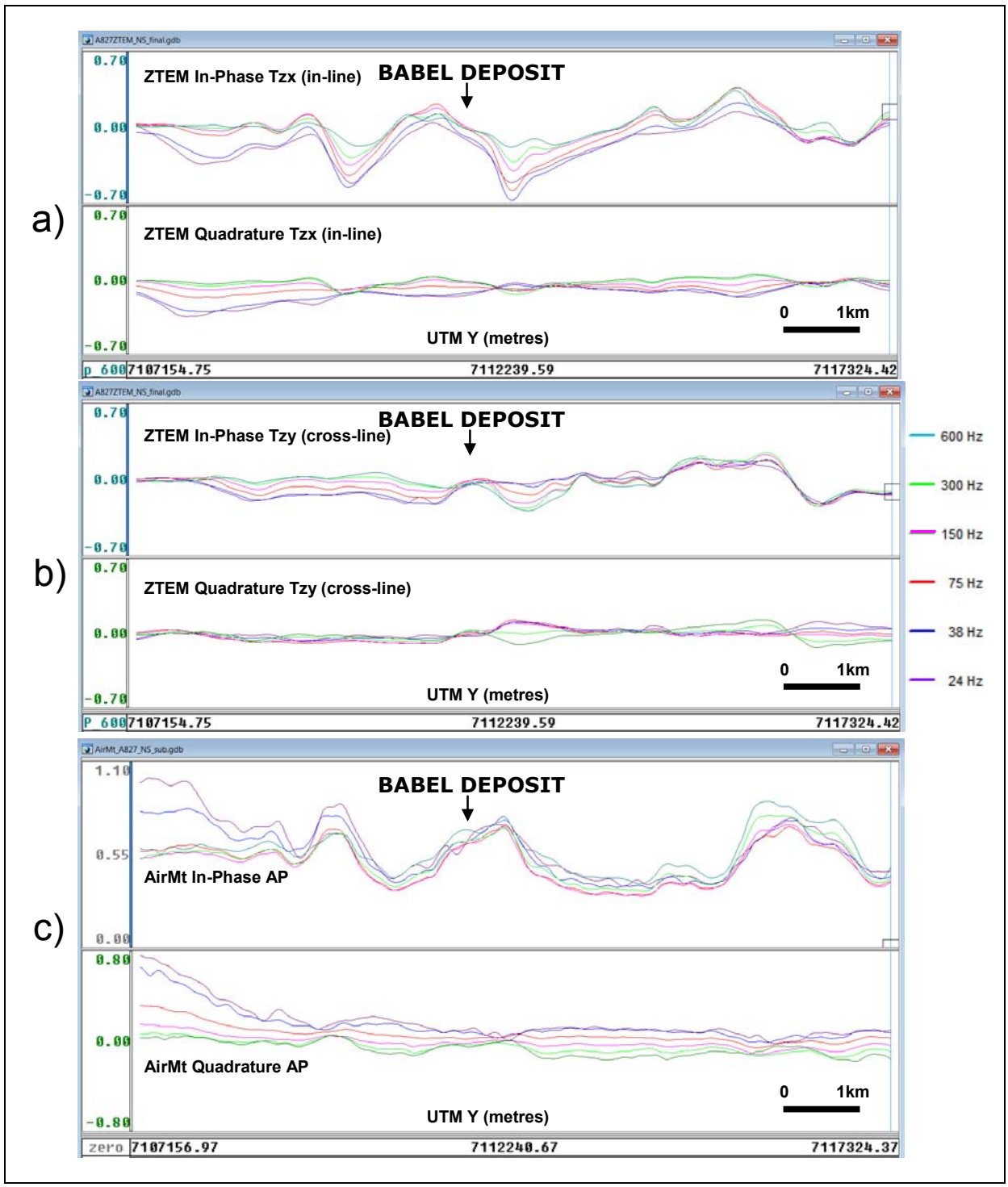

Figure 6. Multi-frequency (24-600 Hz) In-Phase and Quadrature data profiles for L1430 across the Babel Deposit, West Musgrave, Western Australia. (a) ZTEM In-line (Tzx) component (XIP & XQD), (b) ZTEM Cross-line (Tzy) component (YIP & YQD), and (c) AirMt Amplitude Parameter (AIP & AQD). (Courtesy of BHP Billiton)

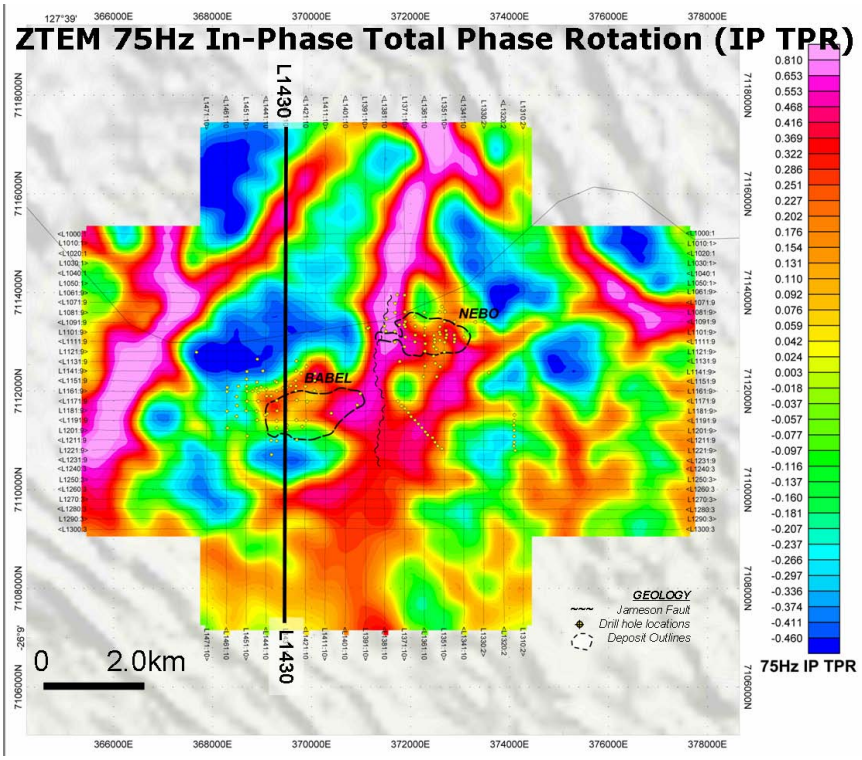

Figure 7. ZTEM 75 Hz In-Phase Total Divergence (DT) data over the Nebo-Babel deposit, West Musgrave, Western Australia, where DT = div (Tzx, Tzy) = d(Tzx)/dx + d(Tzy)/dy. (Courtesy of BHP Billiton)

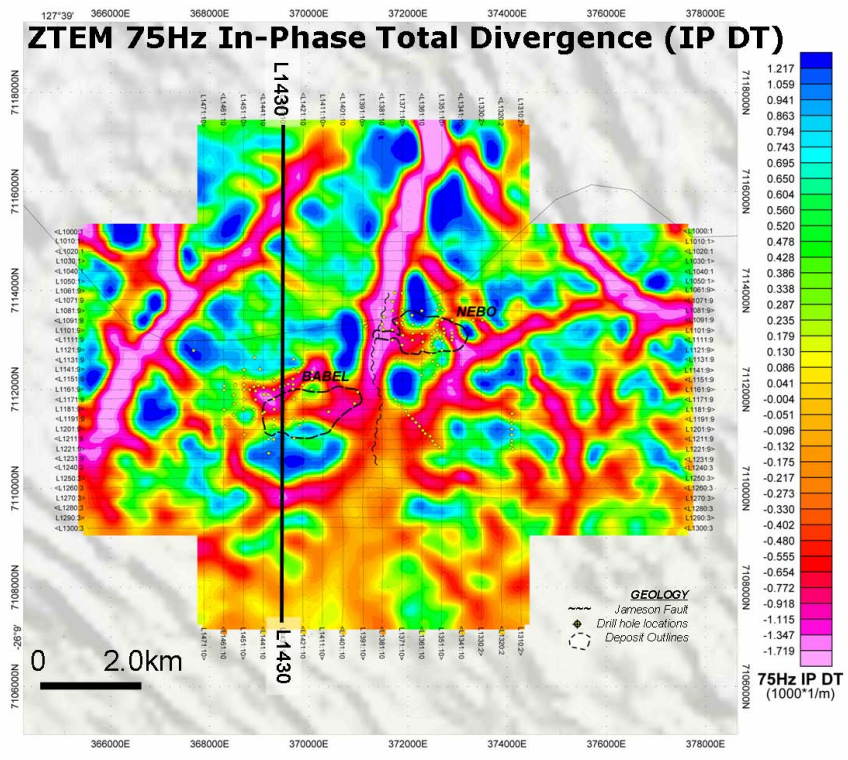

Figure 8. ZTEM 75 Hz In-Phase Total Phase Rotation (TPR) data over the Nebo-Babel deposit, West Musgrave, Western Australia. (Courtesy of BHP Billiton)

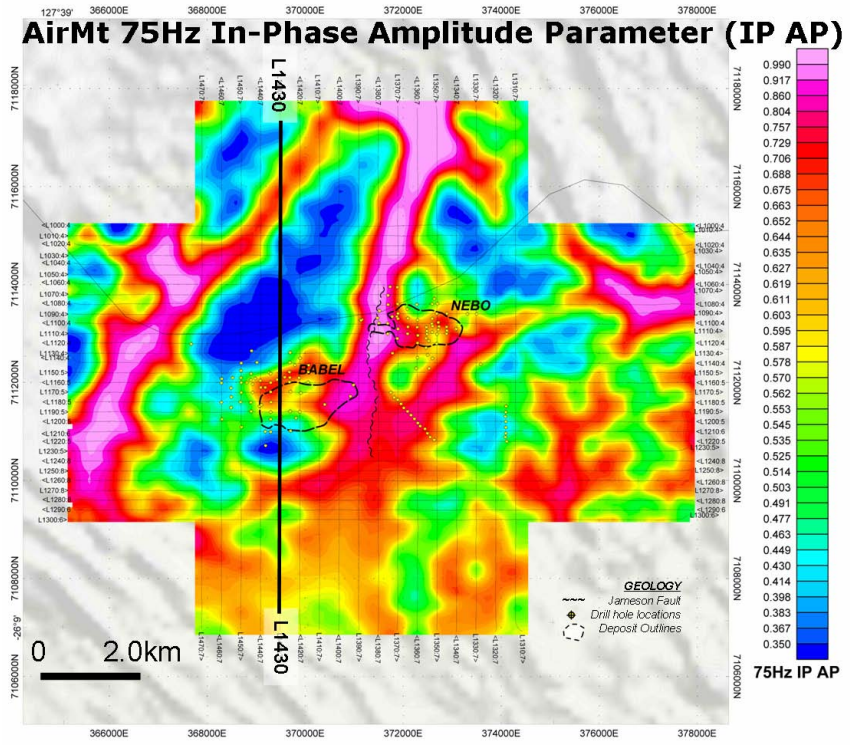

Figure 9. AirMt 75 Hz In-Phase Amplitude Parameter (AP) data over the Nebo-Babel deposit, West Musgrave, Western Australia. (Courtesy of BHP Billiton)

Geotech's standard survey deliverable products for ZTEM and AirMt include a survey logistics report and DVD with digital data that include Geosoft based geo-referenced databases, multi-frequency/multi-component profile maps, plus related total divergence and phase rotation grids.

Geotech also offers advanced interpretative products and services from our in-house Interpretation Services group which includes a suite of data processing, interpretation products and services to support its VTEM electromagnetic, ZTEM and AirMt AFMAG, aeromagnetic-gradiometric and spectrometric data acquisition surveys.

Services for passive EM methods include 2D-3D forward modeling and inversion, as well as related magnetic and gravity data, for drill-targeting. Interpretation reporting suitable for mineral assessment filing are available as options to standard deliverables. Optional additional products include:

- ZTEM post-processing including EM picking, Karous-Hjelt current density-depth imaging, 3D resistivity grid production and resistivity depth-slicing, Geotools 2D and Emigma 3D forward modeling, and recently implemented Avert2D inversion modeling that includes topographic and receiver coil clearance corrections for AirMt and ZTEM data that was introduced in 2011.

- In addition to its proprietary Avert2D inversion modelling for ZTEM and AirMt AFMAG data (Figure 10), Geotech has partnered with Mira Geoscience and TechnoImaging to offer a more advanced 3D EM inversion capability to meet its clients' needs. This relationship is expected to develop new products for release in 2012.

- Magnetic post-processing for Geotech's VTEM Hgrad and Heligrad systems including the total horizontal gradient and tilt-angle derivative, that can be derived from the measured cross-line and calculated in-line and vertical gradients.

- Geotech also offers 3D magnetic modeling and inversion using UBC-GIF 3D magnetic inversion code, as well as potential field analyses based on the Geosoft Oasis Montaj Magmap toolbox.

Geotech developed the Avert2d 2D Gauss-Newton inversion based upon modifications to algorithms by Wannamaker et al. (1987), de Lugao and Wannamaker (1996), and Tarantola (1987). Third parties provide additional products such as 2D pseudo-sections by Karous-Hjelt filters (e.g., Sattel et al., 2010) or 2D Occam inversions based on their own modifications of algorithms by Wannamaker et al. (1987) and Constable et al. (1988). Mira Geoscience offers the 3D ZTEM inversion introduced by Holtham and Oldenburg (2010) and modifications of the 3D MT inversion by Farquharson et al. (2002). TechnoImaging also provide their own 3D MT inversion in support of ZTEM and AirMt that is based on the work of Zhdanov et al. (2011).

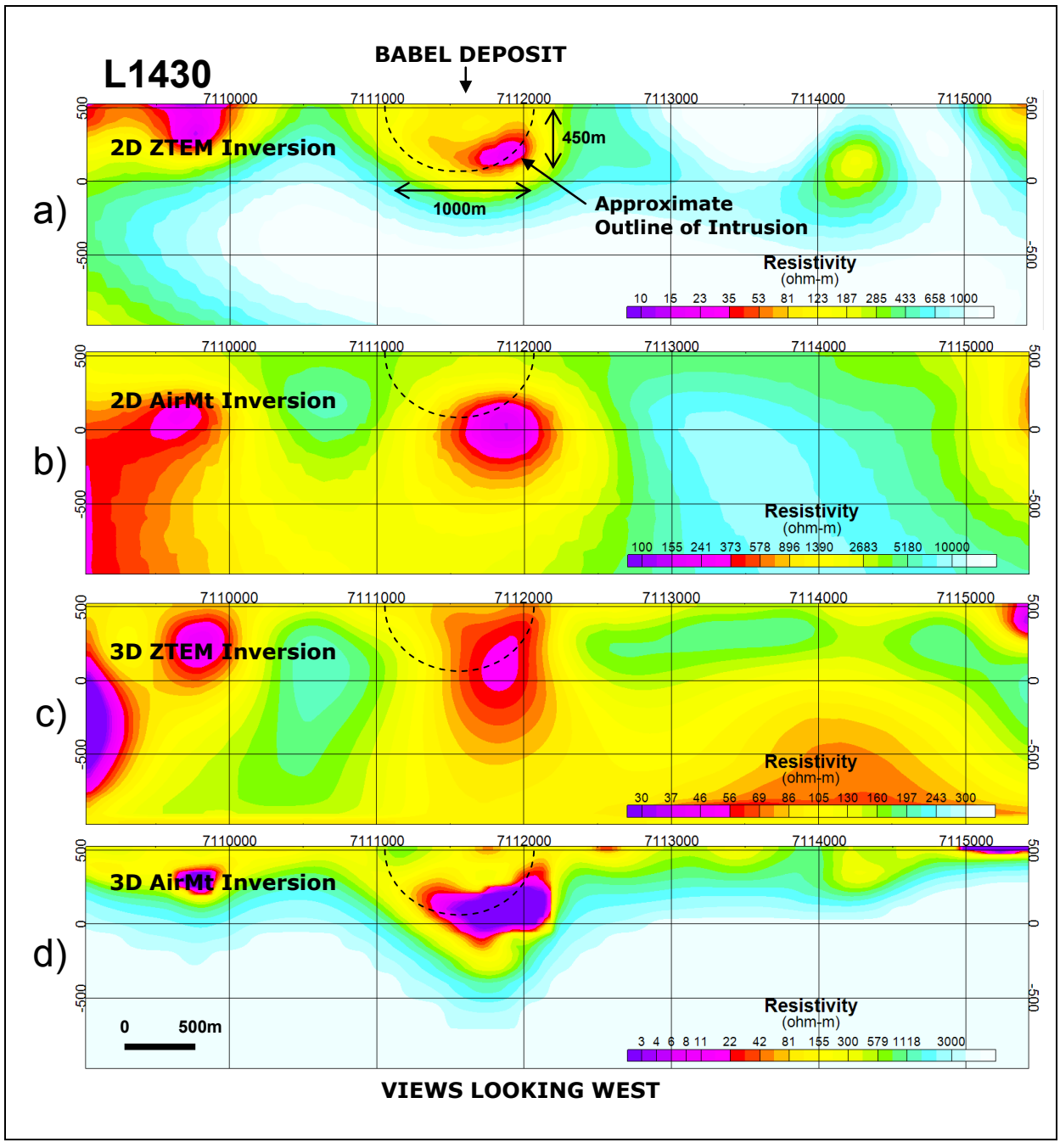

Figure 10. Resistivity cross-sections over the Nebo-Babel deposit, West-Musgrave, Western Australia. (a) ZTEM 2D Inversion, (b) AirMt 2D Inversion, (c) ZTEM 3D Inversion, and (d) AirMt 3D Inversion. (3D inversions by TechnoImaging (Salt Lake, UT); results courtesy of BHP Billiton)

Contact information

Canada

Geotech Ltd.
245 Industrial Parkway North, Aurora, Ontario L4G 4C4, Canada

P: +1 (905) 841-5004
F: +1 (905) 841-0611
http://geotech.ca/
info@geotech.ca

Australia

Geotech Airborne Australia
Unit 1, 29 Mulgul Road Malaga, Western Australia, Australia, 6090
P: +61 (0)8 9249 8814
F: +61 (0)8 9249 8894
http://www.geotechairborne.com.au/
info@geotechairborne.com.au

References

de Lugao, P. P., and Wannamaker, P. E., 1996, Calculating the two-dimensional magnetotelluric Jacobian in finite elements using reciprocity: Geophysical Journal International, 127, 806-810.

Farquharson, C. G., Oldenburg, D. W., Haber, E. and Shekhtman, R., 2002, An algorithm for the three-dimensional inversion of magnetotelluric data: 72nd Annual International Meeting, SEG, Expanded Abstracts, 649-652.

Holtham, E., and Oldenburg, D. W., 2010, Three-dimensional inversion of ZTEM data: Geophysical Journal International, 182, 168-182.

Izarra, C., Legault, J. M., and Fontura, C., 2011, ZTEM airborne tipper AFMAG results over the Copaquire Porphyry, northern Chile: SBGF Conference Expanded Abstracts, 30, 1257-1261.

Kaminski, V. F., Kuzmin, P., and Legault, J. M., 2010, AirMt – passive airborne EM system: Paper presented at the 3rd CMOS-CGU Congress, Ottawa, Canada.

Kuzmin, P., Lo, B., and Morrison, E., 2005, Final report on modeling, interpretation methods and field trials of an existing prototype AFMAG system, for Ontario Mineral Exploration Technology Program (OMET) Project No. P0102-007b: Ontario Ministry of Natural Resources publication MRD-167, 75 pp.

Kuzmin, P. V., Borel, G., Morrison, E. B., and Dodds, J., 2010, Geophysical prospecting using rotationally invariant parameters of natural electromagnetic fields: WIPO International Patent Application No. PCT/CA2009/001865.

Labson, V. F., Becker, A., Morrison, H. F., and Conti, U., 1985, Geophysical exploration with audiofrequency natural magnetic fields: Geophysics, 50, 656-664.

Lo, B., and Kuzmin, P., 2008, Z-TEM (airborne AFMAG) as applied to hydrocarbon prospecting: Paper presented at AEM2008 – 5th International Conference on Airborne Electromagnetics, Haikko, Finland.

Lo, R., Kuzmin, P., and Morrison, E., 2006, Field Tests of Geotech's Airborne AFMAG EM System: Paper presented at the AESC 2006, Melbourne, Australia.

Lo, B., Legault, J. M., Kuzmin, P., and Combrinck, M., 2009, Z-TEM (Airborne AFMAG) tests over unconformity uranium deposits: ASEG Conference Extended Abstract.

Lo, B., and Zang, M., 2008, Numerical modeling of Z-TEM (airborne AFMAG) responses to guide exploration strategies: SEG Expanded Abstracts, 27, 1098-1101.

Pare, P., and Legault, J. M., 2010, Ground IP-resistivity and airborne SPECTREM and helicopter ZTEM survey results over Pebble copper-moly-gold porphyry deposit, Alaska: 80th Annual International Meeting, SEG, Expanded Abstracts, 1734-1738.

Pedersen, L. B., 1998, Tensor VLF measurements: Our first experiences: Exploration Geophysics, 29, 52–57.

Sattel, D., Thomas, S., and Becken, M., 2010, An analysis of ZTEM data over the Mt Milligan porphyry copper deposit, British Columbia: 80th Annual International Meeting, SEG, Expanded Abstracts, 1729-1733.

Tarantola, A., 1987, Inverse problem theory: Elsevier, Amsterdam.

Thomson, S., Fountain, D., and Watts, T., 2007, Airborne geophysics – evolution and revolution: In "Proceedings of Exploration 07: Fifth Decennial International Conference on Mineral Exploration", edited by B. Milkereit, 19-37.

Wannamaker, P. E., Stodt, J. A., and Rijo, L., 1987, A stable finite element solution for two-dimensional magnetotelluric modeling: Geophyiscal Journal of the Royal Astronomical Society, 88, 277-296.

Ward, S., 1959, AFMAG – airborne and ground: Geophysics, 24, 761-787.

Witherly, K., Irvine, R., and Morrison, E. B., 2004, The Geotech VTEM time domain helicopter EM system: SEG Expanded Abstracts, 23, 1217-1221.

Zhdanov, M. S., 2002, Geophysical inverse theory and regularization problems: Elsevier, Amsterdam.

Statement of Capability - Moombarriga Geoscience Pty Ltd

Shane Evans [1]

[1] *Moombarriga Geoscience Pty Ltd (shane@moombarriga.com.au)*

Introduction

Moombarriga Geoscience is owned and operated by Shane Evans. The company was formed in 2005 and commenced acquisition services in 2008. The company name, “Moombarriga”, is the Noongaar (indigenous people of the southwest of Western Australia) translation for “cherry tree” - with “Cherry Tree Farm” being the name of the farm that Shane grew up on.

Shane has a Bachelors degree with honours in geophysics from Curtin University and a Masters degree from Queens University in Canada where he used the magnetotelluric technique to study the boundary between the Rae Craton and the Trans Hudson Orogen in Northern Canada. Prior to forming Moombarriga Geoscience, Shane worked in the DeBeers Geoscience Centre in Johannesburg, using magnetotellurics to map Archean craton boundaries through Africa and Canada to assist in targeting for diamond exploration.

Products and services

Moombarriga Geoscience is a Perth-based company that provides services for acquisition, processing and interpretation of magnetotelluric (MT), audio-magnetotelluric (AMT) and electromagnetic (EM) data. The company operates within Australia and internationally.

Data Acquisition

Moombarriga Geoscience uses Phoenix MTU-5A data acquisition units for the acquisition of full-tensor MT and AMT data (Figure 1). The rugged and compact design allows these units to be operated in remote areas and they can be left to record unattended for up to two weeks. GPS synchronization allows multiple stand-alone units to be deployed simultaneously, facilitating the recording of remote reference data. Low noise magnetic induction coils (Phoenix MTC-80, MTC-50 and MTC30 models, Figure 1) are used to measure natural magnetic field changes in the 300 to 0.001 Hz frequency range for MT measurements and 10,000 to 5 Hz range for AMT measurements. More detailed information for these systems can be found on the Phoenix Geophysics website (link provided in the references).

Field staff perform QC on the data recovered from each site by inspection of times series and power spectra. Remote reference processing is performed daily on all acquired data. Processed data are delivered to the client in industry standard EDI format.

Moombarriga Geoscience uses a SMARTem24 unit built by EMIT (Electromagnetic Imaging Technology) for the acquisition of EM data (Figure 1). Further information regarding these units can be found on the EMIT website (link provided in the references). GPS synchronisation, 24 bit ADC’s, full time-series recording, long-life batteries, a library of customisations for many different sensors, and a bright colour touch screen are features that make the SMARTem24 instrument an appropriate choice for simple, efficient, and reliable field operations.

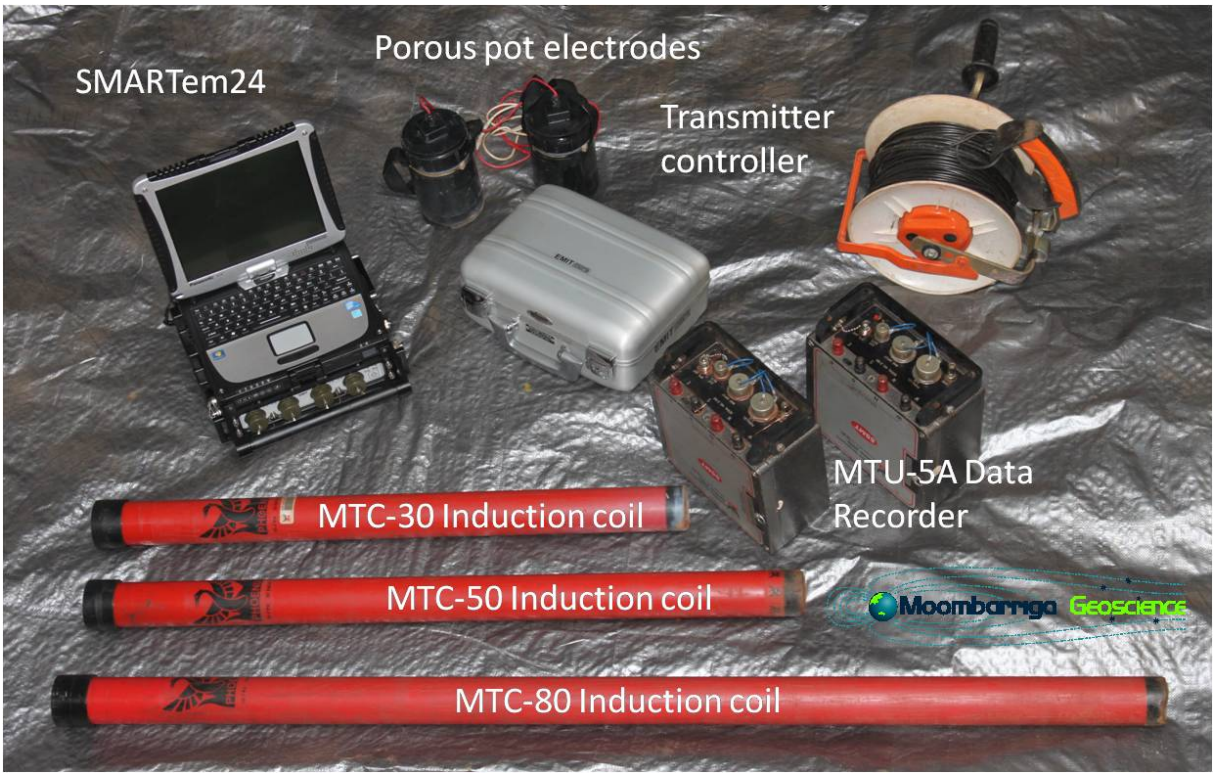

Figure 1. Photograph of a selection of the field equipment used by Moombarriga Geoscience to acquire MT, AMT and EM data.

Consulting

Although Moombarriga Geoscience is predominantly an acquisition business, we do offer consulting services for the modeling, interpretation and QC of MT data. Moombarriga Geoscience uses commercial and in-house software for 2D and 3D inversion.

Contact information

Australia

Moombarriga Geoscience Pty Ltd
32 Townshend Rd, Subiaco, 6008, Western Australia, Australia
PO Box 1184, West Perth, 6872, Western Australia, Australia
P: +61 (0)8 9388 9922
F: +61 (0)8 9388 0066
ABN: 25259685138
ACN: 116723516
www.moombarriga.com.au

Shane Evans
shane@moombarriga.com.au

References

Electromagnetic Imaging Technology (EMIT) website. Accessed 10 January 2012 http://www.electromag.com.au.

Phoenix Geophysics website. Accessed 10 January 2012. http://www.phoenix-geophysics.com.

Statement of Capability - Phoenix Geophysics Limited

Damien Fox [1]

[1] *Phoenix Geophysics Limited (dfox@phoenix-geophysics.com)*

Introduction

Founded in 1975 in Toronto, Canada, Phoenix Geophysics Limited is a geophysical instrumentation and services company.

Electromagnetic products and services

Phoenix has manufactured and exported both natural-source (MT/AMT) and controlled-source (CSEM) equipment to over 80 countries.

Phoenix electromagnetic instruments have been used in a wide variety of applications that include the following:

- Petroleum applications
  - Providing great depth of exploration, small equipment footprint, minimal environmental disturbance, and flexible deployment.
  - Complementing seismic in areas where high quality seismic information is difficult to acquire.
  - Providing rapid reconnaissance of new basins where seismic is expensive or difficult to acquire.
  - As a direct indicator of hydrocarbons under some circumstances.
- Minerals applications
  - Exploration for coal, diamonds, uranium, other base and precious metals, and industrial minerals.
- Geothermal applications
- Groundwater applications
- Engineering applications
  - Including dam site studies, railway tunnel planning, and mining hazards prediction (e.g., water flooding).
- General crustal mapping and research applications
  - Including earthquake prediction research and crustal mapping.

Contact information

Canada

Phoenix Geophysics Limited
3781 Victoria Park Avenue, Unit #3
Toronto, Ontario, Canada
M1W 3K5

P: +1 416 491 7340
F: +1 416 491 7378
www.phoenix-geophysics.com

contact@phoenix-geophysics.com

Statement of Capability - Quantec Geoscience Ltd.

Trent Retallick [1]

[1] *Quantec Geoscience Pty. Ltd. (tretallick@quantecgeoscience.com)*

Introduction

Quantec Geoscience Ltd. (Quantec) was formed in 1986 as a service provider for the mineral, geothermal, and oil and gas exploration markets. It specialises in the design, acquisition, modelling and interpretation of data for ground-based, non-seismic geophysical surveys. More than 3500 projects have been completed during the 25 years of operations.

The company operates from a large number of global locations;
Quantec Geoscience Ltd. - Toronto, Ontario, Canada (head office)
Quantec Geoscience USA Inc. - Reno, Nevada, USA
Quantec Geoscience Argentina S.A. - Mendoza, Argentina
Quantec Geoscience Chile Ltda. - Santiago, Chile
Quantec Geoscience (Peru) S.A.C. - Arequipa, Peru
Quantec Geosciencia de Mexico - Hermosillo, Mexico
Quantec Geoscience Pty. Ltd. - Queensland, Australia
Quantec International Project Services - Barbados

Products and services

Quantec's original ground geophysical survey suite was based on conventional technologies (i.e., IP, TDEM, DHEM, gravity, magnetics, CSAMT, DHIP) – services that are still provided on a global basis through the company's network of offices around the world. In 2000, the company developed the "Titan 24" Deep Earth Imaging system. Since 2000, more than 500 Titan 24 surveys have been completed. The "Spartan Magnetotellurics" ("Spartan MT" system) was developed to provide imaging where even greater depth penetration than can be achieved with the Titan 24 system is required. At present, the "Titan 3D" 3D DCIP acquisition and modelling system is being rolled out across the company. This latter system can be configured to acquire MT data in combination with DCIP data.

Quantec is an integrated geophysical services and consulting group that can provide survey design, data acquisition, processing, modelling, data integration, and interpretation services for survey data acquired by Quantec or for data obtained from third-party surveys.

Data Acquisition

Quantec provides surveys utilizing proprietary Titan 24, Titan 3D and Spartan MT systems as well as MLEM, FLEM, DHEM, IP, DHIP, CSAMT, gravity and ground magnetics surveys.

Data Processing

Using full waveform results from Titan 24, Titan 3D and Spartan MT surveys, processors have the opportunity to remove noise and improve data quality through post-acquisition processing. Quantec can also re-process data from pre-existing surveys or from surveys conducted by other contractors as required.

Modelling

Quantec can perform 1-D, 2-D, 3-D and 4-D modelling. The modelling software is a combination of commercial programs and in-house programs specifically developed for the Titan 24 and Spartan MT systems.

Interpretation

Quantec actively involves clients in the interpretation process. Interpretations progress through an iterative cycle whereby they are presented and then refined through interactive client discussions before being recorded in a final interpretation report. Interpretations and interpretation products can be provided on request for conventional surveys.

Data Integration

It is deemed essential to integrate results from geophysics with the other available information such as geology and geochemistry. Quantec uses applications including GOCAD and other commercially available software packages to either integrate data from clients or to provide data in a format that can be easily integrated with other results by the client's personnel.

Consulting

Quantec can also provide a number of more general consulting services to meet client requirements for exploration programs, survey designs, or advice on technologies most suited to specific exploration projects.

Proprietary products and services

Titan 24 DCIP and MT systems

Titan 24 is the name given by Quantec to a multi-channel, multi-parameter, distributed acquisition system (DAS) that can be used to record broad-band tensor audio-magnetotelluric data, DC resistivity data, and induced polarization data (Figure 1). It is used with large, multi-channel, fixed receiver arrays in combination with a wide variety of possible current injection arrays, and provides 24-bit sampling of received signals to maximise the quality of the recorded signals and to thus maximise the opportunity to record the response from target features (Figure 2). Target detection and delineation is further enhanced through acquisition with a data spatial density that is up to four times higher than conventional IP surveys, full-waveform digital signal recording and processing, and application of 2D-3D forward and inverse modelling of processed data.

The Titan 24 system can measure three data parameters: DC resistivity, Induced Polarization, and tensor MT resistivity. The system can operate in one of three modes; full Titan 24 mode (i.e., acquiring both DCIP and MT data), Titan 24 IP only (i.e., acquiring only DCIP data), and Titan 24 MT only (i.e., only acquiring MT data). In full Titan 24 mode, active source DCIP and passive, natural field EM measurements are acquired sequentially.

Figure 1. Photographs of (a) a Titan 24 array reading being taken in an operating pit in South Africa, and (b) a Titan 24 receiver and battery linked into an array for a survey in Greenland.

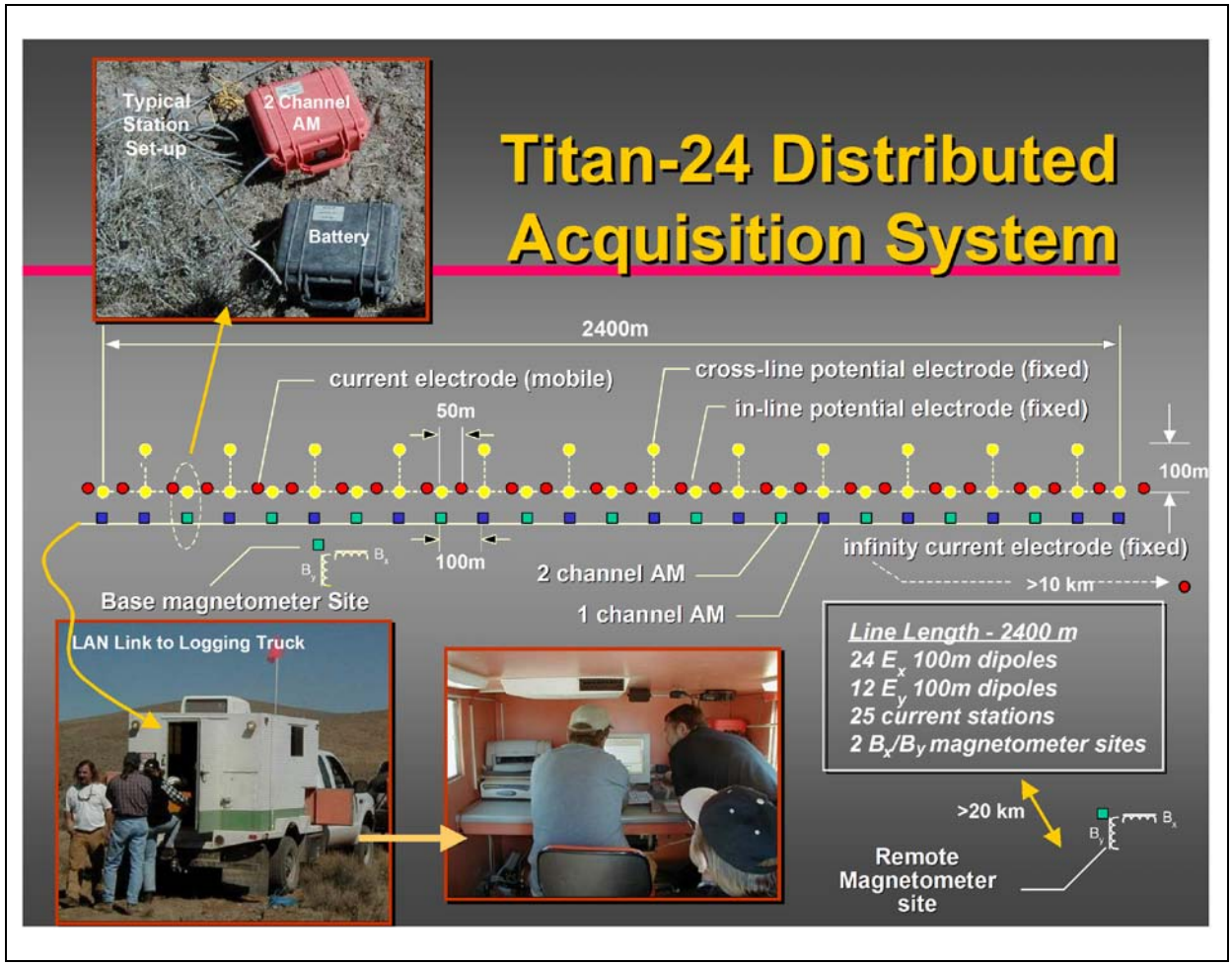

Figure 2. Schematic diagram showing the Titan 24 layout, snapshots of Titan 24 units, and a central recording truck.

Titan 24 DCIP data can be acquired using different survey configurations depending on the survey objectives and budget. The coverage provided with 2 different configurations is illustrated in Figure 3.

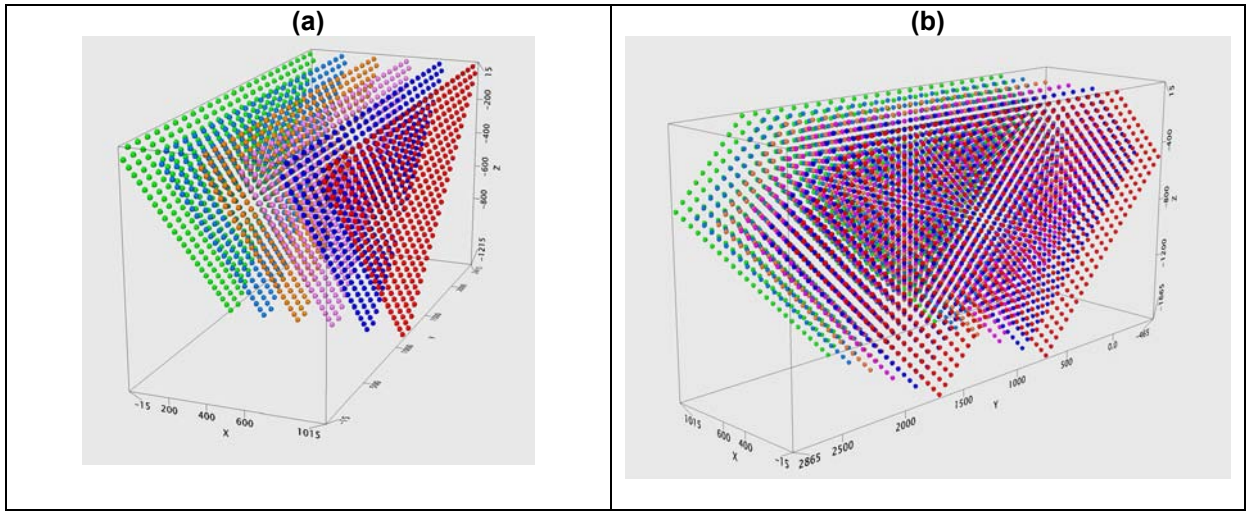

Figure 3. Schematic diagrams showing plotting points for different Titan-24 arrays. (a) Standard configuration, and (b) configuration with current extensions.

Titan 3D

Titan 3D incorporates elements of both the Titan 24 and Spartan MT systems. It was designed for high resolution DC resistivity and IP chargeability acquisition utilising 24-bit acquisition technology and full waveform recording. The system can acquire data with very high density spatial sampling, providing high resolution 3D imaging of the subsurface (Figure 4). At the same time, a high density sampling of the MT field is acquired at all logger locations.

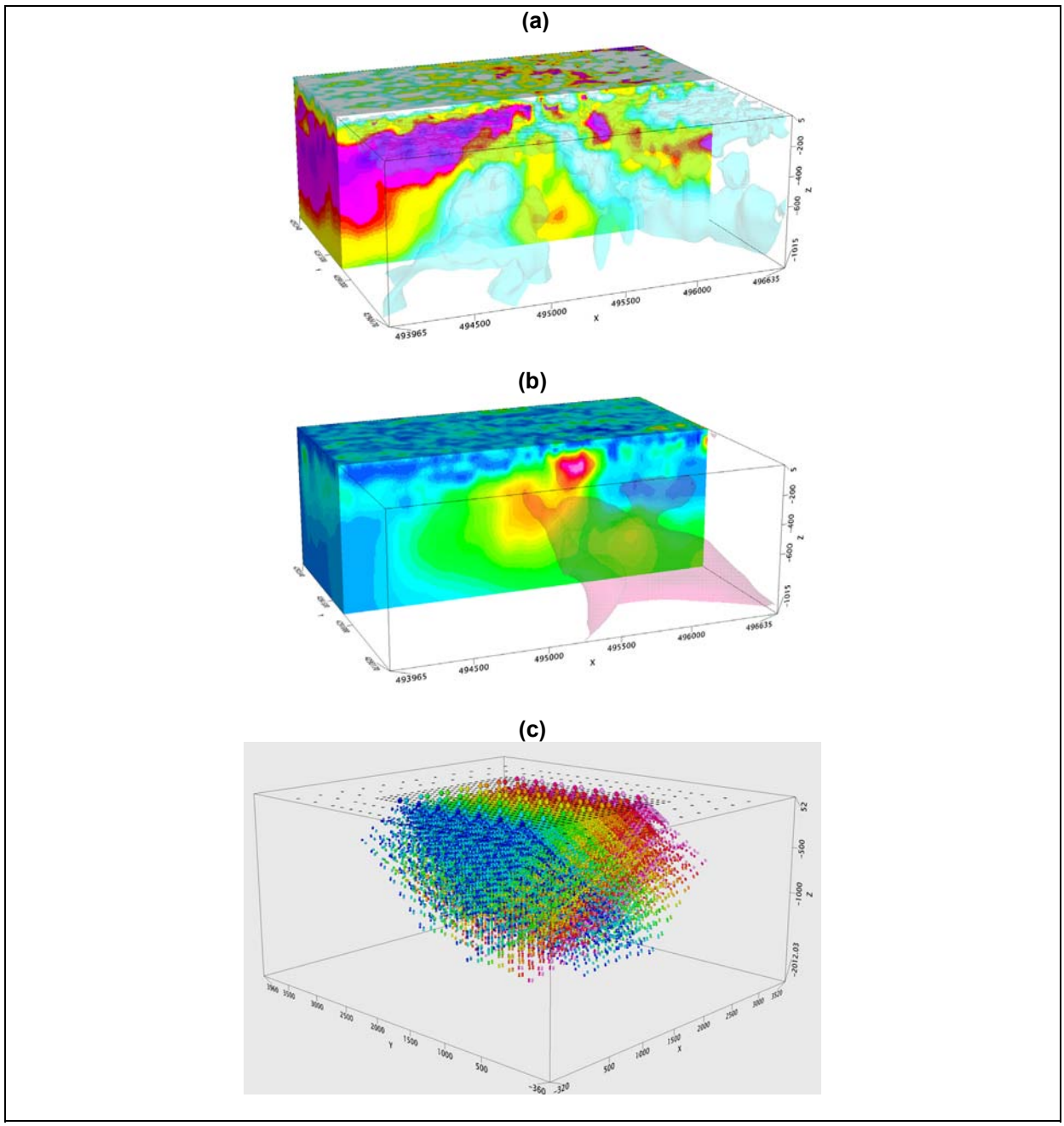

Figure 4. Examples of (a) Titan 3D data, (b) corresponding Titan 3D model results, and (c) the Titan 3D DCIP plotting points.

The choice of dimensions for the array and the dipole size reflects the geologic challenge at hand. If high resolution but shallower depths of investigation only are required and/or smaller anomalous bodies are to be detected, the use of array and dipoles with 50 m dimensions is appropriate. Standard 100 m dipoles allow acquisition of IP and DC resistivity information to depths of 750 m to 1000 m in a typical environment, whilst use of 200 m dipoles will provide results even deeper than this. Data acquired on Titan 3D DCIP and MT surveys are typically recorded over a 24 hour period.

Spartan MT

Quantec's Spartan MT system (Figure 5) provides a method for obtaining deep resistivity over a variety of terrains. With high portability and flexibility of station distribution, Spartan MT is environmentally friendly and non-invasive, with depths of investigation from surface to 10,000 metres and beyond.

Spartan MT is a full tensor MT system using a combination of proprietary receiver unit hardware and software in combination with commercially available magnetic field coils and standard electric field dipole sensors. The system is remotely referenced and timing is synchronized using GPS clocks. The effective operating range is 0.001 Hz to 300 Hz.

Figure 5. Typical Spartan MT station set up.

The robust and highly portable Spartan MT system can be used to acquire data for many different applications including;

- Deep terrain-scale structural mapping
- Evaluation of the potential for large-area targets
- Electrical imaging of targets in environmentally-sensitive, rugged and remote terrains
- Geothermal exploration
- Oil and Gas exploration

Quality Assurance (QA / QC)

For any of the Titan, Titan 3D, or Spartan systems, an on-site processor performs first-pass QC and data reduction procedure. Results are also checked daily by a senior geophysicist from the Interpretation Group based in Toronto, Canada. All MT data are acquired using remote reference sites. Data are processed on-site and undergo coherent noise evaluation using remote reference information, digital filtering using proprietary in-house software, coherency sorting, and impedance estimate stacking.

Contact information

Australia

Quantec Geoscience Pty. Ltd.
PO Box 276, Ashgrove, QLD, Australia, 4060

P: +61 7 3359 0444
F: +61 7 3359 0011
M: +61 410 529 992
www.quantecgeoscience.com

Trent Retallick - General Manager Australia - Quantec Geoscience Pty. Ltd.
tretallick@quantecgeoscience.com

Statement of Capability – The University of Adelaide

Graham Heinson [1], Stephan Thiel [2], and Goran Boren [3]

[1] *The University of Adelaide (graham.heinson@adelaide.edu.au)*
[2] *The University of Adelaide (stephan.thiel@adelaide.edu.au)*
[3] *The University of Adelaide (goran.boren@adelaide.edu.au)*

Introduction

The University of Adelaide hosts the AuScope National MT facility under the National Collaborative Research Infrastructure Scheme (NCRIS). The Facility comprises approximately 25 broadband MT sets and up to 40 long-period MT sets, along with access to training, software, and assistance with analysis. Access to the Facility is by proposal to the ANSIR National Research Facility for Earth Sounding. Proposals must be eligible research projects as assessed by the ANSIR access committee. Note that purely commercial projects are not usually considered eligible.

Bartington 3-axis fluxgate sensors are available for long-period measurements, and KMS LIC-120 land induction coil magnetometers for broadband measurements. Data are recorded on PR 6-24 Portable Earth Data recorders with GPS timing synchronisation.

Over the last three years, the facility has been used by Geoscience Australia (Duan, 2011a, 2011b; Milligan, 2011), three of the Australian State Government Geological Surveys, and four Universities. The University of Adelaide group are also working with GA and with State Geological Surveys to make prior data available.

References

ANSIR website. Accessed 18 January 2012. http://rses.anu.edu.au/seismology/ANSIR/ansir.html

AuScope website. Accessed 18 January 2012. http://auscope.org.au/site/index.php

Duan, J., 2011a, Gawler-Officer-Musgrave-Amadeus Magnetotelluric Survey - Processed EDI files and support data from sites associated with 08GA-OM1 seismic traverse: Geoscience Australia Data Download, Catalogue Number 72890. Accessed 18 January 2012. https://www.ga.gov.au/products/servlet/controller?event=GEOCAT_DETAILS&catno=72890

Duan, J., 2011b, Georgina-Arunta Magnetotelluric Survey - Processed EDI files and support data from sites associated with 09GA-GA1 seismic traverse: Geoscience Australia Data Download, Catalogue Number 72889. Accessed 18 January 2012. https://www.ga.gov.au/products/servlet/controller?event=GEOCAT_DETAILS&catno=72889

Milligan, P. R., 2011, Gawler Craton Magnetotelluric Survey - Processed EDI files and support data from sites associated with 08GA-G1 seismic traverse: Geoscience Australia Data Download, Catalogue Number 72862. Accessed 18 January 2012. https://www.ga.gov.au/products/servlet/controller?event=GEOCAT_DETAILS&catno=72862

NCRIS website. Accessed 18 January 2012. http://ncris.innovation.gov.au/Pages/default.aspx

Contact information

Australia

The University of Adelaide
School of Earth and Environmental Sciences
North Terrace Campus
Adelaide, South Australia, 5005, Australia

P: +61 (0)8 8303 5377
F: +61 (0)8 8303 4347

Graham Heinson
Graham.Heinson@adelaide.edu.au

Stephan Thiel
Stephan.Thiel@adelaide.edu.au

Goran Boren
Goran.Boren@adelaide.edu.au

Statement of Capability – WesternGeco Land EM

Efthimios Tartaras [1]

[1] *WesternGeco Geosolutions (etartaras@slb.com)*

Introduction

WesternGeco's EM group has more than 27 years experience as a geophysical contractor. Originally formed as Geosystem in 1982, the company was acquired by Schlumberger in 2007 and is now part of the WesternGeco Integrated EM Center of Excellence, based in Milan, Italy (Schlumberger press release, 2007).

Our Land EM group provides geophysical services to the Mining, Geothermal and Oil&Gas industries and has carried out operations in more than 35 countries.

We specialize in the acquisition and interpretation of MT data for the exploration industry, focusing on developing and delivering 24-bit instrumentation, robust processing and both 2D and 3D inversion modelling. We also acquire and process time-domain EM (TDEM) and controlled-source EM (CSEM) data.

Our experience extends to gravity exploration projects and geophysical data integration. We employ proprietary algorithms for simultaneous joint inversion (SJI) of seismic, MT and gravity data, and our proprietary WinGLink® software is the worldwide industry standard for MT data modelling and inversion.

Our data interpretation capabilities extend beyond qualitative methods to full 3D inversion modelling that can be constrained using seismic or other available geological or geophysical information. During the last 5 years alone, we have carried out 3D modelling and interpretations of over 150 MT surveys in diverse environments from the geothermal, mining and petroleum sectors.

Products and services

Data acquisition for MT surveys

Prior to carrying out a survey, we undertake a reconnaissance of the field area to identify the main access routes, meeting points and the likely EM noise sources, and we choose a suitably quiet and secure MT remote reference site. Each MT crew operates two 5-channel full-tensor MT systems (Figure 1). Each crew deploys 2 overnight MT recordings (14 hours duration) per 24 hours.

We use the following equipment:

- 5-channel, GPS-synched Metronix ADU-06 / 07 or Phoenix MTU-5a MT recording units (>50)
- MFS-06/MFS-07 Metronix broadband induction coils
- Wolf non-polarizable Pb/PbCl electrodes

The Metronix ADU-06 / 07 and Phoenix MTU-5a systems are used by WesternGeco in conjunction with the broadband Metronix MFS-06 and MFS-07 coils, offering standard broadband recording of AMT and MT data at all sites without requiring separate AMT and MT coils. Most commercially available AMT coils have an optimum (flat) response from high frequencies down to around 1 Hz, decreasing thereafter to a lower frequency limit at or before 0.1 Hz. Via software control, switching in a chopper amplifier for low frequencies allows the MFS coils to offer optimal response from 10,000 Hz down to 0.001 Hz. The MFS-06 coil has an identical electronic construction as the MFS-07 but is physically longer and sensitive to frequencies down to 0.0003 Hz.

In areas of high electrical contact resistance (e.g., dry sandy, volcanic, carbonate or other hardrock surface), WesternGeco deploys custom-made buffer amplifiers. These ameliorate phase distortion and noise issues for contacts up to 5 Mohm.

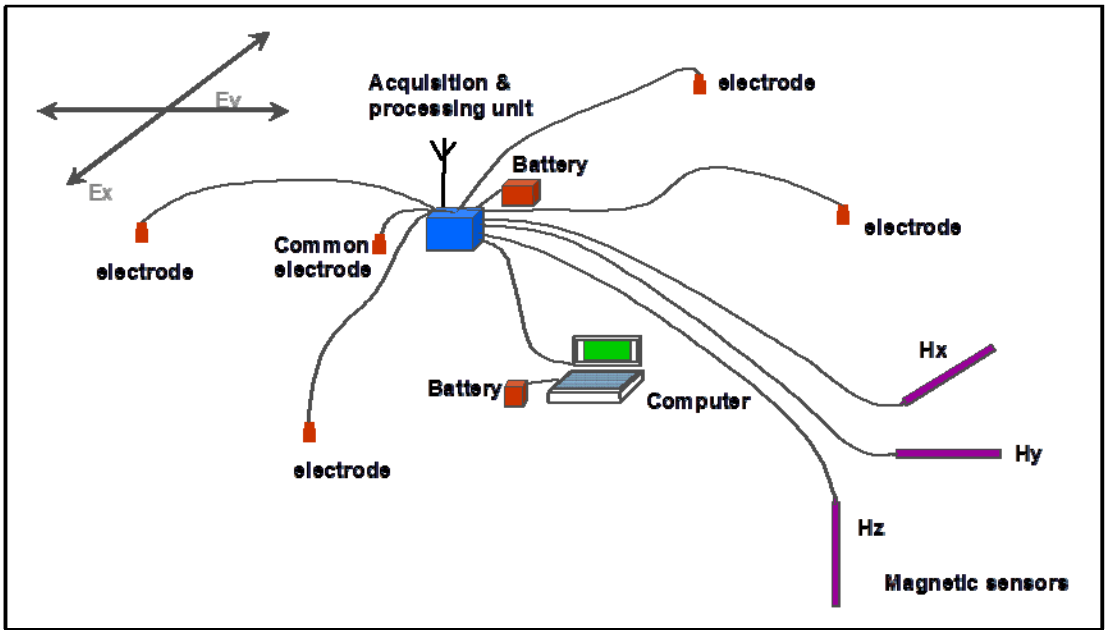

Figure 1. Schematic diagram of a 5-channel MT layout. The total system weight is 45 kg, including the 12 V, 24 Ah sealed battery. The field computer is present only during site set-up and data downloading, otherwise it remains with the operator. Auxiliary tools include machete, shovel and pick, water jugs, and backpacks.

The system operates over a 7-decade frequency band 0.001 to 10,000 Hz, equivalent to a depth range under typical conditions of 30 m to more than 10 km. The low power system hardware can operate on an external 12 volt battery without interruption for up to 4 days.

Field data are acquired using orthogonal pairs of electrical field sensors (grounded wire dipole) and magnetic field detectors (induction coils), carefully installed at surface and buried at least 30 cm to minimize disturbance during recording. The station installation normally takes 45 minutes, and consists of stretching the 4 x 50 m long wires, and burying and aligning induction coil magnetometers. Signals detected are continually streamed into the digital recording system (Figure 2).

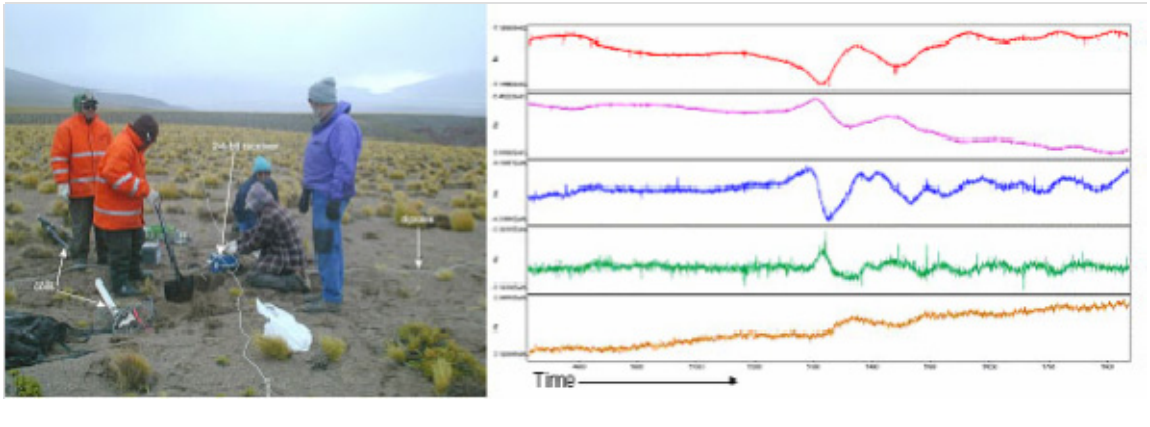

Figure 2. Data Acquisition. A 5-channel MT set-up along with a data example of time series; duration 1024 seconds. From top to bottom, channels are Ex, Ey, Hx, Hy, Hz.

Stations are simultaneously deployed for overnight recording, for periods of 12-16 hours. The data quality is influenced by the ratio between natural EM field signal levels and background (cultural) EM noise, but 14 hours is normally sufficient for recovery of good quality data over a wide spectrum. In order to provide for elimination of any local EM noise, MT data are recorded at a parallel system

installed at a remote and quiet location. This location is chosen to be at least 25 km away depending on the local noise content. Data are downloaded from the recorders at intervals during the acquisition run for QC, and at the end of each sounding's full recording. The data are then taken to the field office for processing on-site.

Data processing for MT surveys

Processing of MT time series field data is based on the Larsen and Chave robust remote-reference method (Chave et al., 1987; Larsen, 1989). This is a sophisticated approach that includes pre-filtering to remove harmonic noise (line frequencies from powerlines) and de-spiking to remove the effects of very close (non-plane wave) lightning spikes, if present. The output files are stored in standard SEG EDI format. Data is processed to EDI format within 24 hours of acquisition, and e-mailed to our offices in Milan for analysis and interpretation. Example MT curve plots are shown in Figure 3.

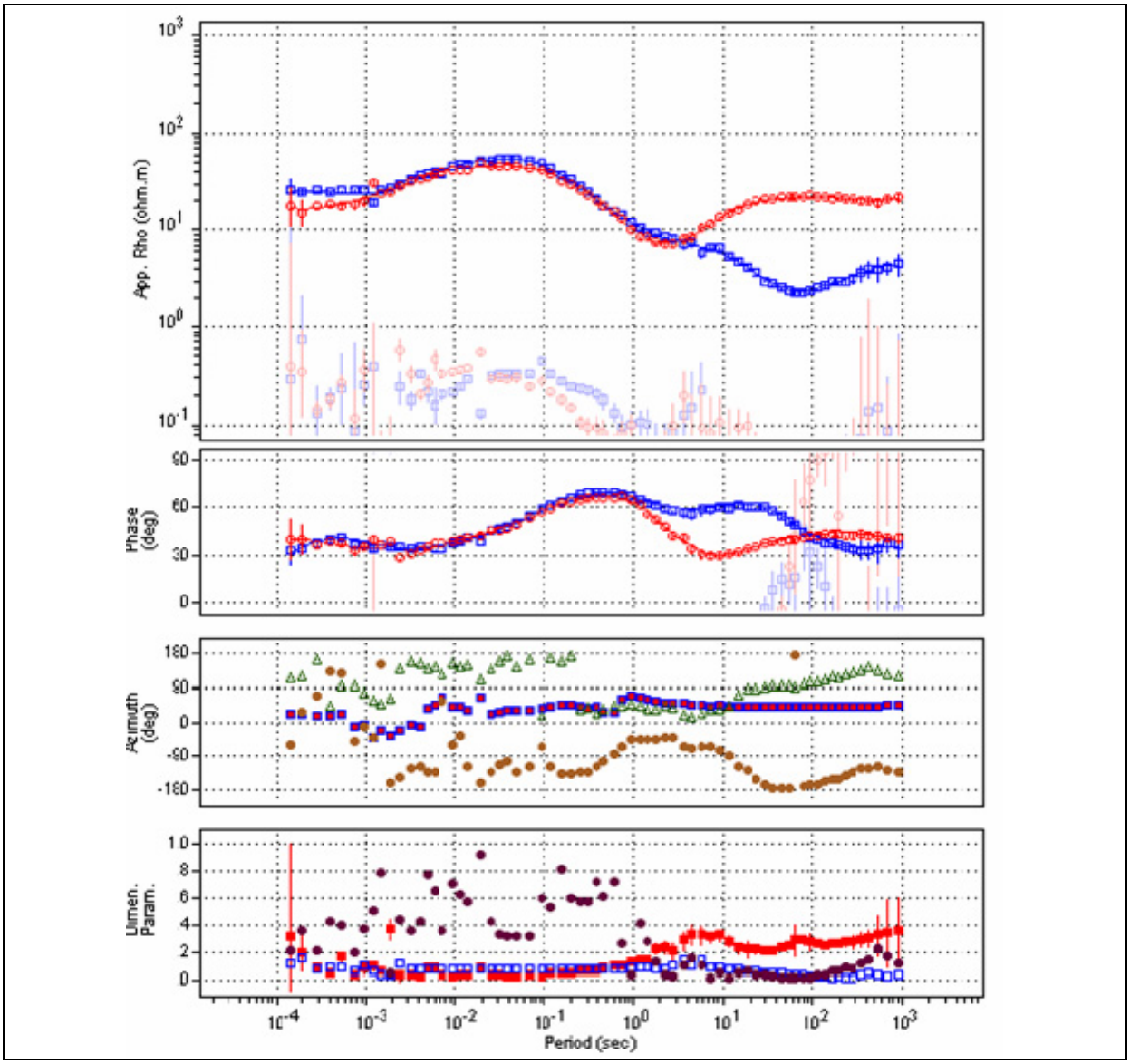

Figure 3. Example of typical data for an MT sounding from a deep geothermal MT survey. Rotation to principal axes, Impedance Apparent Resistivity and Phase for Zxy, yx, xx, and yy components are shown in red, blue, faint red and faint blue in the upper two windows. Impedance rotation (purple), Impedance Strike (green) and Induction Angle (real component, brown) azimuth are shown in the 3rd window, whilst Tipper Magnitude (red) and Impedance Skew (blue) and Impedance Ellipticity (purple) are shown in the lowermost, 4th window. The smooth line is the D+ solution.

2D and 3D modelling for MT surveys

The processed MT data, in the form of EDI files, are e-mailed to our Milan office for analysis and 2D (if required) and 3D modelling, including in-survey inversions. This work incorporates;

1. Editting of each MT sounding to mask data distorted by powerlines or other cultural interference; digitizing and plotting all cultural features on the MT database maps and sections;
2. 2D inversion modelling using TE, TM and Tipper modes. Static Shift included in inversion;
3. 3D modelling in-survey (optional). Preliminary 3D inversion modelling results during survey are available within 48 hours in order to permit adjustments to be made to the survey design and in-fill programs to be considered. This work is typically made after 40-50% of the survey acquisition has been completed.
4. 3D modelling post-survey (optional). Final 3D modelling includes up to 5 runs per model area in order to fine tune resistivity model sensitivity to the target area (i.e., adjusting the smoothing, horizontal vs vertical structure weighting, mesh detail, boundary conditions, etc.). Static Shift is included.

2D and 3D inversions are carried out using proprietary code that is based on the work of Rodi and Mackie (2001). Our code uses the full tensor as input (Zxy, Zyx, (+ Zxx, Zyy in 3D), and Tzx, Tzy). The mesh includes detailed topography to compute correct, full responses as seen in the measured data (Figure 4). A 90 x 90 m resolution digital topographic model (DTM) is typically available from SRTM; finer ones may be used if available from the client.

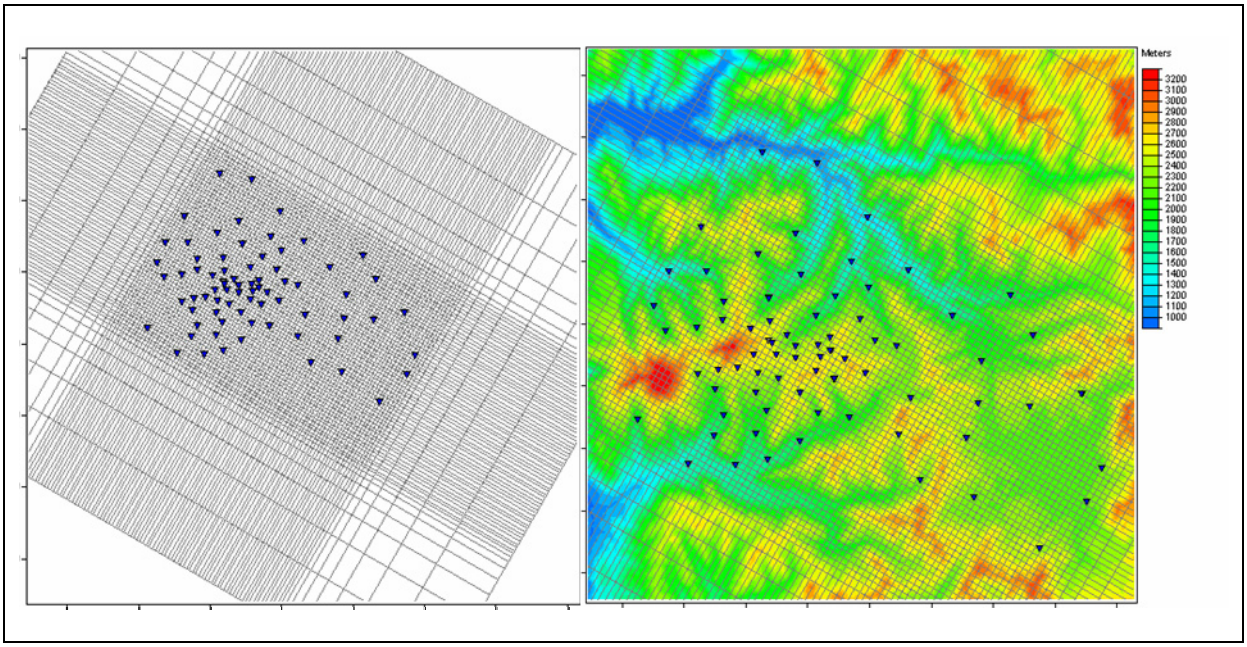

Figure 4. Plan views of an example of a 3D model mesh over a volcanic centre. On the left hand side, the tick interval is 10 km. The region of the fine mesh is centred on the MT station locations shown as blue triangles. The tick interval on the right hand side is 5 km. The colour grid is topography from a 90 m SRTM DEM).

Data acquisition for TDEM surveys

TDEM surveys are used in three main applications:

- Shallow geophysical investigations
- Estimation of MT static shifts
- Delineation of shallow weathered zone to reduce the number of upholes in seismic surveys

The crew acquires TDEM data using highly portable receiver-transmitter systems in central loop mode, powered by internal batteries. We use the Geonics PROTEM-D receiver, with fast transient turn-off TEM-47 transmitter, adapted for higher current (10 A) when required.
The transmitter-receiver loop adopted may vary from 50 x 50 m to 150 x 150 m to obtain deeper signal penetration. Single core, multi-strand wire with a 2.5 to 4 mm core diameter is employed to optimise

the transmitted current (2 to 10 A, depending on resolution required), respecting the limitations of the transmitter output (<10 A) whilst avoiding saturation of the receiver voltage. The effective PROTEM time decay bandwidth ranges from 0.003 to 100 ms, providing adequate coverage for the target depths.

Data processing for TDEM surveys

The systems allow the operator to view and check all data in-field, in numerical and in graphical format (i.e., voltage decay or apparent resistivity curves). After an initial noise run that measures ambient noise without the transmitter being switched on, 3 recordings are made at three increasing gain settings, for a total of 10 data runs. This provides optimum coverage of early-time data at low gain to avoid saturation and late-time data at higher gains. At any time, the operator may scroll through the results and repeat runs if noise levels seem high. Both the stacked voltage data and statistics are stored in the receiver dump files. On return to the field base each day, data are transferred from each of the field instruments to the data processing computer, immediately backed up and processed.

The instrument dump files contain normalized voltages (μV/A) and header information detailing the recording parameters (ASCII files, formats available). Files are loaded into the WinGLink data reduction software for data editing and merging. The voltage decay curves are evaluated to determine early time saturation and the asymptotic (late time) noise levels. Data points considered at or close to this level are removed prior to merging of multiple runs (Figure 5). The measured noise runs are used as a guide when applying this procedure.

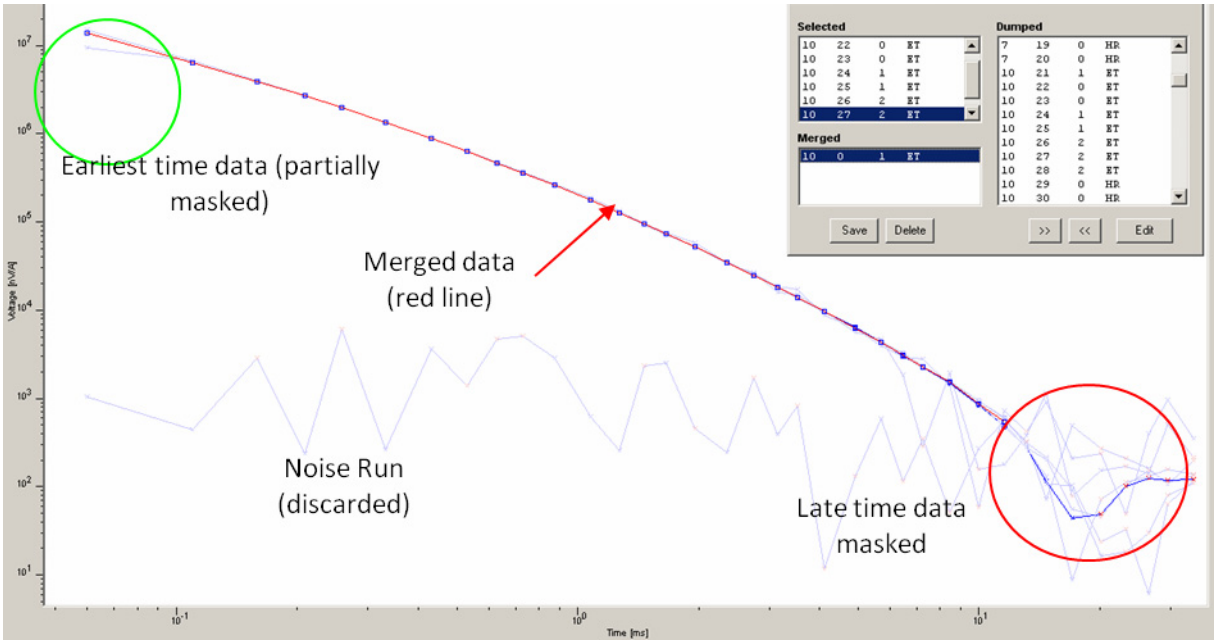

Figure 5. Voltage decays from 7 runs, including noise run, at an example site showing masking and final merged data. The latter acts as the input data for 1D modelling.

1D inversion of TDEM data

One dimensional modelling is performed using a Central Loop TDEM inversion routine in WinGLink that incorporates:

- calculation of turn-off and run-on corrections
- display of late time apparent resistivity and voltage
- forward calculation to obtain an initial model
- inversion to obtain a 1-D layered Earth model
- inversion to obtain a 1-D detailed Earth (Occam) model.

For each TDEM sounding, detailed, smooth (minimum structure or resistivity variation) 1-D inversion models are calculated, containing 12-20 layers of constant thickness on a logarithmical depth scale, and covering a depth range of typically 8 to 200 m. An additional set of 1-D models is modelled, referred to as 'layered', containing the minimum number of layers necessary to fit the data to about 5% RMS data misfit, with usually 2-5 layers.

Gravity and dGPS survey data acquisition

The gravity crew acquire all necessary information in one pass at each station. These crews consist of one vehicle, an experienced driver, an operator, and 3 assistants. They are equipped with Scintrex CG-5, Scintrex CG-3 or LaCoste&Romberg-G gravimeters, plus Trimble R7/R8 dGPS receivers, a handheld GPS unit for auxiliary navigation, and autonomous safety/recovery equipment including cellphone and satellite phone where required. All equipment is highly portable and can be carried in backpacks, with the heaviest component weighing 8 kg, so for stations without vehicle access, the equipment can be carried to site, walking to and from the sites.

If required, at project start-up, the gravity crew establishes the GPS control and gravity base network via industry standard triangulation methods. Each is tied to the primary gravity and geodetic networks respectively. They also establish a base magnetometer reference station. The gravity-GPS base network, and the use of block surveying rather than strict along-line surveying, provides for repeat measurements, cross-loop checks, and total survey network analysis.

Gravity and dGPS survey data processing

QC is carried out at the field office using processed gravity and dGPS data in the form of gravity and coordinate data listings files.

Data processing, reduction, terrain corrections, final QC and 2D inversions can be carried out within 48 hours of acquisition at the field office, so that the anomaly definitions may be used to optimize the station layout, fill-in and schedule.

Gravity data are processed in WinGLink, including base station network adjustments, data reduction, terrain corrections (from field data and/or digital elevation models, DEM), full Bouguer anomaly calculation including curvature corrections, calculation of isostatic residuals, application of polynomial and high-low-band-passed filters, upward continuation, and calculation of horizontal and vertical gradients.

GPS processing is performed in Trimble Office Solutions software. Nominal parameters for GPS processing include the following constraints; baselines <25 km, recording sample rate <3 s, maximum PDOP <6, Max HDOP <4, minimum number of satellites 5, mask angle 15° above the horizon.

Gravity data reduction

LaCoste G-meter data are logged in-field and transferred to a PC the same evening. Scintrex CG3/5 data are dumped to PC every day, and checked immediately for anomalous drift. Final Bouguer anomalies are processed within 48 hours of acquisition, incorporating residual drift, latitude, free-air, terrain and Bouguer corrections. Earth tide, tilt, temperature correction and long-term drift are calculated by the AutoGrav internally. Gravity values are referenced to absolute gravity at the operational base station. Bouguer and terrain corrections at 3 reduction densities are updated daily to provide profiles and maps for QC purposes.

The isostatic residual anomaly is calculated using a digital topographic and bathymetric model (e.g., ETOPO-2) to estimate Moho relief over an extended area (250 x 250 km) assuming variable lithospheric strength models. Other residuals (e.g., polynomial, low pass, band pass) can be easily created in WinGLink.

dGPS data reduction

In-field receiver raw data from the dGPS survey are stored in-field for downloading and post-processing using standard Trimble software. The database manager facilitates individual and final survey loop and least squares network adjustment for Static Rapid Static GPS data (for the Control station network), individual vector processing, and production of orthometric heights from the latest

geoidal models. Output station coordinates in ASCII are directly read by WinGLink for gravity data reduction, full terrain corrections, QC, Bouguer anomaly and image analysis, filtering etc.

2.75D and 3D inversion

Image processing, 2.75D and 3D inversion modelling and interpretation of the gravity data can be carried out within WinGLink on the Milan computer cluster (Figure 6).

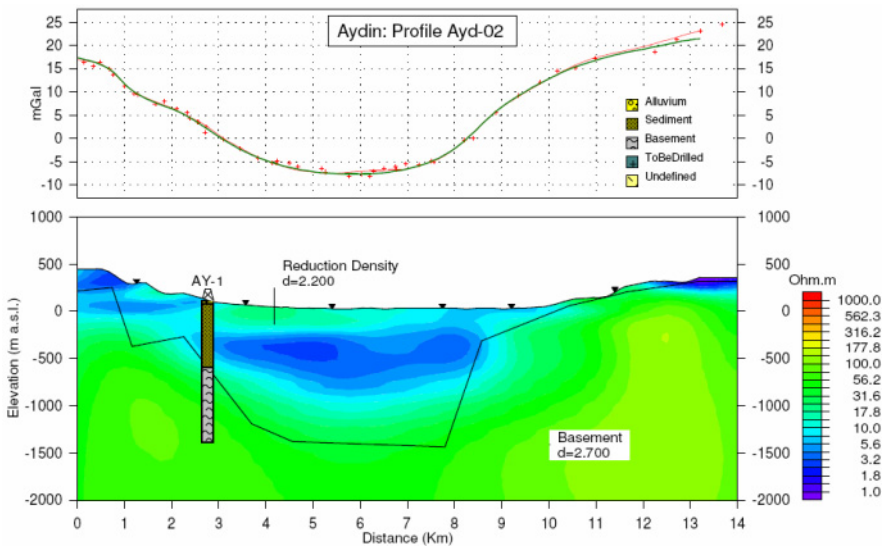

Figure 6. Example of a gravity data profile (upper panel) and 2.75D gravity model (black line) across a graben (lower panel), superimposed on resistivity from a 3D MT inversion (coloured image), and production well lithology. The model and display was generated using WinGLink software.

Stand-alone 3D gravity inversion is carried out using propriety software. The inversion process includes the ability to strip anomalies from shallower structure defined by seismic horizons. All MT and gravity products are integrated within WinGLink or Petrel, as required.

Integrated modelling and Interpretation

Our Integrated EM Center of Excellence specializes in the integration of multiple datasets in order to construct more accurate subsurface models (Figure 7). This can be achieved either through Constrained Inversions (CI) or through Simultaneous Joint Inversion (SJI).

Constrained Inversion

Using WinGLink's Integrated Project Tool, together with Petrel via established exchange tools, the well logs, gravity and seismic horizons are used to control the 3D MT inversion. Tear surfaces in the regularization are introduced along seismic or otherwise defined depth horizons. Well logs of resistivity are interpreted via cumulative conductance plots and analysis to provide effective formation resistivities (i.e., logs are interpreted, not simply averaged) to provide an *a priori* 3D starting model that weights the model domains accordingly during the subsequent inversion.

Gravity data are imported to WinGLink for QC, terrain correction and reduction to Bouguer anomaly as required, eliminating single point anomalies before modelling. Imaging includes analysis of regional (including isostatic) versus residual fields, calculation of gradients, and stripping of near-surface sources (if required) using layer boundaries interpreted from seismic horizons and density logs. Final modelling includes 2.75D forward and 3D inversion.

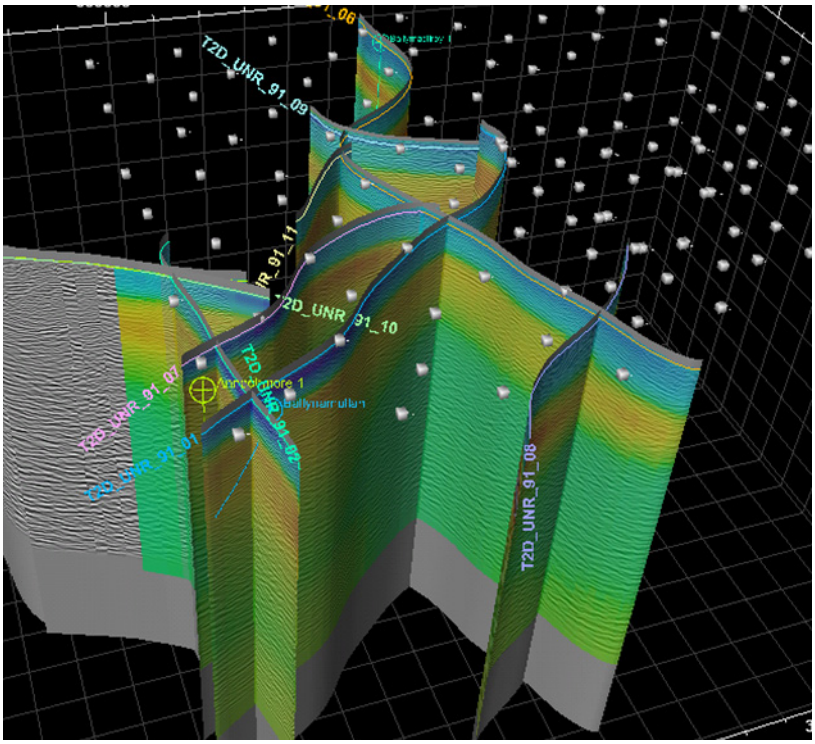

Figure 7. Example of integration of existing 2D seismic data and well logs with resistivity from a 3D MT inversion model (colour grid, red is conductive, blue near surface are resistive basalts).

Simultaneous Joint Inversion

Simultaneous Joint Inversion (SJI) is an innovative and efficient tool for geophysical integration that allows the exchange of information between different physical measurements with the aim of producing a multi-parameter model that contains various geophysical properties (i.e., density, resistivity, velocity). More specifically, SJI inverts simultaneously two different datasets (seismic time gathers and MT data or Bouguer anomaly) and in the process it effectively reduces the uncertainties and mitigates the weaknesses of each one, by using information present in the other (Figure 8).

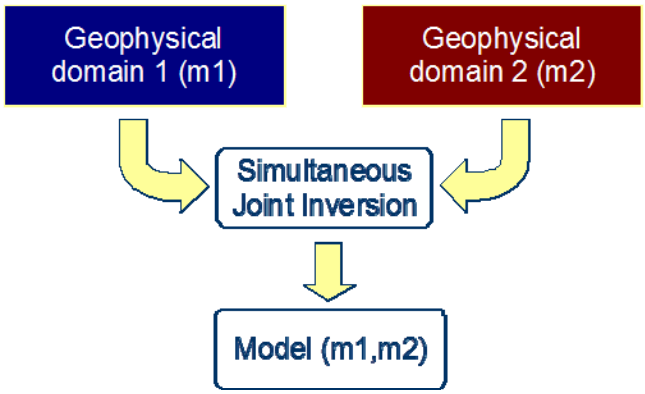

Figure 8. Simultaneous Joint Inversion approach.

WinGLink software

WinGLink is a module-based software package focused primarily on MT data processing and modelling and, in this regard, is recognized as the worldwide standard. Program modules are also available for processing and modelling gravity and magnetic data, modelling of TDEM data, as well as the capability to post information from vertical or deviated wells on maps and cross-sections to add model constraints. Due to its modular structure, modules can easily be added to meet particular needs.

The individual software modules and their functionality are outlined below:

WG-1 Core Module (required)
Database creation, project generation, coordinate conversion, import/export, mapping, profile construction, printing.

WG-2 Interpreted Views and Montage
Production of composite maps or cross-sections by superimposing maps or sections from different projects in the database. Creates interpreted views with user-defined lithological patterns, imported images, annotations and cultural data to integrate composite maps and cross-sections. Construct printing plates with multiple maps and cross-sections.

MT-1 Basic Processing (2D Smooth)
Import sounding datasets, editing, static shifting/stripping, decomposition, TE/TM mode selection, 1D smooth and layered inversion, pseudo-sections, 1D model sections, extraction of resistivity and MT parameter maps, 2D (Randy Mackie) smooth inversion.

MT-2 2D Sharp Boundary Inversion
2D sharp boundary (Randy Mackie) inversion add-on for MT-1 module.

MT-3 MT Tools
Time series display and processing, cascade decimation w/ cross-power editor, data analysis.

MT-4 3D Forward Modelling
Construction of a 3D mesh via graphic, interactive editing tools. Import/Export of Randy Mackie format 3D Meshes. Extraction of depth maps and sections from 3D Mesh using "Maps" and "Cross-Sections" programs. Calculation of MT responses at given stations for display with "Soundings" program; responses at individual stations stored internally or as external EDI files.

DC-1 Schlumberger Soundings
Edit sounding datasets, 1D smooth and layered model inversion, pseudo-sections, 1D model sections, extraction of resistivity maps.

EM-1 TDEM Soundings
Import, edit and merge raw data from field dump files (Geonics, Zonge, Sirotem). 1D smooth and layered inversion, pseudo-sections, 1D model sections, extraction of resistivity maps.

GR-1 Gravity Basic
Bouguer computation, wavelength filtering, upward/downward continuation, polynomial fitting, 2.75D gravity forward modelling.

MG-1 Magnetics Basic
IGRF removal, wavelength filtering, reduction to pole, upward/downward continuation, polynomial fitting, 2.75D forward modelling.

WL-1 Wells Basic
Generation of well projects, edit/import well location and courses, projection of deviated well courses on maps and cross-sections.

WL-2 Wells Advanced
Import well stratigraphy and log data. Cross-sections showing well stratigraphy using custom-defined lithology patterns and symbols (deviated wells supported). Depth maps and imaged sections of interpolated log data.

References

Chave, A. D., Thomson, D. J., and Ander, M. E., 1987, On the Robust Estimation of Power Spectra, Coherences, and Transfer Functions: Journal of Geophysical Research, 92, 633-648.

Larsen, J. C., 1989, Transfer functions: smooth robust estimates by least-squares and remote reference methods: Geophysical Journal International, 99, 645-663.

Rodi, W., and Mackie, R. L., 2001, Nonlinear conjugate gradients algorithm for 2-D magnetotelluric inversion: Geophysics, 66, 174-187.

Schlumberger press release, July 5, 2007. Accessed 17 January 2012.
http://www.slb.com/news/press_releases/2007/20804.aspx

Contact information

Italy

WesternGeco Geosolutions
via Celeste Clericetti 42/A, Milano, 20133, Italy

P: +39 02 266 279 206
F: +39 02 266 279 279
M: +39 340 902 8216
http://www.slb.com/services/westerngeco/services/land/landem.aspx

Efthimios Tartaras - Sales & Marketing Manager
etartaras@slb.com

Statement of Capability - Zonge Engineering and Research Organization Australia Pty Ltd

Simon Mann [1]

[1] *Zonge Engineering and Research Organization Australia Pty Ltd (stmann@zonge.com.au)*

Introduction

Zonge Engineering and Research Organization Australia Pty Ltd (Zonge Australia) have offered ground electrical geophysical services in Australia since 1984. The company has been Australian-owned since 2006 and is no longer a subsidiary of the US parent company, known as Zonge International. Although being a separate and independent entity, Zonge Australia continues to use equipment manufactured in large part by the parent company. The "Zonge" equipment and software described herein are those developed by Zonge International.

The services offered by Zonge Australia include survey design, acquisition, processing, modelling (forward and inverse), and interpretation for a range of ground electrical geophysical data types (e.g., IP, EM, down-hole EM and MT data). Zonge Australia have acquired AMT/MT data using scalar arrays for rapid delineation of deeper targets and structure, as well as utilising a variety of tensor arrays for more complete characterisation of the subsurface.

Products and services

Zonge Australia's services include field acquisition and processing of data within the MT and AMT frequency bands. Much of Zonge Australia's natural source experience has been in audio-frequency MT acquisition (AMT) for the 1/8 to 8 kHz frequency range, suitable for mineral and structural investigations from near surface to depths of 1 to 2 kilometres. Zonge Australia's natural source capability is based around the GDP-32 receiver unit, which allows multi-purpose, multi-channel data to be acquired for a wide variety of array configurations. This flexibility allows Zonge Australia to collect MT data using both scalar and tensor arrays. Additionally, multiple synchronised receivers units may be used to increase production rates and to set up remote reference arrays to acquire data for noise reduction. Zonge Australia provides in-house processing, editing and modelling of acquired data from its offices in Adelaide, South Australia.

Natural source MT survey capability

Zonge Australia can acquire data using either scalar (Figure 1a) or tensor (Figure 1b) acquisition array configurations to suit different target types and exploration objectives. Zonge Australia commonly uses scalar acquisition for high resolution resistivity profiling of two-dimensional targets. In this acquisition mode, the GDP-32 receiver unit allows multiple E-field measurements to be taken (i.e., from 1 to 15) with a single H-field sensor measurement (Figure 1a), thereby providing rapid linear production rates.

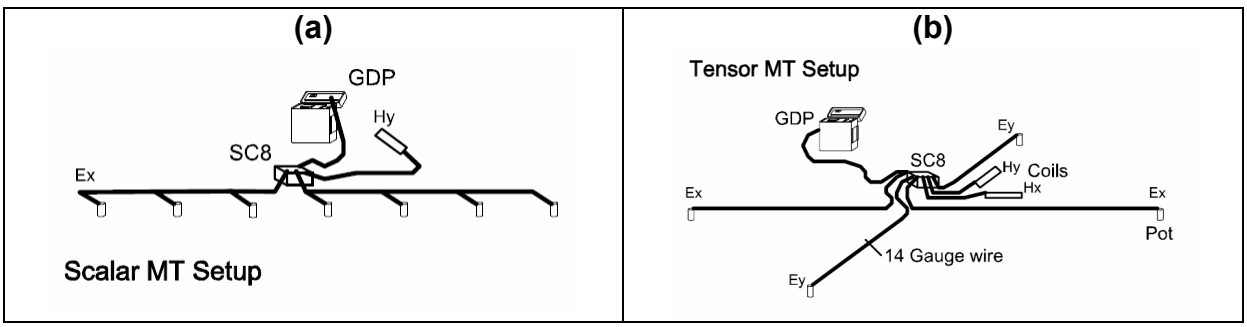

Figure 1. Typical scalar (a) and tensor (b) AMT/MT setups.

A number of different arrays may be used when acquiring full-tensor MT data depending on the aims of the survey. Figure 1b shows the "classic" single station tensor arrayconfiguration. More commonly,

Zonge Australia deploy tensor arrays that consist of multiple orthogonal E-field measurements, normalised using data from a single pair of orthogonal H-field antennae. This configuration increases production rates for tensor profiling. The number of TE mode measurements per array can be varied to balance data density with the optimal production rate. A common compromise between production rate and tensor data coverage involves acquiring multiple TM mode soundings per TE sounding for each receiver unit array (e.g., one TE sounding for every two TM soundings). This style of surveying allows electrical dimensionality to be assessed whilst also providing a moderate degree of data coverage at production rates that are reasonably efficient. In addition to the configurations described above, regional-style tensor MT surveying may also be performed. This will typically involve acquisition of Ex, Ey, Hx, Hy and Hz data at separated sites using an acquisition configuration similar to that shown in Figure 1b.

Regardless of configuration, data at a remote reference site can be acquired using a second, synchronised GDP receiver. Remote reference data acquired from a single set of E and H field sensors can be used to assist in noise reduction. Multiple roving receiver units can also be used to both increase production rates and to acquire data that act as remote reference data for the stations occupied with a different instrument.

If higher frequency data are needed to supplement the natural field signals in the “dead band” that is present at approximately 1000 Hz, it is possible to deploy a transmitter and acquire data at the higher frequencies using a controlled source (i.e., using a CSAMT configuration). Near-field effects, particularly in conductive Australian conditions, often limit the usefulness of CSAMT data at low frequencies. Since the acquisition of CSAMT data generally involves the same receiver and sensor arrays as those used for AMT data acquisition, particularly in scalar mode, there is minimal loss of efficiency in combining the two techniques. Data from a scalar AMT TM sounding over the frequency range 0.75 to 1024 Hz is shown in Figure 2. For comparison, an example of data from a merged CSAMT/AMT sounding covering the frequency range 0.75 to 8192 Hz is shown in Figure 3. The significant difference in signal strength between the natural and controlled source data is evident in the right hand panels of Figure 3.

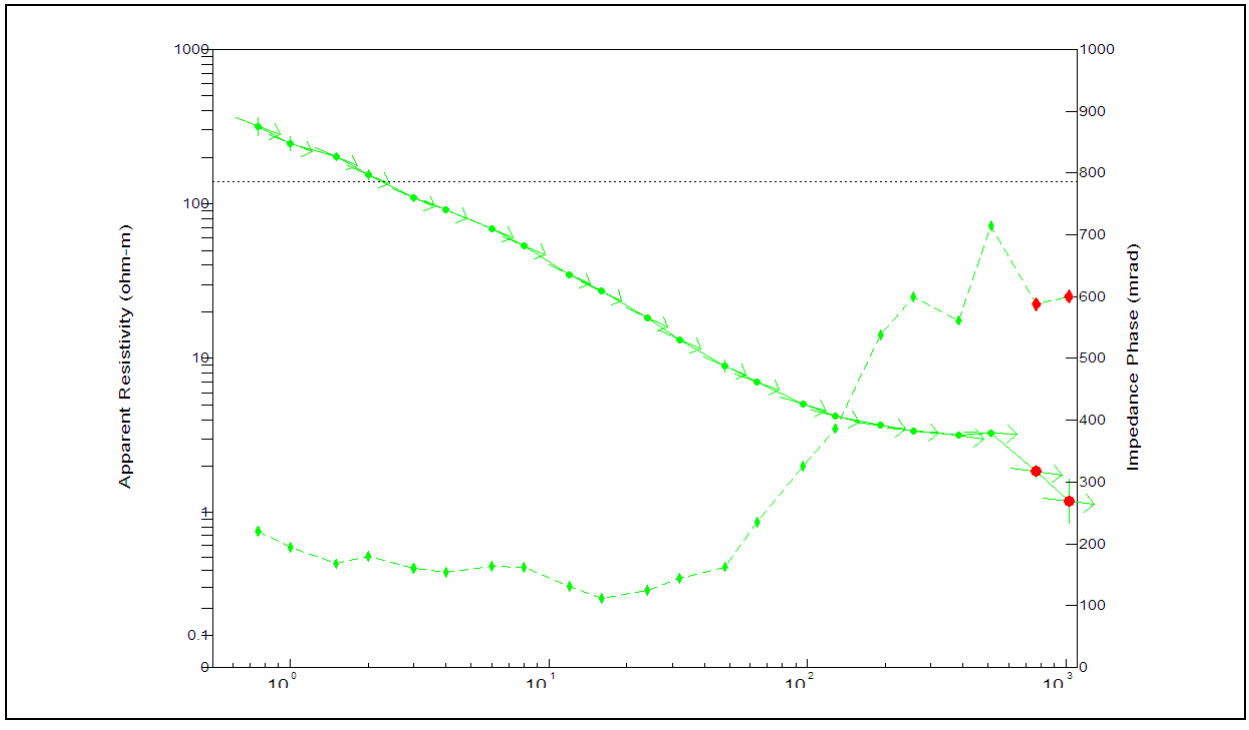

Figure 2. Typical scalar MT sounding (0.75-1024 Hz).

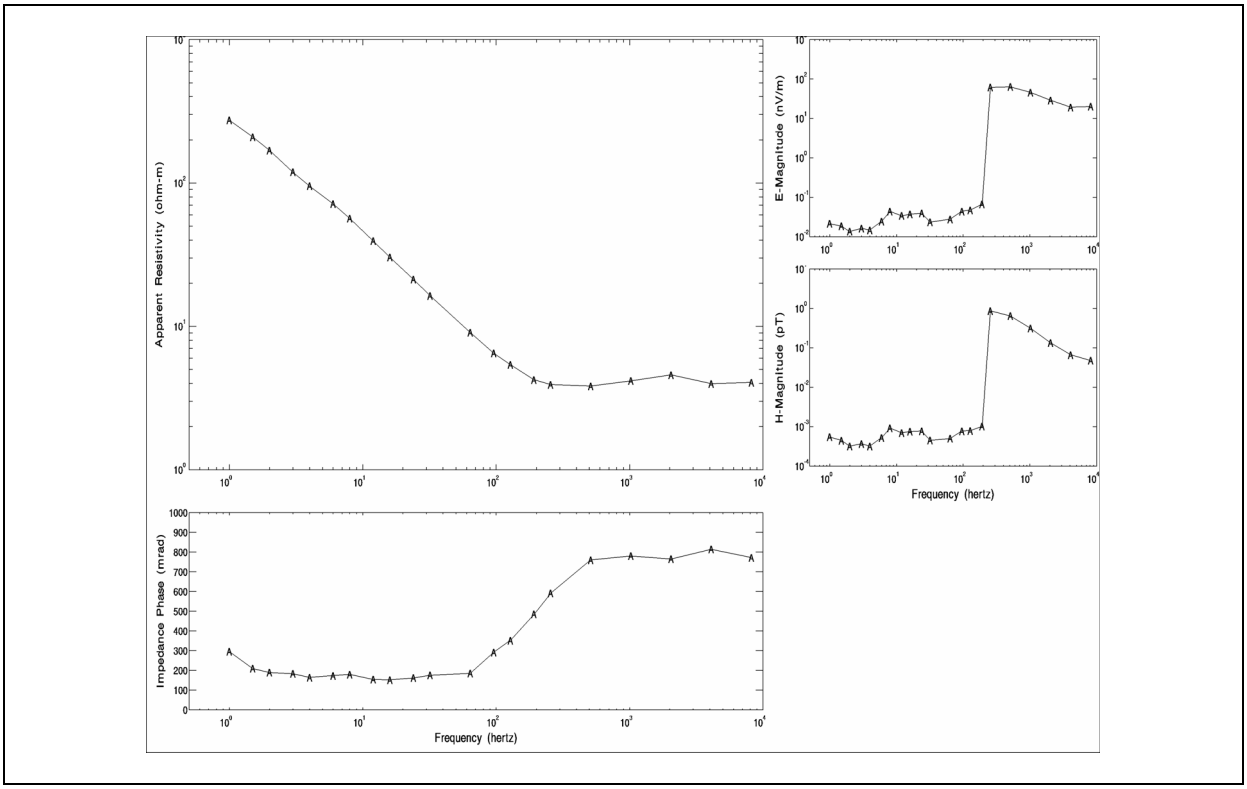

Figure 3. Example of combined CSAMT and AMT data sets. All data above 256 Hz are CSAMT. Subfigures on the right hand side show relative signal strengths of AMT data (below approx. 256 Hz) and CSAMT data (above 256 Hz).

Equipment

The GDP-32 range of receiver units, including the GDP-32 and the recently introduced GDP-32/24, are multi-purpose, multi-channel broadband receivers. They are capable of scalar and tensor MT data acquisition over the frequency range from 0.0007 to 8 kHz (i.e., periods of 0.00012 to 1400 s). They also allow simultaneous acquisition of data for 2 to 16 electric or magnetic field channels per receiver.

Although raw time series data are recorded to allow complete re-processing of data in the office, real-time processing of the incoming data in the field allows on-site assessment of E to H-field coherency, apparent resistivity and impedance phase information to be carried out. Text files containing on-board processed data are recorded in addition to the raw time series data. Data are acquired for frequencies spanning four decades to ensure that data coverage will be appropriate for the target regardless of varying ground conductivity conditions. Multiple receiver units can be time synchronised to permit remote referencing to be employed. Copies of the GDP-32 receiver manual can be provided if a more complete description of data collection in the receiver unit is required.

Incoming signals are amplified and filtered using Zonge SC-8 signal conditioner units. Different filter settings are used to suppress noise depending on the target frequency range. Magnetic fields are sensed using induction coils. For higher frequency CSAMT and AMT work (i.e., within the 0.1 to 10,000 Hz range), Zonge ANT-6 coils are used, whilst for lower frequency work (i.e., within the 0.0005 to 1,000 Hz range), Zonge ANT-4 coils are more suitable. Non-polarisable ceramic porous pots connected to the receiver via single conductor wire are used as electric field sensors. A photograph of the field equipment is shown in Figure 4.

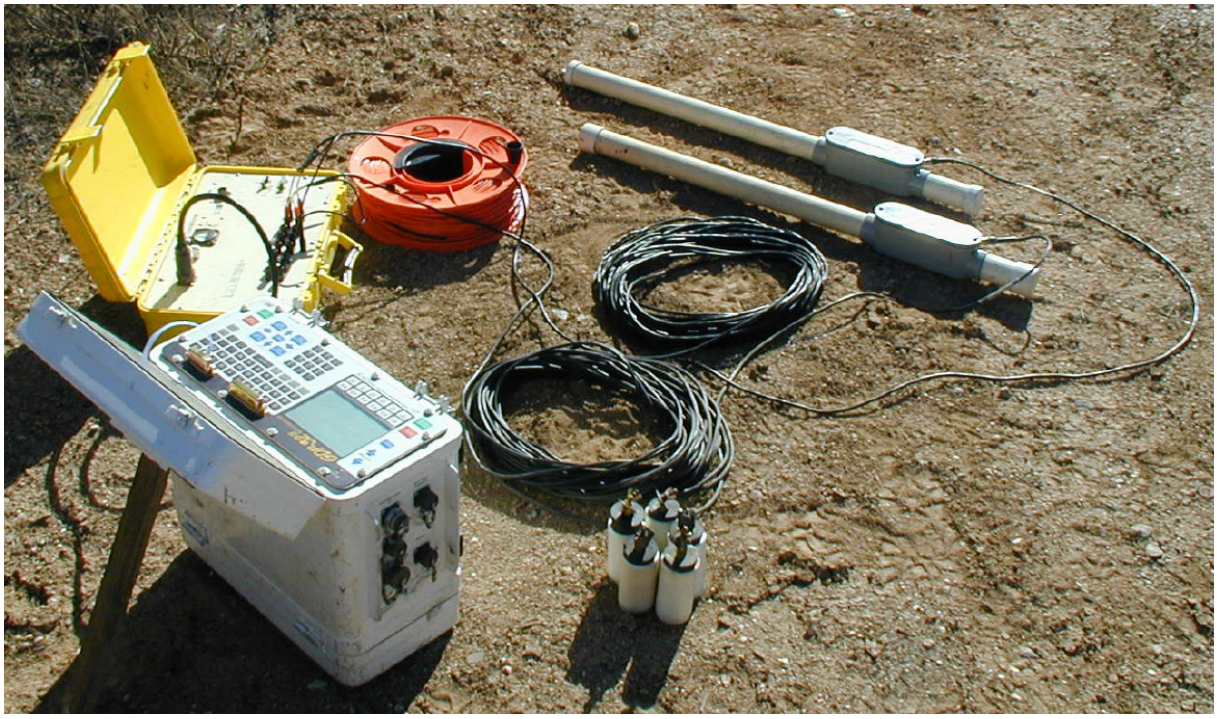

Figure 4. Photograph of equipment used for acquisition of MT data; a GDP-32 receiver unit (white case), SC-8 signal conditioner unit (yellow case), magnetic induction coils, porous pots, and signal wires.

Data Processing

Time series records and data processed on-site in the receiver unit are sent to Zonge Australia's Adelaide office each day for processing. The time series data are processed using software developed by Zonge International. This software allows the time series and associated amplitude spectra to be examined for data quality (Figure 5). Additionally, the software allows the data processor to either automatically or manually filter impedance estimates at individual frequencies based on various thresholds, including coherency, resistivity, impedance phase and signal magnitude before an average estimate for each frequency is calculated (Figure 6). These data are then output in a standard Zonge format for further processing and modelling, or in EDI format if that is desired. The Zonge program "NSSKEW" can be used to rotate the impedance tensor data and to produce polar or phase plots of tensor data.

Inverse modelling of scalar and dual mode (TM and TE) data is performed using Zonge International's "SCS2D" inversion modelling software to produce 2D resistivity sections of acquired data (Figure 7). The SCS2D program provides options for the user to include topography, run 1D modelling, modify the starting model structure, and to adjust various model fit parameters including directional smoothness constraints.

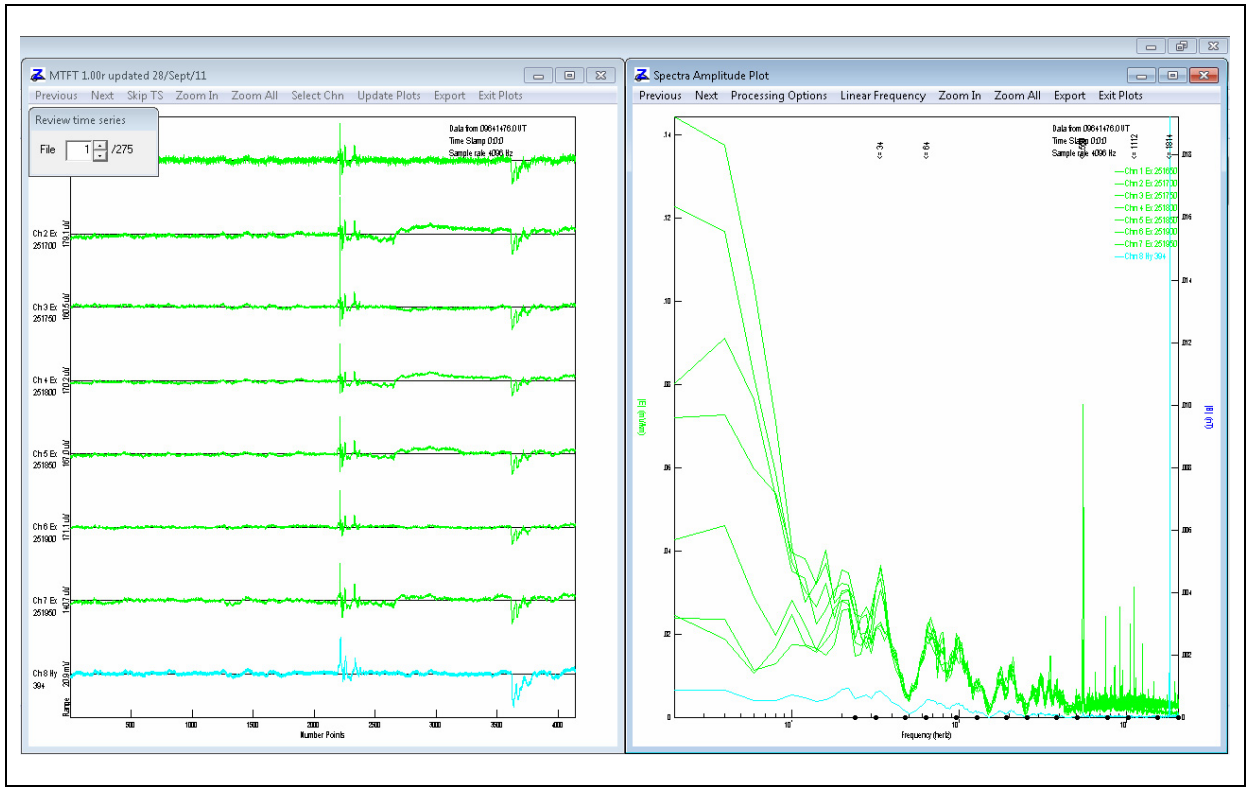

Figure 5. Example of the user display of time series data and corresponding frequency spectra.

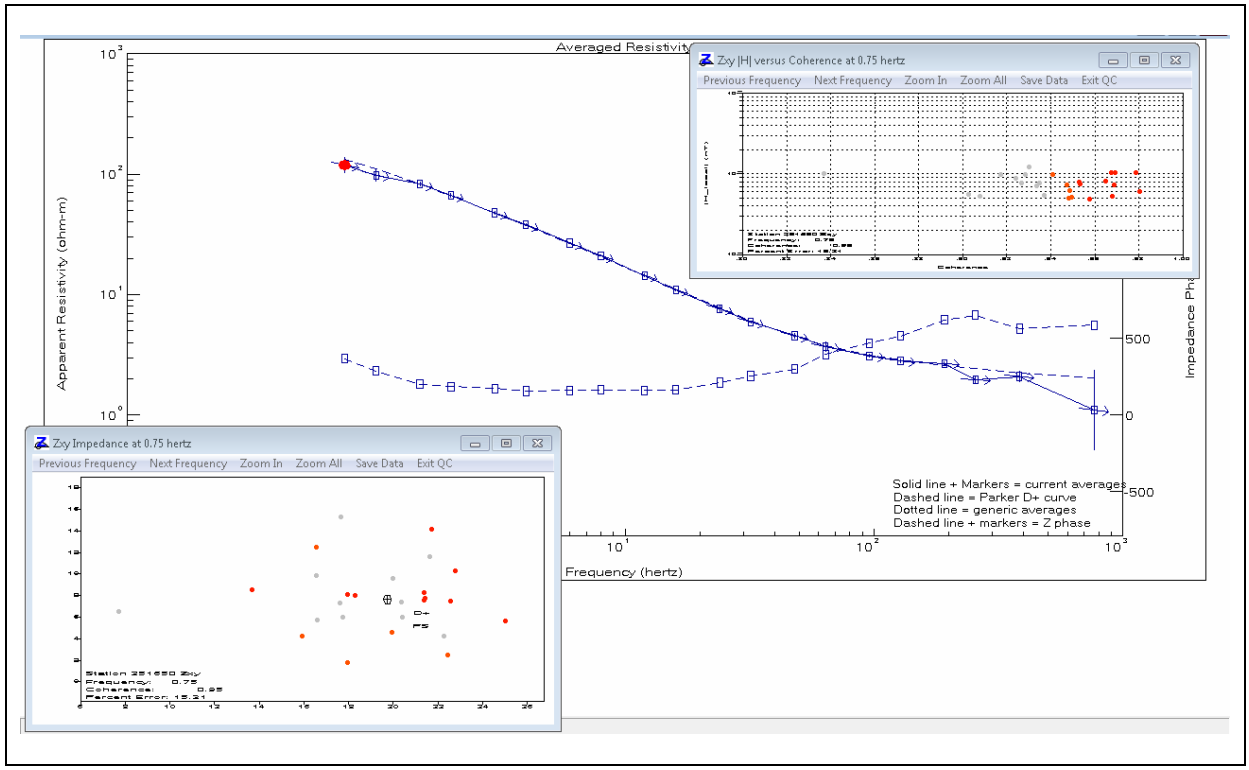

Figure 6. Example of the user display for filtering of impedance estimates at individual frequencies.

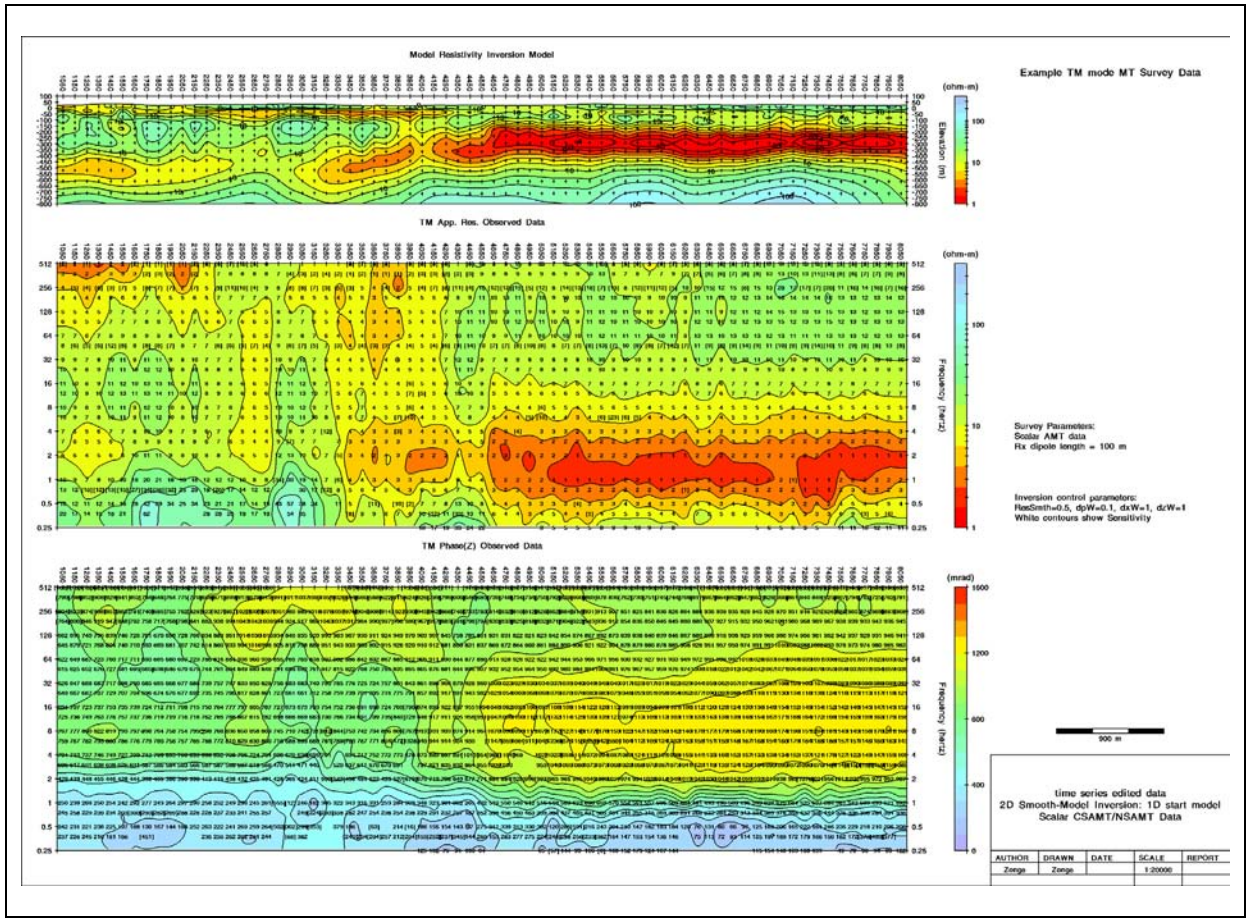

Figure 7. Example of a 2D resistivity section (upper panel) produced with the "SCS2D" inversion modelling software. The observed apparent resistivity and phase data for this line are shown in the middle and lower panels respectively.

Contact information

Australia

Zonge Engineering and Research Organization (Aust) Pty Ltd
39 Raglan Avenue, Edwardstown, South Australia, Australia, 5039

P: +61 8 8371 0020
F: +61 8 8371 0080
http://www.zonge.com.au/

zonge@zonge.com.au

Statement of Capability - Zonge International, Inc.

Scott Urquhart [1]

[1] *Zonge International, Inc. (scott.urquhart@zonge.com)*

Introduction

Zonge Engineering and Research Organization, Inc. was founded in 1972. The company has recently changed its name to Zonge International, Inc. (Zonge) to better reflect the nature and scope of the company. With the sale of subsidiary offices to Australian and Chilean groups in 2006, Zonge now provides worldwide field data acquisition, manufacturing, and R&D services from facilities in Tucson, Reno, Denver, and Portland in the USA.

Products and services

Zonge provide a range of electrical and electromagnetic instruments and services, including those used for natural source MT investigations. Company personnel can perform MT survey design, data collection, data processing, 2D and 3D modelling, and interpretation. Furthermore, the data can be integrated with gravity, magnetic, and seismic data (either seismic reflection or seismic refraction data). If required, complementary seismic data can be collected by Zonge field personnel with a 500-channel, wireless seismic receiver system from Wireless Seismic, Inc. (see references for company website address) using accelerated weight drop sources produced by United Service Alliance, Inc. (see references for the "AF450 Hammer brochure" web address).

MT instruments and software

Besides offering contract survey services, Zonge develop, sell, and service integrated MT instrument systems including acquisition hardware, data processing tools, and 2D modelling software.

The ZEN™ High-Resolution Receiver (Figure 1) and distributed EM/IP system was developed as part of a collaborative arrangement between Zonge and Oregon State University. The receiver unit integrates a multi-channel 32-bit ADC designed specifically for geophysical applications with GPS timing functionality, processor, and long range wireless control, all housed in a weather-sealed enclosure. Using sample rates up to 4096 Hz, data can be acquired from DC to 1024 Hz whilst using a separate ADC for each channel for optimal phase stability. A six-channel instrument, with batteries sufficient for 24 hours of continuous recording, weighs approximate 6.5 kg. Further information about the ZEN receiver unit can be found on the Oregon State University website (see references for the "The Zonge 5th Generation (Zen/5) Receiver System and Sensor Configurations" web address).

In addition to the ZEN receiver system, Zonge has developed the GDP-3224™ integrated GPS-synchronized multi-function receiver unit (Figure 2). Using 24-bit ADC technology, this system provides spectral coverage for acquired data from DC to 8 kHz. The receiver unit can be used to collect MT, CSAMT, TEM, and time and frequency domain IP data. This instrument is also available as an upgrade to existing Zonge customers with GDP-32^{II} receiver systems. See the references section for the web address for a brochure "GDP-32/24 Geophysical Receiver".

As well as receiver units, Zonge can supply the following for use in MT surveys;

- Low-noise magnetic field sensors (fluxgate sensors and search coil technologies) covering the frequency range from 0.00002 to 250 kHz.
- Graphical processing and QC software tools for scalar, vector, and tensor data collection, with or without remote reference.
- 2D modelling codes (forward and inverse) for use with natural source and controlled source AMT/MT data. See the references section for the web address of the documentation for the SCS2D program ("SCS2D Documentation").
- 3D modelling (forward and inverse) of natural source MT data on a contract basis.

Figure 1. Operator carrying a light-weight ZEN receiver unit.

Figure 2. A GDP-3224 receiver unit.

Data processing software that is optimized for use with Zonge receiver systems has been developed by Zonge specifically for use in processing of MT data. As part of a typical data processing sequence, these tools can be used to examine time series data from both local and remote sites, and to edit data in the frequency domain if required. Local data and remote reference data can then be merged, permitting robust processing methods to be used to develop estimates of the MT impedance values and their associated uncertainty standard deviation values. The data processing software supports scalar, vector, and tensor measurements. These tools are also available for purchase from Zonge.

The SCS2D program can be used for 2D forward and inverse modelling of MT data. This program calculates topographical effects, provides a facility for integrated examination and editing of data from within the inversion framework, and allows the user to export model results directly to the Geosoft Oasis Montaj environment. The SCS2D program also includes support for 1D controlled source modelling. 3D modelling of MT data is available as a consulting service from Zonge.

MT QA/QC procedures

Zonge use the following procedures for QA/QC of the data that they acquire, process, model and interpret.

1. Perform regular factory system checks of both receivers units and antennae.
2. Test system stability:
   a. Perform parallel sensor tests for both electric and magnetic field sensors at the commencement of field investigations. Examine apparent resistivity and phase outputs for consistency, check that resistivity is a linear function of frequency, and that the phase equals zero degrees.
   b. Perform daily system checks using an internal signal generator.
3. Examine acquired data:
   a. Display time series data and frequency spectra in the field and during post-survey processing.
4. Apply sound and recognized data processing methods:
   a. Local and remote data are processed using robust processing tools based on the research of Chave et al. (1987) and Egbert (1997). Error estimates are generated using jack-knife estimates as suggested by Chave et al. (1987). The processing software allows the user to interactively examine and edit spectral estimates based on the magnitude of each component, the coherence of specific E/H sets, or the time period during which the data were acquired to provide an effective

means of identifying and removing data known to be impacted by time-dependent cultural noise sources.

5. Apply good practice during modelling:
   a. Integrate known geological controls into modelling work.
   b. Examine the fit between observed and modelled resistivity and phase data in both sounding curve and pseudo-section formats.

References

AF450 Hammer brochure, United Service Alliance, Inc. website. Accessed 19 January 2012. http://www.usallianceinc.net/index_files/AF450.pdf

Chave, A. D., Thomson, D. J., and Ander, M. E., 1987, On the Robust Estimation of Power Spectra, Coherences, and Transfer Functions: Journal of Geophysical Research, 92, 633-648.

Egbert, G. D., 1997, Robust multiple-station magnetotelluric data processing: Geophysical Journal International, 130, 475-496.

GDP-32/24 Geophysical Receiver. Zonge website. Accessed 19 January 2012. http://www.zonge.com/PDF_Equipment/Gdp-32-24.pdf

SCS2D Documentation. Zonge website. Accessed 19 January 2012. http://www.zonge.com/PDF_Modeling/Scs2d.pdf

The Zonge 5th Generation (Zen/5) Receiver System and Sensor Configurations. Oregon State University website. Accessed 19 January 2012. http://ngf.oregonstate.edu/node/4

Wireless Seismic, Inc. website. Accessed 19 January 2012. http://www.wirelessseismic.com/

Contact information

USA

Zonge International, Inc.
3322 E. Fort Lowell Road, Tucson, AZ 85716, USA

P: +1 520 327 5501
F: +1 520 325 1588
www.zonge.com

Scott Urquhart
scott.urquhart@zonge.com

Electrical images of the Forrestania Greenstone Belt

Shane Evans [1], Bill Amann [2], and Mike Dentith [3]

[1] *Moombarriga Geoscience (shane@moombarriga.com.au)*
[2] *Newexco Services (bill@newexco.com.au)*
[3] *Centre for Exploration Targeting, University of Western Australia (mdentith@cyllene.uwa.edu.au)*

Abstract

Magnetotelluric (MT) and audio-magnetotelluric (AMT) data have been acquired across the Forrestania Greenstone Belt (FGB) of Western Australia as part of an ongoing regional MT survey between Hyden and Norseman designed to investigate the lithospheric structure of the southern Yilgarn Craton. Modelling of the data from this regional survey indicated the presence of a crustal conductor spatially coincident with the FGB. This observation prompted the acquisition of high-resolution data to resolve this feature in greater detail. Result from these two surveys are presented and interpreted.

Introduction

The FGB, which corresponds to the southern extension of the Southern Cross Greenstone Belt, is located around 350 km east of Perth (Figure 1). The FGB comprises a lower sequence of tholeiite-komatiite-banded iron formation, overlain by an upper sequence of felsic metasediments (Collins and McCuaig, 2010). Nickel sulphide deposits occur over a 90 km strike length of the greenstone belt, within three of the six ultramafic belts of predominantly komatiite rock-types (Figure 2). These ultramafic belts have a high magnetic response and are well defined in regional magnetic maps.

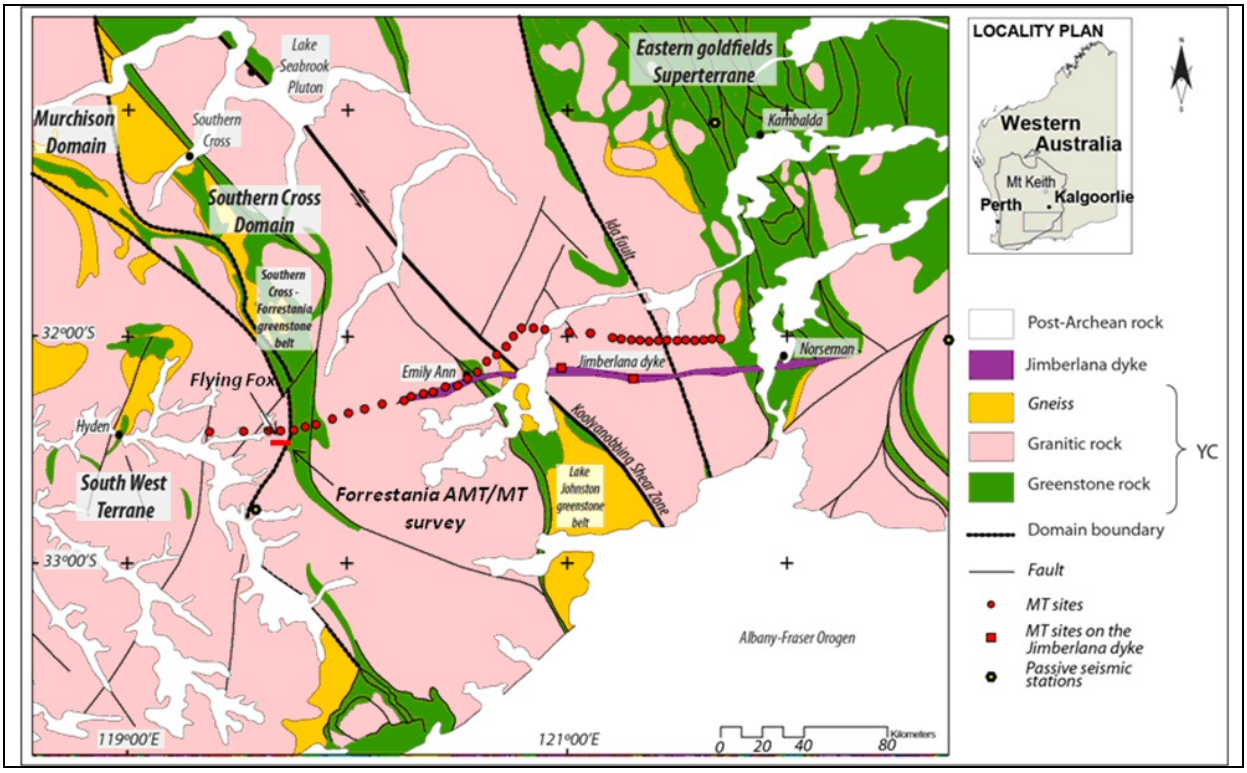

Figure 1. Regional geological map of the southern Yilgarn Craton.

The recently discovered Flying Fox and Spotted Quoll nickel sulphide deposits are hosted within the Western Ultramafic Belt (Perring et al., 1996). This belt dips from 40° to 80° east and comprises a footwall sequence dominated by psammitic to pelitic schists. The footwall is in turn overlain by a differentiated suite of komatiite rock-types, basalt and banded iron formation. This differentiated suite is sulphidic and associated with a continuous conductive horizon well-known from down-hole and surface transient EM surveys.

The objective of the detailed AMT/MT survey was to map this conductive horizon at depth and to determine the structural relationships between the Western Ultramafic Belt and the other belts.

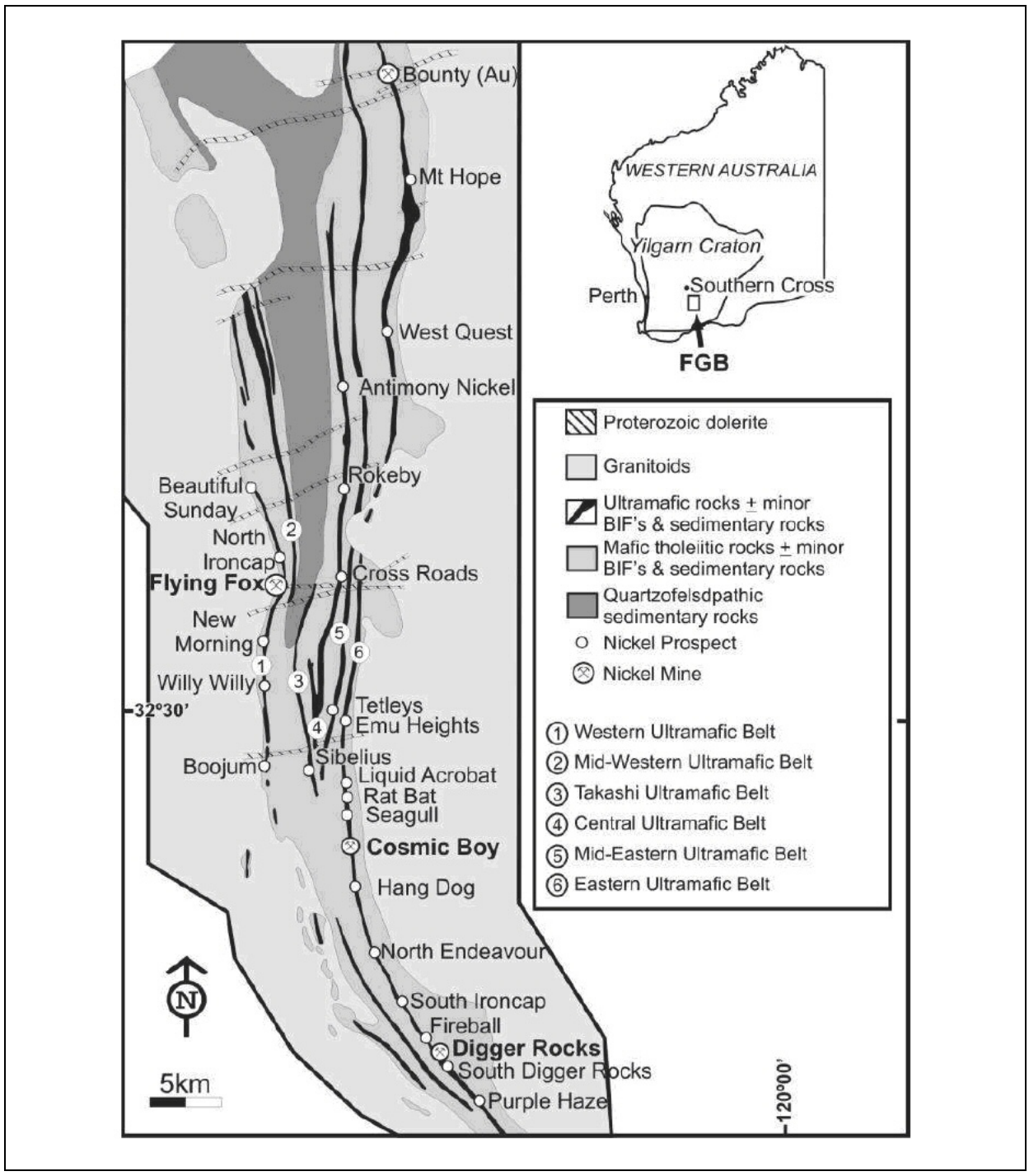

Figure 2. Simplified geological map of the Forrestania Greenstone Belt (FGB) (from Collins and McCuaig, 2010).

The magnetotelluric method

The MT method involves measurements of the time-variations in natural field electromagnetic (EM) signals at the surface of the Earth. Low-frequency variations in the EM field in the 1 to 0.0001 Hz range are primarily caused by the interaction of the solar wind with the terrestrial magnetic field. High-frequency variations in the EM field (i.e., those that have a frequency greater than 1 Hz) are predominantly ascribed to the effects of distance lightning storms.

The EM field comprises a magnetic field $(\overline{H})$ and an associated electric field $(\overline{E})$. By Faraday's Law of Induction, this time-varying magnetic field induces an electric field within the Earth, and, in turn, according to Ohm's Law, the electric field generates an electric current. The scaled magnitude ratio of the electric and magnetic fields, as well as the phase differences between the electric and magnetic fields, at a number of sites are utilized to determine the size and locations of zones of enhanced conductivity. The MT impedance tensor (Z) describes the relationship between orthogonal components of the horizontal electromagnetic field (E_x, E_y, H_x and H_y) at a given frequency such that

$$\begin{pmatrix} E_x \\ E_y \end{pmatrix} = \begin{pmatrix} Z_{xx} & Z_{xy} \\ Z_{yx} & Z_{yy} \end{pmatrix} \begin{pmatrix} H_x \\ H_y \end{pmatrix}. \quad (1)$$

In the 1-D case, Z_{xy} is equal to $-Z_{yx}$, with Z_{yy} and Z_{xx} equal to zero. In a 2-D Earth, if either $\overline{E}$ or $\overline{H}$ is aligned with the geoelectric strike, then Z_{yy} and Z_{xx} will be equal to zero and Z_{xy} will not be equal to $-Z_{yx}$. If $\overline{E}$ or $\overline{H}$ are not aligned with the strike direction, then H_x will generate an electric field $\overline{E}$ in both the x and y directions, and similarly, H_y will generate an electric field $\overline{E}$ in both the x and y directions (i.e., Z_{yy} and Z_{xx} will be nonzero).

Apparent resistivity (ρ) and the phase lead (φ) of the electric field over the magnetic field can be calculated through the relationships

$$\rho_{xy} = {}^{1}\!/\!_{\mu\omega} \left| {}^{E_x}\!/\!_{H_y} \right|^2, \quad (2)$$

$$\rho_{xy} = {}^{1}\!/\!_{\mu\omega} \left| Z_{xy} \right|^2, \text{ and} \quad (3)$$

$$\phi_{xy} = \arctan \left| \frac{E_x}{H_y} \right| \quad (4)$$

where μ is the magnetic permeability of free air and ω is the angular frequency.

As an EM wave propagates through the Earth, its amplitude will decay at a rate dependent on the conductivity of the medium and the rate of time variation (frequency) of the wave. Information about smaller near-surface features is concentrated in the high-frequency variations whilst information on deeper or broader structures is proportionally higher in low-frequency variations. In a half-space of uniform resistivity, the depth at which an EM wave decays to 1/e of its original value is known as the "skin depth" (δ) and is an approximate measure for the depth of penetration:

$$\delta = \sqrt{{}^{2}\!/\!_{\mu\sigma\omega}} \quad (5)$$

where σ is the conductivity (i.e., the inverse of electrical resistivity ρ).

The electrical resistivity of rocks can vary by over eight orders of magnitude (i.e., from more than 100,000 Ωm to less than 0.001 Ωm). Figure 3, modified from Haak and Hutton (1986), gives an

overview of the typical ranges of resistivity and conductivity for various types of rocks. Typically, competent, unfractured, crystalline rocks within the continental crust have a high resistivity of approximately 100,000 Ωm, but values less than this are often observed. Regions of low resistivity can be attributed to the presence of interconnected conductive material that is, typically, a minor component of the whole rock. Electrical conduction within the Earth for the frquencies relevant to AMT and MT studies occurs either through ionic conduction (i.e., movement of charged particles) or by electronic conduction (i.e., movement of electrons). Ionic conduction may be due to the presence of partial melts along grain boundaries or saline water filling pore space or intruding along fracture zones (Jones, 1992). Electronic conduction generally occurs when interconnected graphite, sulphide or iron minerals occur within a rock.

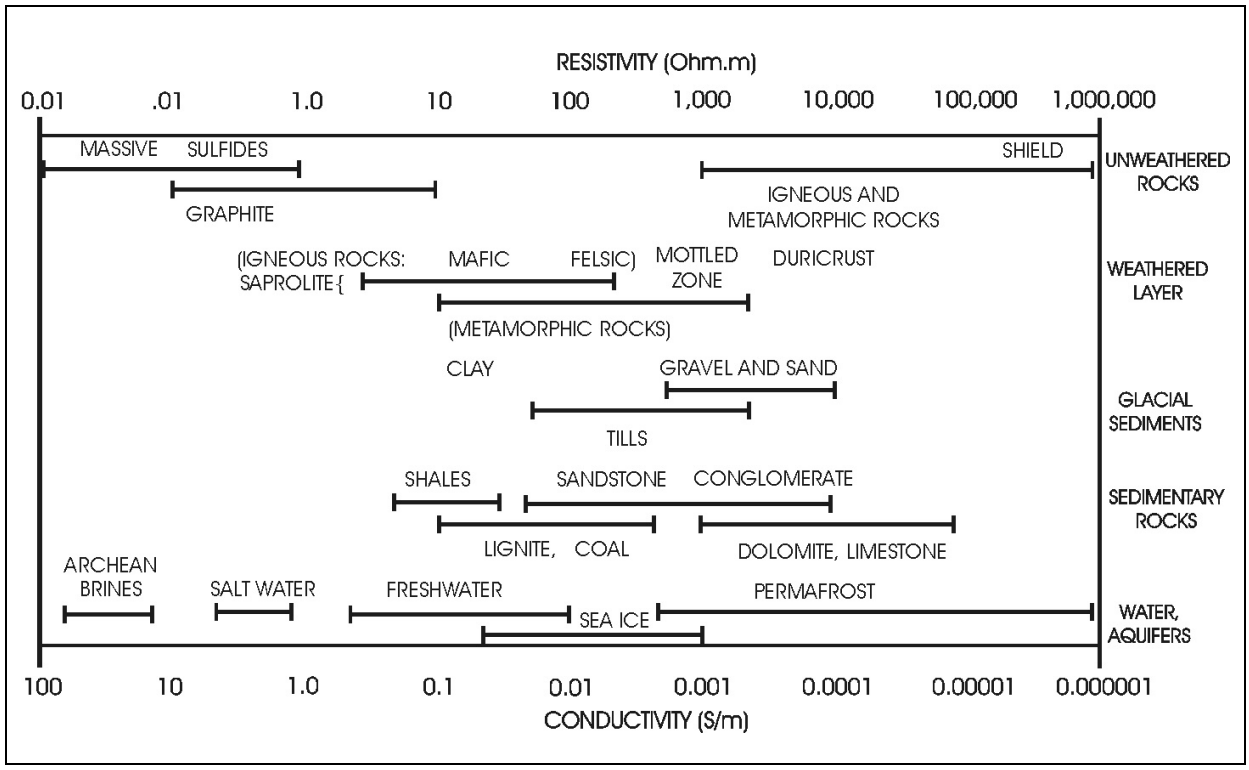

Figure 3. Conductivity and resistivity ranges for various rock types, modified from Haak and Hutton (1986).

Regional MT data

An MT survey comprising 40 stations has been completed in the southern Yilgarn Craton (Figure 1). The preferred model of resistivity that was interpreted from these data (Dentith et al., 2011) shows the local lithosphere comprised of three distinct units separated by steep boundaries (Figure 4). The central unit (Unit 2), interpreted to be equivalent to the Southern Cross Domain, has a resistive crust overlying a more conductive mantle. The two units on either side (Unit 1 (western) and Unit 3 (eastern)) comprise a conductive lower crust overlying a resistive mantle. Dipping narrow zones of increased conductivity in the crustal part of the model correlate with known surface structures labelled A to H. Feature A is coincident with the location of the FGB and is the focus of this paper. The eastern margin of the Southern Cross Domain as inferred from deep crustal and mantle resistivity occurs about 50 km to the west of the Ida Fault, the margin of the domain at the surface. The three-fold subdivision of the local lithosphere is consistent with the geologically and geochemically defined terranes and domains in this part of the Yilgarn. Features I and J are conductive regions in the lower crust or top of the upper mantle that are characteristic of Unit 3 and Unit 2

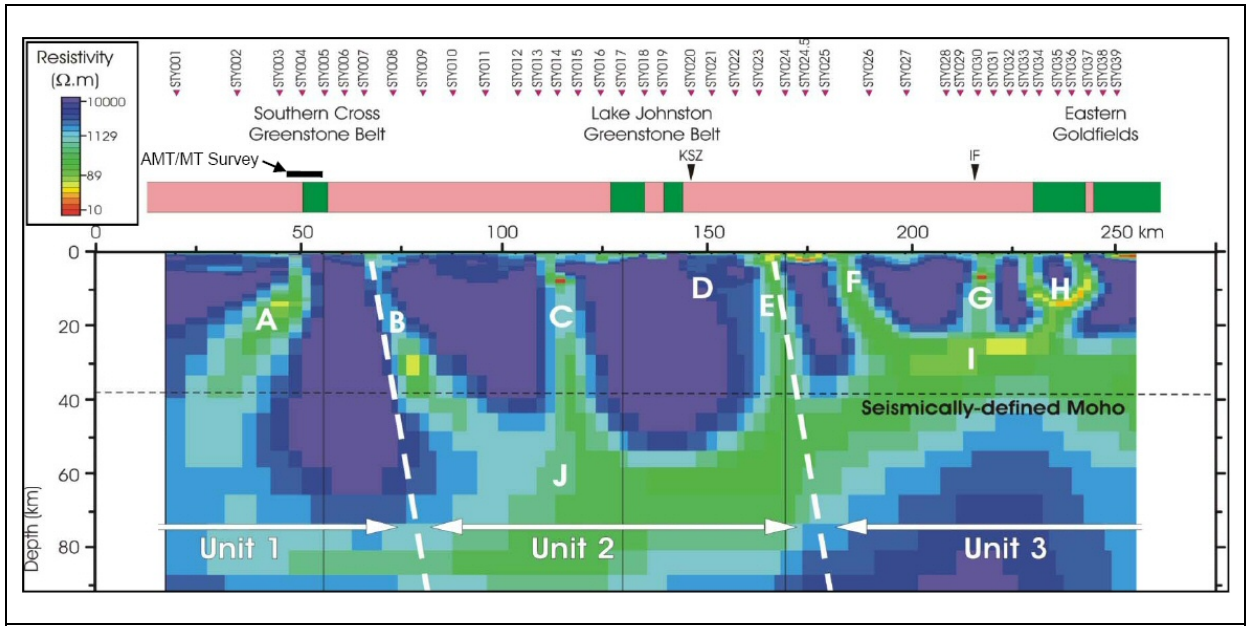

Figure 4. 2D resistivity model from regional MT survey data (modified from Dentith et al., 2011).

AMT/MT acquisition and processing

During December 2010, AMT and MT data were collected at 31 sites along a 10 km profile with a site spacing of 250 m. Three components of the magnetic field (H_x, H_y and H_z) and 2 components of the electric (E_x and E_y) field were recorded at all sites except at sites where the H_z component was omitted because of difficult digging conditions. Figure 5 shows the layout for a typical site. AMT data were acquired at all sites and MT data were collected at 11 sites (approximately every third site). Phoenix-made MTU-5A data recorders were used, with MTC-50 induction coils for MT recordings and MTC-30 induction coils for AMT recordings. MT data were recorded for at least 12 hours and AMT data for approximately 1 hour.

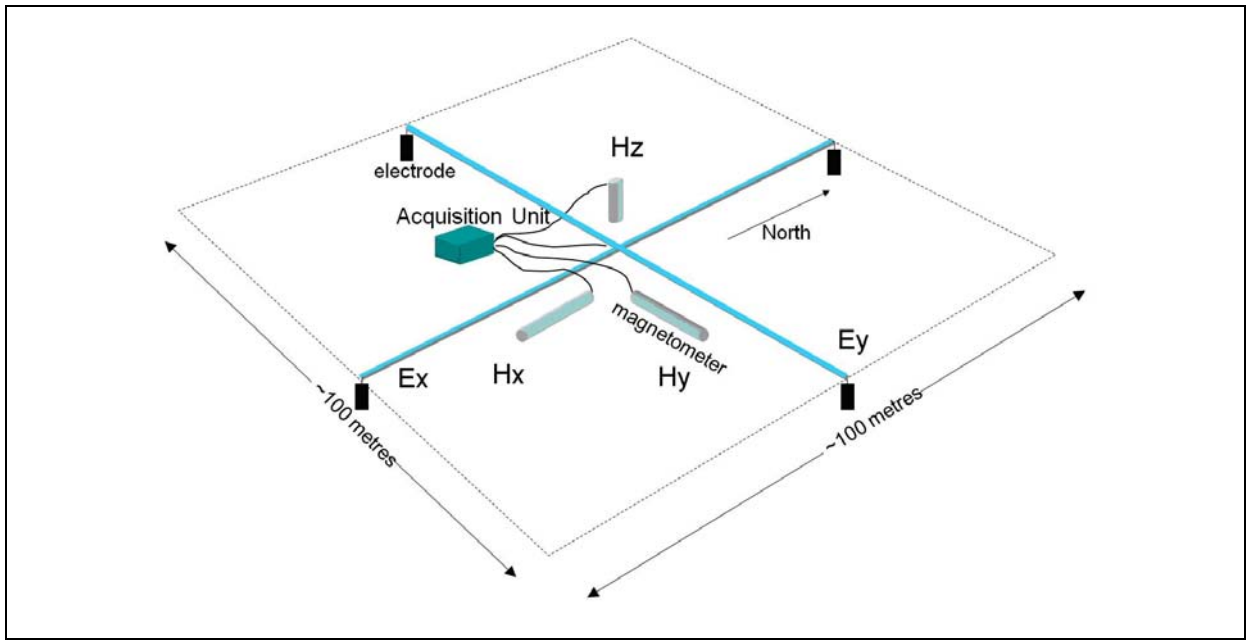

Figure 5. Layout for a typical MT site.

The time-series data acquired at each of the sites along the profile (Figure 6) were processed using robust remote-reference algorithms supplied by Phoenix Limited. These algorithms are based on the coherence-sorted cascade decimation method of Jones and Jödicke (1984). Remote reference

processing (Gamble et al., 1979) involves the use of data acquired simultaneously at stations along the profile and data recorded at a distant location. Processed data consisted of apparent resistivity and phase curves in the band 10,000-5 Hz for the AMT recording and 200-0.01 Hz for the MT recording.

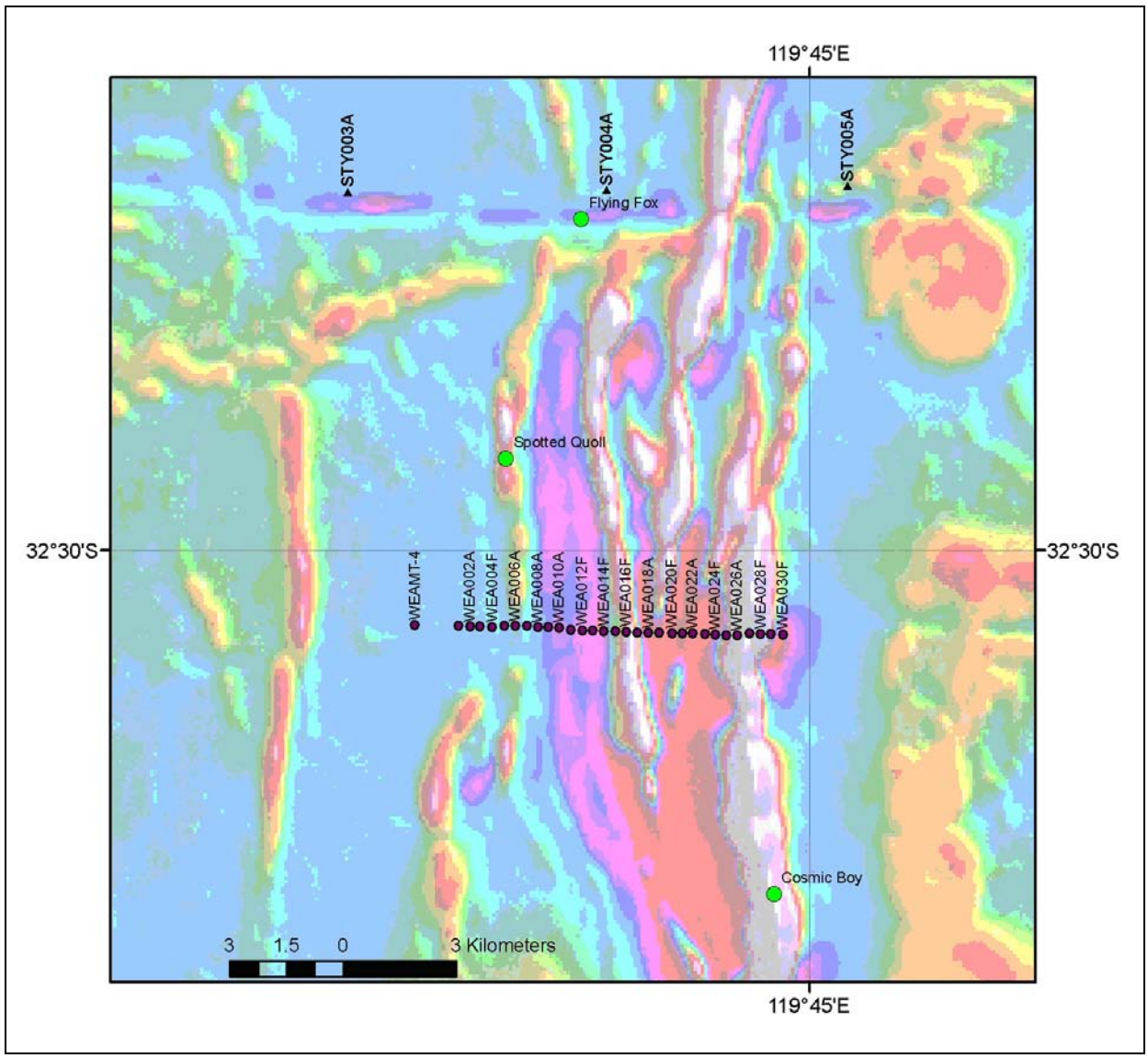

Figure 6. AMT/MT site locations (red dots), regional MT site locations (black triangles) and nickel mines (green circles), with a regional magnetic image as the background.

Modeling

The apparent resistivity and phase data were modelled using the 2D non-linear conjugate gradient inversion algorithm of Rodi and Mackie (2001) as implemented in the WinGLink® software package (Geosystem SRL, 2008). This inverse modelling method minimizes an objective function consisting of the data misfit and a measure of model roughness, with the user-specified trade-off parameter, τ, defining the balance between these two terms. Both TE and TM modes were modelled using data in the frequency range 200-0.01 Hz. These data were inverted assuming a north-south strike direction, which is the known geological strike direction. The resulting resistivity model is shown in Figure 7.

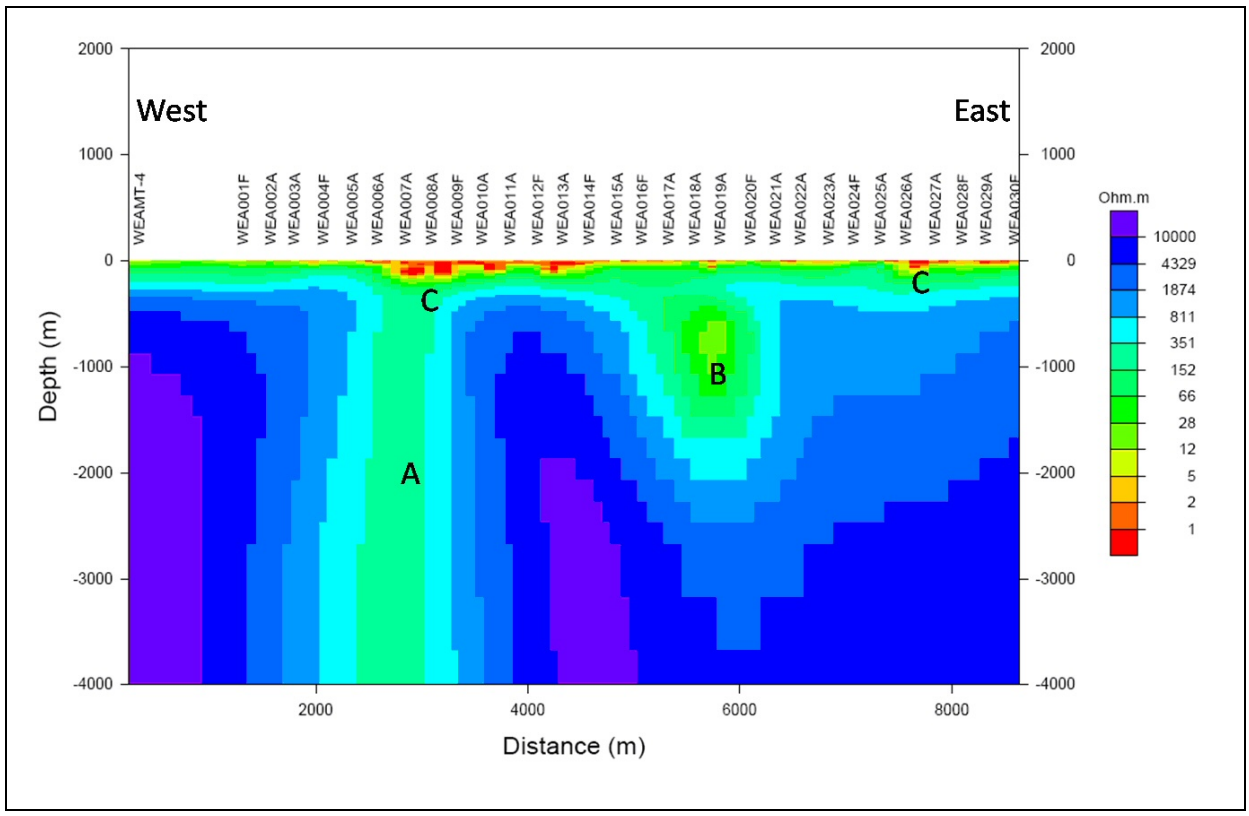

Figure 7. 2D Resistivity model calculated from the AMT/MT survey data. Features A, B and C are discussed in the text.

Interpretation

Feature A from Figure 7 is spatially coincident with the Western Ultramafic Belt that is known to be conductive. The model shows Feature A to be steeply dipping to the west. It should be noted that the dip of sub-vertical conductors is not well resolved using MT, so a conductor dipping steeply to the east may also fit the data. Feature B appears to be a response associated with a unit near the southern end of the Central Ultramafic Belt (Figure 2). During the modelling process, it could be seen that Feature B was not robust and that a conductor could be located at various locations between sites 17 and 20 at depths between 500 and 1500 m whilst still fitting the data to an acceptable degree. This may due to the local 3D nature of the geology in the area. It can be seen in Figure 6 that the Central Ultramafic Belt, which is defined by the highly magnetic linear feature north of site 19, does not appear to cross the survey line. The MT sites in this area may be detecting features that are not directly beneath the profile. This may invalidate the 2D assumption that is required for inversion using our present 2D modelling software approach, and hence make it difficult to generate a robust 2D model. Feature C may be related to clays that have been produced in the near-surface through weathering of ultramafic or BIF rocks.

Conclusions

The Western Belt contains a highly conductive horizon as expected. This horizon does not appear to dip to the east at 45 degrees under the Central Belts as was expected prior to the survey based on deep drilling results at Spotted Quoll. The conductor appears to be truncated to the east and continues steeply to a depth of at least 5 km. This could be explained by a fault repetition of the horizon that is displaced below the present position or an overturning of the sequence to a westerly dip. Interpretation of the inversion results suggests that the conductive horizon, if present, does not extend to depth on the other ultramafic belts. Only the Central Belt has some evident of enhanced conductivity at depth, but this is not well resolved in this model. One could infer that the sulfides that enhance the electrical conductivity of the Western Belt are not present in the other ultramafic belts, making these other belts less economical prospective.

The electrical model of the FGB (Figure 7) appears to be in good agreement with the model produced from the regional MT survey (Figure 4). The regional model suggests that the conductor extends through to the Moho. One could reasonable assume that the Western Belt itself does not extent to the base of the crust, but could postulate instead that the Western Belt, and most likely the entire FGB, is intimately linked to a crustal fracture or boundary that does extend to the Moho.

References

Collins, J. E., and McCuaig, C. C. 2010, The Flying Fox Ni-Cu-PGE komatiite-hosted deposit, Forrestania Greenstone Belt: In Geological Survey of Western Australia Record 2010/26 (Chapter 7), “Controls on giant mineral systems in the Yilgarn Craton – A field guide”.

Dentith, M., Evans, S., Thiel, S., Gallardo, L., and Joly, A., 2011, A magnetotelluric traverse across the southern Yilgarn Craton: Unpublished Geological Survey of Western Australia Report (submitted).

Gamble, T. D., Goubau, W. M., and Clark, J., 1979, Magnetotellurics with a remote magnetic reference: Geophysics, 44, 53-68.

Geosystem SRL, 2008, WinGLink® User's Guide: GEOSYSTEM SRL, Milan, Italy.

Haak, V., and Hutton, V. R. S., 1986, Electrical resistivity in continental lower crust: In J. B. Dawson, D. A. Carswell, J. Hall, and K. H. Wedepohl (eds), The Nature of the Lower Continental Crust, Geol. Soc. London, Sp. Publ. 24, 35-49.

Jones, A. G., 1992, Electrical conductivity of the continental lower crust: In D. M. Fountain, R. J. Arculus, and R. W. Kay (eds), Continental Lower Crust, Elsevier, Amsterdam, Chapter 3, 81-143.

Jones, A. G., and Jodicke, H., 1984, Magnetotelluric transfer function estimation improvement by a coherence-based rejection technique: SEG Technical Program Expanded Abstracts, 3, 51-55.

Perring C. S., Barnes, S. J., and Hill, R. E. T., 1996, Geochemistry of Archaean komatiites from the Forrestania Greenstone Belt, Western Australia: evidence for supra-crustal contamination: Lithos, 37, 181-197.

Rodi, W., and Mackie, R. L., 2001, Nonlinear conjugate gradients algorithm for 2-D magnetotelluric inversion: Geophysics, 66, 174-187.

A comparison of transient and conventional approaches to AMT

David Goldak [1] and Peter Kosteniuk [2]

[1] *EMpulse Geophysics Ltd. (empulse@sasktel.net)*
[2] *Kosteniuk Consulting Ltd. (kostp@sasktel.net)*

Abstract

The natural electromagnetic field in the frequency range above 1 Hz is predominantly due to lightning discharges. The random, incoherent sum of globally distributed sources gives rise to a low level quasi-continuous component which is, in general, elliptically polarized. The effects of discrete events related to individual lightning discharges from either relatively nearby and/or very large current moment discharges are superimposed on this continuous component. 'Nearby' in this context is defined relative to the scale of global waveguide attenuation, which at 100 Hz is of the order of 5000 km whilst at 5000 Hz it is perhaps more like 1500 km.

The transient event signals can be much larger amplitude than the background component, but they are also strongly linearly polarized. The diversity of the polarization affects the stability with which Earth response curves can be estimated.

A 'transient' approach to AMT involves the time localized recording of linearly polarized transient event signals. Although not widely adopted, this is not a new approach, having been used previously by many others, including Don Hoover of the USGS in the 1970's, Keeva Vozoff, Ken Paulson and Andreas Tzanis in the 1980's, and Stephen Garner in the late 1990's.

The use of linearly polarized transients with conventional estimation procedures such as remote reference (RR) produces a bias that is additional to that caused by finite signal-to-noise ratio (SNR) and sample size. To improve the transient approach, we have developed a data processing algorithm called Adaptive Polarization Stacking (APS) that is specifically designed to work with linearly polarized transients. This new method produces results which properly reflect the polarization diversity, SNR and sample size in the final Earth response curves and error bars. We have shown that our APS algorithm has a higher order bias convergence than RR when applied to transients with typical polarization characteristics.

In this paper, we compare results obtained with conventional and 'transient' AMT data collected on the same seismic line by survey crews that were in the survey area at the same time.

Despite our first generation coils being at least four times noisier at low frequency and ten times noisier at high frequency than those used by our conventional survey colleagues, and that our 12 bit analog-to-digital-converter (ADC) (c/f the 24 bit ADC used in the conventional survey) had a software bug that required the removal of all of our pre-trigger data, we believe that our impedance data turned out as good as our colleague's in terms of curve smoothness and width of dead-band, and that our tipper data is demonstrably better.

Introduction

The Mesoproterozoic Athabasca Basin (AB) in northern Saskatchewan, Canada, consists of flat lying terrestrially-derived sediments that exceed 1 km thickness in places. The AB rests unconformably on crystalline basement rocks which are generally comprised of felsic gneiss, metavolcanic rocks and graphitic pelitic schist. Typical exploration practice is to use electromagnetic methods to map graphitic shear zones (i.e., basement conductors) and subsequently carry out DC resistivity surveys to search for alteration halos in the sandstone above the basement conductors. The goal is to find areas of increased fluid flow and therefore possibly areas of uranium deposition (Leppin and Goldak, 2005). However, recent 'transient' AMT surveys have shown the ability to map conductive sandstone alteration with resolution comparable to DC resistivity (Powell et al., 2007; Nimeck and Koch, 2008).

As part of a multi-disciplinary study ('EXTECH IV'), an audio magnetotelluric (AMT) survey was carried out in the Shea Creek area, less than 15 km south of the formerly producing Cluff Lake mine, Athabasca Basin region of northern Saskatchewan (Craven et al., 2007) (Figure 1). Although not formally a part of the EXTECH IV program, the authors were given the opportunity by AREVA Resources to survey seismic line WAS-4 with their transient AMT equipment. This paper deals with the two AMT data sets collected on this line where a relatively direct comparison can be carried out of the results (i.e., those obtained using a transient approach by the authors, and those obtained using the more conventional approach in a survey performed by a different service provider). Reflection seismic, gravity, DC resistivity and UTEM III fixed loop surveys have also been completed on WAS-4.

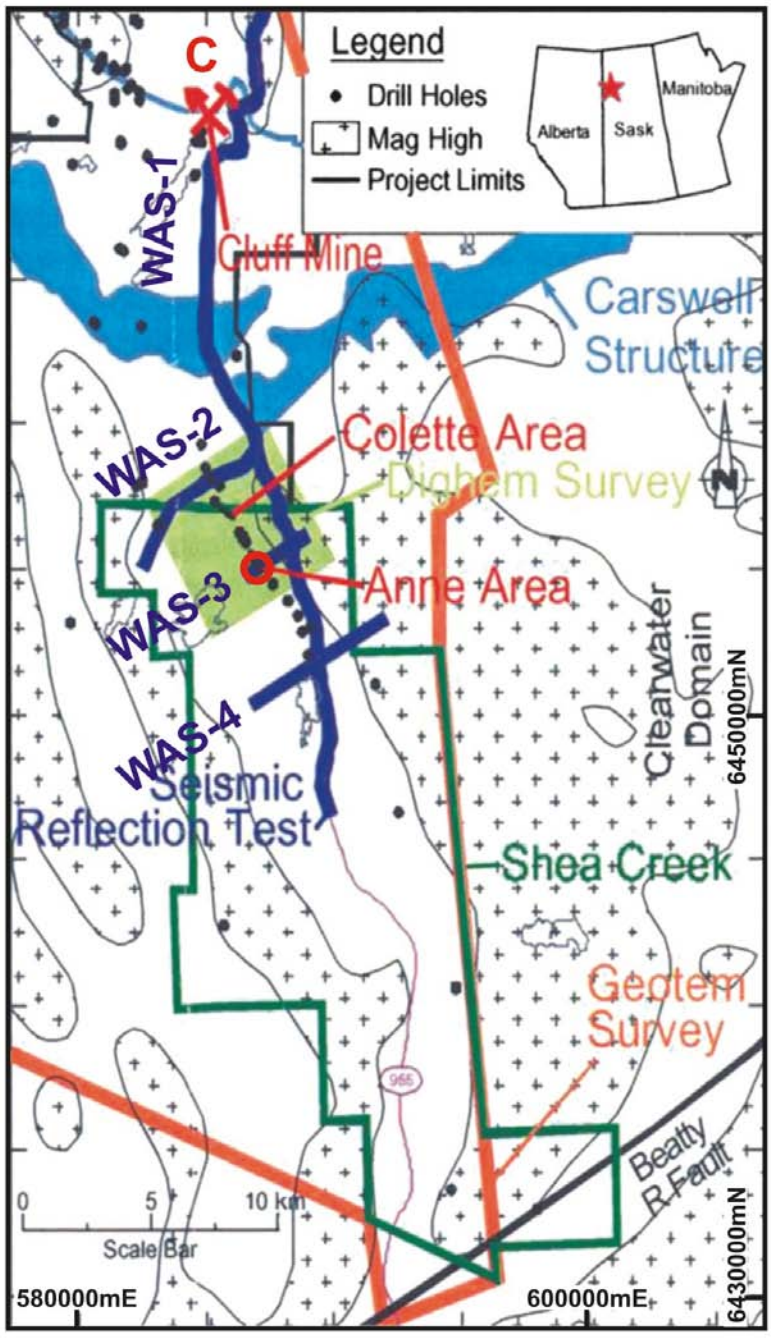

Figure 1. Location map for the survey area, courtesy of Hajnal et al. (2010).

Transient and Conventional AMT

The natural electromagnetic field in the frequency range above 1 Hz is predominantly due to lightning discharges, the energy from which is partially trapped within the Earth-ionosphere waveguide. The natural field can be considered as having two components; a transient component due to individual lightning discharges, and a low-level background component due to the random, incoherent sum of global activity. It is estimated that there are of the order of 50 lightning discharges per second (Kotaki and Katoh, 1983). Global waveguide attenuation is such that the continuing component is most significantly present at frequencies in the range of approximately 7 to 200 Hz, and to a lesser degree from 7,000 to 15,000 Hz, i.e., these are the frequency bands in the ELF/VLF range (i.e., ELF – 3 Hz to 3 kHz, VLF – 3 kHz to 30 kHz) where global waveguide attenuation is less than 3 dB/1000 km (Barr, 1970).

To enhance data quality, especially outside of these frequency ranges, we take a 'transient' approach to AMT. Namely, the time localized recording of individual transient events, so called 'sferics', from individual lightning discharges. This is not new and has been done by many others, including Hoover et al. (1976), Tzanis and Beamish (1987), Kosteniuk and Paulson (1988), Vozoff (1991) and Garner and Thiel (1999).

This is contrasted with conventional AMT practice which is to extract information related to the background continuous signal assuming a constant influx of energy. While the source field is to a good approximation continuous in certain frequency ranges, significant enhancement of signal-to-noise ratio (SNR) is afforded by recording the transient component in a time localized fashion (Figure 2).

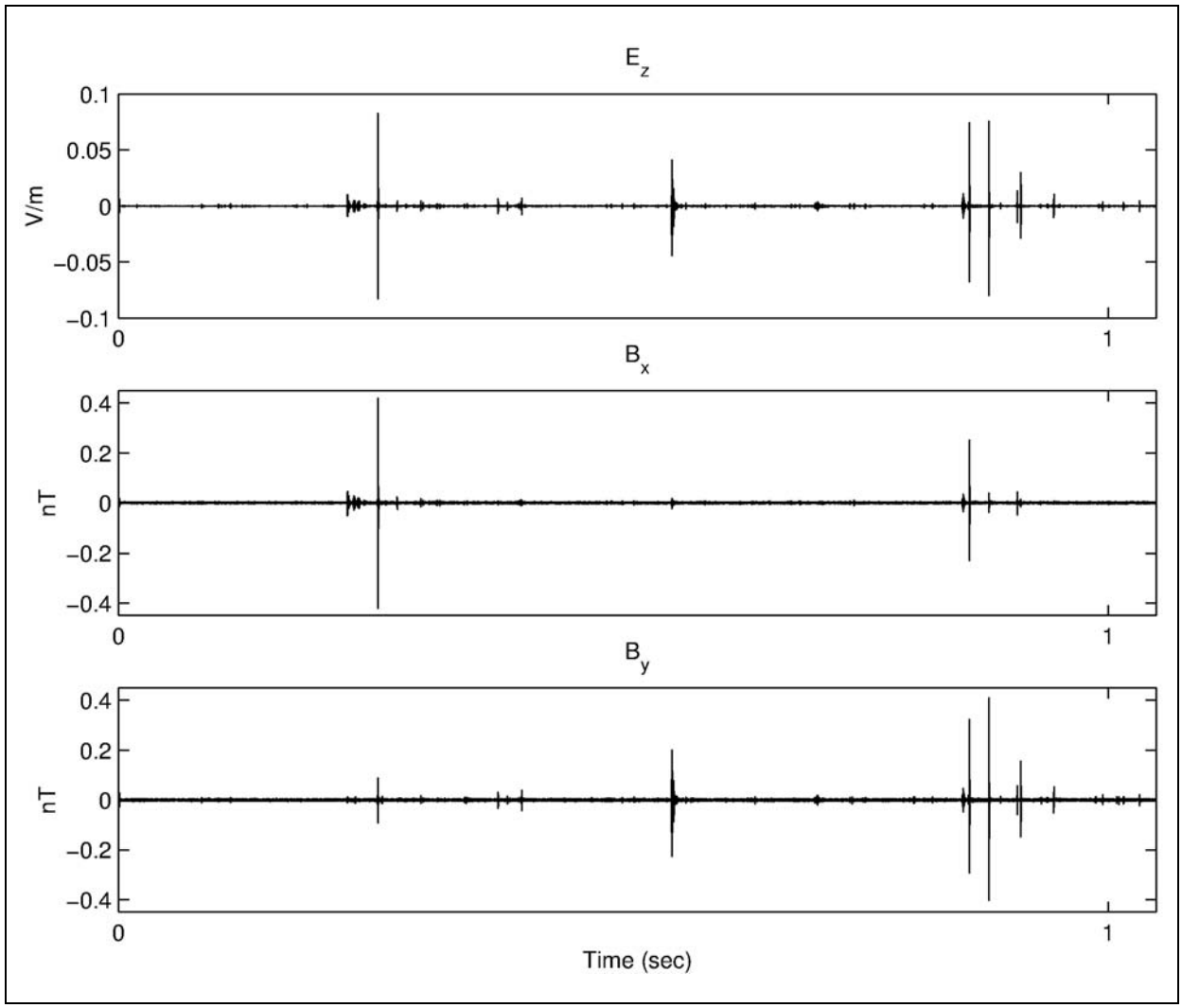

Figure 2. Time series record of electric and magnetic field signals illustrating the presence of discrete, high amplitude events.

The rate at which these discrete events are present depends on location and season. For example, it has been our experience in high northern latitudes during winter that the rate of arrival of useful events may be as little as one or two per minute, and consequently, a short continuous recording of several seconds is unlikely to contain any useful transients.

The transient events are strongly linearly polarized, the polarization diversity of which affects the accuracy of estimated Earth response curves (i.e., the level of bias in the solution). If we consider a scatter plot of two events (Figure 3), the angle between events is akin to specifying the condition number of the pairs of simultaneous linear equations involved in the estimation of the impedance tensor and/or tipper. A narrow angle produces a large condition number and an unstable system, whilst a wider angle increases stability, with 90 degrees between events being ideal. The stability of the linear system, as partly dictated by the angle between events, produces a bias additional to that caused by finite SNR and finite sample size (Goldak and Goldak, 2001).

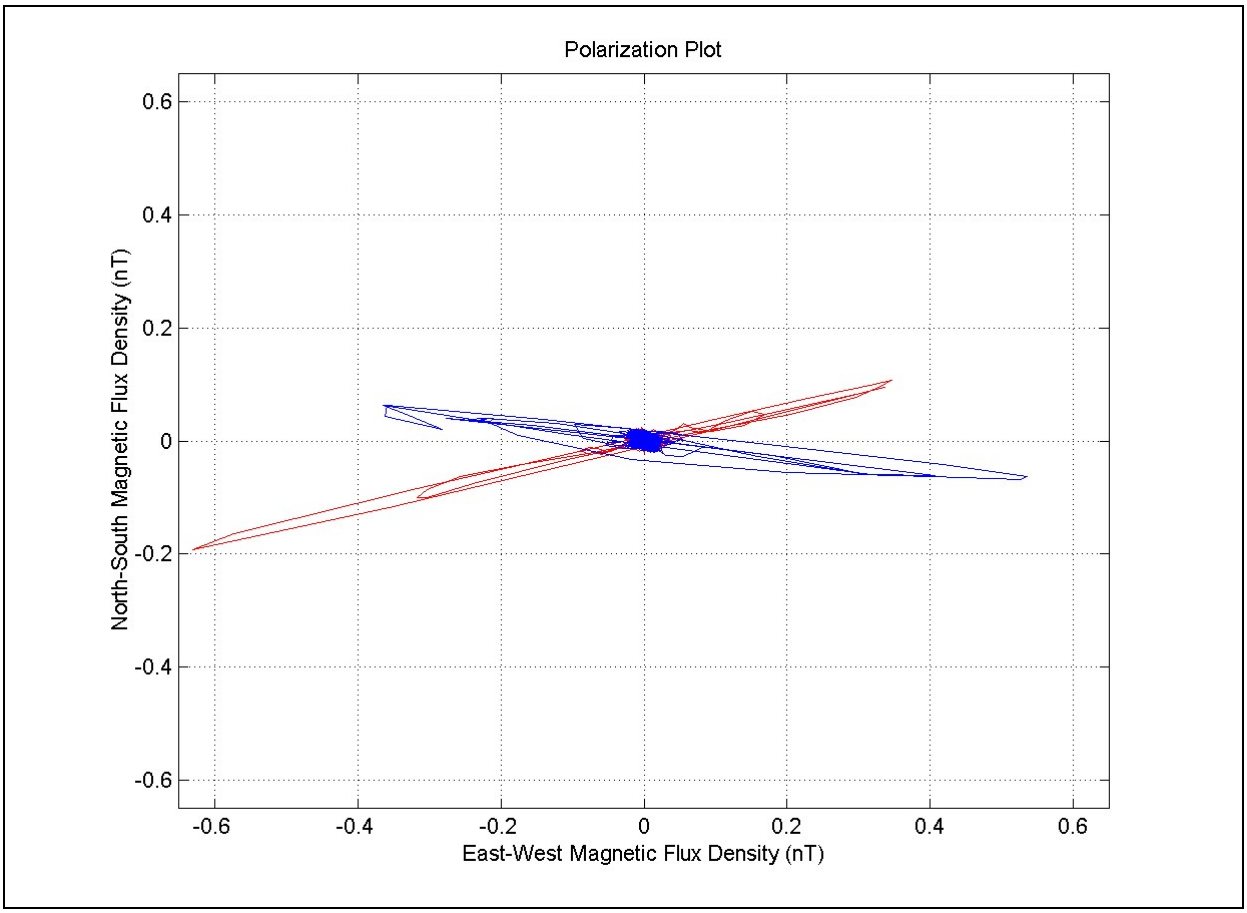

Figure 3. Scatter plot illustrating the strong polarization present in the signals from individual events.

This situation was the motivation behind the development of our Adaptive Polarization Stacking (APS) algorithm. We sought a method that can detect and 'adapt' to the diversity of polarization of the linearly polarized (transient) data, SNR and sample size, and one that communicates the stability of the linear system involved through the final Earth response curves and error bars.

A key feature of APS is the ability to enhance the SNR, to an extent, through a time-domain averaging of the transients. High quality estimations of impedance and tipper are then possible, even with narrow angle sources. An example of the stacking process is shown in Figure 4 where we note that peak-to-peak signal amplitude has been increased by approximately a factor of twenty after thirty-eight averages.

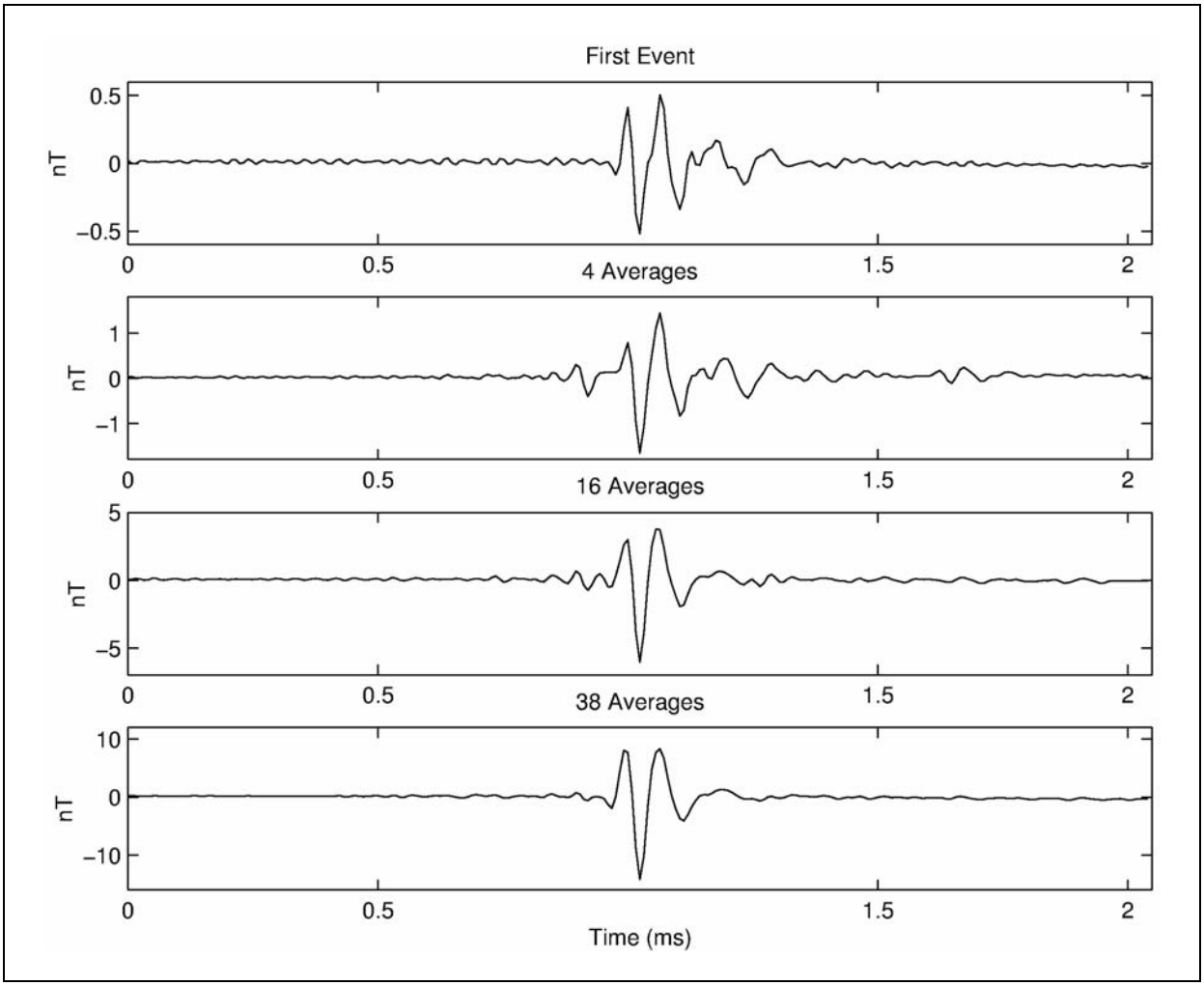

Figure 4. Time series magnetic field results for increasing levels of stacking.

Even though some fine-scale signal cancellation occurs due to non-similarity of time-domain waveforms, our belief is that extensive Monte Carlo analysis of bias and error bar capture indicates that APS provides the greatest benefit of bias reduction and precision of data (i.e., error bar size and error bar capture of true curve), making it the preferred approach for processing transient data. Many different algorithms have been tested, including what we called ‘curve-stacking’ whereby multiple impedance and tipper estimates were obtained from unique, multiple pairs of events and the curves stacked in a weighted sense, either with one single weight per curve or with frequency dependent weights across each curve. Even though the "curve-stacking" technique has absolutely no signal cancellation, APS still provides a far greater benefit in terms of accuracy (i.e., level of bias, error bar size, error bar capture), especially for the diagonal elements of the impendence tensor ‘Z’ and the secondary tipper component, both of which are very important for 3D inversion.

Many different weighting/stacking schemes have also been tested with APS and in the end, it would seem to us that ensuring maximum noise cancellation is the most important consideration, even if that means accepting some fine scale signal cancellation. We have further shown that, given transients with typical polarization characteristics, our APS algorithm has a higher order bias convergence than remote referencing methods (Goldak and Goldak, 2001).

Survey parameters and results

Survey coverage at Shea Creek is shown in Figure 5, with seventeen ‘conventional’ AMT stations and thirty-six ‘transient’ AMT stations. Only those stations jointly occupied will be compared. A right handed co-ordinate system was used, with the positive x-axis direction being perpendicular to the survey line direction (327°), the positive y-axis direction being parallel to the survey line (57°), and the

positive z-axis being downwards. Table 1 provides a summary of the acquisition and processing parameters of the two survey methods. The estimated resistivity/phase results are shown in Figure 6 whilst the tipper results are shown in Figure 7.

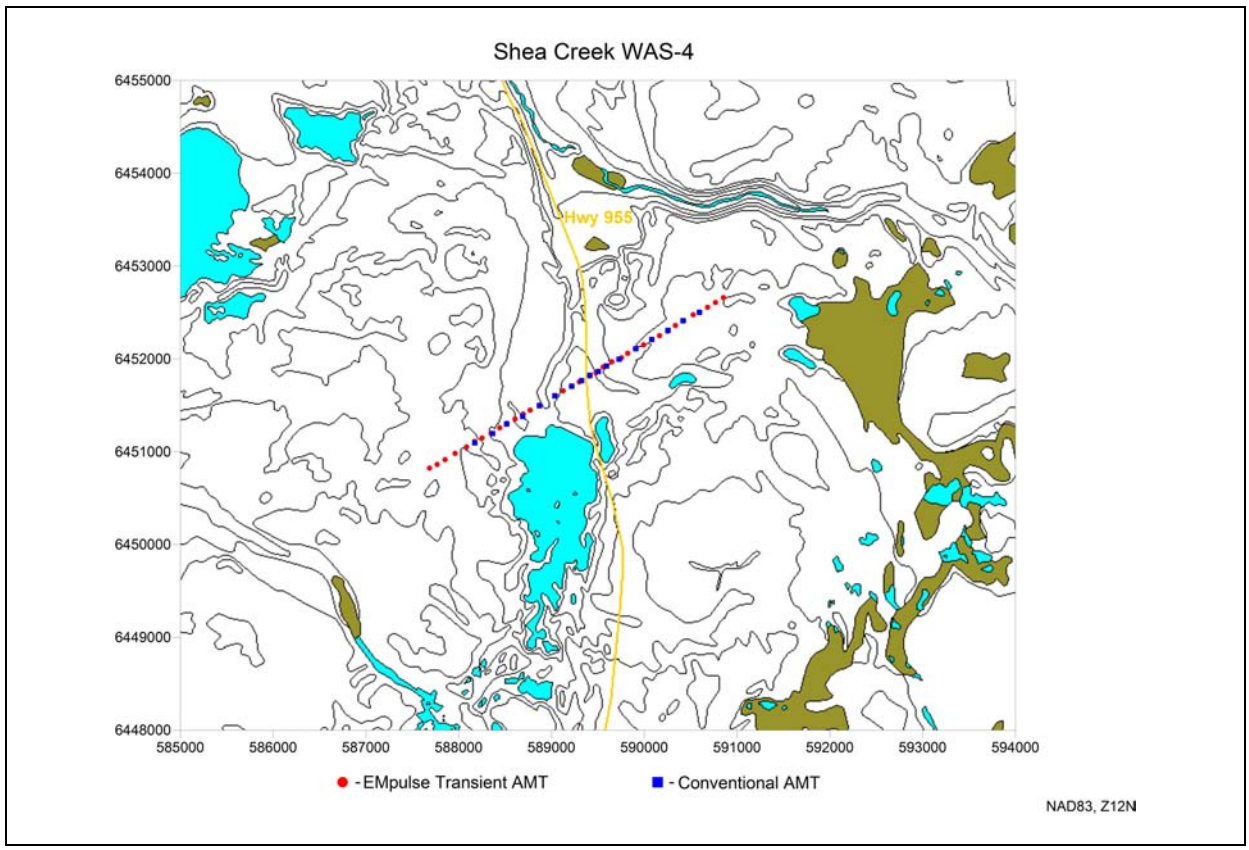

Figure 5. AMT station coverage for the Shea Creek Survey.

Table 1. Summary of AMT survey parameters.

	Transient	Conventional
Recording Method	Threshold triggered one second bursts, pre-trigger data (0.25 s) discarded due to an ADC driver bug, 20 minute typical recording length.	Continuous 7 minute recording for f < 1000 Hz, continuous 7 s recording for f > 1000 Hz
Data Bandwidth	5 Hz to 32 kHz	8 Hz to 20 kHz
Sample Rate	125 kHz	2048 Hz for f < 1000 Hz, and 4096 Hz for f > 1000 Hz
ADC Resolution	12-bit	24-bit
Induction Coils	First generation GRG-1, negative field feedback, noise floor of 9 fT per root(Hz) at 1000 Hz, secondary resonance (shielding) issues (see Figure 9).	EMI BF-6 (current-voltage converter style ?), advertised noise floor of 1 fT per root(Hz) at 1000 Hz (see Figure 9).
Electric Field	Lead-Lead-Chloride porous pot electrodes with 100 m separation.	Stainless steel stakes with 50 m separation.
Data Processing Algorithm	Adaptive Polarization Stacking	Robust remote-reference
Analog signal conditioning	Yes	No

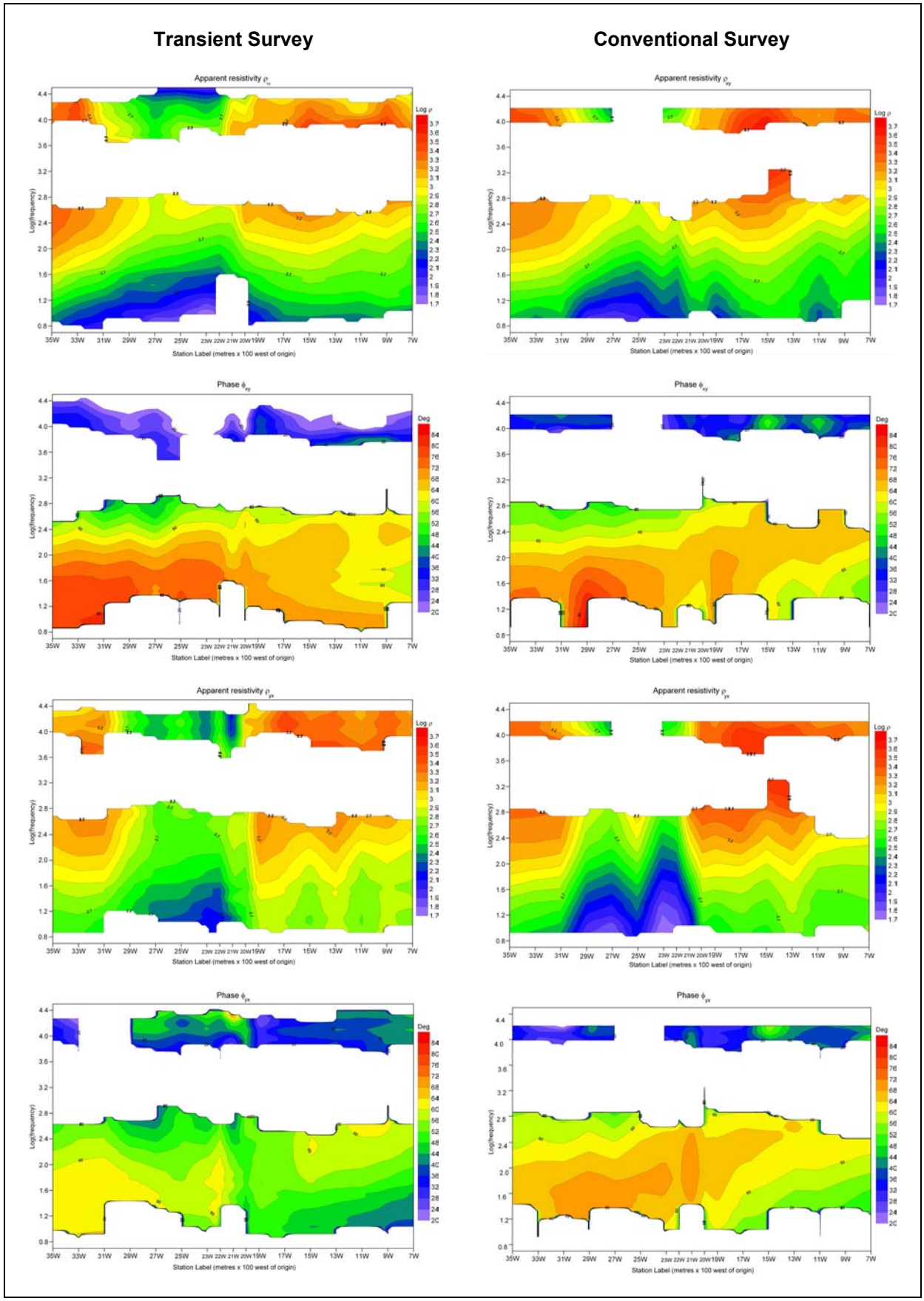

Figure 6. TE mode (xy) and TM mode (yx) apparent resistivity and phase results.

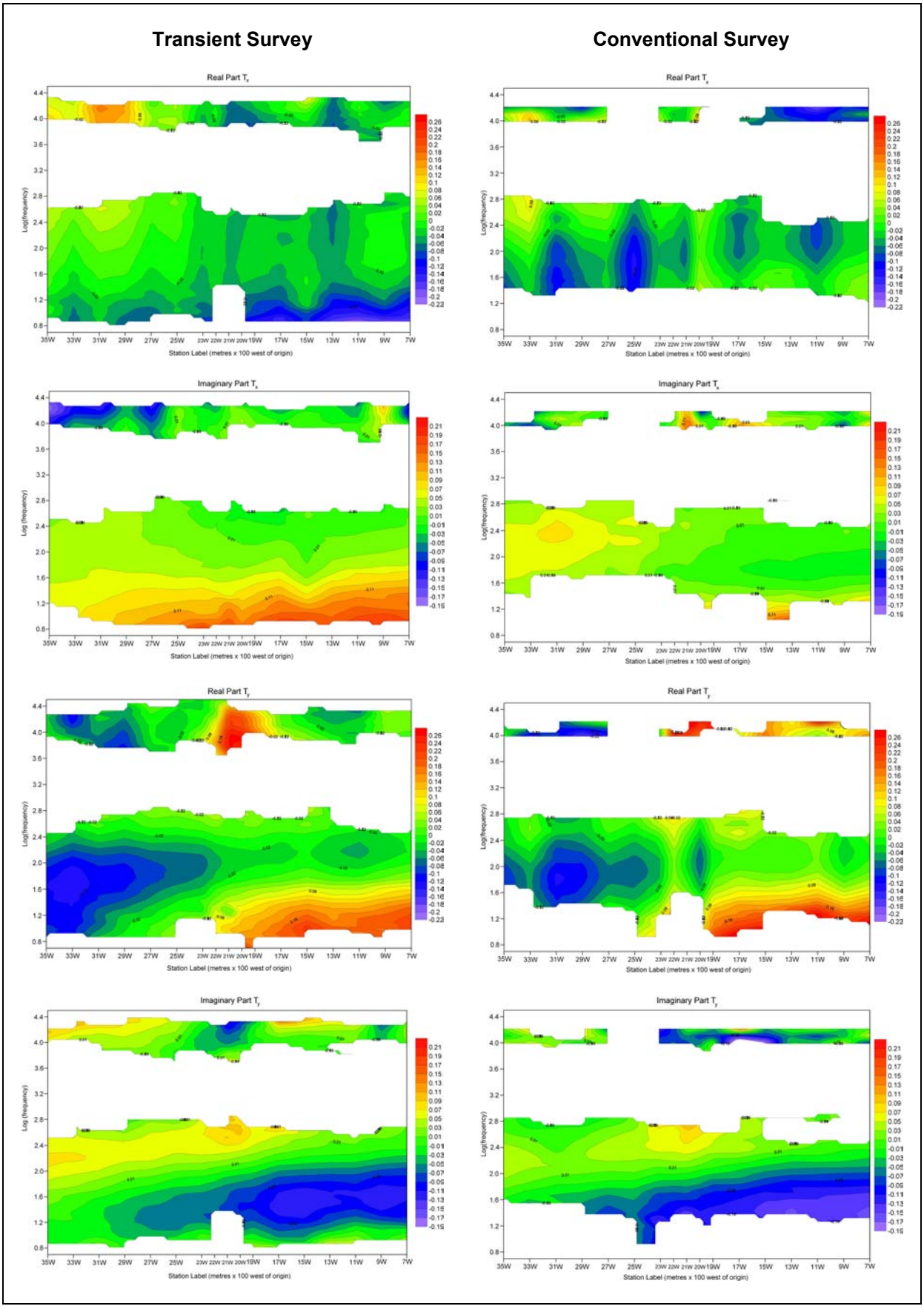

Figure 7. Tipper results.

Discussion

The APS estimates shown in Figure 6 and Figure 7 use a constant frequency vector with 15 points-per-decade. Conversely, the robust RR code (Larsen et al., 1996) outputs a variable length frequency vector which depends on data quality with respect to bandwidth. For the sake of plotting and subsequent 2D inversion (i.e., interfacing with our software), a simple linear interpolant was used to interpolate the conventional robust remote-reference estimates to the constant APS frequency vector. Blank areas of the plots indicate frequencies for which the codes produced bad data.

With respect to the resistivity and phase data, the APS estimates are significantly more 'bi-modal' in that the TE mode (xy) and TM mode (yx) APS estimates show significant differences whilst the robust RR estimates produce very similar TE and TM mode estimates, especially with respect to the phase. Compared to the robust RR estimates, the TE mode APS results are spatially broader and smoother whilst the TM mode APS results are more sharply varying. The largest discrepancy between APS and robust RR estimates is with the TM mode (yx) phase (i.e., the bottom pair of plots in Figure 6).

Despite the fact that the GRG-1 coils were ten times noisier at high frequency (Figure 8), the high frequency APS resistivity estimates are as good as or better than the conventional estimates. The shallow alteration zone is better seen in the TE mode APS estimates (i.e., the upper two sets of plots in Figure 6), and evidence of a lateral contact is clearly seen in the TM mode APS estimates between stations 20W and 21W (i.e., the centre of the lower two sets of plots in Figure 6).

The APS high frequency phase estimates were unfortunately corrupted by secondary resonance issues due to inadequate electro-static shielding of our first generation coil. The width of the dead band at about 2 kHz is very similar between the two systems, despite our GRG-1 coil being ten times noisier than the BF-6 coils used on the conventional survey above 1 kHz (Figure 8).

With respect to the tipper data, higher quality estimates are seen with the transient data which shows a higher degree of self consistency and wider bandwidth. A clear low frequency crossover on T_y is evident in the vicinity of 23W which also corresponds to the regions of lowest resistivity seen in the xy and yx apparent resistivity data. In agreement with the TM mode APS estimates, a high frequency tipper anomaly occurs at 20W/21W (T_y) which is further indicative of the lateral contact there. Interestingly, the western edge of the contact in the vicinity of 29W produces more of a T_x anomaly (VLF range), and therefore may be more oblique to line than the contact at 20W/21W.

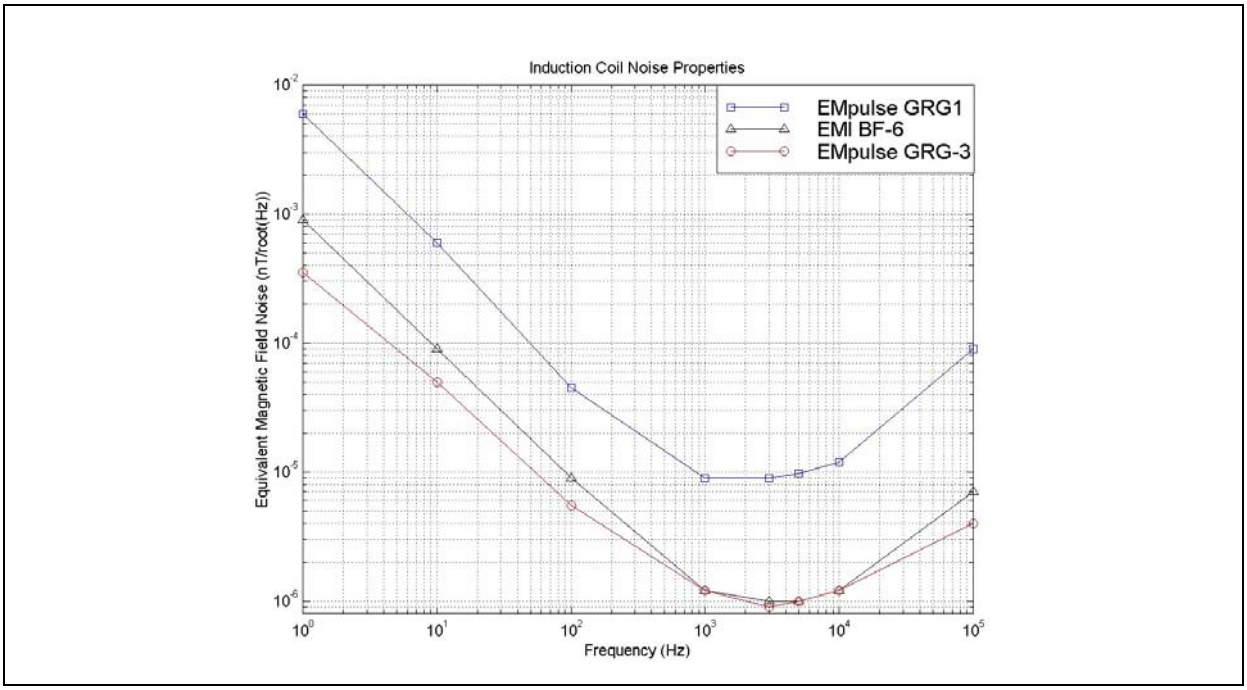

Figure 8. Induction coil noise property curves.

The interpretation of a shallow lateral contact at approximately 100 m depth, with an abrupt eastern edge at 20W/21W (i.e., indicated by a TM mode undershoot with strong Ty tipper anomaly) and a more gradational western edge at 29W (i.e., indicated by a weak Tx anomaly, whilst there is no TM mode contact effect evident), and with a basement conductor in the vicinity of 23W/24W agrees very well with the interpretation of gravity data (Figure 9) and fixed loop UTEM III data (Figure 10).

The prominent residual gravity low, as large as 1.8 mGal, is present with width of the order of 800 to 1200 m. It is postulated to be due to a shallow source that is present in the sandstone and is interpreted to be associated with fracturing and/or alteration in the sandstone, possibly related to major north-south trending basement structure. Modelling of the Bouguer gravity data on line WAS-4 indicates that the depth to the top of the body is less than 200 m, and that the source of the gravity low is a wedge that is tapered at depth. The eastern boundary of the edge is generally steeper compared to the western edge (pers. comm., Mr. Rod Koch). Reflection seismic data collected on WAS-4 also shows an anomalous zone of highly fragmented reflectivity over this lateral interval (pers. comm., Dr. Z. Hajnal).

Modelling of UTEM III fixed loop data indicates a basement conductor with 32 S conductance at a depth of 700 to 800 m, located at 2350W (Craven et al., 2007). Note the migration of the peak in the H_x component from 19W/20W at early time to approximately 2350W/24W at late time (Figure 10). The early time peak at 19W in the UTEM III data would appear to be a response to the steep eastern contact of the presumed wedge like conductive body in the sandstone.

The only puzzling part of the integrated picture is that DC resistivity data and VLF-R collected on WAS-4 (Figure 10). These do not appear to be in agreement with the other data sets with respect to the interpreted shallow sandstone structure/alteration. Despite the use of a moving Schlumberger array with a current electrode spacing of 300 m and MN/2 of 25 m, there is no evidence of a shallow resistivity anomaly between 29W and 21W. Instead, there is a resistivity low of 1000 Ωm much further to the east, in the vicinity of 4W. The resistivity low seen in the 'transient' AMT data, and partially with the conventional AMT data, between stations 21W and 29W, is of the order of 300 Ωm or less, and this agrees with the resistivity values typically associated with clay alteration zones in the sandstone.

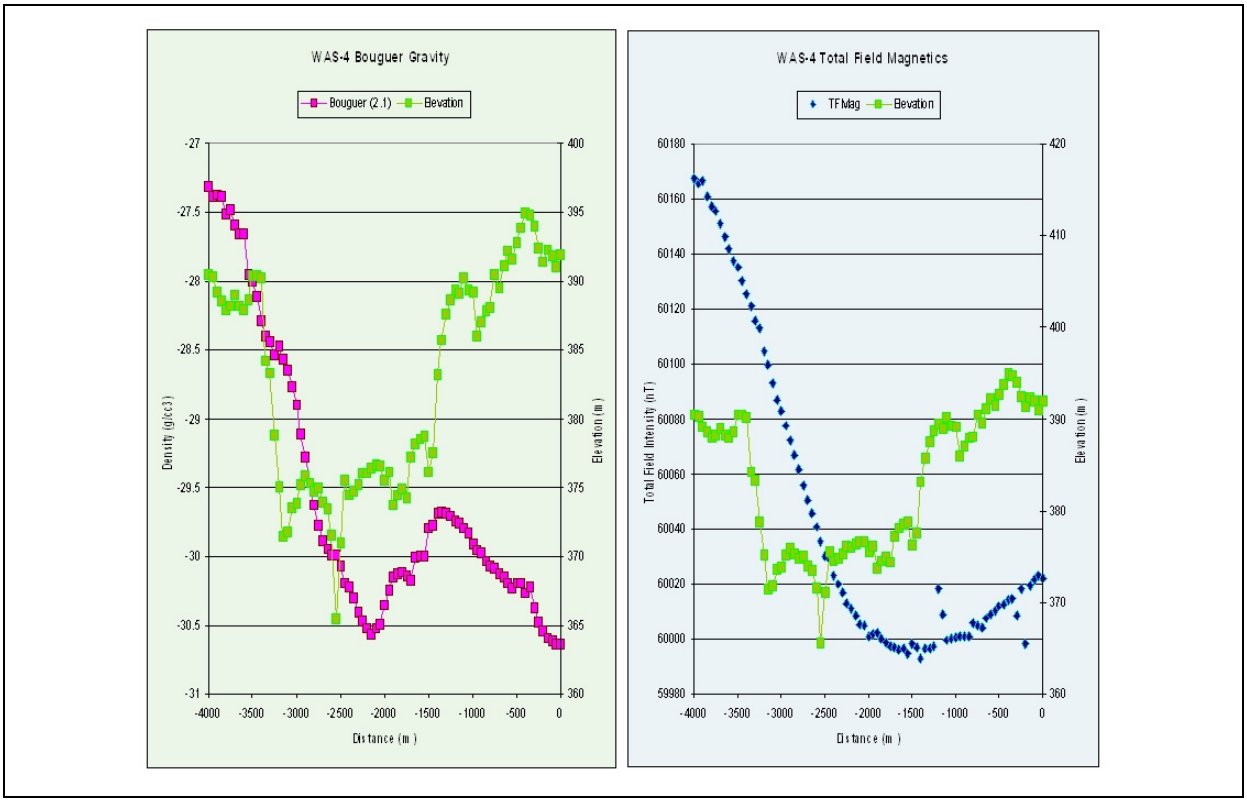

Figure 9. Bouguer gravity, total field magnetic and elevation profiles for line WAS-4.

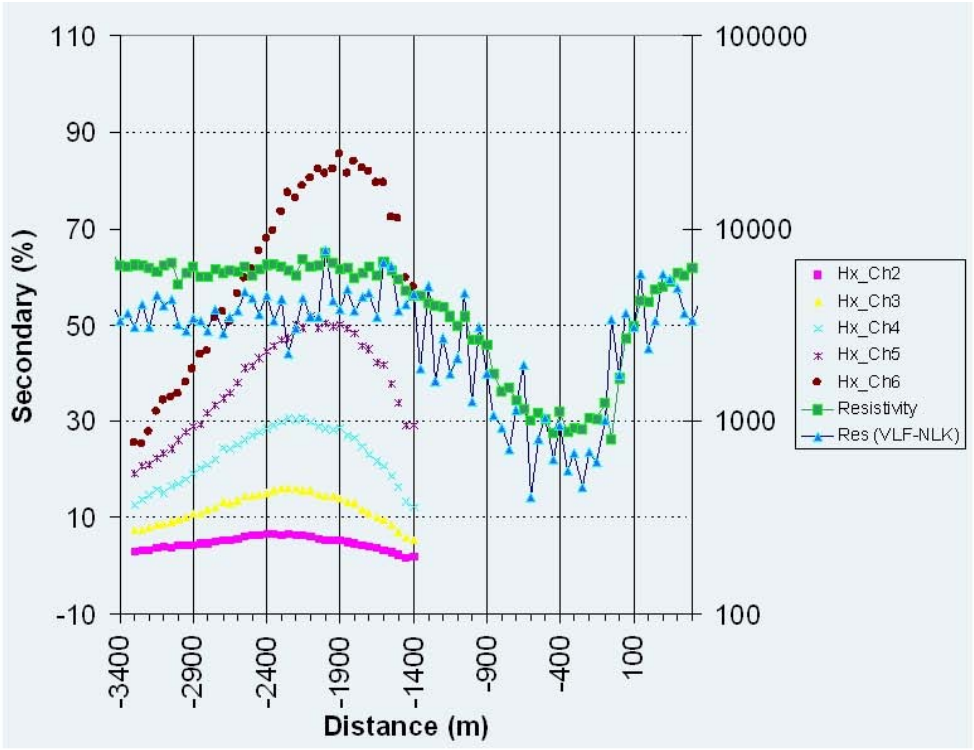

Figure 10. UTEM fixed loop Hx, DC resistivity, and VLF resistivity profiles for line WAS-4.

Conclusions

The effectiveness of our 'transient' approach to AMT with Adaptive Polarization Stacking algorithm has been demonstrated through a direct comparison with 'conventional' AMT with robust remote-reference analysis.

Despite using coils that were approximately ten times noisier above 1000 Hz and approximately 4 times noisier below 100 Hz, and an ADC driver software bug that resulted in the removal of all the pre-trigger data, the APS impedance estimates are arguably as good as the conventional estimates and the APS tipper estimates are clearly better in our opinion.

This would appear to be due to the localization of large amplitude transients and SNR enhancement through our time domain stacking process that takes proper accounting of their polarization and sample size. It should be noted that our recording times of 20 minutes (15 minutes effectively) were considerably longer than the 7 minutes used in the conventional AMT survey for sub-1000 Hz data and 7 s for data greater than 1000 Hz.

The largest enhancements with respect to impedance are seen at high frequency where the APS estimates better map shallow alteration features in the sandstone, although the westerly dip of graphitic metasediments in the basement is also better seen in the TE mode APS estimates. The rather large difference in the TM mode phases of the two systems remains unexplained however.

Our tipper data appear to be better across the entire bandwidth, being smoother and more self-consistent at both low and high frequency. They more clearly reveal the response for the Saskatoon Lake conductor at approximately 23W (T_y) and the shallow contacts at approximately 20W/21W (T_y) and 29W (T_x). Secondary resonance issues, which destroyed the high frequency impedance phase estimates, had less of an effect on the tipper, presumably due to partial cancellation of the effect when taking the ratio of two coil responses.

Most importantly, our 'transient' AMT data integrates very well with what is known about the geology in the area of line WAS-4. The westerly dip of graphitic metasediment gneiss is clearly seen in our TE

mode resistivity data, the Saskatoon Lake conductor at 2350W is evident in our impedance but especially the tipper data (T_y). Shallow structure with a sharp eastern edge and a more gradational western edge is clearly apparent in the TM impedance and the tipper. This corroborates very well the previous, completely independent, interpretation of gravity data collected on WAS-4.

In order to obtain the best possible Earth response curves, especially outside the continuing 'windows', the use of transients to maximize SNR is mandatory. Whether one field records them in a time-localized fashion or streams data to disk continuously and searches for them after the fact, is not really important. What matters most is that recording take place for a long enough time to receive enough events from as many different directions as possible and an algorithm such as APS is used to properly locate and process the transients. If using RR, Monte Carlo simulation would be required to obtain more realistic error bars, as we do with APS, due to non-circularity of the source field.

The collection of a larger data set with one set of equipment would provide a common time series that would enable a better comparison of the performance of robust RR with APS. Most conventional AMT recordings, at least at high frequency, are too short for proper application of the APS method.

Along similar lines, we are working towards testing the BIRRP code (Chave and Thomson, 2004) with respect to bias and error bar capture in order to compare with APS. This is done via Monte Carlo simulation whereby a pool of many hundreds of real magnetic field events is used to create the perfectly matching electric field events assuming a known 3D impedance and tipper. The perfect relation between electric and magnetic fields is then perturbed with Gaussian noise of some level, a chosen number of noisy events are randomly selected out of the pool of events, and an impedance and tipper estimated. The result is stored and repeated many thousands of times. In this fashion, the level of bias and error bar performance of APS (already completed) and BIRRP could be compared.

References

Barr, R., 1970, The propagation of ELF and VLF radio waves beneath an inhomogeneous anisotropic ionosphere: Journal of Atmospheric and Terrestrial Physics, 33, 343-353.

Chave, A. D., and Thomson, D. J., 2004, Bounded influence estimation of magnetotelluric response functions: Geophysical Journal International, 157, 988-1006.

Craven, J. A., McNeice, G., Powell, B., Koch, R., Annesley, I. R., Wood, G., Mwenifumbo, C. J., Unsworth, M. J., and Xiao, W., 2007, Audio Magnetotelluric studies at the McArthur River mining camp and Shea Creek area, northern Saskatchewan:, In Jefferson, C.W. and Delaney, G. (ed.), EXTECH IV: Geology and Uranium EXploration TECHnology of the Proterozoic Athabasca Basin, Saskatchewan and Alberta: Geological Survey of Canada, Bulletin 588 (also Saskatchewan Geological Society, Special Publication 18; Geological Association of Canada, Mineral Deposits Division, Special Publication 4), 413-424.

Garner, S. J., and Thiel, D. V., 1999, Broadband (ULF-VLF) surface impedance measurements using MIMDAS: Exploration Geophysics, 31, 71-76.

Goldak, D. K., and Goldak, M. S., 2001, Transient magnetotellurics with adaptive polarization stacking: SEG, Expanded Abstracts, 20, 1509-1512.

Grillot, L. R., 1975, Calculation of the Magnetotelluric Tensor Impedance: Analysis of Band Limited MT Signal Pairs: Geophysics, 40, 790-797.

Hajnal, Z., White, D. J., Takacs, E., Gyorfi, I., Annesly, I. R., Wood, G., O'Dowd, C., and Nimeck, G., 2010, Application of modern 2-D and 3-D seismic reflection techniques for uranium exploration in the Athabasca Basin: Canadian Journal of Earth Sciences, 47, 761-782.

Kosteniuk, P. R., and Paulson, K. V., 1988, The application of polarization stacking to natural source magnetotellurics: Paper presented at the Annual Meeting of the Canadian Geophysical Union.

Larsen, J., Mackie, R. L., Manzella, A., Fordelisi, A. and Rieven, S., 1996, Robust smooth magnetotelluric transfer functions: Geophysical Journal International, 124, 801-819.

Hoover, D. B., Frischknecht, F. C. And Tippens, C. L., 1976, Audio-magnetotelluric sounding as a reconnaissance exploration technique in Long Valley, California: Journal of Geophysical Research, 81, 801-809.

Kotaki, M., and Katoh, C., 1983, The global distribution of thunderstorm activity observed by the Ionospheric Sounding Satellite (ISS-b): J. Atmos. Terr. Phys., 45, 843-847.

Leppin, M., and Goldak, D., 2005, Mapping deep sandstone alteration and basement conductors utilizing audio-magnetotellurics: Exploration for uranium in the Virgin River area, Athabasca Basin, Saskatchewan, Canada: SEG, Expanded Abstracts, 24, 591-594.

Nimeck, G., and Koch, R., 2008, A progressive geophysical exploration strategy at the Shea Creek uranium deposit: The Leading Edge, 27, 52-63.

Powell, B., Wood, G., and Bzdel, L., 2007, Advances in Geophysical Exploration for Uranium Deposits in the Athabasca Basin: In B. Milkereit (ed.), Proceedings of Exploration 2007, Fifth Decennial International Conference on Mineral Exploration, 771-790.

Tzanis, A., and Beamish, D., 1987, Audio-magnetotelluric sounding using the Schumann resonances: Journal of Geophysics, 61, 97-109.

Vozoff, K., 1991, The magnetotelluric method: In Electromagnetic methods in applied geophysics – Applications (edited by M. Nabighian), Society of Exploration Geophysicists, 641-711.

Practical issues of inverting 3D natural source electromagnetic data

Elliot Holtham [1] and Doug Oldenburg [2]

[1] *UBC-Geophysical Inversion Facility, Department of Earth and Ocean Sciences, University of British Columbia (eholtham@eos.ubc.ca)*
[2] *UBC-Geophysical Inversion Facility, Department of Earth and Ocean Sciences, University of British Columbia (doug@eos.ubc.ca)*

Introduction

Natural source electromagnetic methods play an important role in understanding the electrical conductivity of the upper regions of the Earth. Their greater depth of investigation compared to controlled source electromagnetic methods (CSEM), is a consequence of the plane wave excitation. Furthermore, computing the forward model response data at each frequency only requires the solution of a matrix system with two right hand side vectors which can result in significant computational advantages over multi-transmitter controlled source electromagnetic calculations. Whilst traditional natural source methods have been limited to ground based surveys (Cagniard, 1953) which can be costly and time consuming, airborne methods such as the AFMAG (Audio Frequency Magnetics) (Ward, 1959) and recently the Z-Axis Tipper Electromagnetic Technique (ZTEM) (Lo and Zang, 2008) have been developed that measure magnetic fields due to natural sources. For the ZTEM system, the data are frequency domain relations that relate the vertical fields over the survey area to the horizontal fields at the reference station. The 30 to 720 Hz frequency range of the data allow the method to be effective for finding targets at moderate depths of up to a few kilometres in many geologic settings. Although the ZTEM system may have a greater depth of investigation than many other airborne electromagnetic methods, the depth of investigation is still far below that possible with the ground-based magnetotelluric (MT) survey method. Apart from collecting ground based MT data or airborne ZTEM data, a further option is to collect both MT and ZTEM data. Here, the economical airborne ZTEM data can be used to gain high resolution in the shallow to moderate depths, while sparse MT data coverage can be used to provide information at greater depths. Regardless of which natural source method is used, robust interpretation methods must be employed in order to get meaningful results from the data. Whilst advances in computer technology have made it possible to invert large natural source datasets in 3D, a systematic multi-step procedure is required to properly invert the data. In this paper, we examine some of the practical issues of inverting MT (Farquharson et al., 2002), ZTEM (Holtham and Oldenburg, 2010a), and a combination of MT and ZTEM data (Holtham and Oldenburg, 2010b) by describing in general form the sequence of steps for the inversion of synthetic and field data sets.

Data preparation

The first element of our workflow procedure (Figure 1), and probably the most critical aspect of the entire inversion process, is preparing the data for inversion. In this step it is critical that the user understands exactly what data were collected and how to get the data into the appropriate format for inverting. Inversion users must be able to correctly determine where the electric and magnetic fields measurements were collected, as well as understanding data sign conventions, data rotations and time dependences of each contractor's data. While the MT community has tried to adopt certain standards, those are not always adhered to, and thus the data preparation step can be incredibly frustrating and time consuming.

Discretise the problem

In order to solve the necessary differential equations, the Earth must be discretised into a mesh and the discrete Maxwell's equations solved. In this discretisation, a compromise must be achieved between the numerical accuracy in the forward modelling and the computational resources required. As with MT discretisation problems, the usual guidelines that cell sizes must not violate skin depth rules apply. An important consideration when constructing a mesh is the topography of the area. Especially in areas with significant variations in elevation, ensuring that the topography is discretised sufficiently accurately, as

well as positioning MT stations on the surface of the topography, is an important consideration. Discrediting topographic features using regular rectangular meshes can require large meshes since cells added to model a particular topographic feature must extend out to the edges of the mesh. Using more complex mesh structures such as octree meshes (Haber and Heldmann, 2007) can provide significant advantages when trying to deal with complex topography. As natural source data sets become larger, inversion algorithms and methodologies must be able to handle these data sets. Ultimately when data sets reach a certain size, the inverse problem must be split up and solved as many smaller sub-problems. When performing a domain decomposition with a tiling approach to invert large natural source data sets, it is important that each mesh is overlapping so that when individual tiles are merged, the resulting final model will be continuous.

Determine initial and reference models

Determining an initial model for MT data can be relatively straightforward, for instance a uniform conductivity that best reproduces the data can be chosen. If there is no topography then this is the best fitting half-space. Another option when inverting MT data in 3D is to merge the conductivity structures generated from 1D or 2D inversions to create a 3D initial model. When inverting ZTEM data however, generating an initial model can be much trickier since all 1D layered earths produce zero vertical magnetic fields. Ideally then, some additional geophysical data or other explicit *a priori* information will be available that can be used to estimate a good starting model. If this is not available, one method we have found to work fairly effectively is to invert the data set using many different starting models, and then choose the inversion result which looks reasonable and provides the greatest reduction in data misfit. However, determining what constitutes a "reasonable" result implies having some knowledge or expectation regarding the geological structure and rock properties of the survey area (i.e., implicit *a priori* information). A model that is free of major artifacts (i.e., features which are false) is clearly a fundamental consideration in this context. If limited *a priori* information is available, the reference model should generally be simple, most likely a best fitting half-space. If trustworthy additional geologic information is known, then this can be incorporated into the reference model.

Assign uncertainties

Assigning uncertainties to data is a critical step in any geophysical inversion. Overestimating the noise will result in a loss of information which could have been extracted from the data. Similarly, underestimating the noise may create artifacts in the inverted model that are due to the noise in the data or to numerical issues such as the nature of the discretisation that was chosen (i.e., the mesh geometry). Assigning uncertainties for any geophysical field data set is difficult because there are many error sources, each of which is difficult, if not impossible to quantify. Survey errors such as instrument repeatability, human error, external noise, and mis-orientation of receivers are often thought to be the only sources of errors that need to be considered in an inversion. These sources are important, but there are many additional sources of errors such as discretisation, modelling approximations, and matrix solution errors. Ultimately, it is difficult to quantify the individual error sources, let alone their cumulative effect. Nevertheless it is essential that there is a robust and repeatable method to assign uncertainties to the data. Generally, when assigning uncertainties to natural source data, we assign the errors to be some percentage of the data plus some floor. If additional information about relative signal strengths for different frequencies is available, then this information should be included in the error assignment. If MT and ZTEM data are jointly inverted, some additional re-weighting may be required to the MT data to compensate for there being significantly more airborne than ground data.

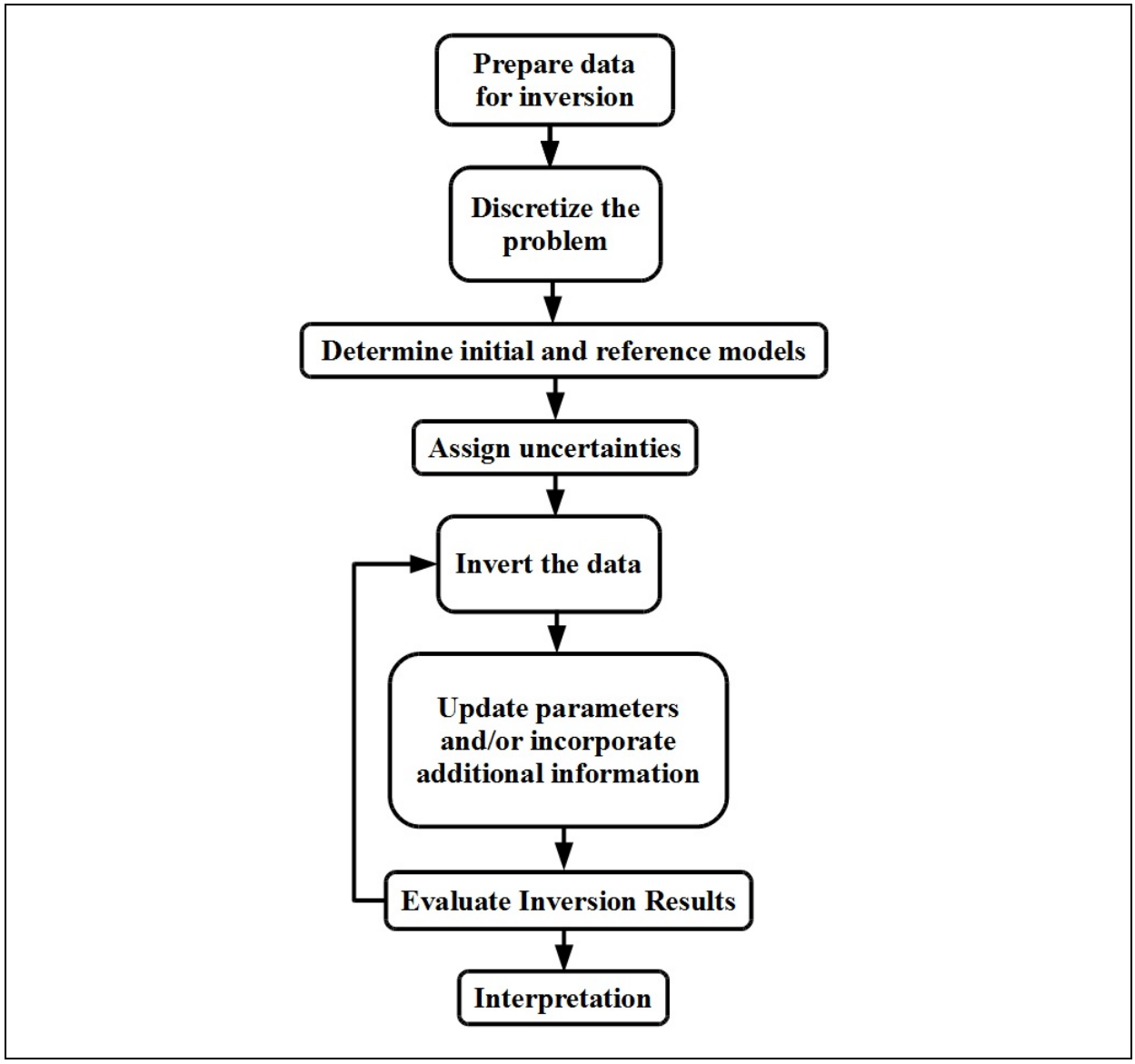

Figure 1. Flowchart of a generalised inversion procedure.

Invert the data

Although inverting natural source data is computationally cheaper than inverting controlled source data with multiple transmitters, it can still be a formidable task in 3D. In order to ensure that the data and inversion parameters have been correctly set, it is a good idea to initially invert the data on a coarse mesh. This can be quite fast and hence multiple inversions can be carried out to experiment with parameters. Once the inversion results look reasonable on these coarse meshes, the mesh can be refined and the data re-inverted. During the inversion process, the most time consuming step is forward modeling the data. In this step, there are many options on how to solve the matrix system depending on your available computing hardware. Direct solvers (Amestoy et al., 2001) or iterative methods (Saad, 2003) on the CPU, or highly parallel GPU algorithms (Bolz et al., 2003) are all effective methods.

Update parameters and incorporate additional information

When inverting geophysical data, the user can tune the inversion results by incorporating additional geologic information. The user can adjust parameters of the model regularization function, apply bounds on the conductivity, or alter the reference model. Because of the non-uniqueness of the inverse problem, adding known pieces of information such as conductivity values from down-hole measurements can significantly improve the inversion results. However, care must be taken to decide whether these values are representative of features at the scale of the discretisation that is being used.

Evaluate and interpret

Once an inversion has been completed, the results must be evaluated. It is essential to check the data misfits to ensure that each component of the data has been fit adequately at each frequency. Additionally, one should check for items such as to whether the recovered conductivities fall within their expected range and whether the result is free of any obvious artifacts. Whilst the inversion may have recovered a good representation of the true conductivity structure, the conductivity values themselves may not ultimately be the quantity of interest. It is thus critical to have a good interaction between the geophysicist that performed the inversion and the geologist/engineer that wishes to interpret the obtained conductivity model. If the conductivity models are interpreted solely by individuals with limited knowledge of inverse theory, then the models can be easily over interpreted.

References

Amestoy, P., Duff, I., L'Excellent, J., and Koster, J., 2001, A Fully Asynchronous Multifrontal Solver Using Distributed Dynamic Scheduling: SIAM Journal of Matrix Analysis and Applications, 23, 15-41.

Bolz, J., Farmer, I., Grinspun, E., and Schroder, P., 2003, Sparse Matrix Solvers on the GPU: Conjugate Gradients and Multigrid: ACM Transactions on Graphics (TOG), 22, 917-923.

Cagniard, L., 1953, Basic theory of the magneto-telluric method of geophysical prospecting: Geophysics, 18, 605-635.

Farquharson, C., Oldenburg, D., Haber, E., and Shekhtman, R., 2002, An algorithm for the three-dimensional inversion of magnetotelluric data: SEG Expanded Abstracts 21, 649-652.

Haber, E., and Heldmann, S., 2007, An octree multigrid method for quasi-static Maxwell's equations with highly discontinuous coefficients: Journal of Computational Physics, 223, 783-796.

Holtham, E., and Oldenburg, D., 2010a, Three-dimensional inversion of ZTEM data: Geophysical Journal International, 182, 168-182.

Holtham, E., and Oldenburg, D., 2010b, Three-dimensional inversion of MT and ZTEM data: SEG Expanded Abstracts 29, 655-659.

Lo, B., and Zang, M., 2008, Numerical modeling of Z-TEM (airborne AFMAG) responses to guide exploration strategies: SEG Expanded Abstracts 27, 1098-1102.

Saad, Y., 2003, Iterative methods for sparse linear systems: SIAM, 2nd Edition, 528p.

Ward, S., 1959, AFMAG - Airborne and Ground: Geophysics, 24, 761-787.

Response estimation in natural EM fields surveys

John Kingman [1]

[1] *Newmont Mining (john.kingman@newmont.com)*

Abstract

Two topics are reviewed:

- the impact of noise and cross-referencing in response estimation, and
- spectral estimation approaches

Measurement noise can propagate into natural-field EM (NFEM) impedance estimates in surprising ways. In addition to impacting repeatability or standard error statistics, it can, more insidiously, bias estimates – yielding incorrect results but with no evidence of such in the repeatability statistics. How least-squares estimation approaches can lead to bias is well documented but bias can still be present even when employing response estimation algorithms that are frequently considered to be "un-biased", including those that incorporate cross-reference approaches.

The complexity of how signal, noise, sensor distortion and impedance estimation interact can be daunting. However, reasonable models for signal and noise are shown to indicate that a poor signal-to-noise frequency band may commonly exist around 0.1 Hz, primarily owing to electrode noise. Noisy magnetic-field measurements, as the impedance denominator term, can be particularly menacing when noise is comparable to signal in amplitude and lead to extremely poor impedance estimates. Jackknife approaches to discovering and weeding outliers is strongly encouraged as a standard practice.

The use of remote-reference measurements is frequently misunderstood. Such data do not serve noise cancellation purposes in a subtractive sense. Noise in local measurements of interest can be attenuated if it is not correlated/coherent with noise at the remote sites, but not completely cancelled. More importantly, remote-reference data also serve to remove bias in impedance estimates by precluding the use of auto-spectral terms. Without some sort of cross-referencing whether remotely located or not to avoid the use of auto-spectra, no amount of averaging will reduce the bias in the final impedance estimates.

One of the most challenging aspects of NFEM processing is that of spectral estimation of non-periodic data. For approaches involving discrete Fourier transforms, the choice of leakage-mitigating window shape is important. The practitioner should balance frequency resolution and bias concerns by considering the impact of time-domain windowing as a convolution operator in the frequency-domain. Narrower, more heavily tapered windows provide wider convolution operators in the frequency-domain and more frequency smoothing - potentially too much smoothing! Furthermore, windows need not be strictly bell-shaped but can reflect quasi-sinusoidal or other shapes. Since log-scale frequency resolution (e.g., the number of impedance estimates per decade) provides the most meaningful information, a single window design for all frequency ranges may not always serve well. The Thomson multi-taper spectral estimation approach (Thomson, 1982), employing multiple different and orthogonal windows, provides a robust range of independent/orthogonal window choices.

Employing more than one window design in spectral and NFEM impedance estimation is encouraged as a general practice. A given window may yield less bias than another, so multiple estimates reflecting different windowing schemes can help provide information regarding the possibility of bias in response estimates. Pre-whitening of data before transforming them to the frequency domain usually improves the impedance estimation accuracy for higher-frequency bands (i.e., many periods per ensemble) and helps to "balance" the differences between different windows. Using different algorithms, such as direct impedance (E/H) and indirect admittance (H/E) estimators, will often illuminate bias problems. A rigorous system of not only monitoring repeatability statistics but also monitoring indicators of response bias is encouraged as a standard practice.

Noise propagation in impedance estimates

Impedance in the context of NFEM measurements refers to the relationship between electric fields (E), posed as response terms, and magnetic fields (H), posed as the input or excitation, and is generally represented by the symbol Z (Cagniard, 1953; Tikhonov, 1950). The physical units of impedance are ohms or V/m:

$$\begin{bmatrix} E_x \\ E_y \end{bmatrix} = \begin{bmatrix} Z_{xx} & Z_{xy} \\ Z_{yx} & Z_{yy} \end{bmatrix} \begin{bmatrix} H_x \\ H_y \end{bmatrix} . \qquad (1)$$

Bias in the context of NFEM impedance estimates implies that the true errors do not diminish with increased averaging or repeated measurements, although the indicated standard repeatability errors may falsely indicate improving statistics.

The manner in which noise in electric field and magnetic field measurements propagates into impedance estimates can be complicated and often surprising. Several related points of interest:

- If the signal-to-noise ratio (SNR) in magnetic field measurements is greater than or equal to 1.0, then clearly there is the chance for the averaged spectra in the numerator term to occasionally be small, statistically speaking, whereby the noise will be amplified in the impedance estimate.
- Least-squares response estimation approaches involve averaging of auto-spectra. The noise in local measurements will not be averaged out unless cross-reference data whose noise is uncorrelated with the noise in the local measurements of interest are used ("cross referencing" or remote referencing"), and thus, these approaches will produce biased impedance estimates (Cagniard, 1953; Simpson and Bahr, 2005).
- It is perhaps surprising that the use of response estimation algorithms not involving auto-spectra (e.g., simply dividing repeated E and H complex values and averaging the results) will still yield biased impedance estimates stemming from noise in the magnetic field data unless this noise is attenuated by using cross-reference data whose noise is uncorrelated with the noise in the local measurements of interest.
- The most effective way of minimizing bias in impedance estimates is by the use of cross-reference data which have noise that is not correlated with the noise in the local measurements of interest.
- In addition to mitigating bias, remote cross referencing will statistically reduce impedance-estimate noise, providing the cross-reference data are low-noise measurements themselves. This improvement in signal-to-noise is generally less than a factor of two and should not be confused with the results of algorithms associated with subtractive telluric noise cancellation in controlled-source applications. The latter can reduce noise by orders of magnitude but cross-referencing in natural-field EM (NFEM) methods never yields these levels of improvement. The primary advantage of employing remotely-located cross-reference data is to reduce bias in impedance estimates.

In general, it is simpler to demonstrate the behaviour described above via Monte Carlo approaches rather than working out the governing equations. Figure 1 through Figure 5 illustrate results obtained with least-squares, single impedance term estimates with various types and sizes of noise. Appendix A provides a description of the noise propagation technique employed here. The bias directions indicated depend primarily on the phase and amplitude of the true impedance.

Figure 6 through Figure 11 show impedance estimation errors comparing cross-referenced results to estimates not employing least-squares minimization. As shown for the stronger noise cases, bias is still a concern even in algorithms that are usually considered as being bias-free.

Applying the same randomized Monte Carlo approach, the error in the impedance amplitude, including both noise and bias effects, is estimated in Figure 12 for data with the following assumptions:

- H-field signal follows f^{-2} below 0.1 Hz and 5×10^{-7} A•m^{-1}•Hz$^{-1/2}$ above 0.1 Hz,
- H-field noise tracks that of typical flux-feedback induction coils: f^{-1} below 0.3 Hz and 20×10^{-15} T•Hz$^{-1/2}$ above 0.3 Hz,

- E-field signal follows that implied by the H-field signal, with a half-space resistivity is 100 Ω•m, and
- E-field noise follows f^{-1} below 0.1 Hz and $4x10^{-8}$ $V•m^{-1}•Hz^{-1/2}$ above 0.1 Hz, again with a half-space resistivity of 100 Ω•m.

Interestingly, for the given assumptions, there is an impedance signal-to-noise low at roughly 0.1 Hz. It is plausible that the data quality problems that typify that frequency band (0.02 – 0.5 Hz) may reflect noise in electric-field measurements more than the natural-field signal low there.

While this example emphasizes the impact of electric-field noise, circumstances whereby magnetic field noise dominates are also of concern. This is especially the case for the 300 Hz to 3 kHz dead band, owing to the leveraged impact of the magnetic field measurement as the denominator term in impedance estimates. When signal-to-noise in magnetic field measurements is roughly 1.0 or worse, it becomes imperative that jackknife-based sorting and outlier-removal scheme, or similar, be employed (Bradley, 1977).

While a great deal of emphasis has been placed on electrode noise from the perspective noise inherent to the electrodes themselves, little mention is given to the fact that, as often as not, electrode noise probably reflects mechanical stability of the environment and material (mud) surrounding the electrode. It is easy to demonstrate that a minute amount of slippage between the electrode and the contacting material, such as from drying or settling, can cause a substantial amount of noise. One further consideration, as suggested by the tests documented in the following figures, is that bias in spectral estimates when the signal period of interest is comparable to the time-series ensemble length (i.e., $1/5^{th}$ the time-series ensemble length or greater) may frequently overshadow sensor noise (See the following section “Multi-Taper Spectral Estimation”). The general subject of how noise propagates into NFEM impedance estimates merits further quantitative investigation.

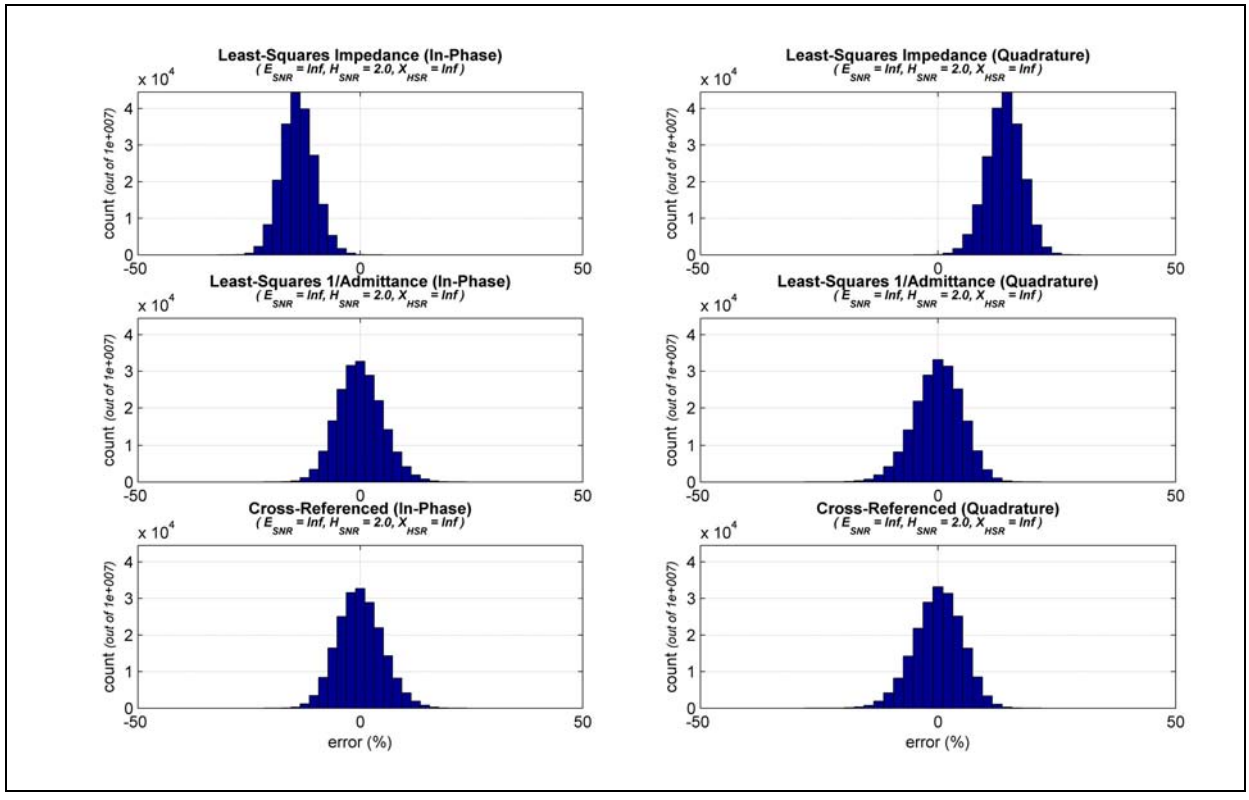

Figure 1. Impedance-estimate errors owing to noise in the magnetic-field measurements only. The bias directions in the least-squares impedance estimates reflect the true impedance phase and amplitude.

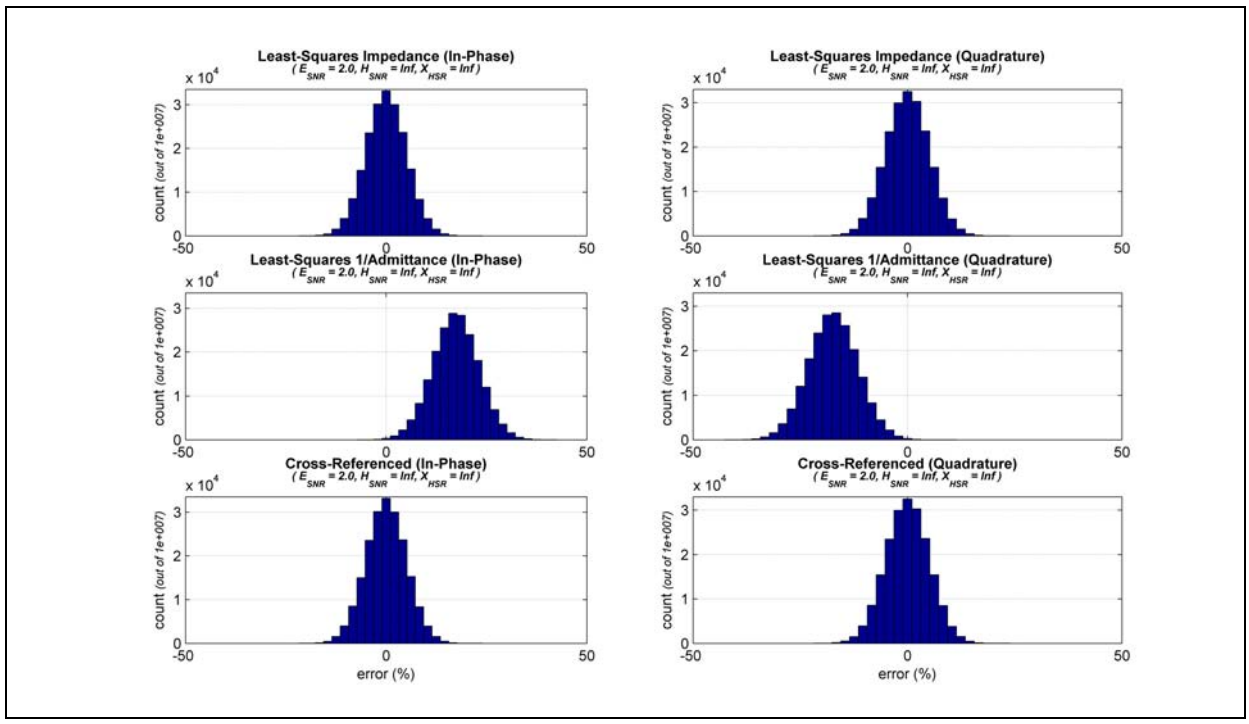

Figure 2. Impedance-estimate errors owing to noise in the electric-field measurements only. The bias directions in the least-squares admittance-based estimates reflect the true impedance phase and amplitude.

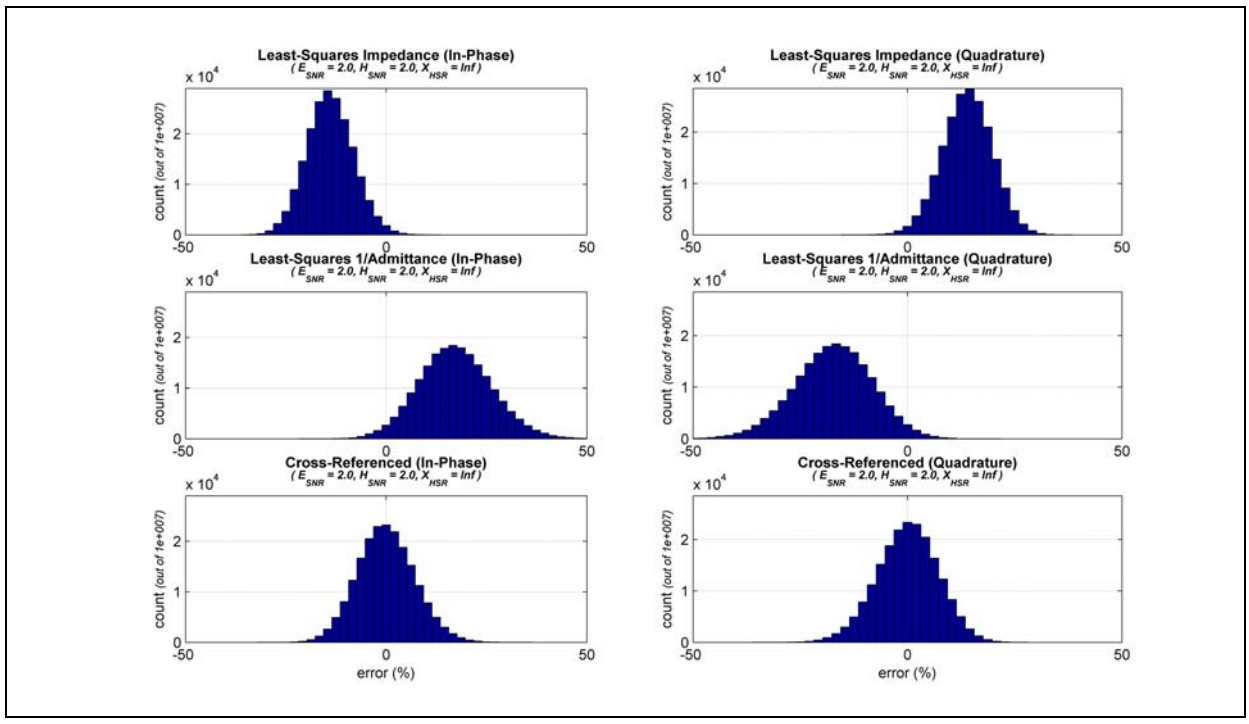

Figure 3. Impedance-estimate errors owing to noise in both the electric-field and magnetic-field measurements. The bias directions in the least-squares estimates reflect the true impedance phase and amplitude. The benefits of using a cross-reference are clearly shown.

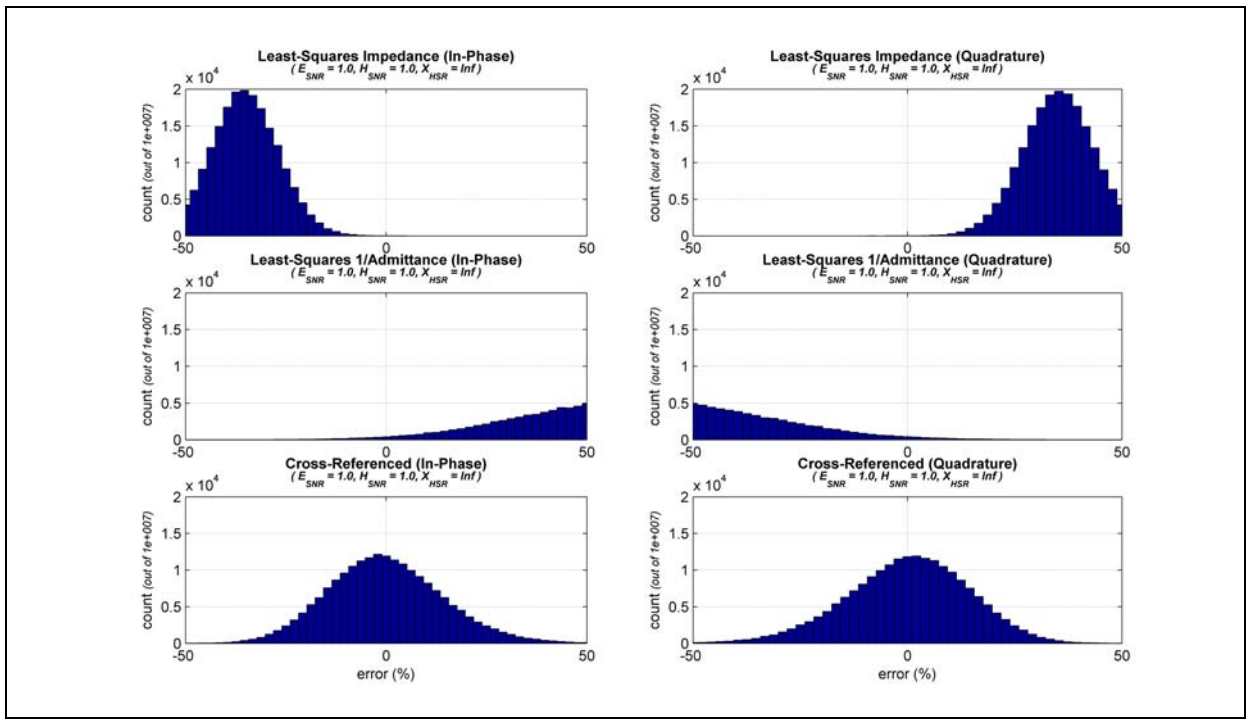

Figure 4. Impedance-estimate errors owing to noise in both the electric-field and magnetic-field measurements. The bias directions in the least-squares estimates reflect the true impedance phase and amplitude. The benefits of using a cross-reference are clearly shown.

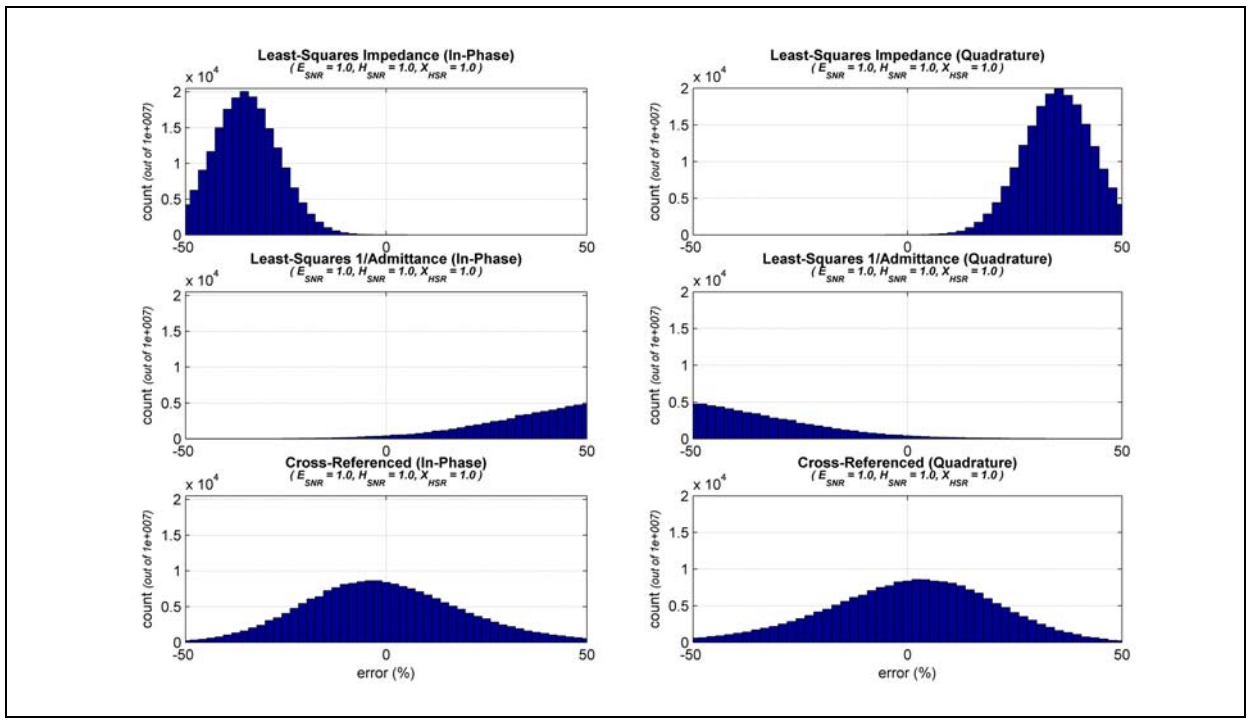

Figure 5. Impedance-estimate errors owing to substantial noise in all measurements, including the cross-reference. The bias directions in the least-squares estimates reflect the true impedance phase and amplitude. The benefits of using a cross-reference, even when it suffers noise that is equal in magnitude to the natural-field signal, are clearly shown. A small amount of bias is evident in the cross-referenced results.

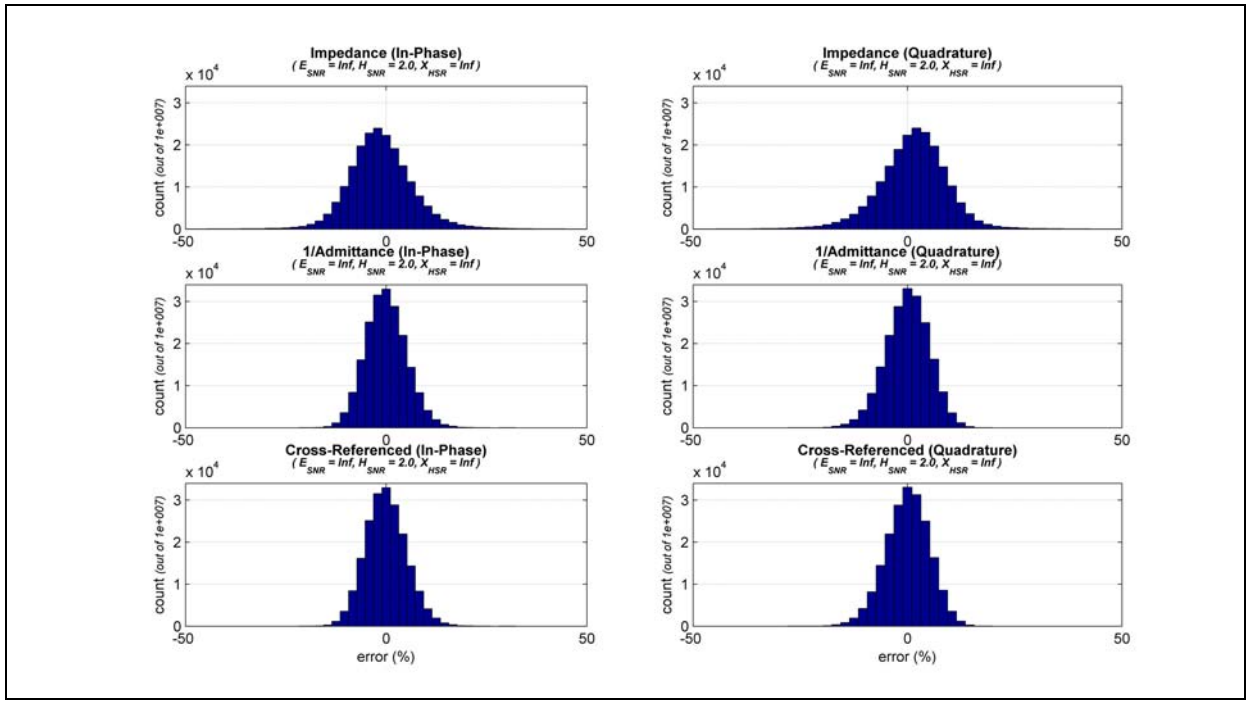

Figure 6. Impedance estimates that do not employ least-squares solutions are compared with cross-referenced results. In this case noise is in the magnetic-field measurements only.

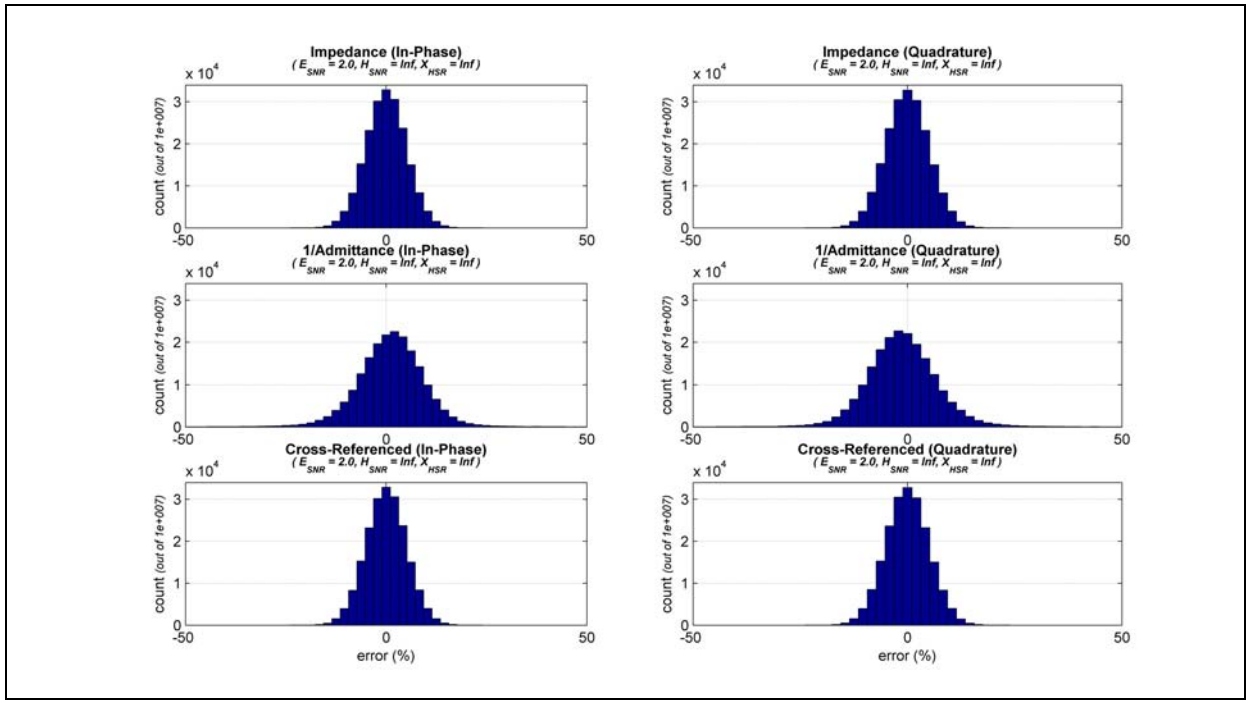

Figure 7. Impedance estimates that do not employ least-squares solutions are compared with cross-referenced results. In this case noise is in the electric-field measurements only.

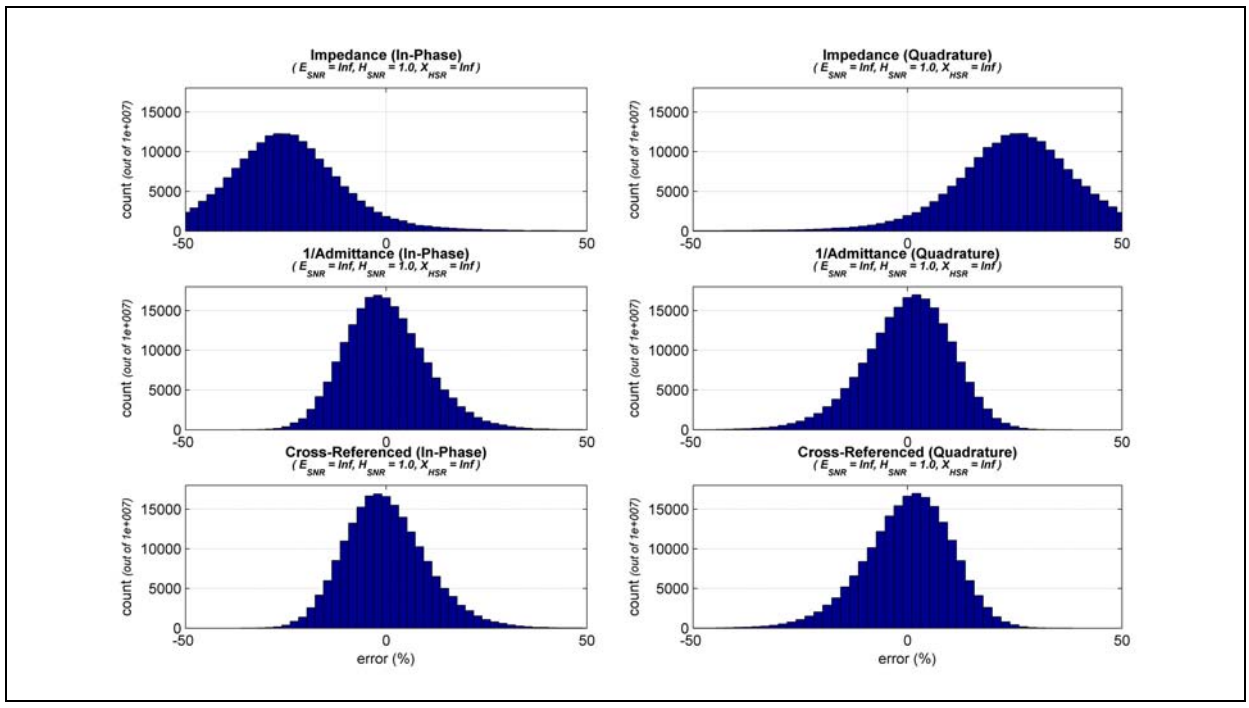

Figure 8. Impedance estimates that do not employ least-squares solutions are compared with cross-referenced results. In this case noise is in the magnetic-field measurements only and elevated as compared with those shown in Figure 6. Note the small amount of bias in the cross-referenced results.

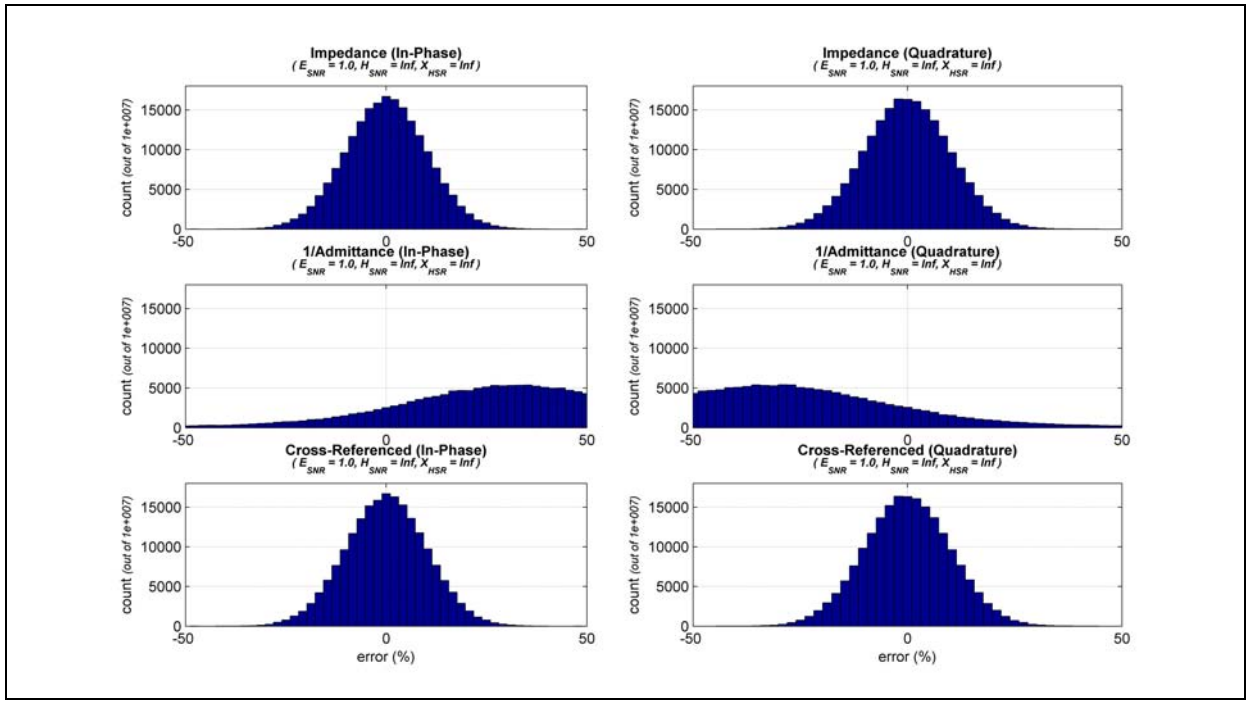

Figure 9. Impedance estimates that do not employ least-squares solutions are compared with cross-referenced results. In this case noise is in the electric-field measurements only and elevated as compared with Figure 7. Note the substantial bias and low signal-to-noise in the admittance-based results.

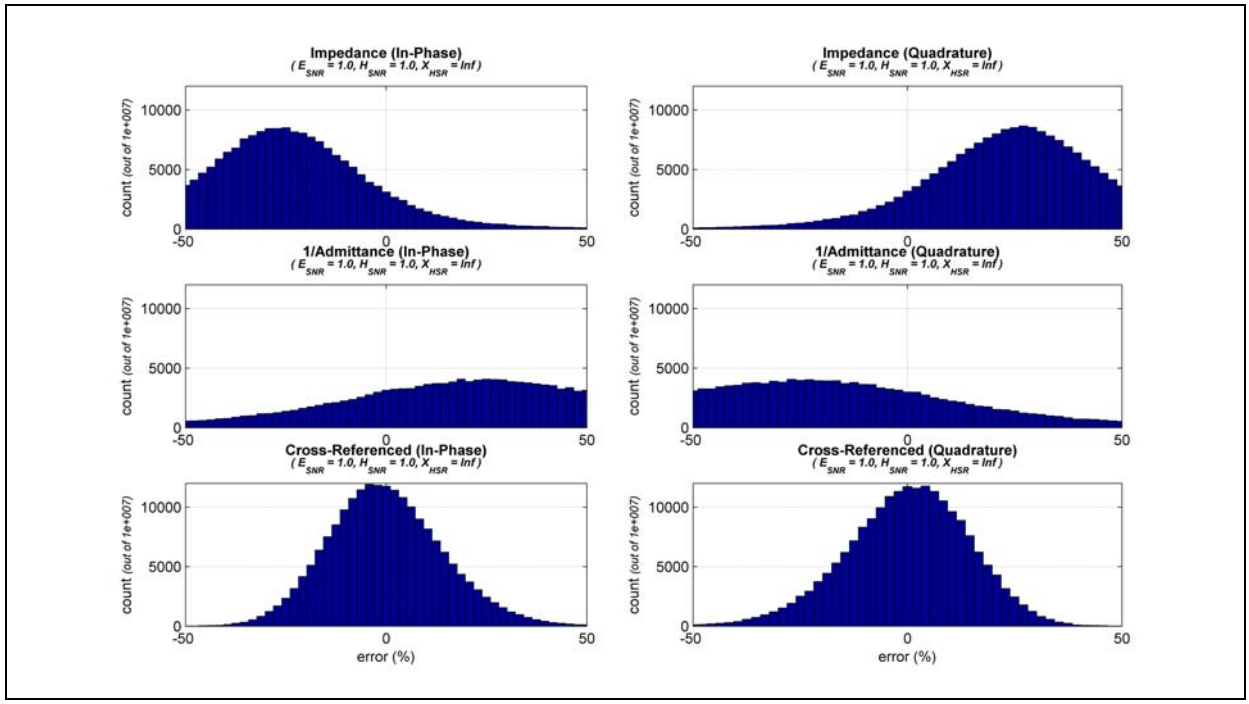

Figure 10. Impedance estimates that do not employ least-squares solutions are compared with cross-referenced results. Substantial noise is present in both electric-field and magnetic-field measurements.

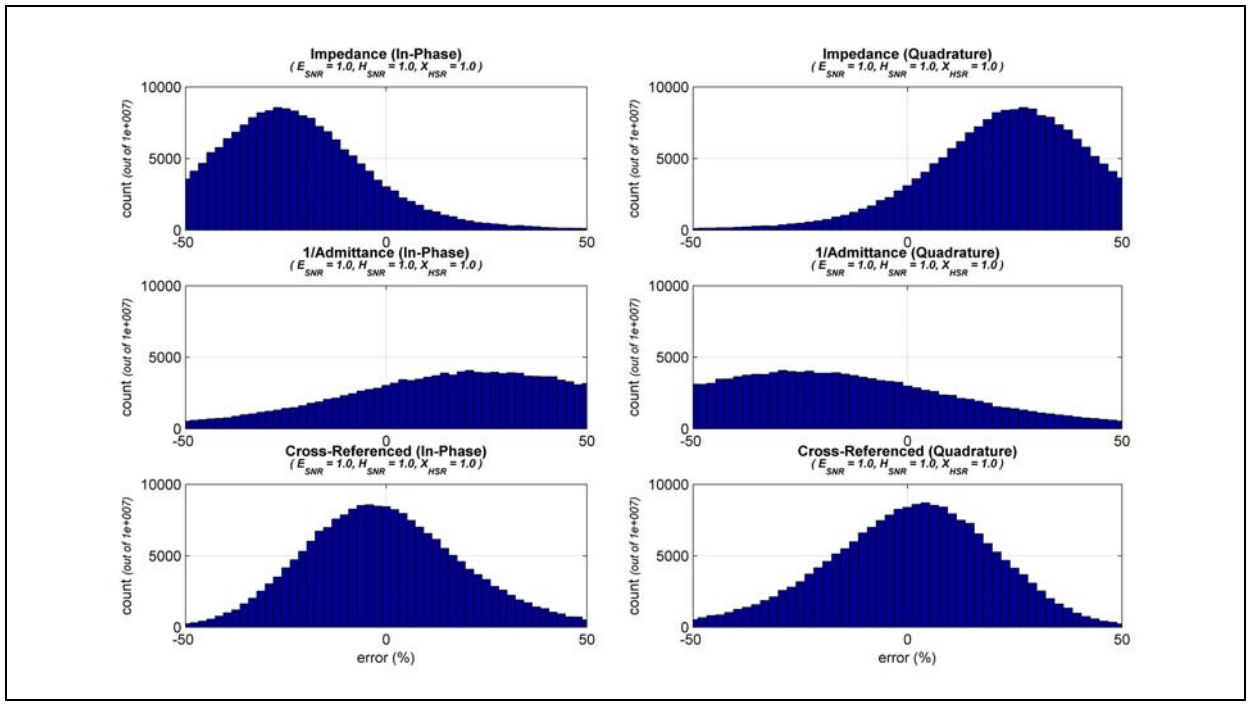

Figure 11. Impedance estimates that do not employ least-squares solutions are compared with cross-referenced results. Substantial noise is present in all measurements. A small amount of bias is evident in the cross-referenced results.

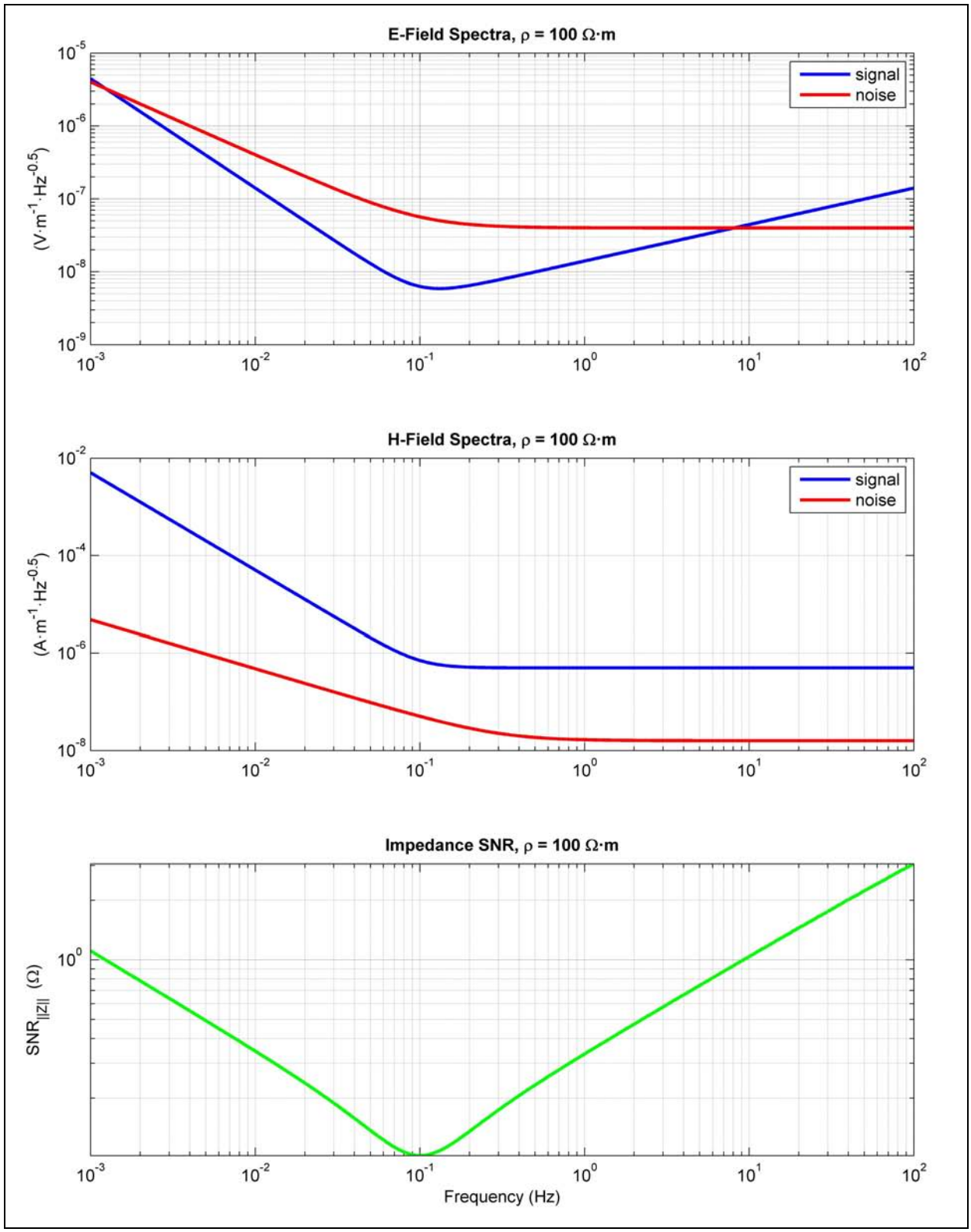

Figure 12. Impact of sensor noise (E-Field and B-Field) on amplitude error in impedance estimates for the given signal levels. The signal and noise level specifics are provided in the preceding text. SNR in the lower graph implies amplitude errors including both bias and repeatability components.

Multi-Taper Spectral Estimation

One of the more challenging aspects of estimating impedances or E/H responses from natural-field EM (NFEM) data stems from the lack of periodicity in the data. Fourier transforms, applied directly to aperiodic measured data, are poorly suited for spectral analysis purposes. The use of time-domain windows is a well-established and somewhat effective approach to mitigating the problems associated with spectral analyses of aperiodic data. There are a large number of popular windows typically employed in various applications, including Hanning, Hamming, Kaiser, Tukey and others (Bendat and Piersol, 1986; Harris, 1978; Oppenheim et al., 1999).

An important perspective to the understanding of windowing is that time-domain windowing equates to convolution of the Fourier Transform of the window in the frequency domain. We are interested in the following basic frequency-domain properties of time-domain windows:

- passband width, and
- stopband depth.

Windows that are heavily tapered (i.e., more heavily weighted towards their center) are characterised by a broader passband and deeper stopband. Wider or less-tapered windows (i.e., the boxcar or uniformly weighted window is the least-tapered possible) are characterized by a narrower passband and shallower stopband. This character is illustrated in Figure 13 below.

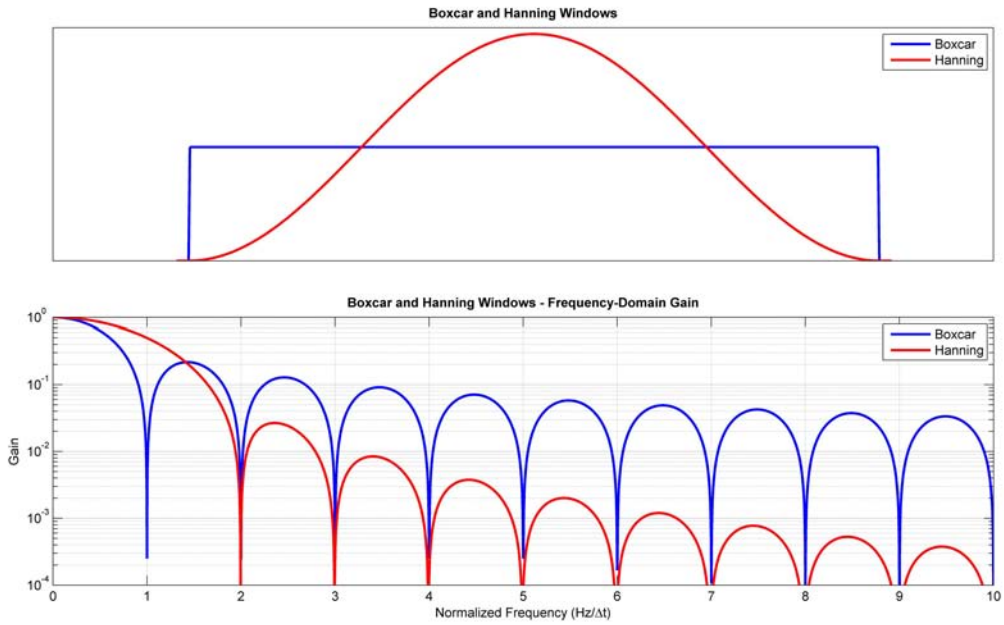

Figure 13. Time and frequency domain representations of the gain characteristics of boxcar (uniform) and Hanning windows. The boxcar window yields a narrower passband and shallower stopband depth. As a convolution operator in the frequency-domain, the spectral character of time-domain windows should be considered in choosing which windows serve best.

A heavily tapered window will provide some degree of frequency averaging: the greater the taper the more frequency averaging, but at the same time, the greater the likelihood of too much averaging and resulting bias at lower frequencies. The practitioner should become familiar with these perspectives regarding the application of time-domain windows in balancing spectral leakage against frequency-smearing concerns.

Consideration of these window perspectives suggests that a given window may be optimal for a given frequency band, but it will therefore almost certainly not be optimal for a substantially different frequency band. For example, heavily tapered windows, while appropriate for high frequency bands, will be inappropriate for periods that are commensurate with the record or ensemble length. This observation gives rise to the notion of employing multiple windows in estimating NFEM impedances.

The term “multi-taper” usually refers to a spectral estimation approach first proposed by David Thomson in 1982 (Thomson, 1982). The approach is popular with some in NFEM circles (Prieto et al., 2007) and involves “Slepian” or discrete prolate spheroidal sequences (DPSSs). Two parameters are required to define a set of DPSSs: the sequence or window lengths, and the half-time-bandwidth product. The larger the half-time-bandwidth, the greater the degree of taper as shown in Figure 14.

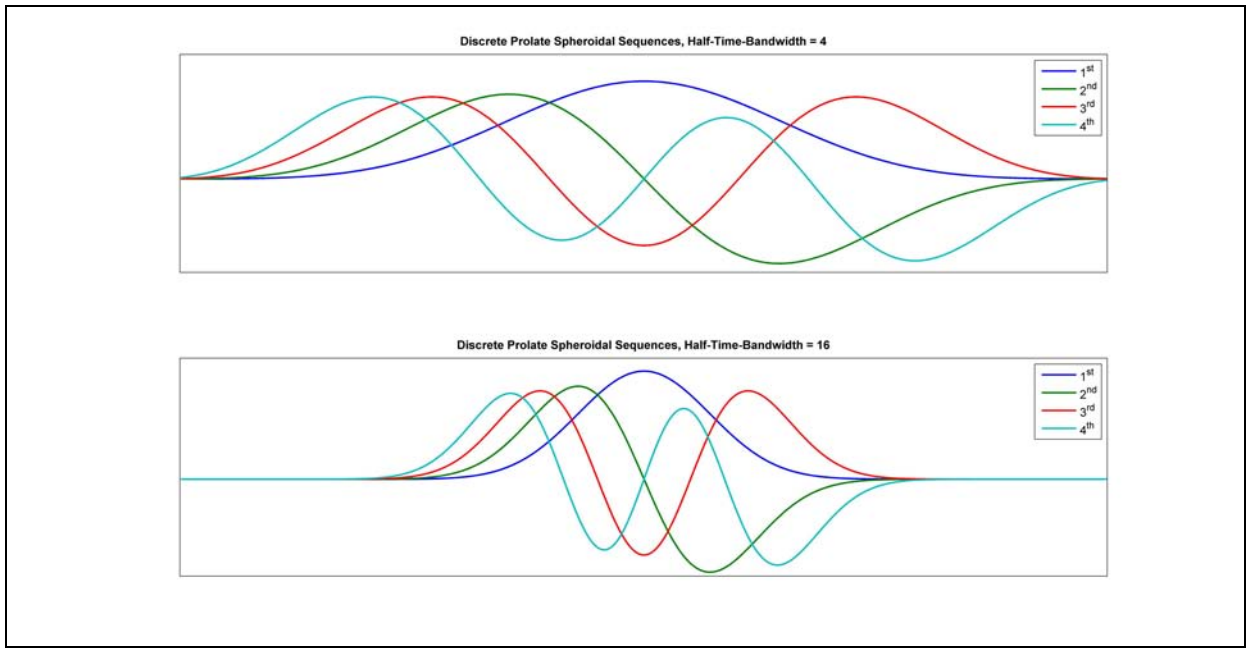

Figure 14. The first four Slepian windows are shown for half-time-bandwidths of 4 and 16. The greater half-time-bandwidth windows are basically just compressed versions of the lesser half-time-bandwidth sequences and as such, reflect frequency-scaled spectral gain versions of each other.

An important feature of DPSSs is that all windows in a given set are orthogonal to each other. Hence, the different results for a given DPSS-windowed time-series will show some degree of independence from each other. Conceivably a given DPSSs window and half-time-bandwidth choice will be optimal for a given frequency band and time-series character. There are no hard and fast specific rules for determining which window is best for a given frequency band of interest. Generally, however, one should set the effective time-bandwidth product of the window(s) such that the resulting degree of frequency averaging in the frequency-domain is commensurate with the width of the frequency band of interest.

A large number Monte Carlo runs, involving synthesized NFEM-like signals, were completed to test the utility of the DPSSs as compared with results employing a more standard window (i.e., Hanning). Details of the spectral estimation testing approach employed here are given in Appendix B. Histograms of the errors of repeated estimates are presented based on the difference between the impedance estimates and the known correct value. The results were mixed, being favorable towards the DPSSs for low frequencies (4 periods per ensemble) and less favorable for higher frequencies (320 periods per ensemble). Figure 16 and Figure 17 show low-frequency results (i.e., one period equal to ¼ of the ensemble length) whereby the first two DPSSs served substantially better than a Hanning window. Cross-referencing was not employed in these tests. Results for un-whitened data are shown in Figure 17.

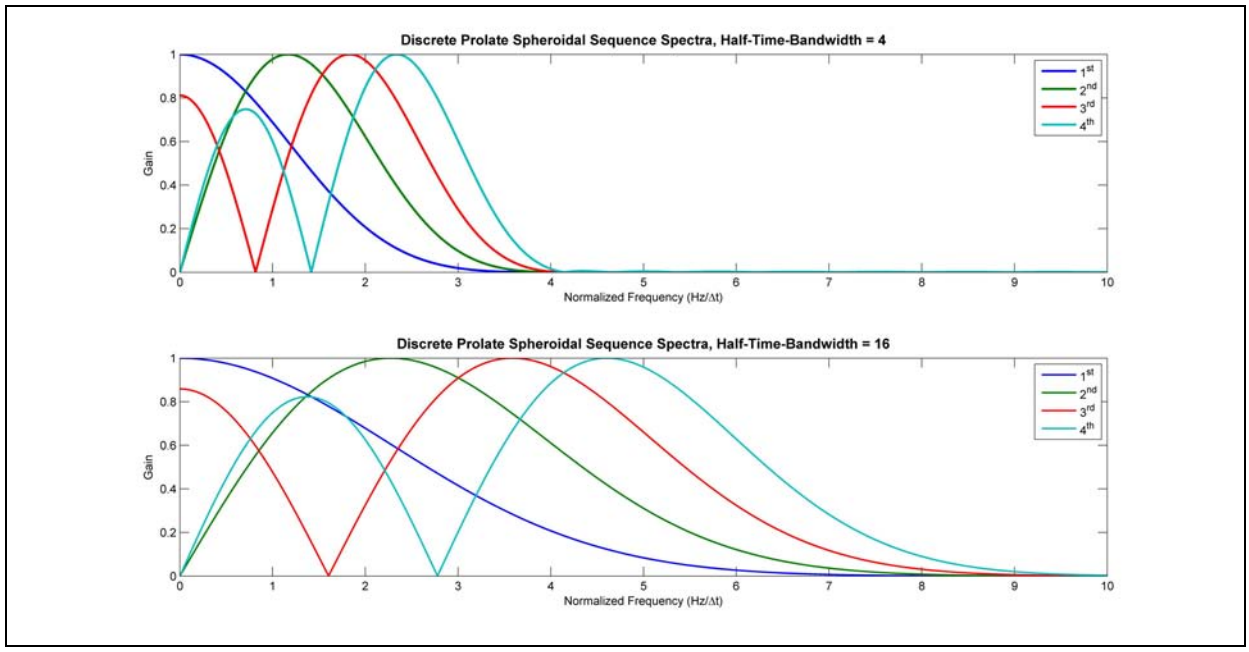

Figure 15. Spectral amplitude (gain) character of the Slepian windows (DPSSs) shown in Figure 14. The frequency shift of the higher-order sequences/windows bears consideration. Given that the windows act as frequency-domain convolution operators, and providing the same window is applied to all time-series ensembles used in the impedance estimate, the related frequency shift should not bias nor otherwise invalidate the impedance estimate.

The advantages of DPSSs were less evident when working at higher frequencies or more periods per time-domain ensemble, when multiple frequencies are averaged in order to accommodate the logarithmically-spaced frequency resolution that is meaningfull to NFEM data. In Figure 18 and Figure 19, the ensemble length reflects 320 periods of the frequency of interest. Thirty-two frequencies were averaged (i.e., the frequency is (320 ± 32)/(ensemble length)). Pre-whitening by taking the first digital derivative improved the repeatability as shown in Figure 18 and Figure 19.

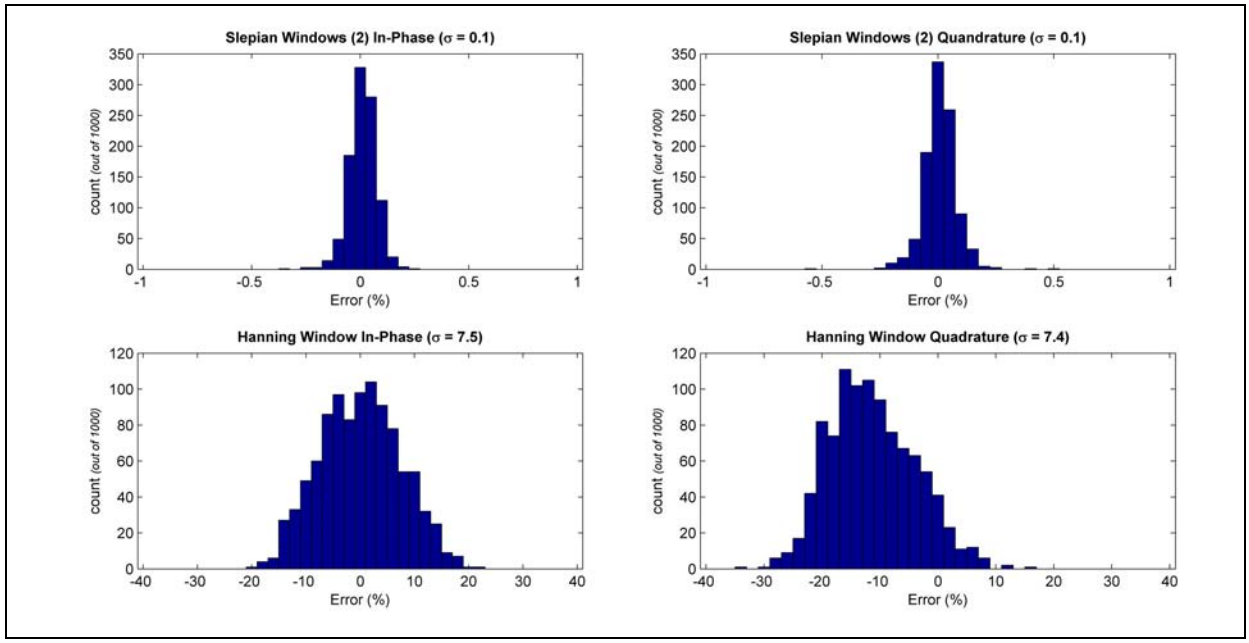

Figure 16. Slepian (DPSSs) vs. Hanning window results are shown for these specifications: impedance frequency equal to 4/ensemble length (i.e., 4 periods per ensemble), half-time-bandwidth equal to 4, first two Slepian windows used, and the time-series data were "pre-whitened by taking the first digital derivative.

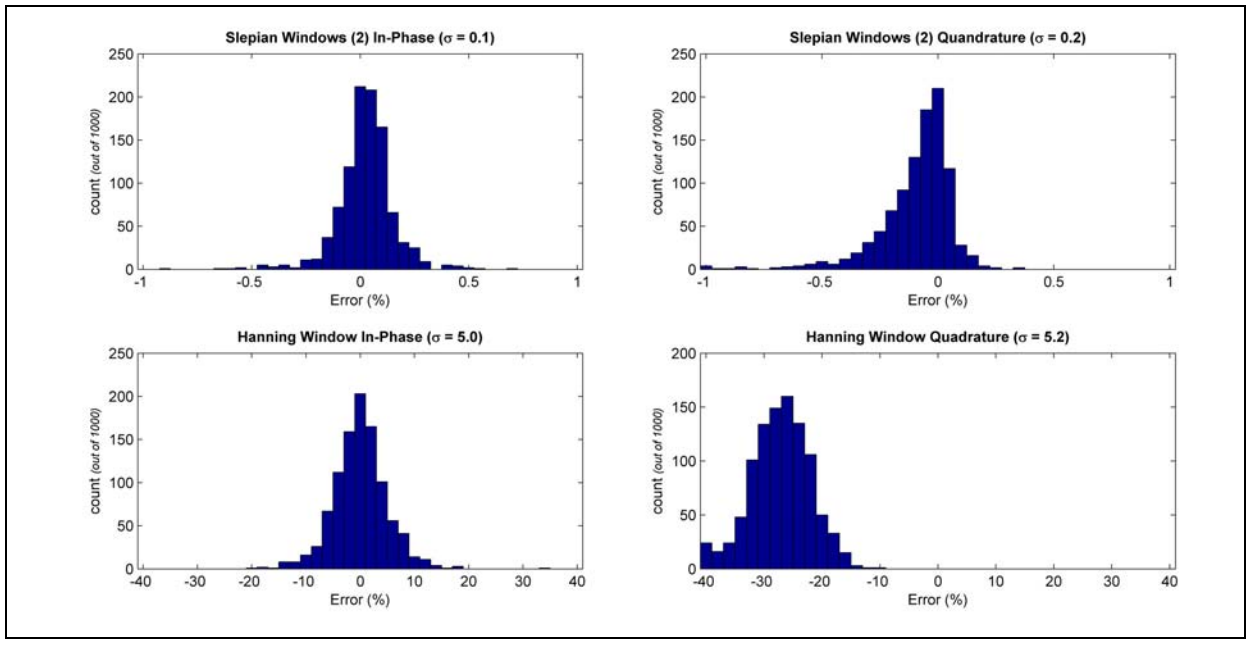

Figure 17. Slepian (DPSSs) vs. Hanning window results are shown for these specifications: impedance frequency equal to 4/ensemble length (i.e., 4 periods per ensemble), half-time-bandwidth equal to 4, and use of the first two Slepian windows. The data were not pre-whitened as in Figure 16.

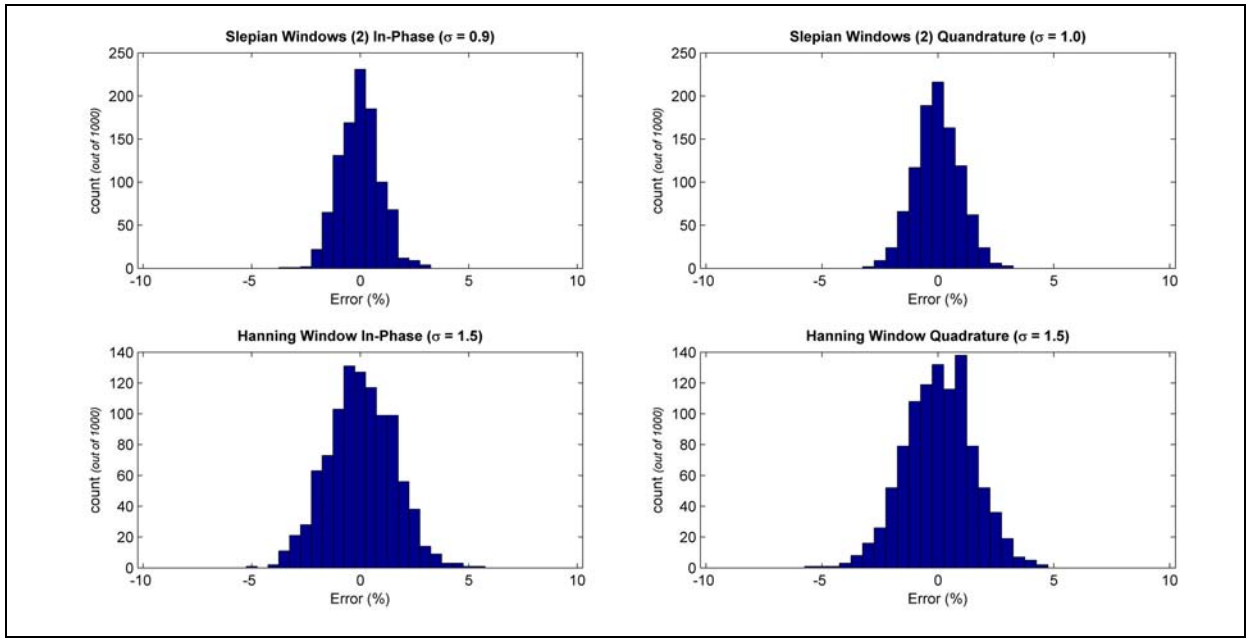

Figure 18. Slepian vs. Hanning window results are compared for a frequency band equal to (320 ± 32)/Δt where Δt is the ensemble length. The half-time-bandwidth was 16, producing 32 DPSSs. The median of the first 30 DPSS results was employed as the best multi-taper estimate. The data were pre-whitened by taking the first digital derivative of all data involved.

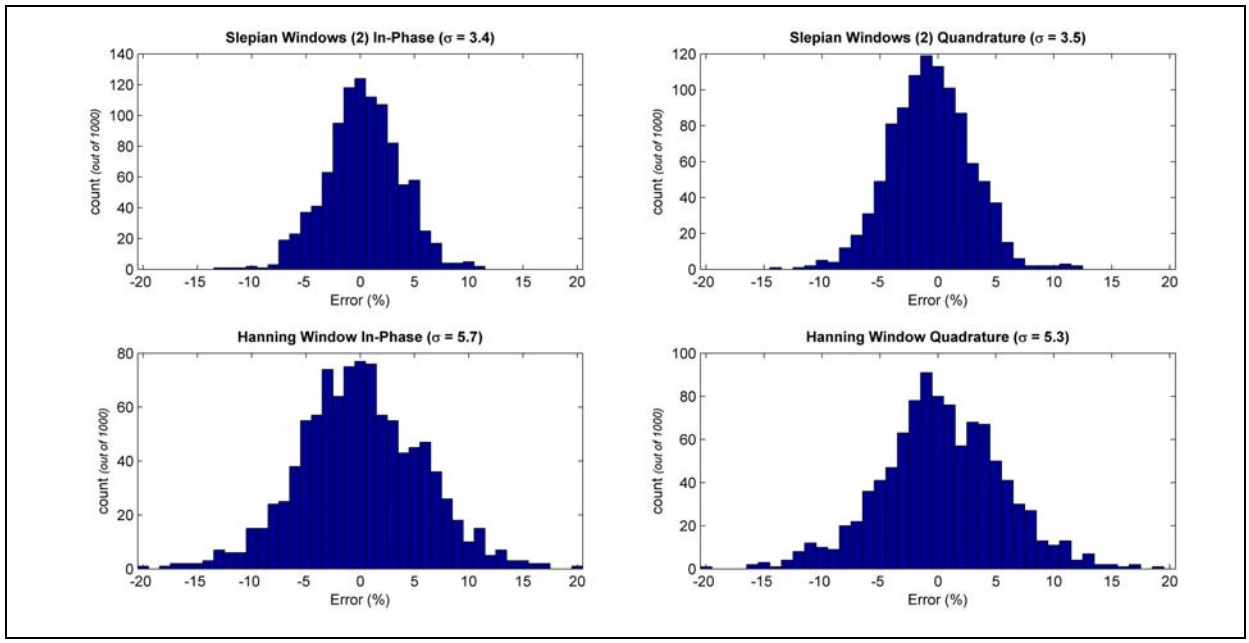

Figure 19. Slepian vs. Hanning window results are compared for a frequency band equal to (320 ± 32)/Δt where Δt is the ensemble length. The half-time-bandwidth was 16, producing 32 DPSSs. The median of the first 30 DPSS results was employed as the best multi-taper estimate. These data were not pre-whitened and show reduced repeatability as compared with the pre-whitened data in Figure 18.

While the Thomson spectral estimation approach (i.e., DPSSs) did not demonstrate consistent advantages in the tests documented herein, the testing did show that different windows can yield significantly different spectral estimation results when aperiodic data are used. This points us to an approach for recognizing the potential for bias in NFEM impedance estimates and possibly minimizing that bias. While cross-referencing is an extremely powerful approach for mitigating bias, it still does not fully guarantee against this bias. A general approach whereby multiple algorithms employing different windows, and both impedance (E/H) and admittance (H/E) based estimators, is encouraged.

References

Bendat, J. S., and Piersol, A. G., 1986, Random Data: Analysis and Measurement Procedures: Wiley Interscience, 2nd edition, NY.

Bradley, E., 1977, Bootstrap Methods: Another Look at the Jackknife: Technical Report No. 32, Division of Biostatistics, Stanford University

Cagniard, L., 1953, Basic theory of the magneto-telluric method of geophysical prospecting: Geophysics, 18, 605-635.

Harris, Fredric J., 1978, On the use of Windows for Harmonic Analysis with the Discrete Fourier Transform: Proceedings of the IEEE, 66, 51-83.

Oppenheim, Alan V., Schafer, Ronald W., Buck, John A., 1999, Discrete-time signal processing: Prentice Hall, pp 870. (Especially pp 468–471)

Prieto, G. A., Parker, R. L., Thomson, D. J., Vernon, F. L., and Graham, R. L., 2007, Reducing the bias of multi-taper spectrum estimates: Geophysical Journal International, 171, 1269-1281.

Simpson, F., and Bahr, K., 2005, Practical Magnetotellurics: Cambridge University Press.

Thomson, David J., 1982, Spectrum estimation and harmonic analysis: Proceedings of the IEEE, 70, 1055–1096.

Tikhonov, A. N., 1950, The determination of the electrical properties of deep layers of the Earth's crust: Dokl. Acad. Nauk. SSR, 73, 295-297.

Appendix A - Noise propagation testing approach

The impact of measurement noise in NFEM impedance estimates was explored using statistically randomized Monte Carlo tests, run within the MATLAB technical programming environment. The approach employed is described below:

1. The true impedance was locked at unity amplitude and 45 degrees phase (i.e., $\sqrt{2} + j\sqrt{2}$).
2. Electric field (E), magnetic field (H) and cross-reference signals were generated to reflect constant amplitude (unity) but random phase. The amplitude ratios and phase differences between E and H were held constant to reflect the impedance. Similarly the amplitude ratios and phase differences between either E or H and the cross-reference were fixed prior to the addition of noise.
3. Specified levels of noise, as indicated in the titles of Figure 1 through Figure 11, were generated with constant amplitude but randomized phase.
4. Impedance estimates were made averaging batches of 50 repeated measurements using these five different algorithms:

$E_i = Z \cdot H_i$ least-squares impedance

$H_i = \left(\frac{1}{Z}\right) E_i$ least-squares admittance-based

$\frac{\sum_{1}^{50}\left(\frac{E_i}{H_i}\right)}{50}$ "un-biased" impedance straight averaging

$\frac{50}{\sum_{1}^{50}\left(\frac{H_i}{E_i}\right)}$ "un-biased" admittance-based straight averaging

$\frac{\sum_{1}^{50}\left(E_i \cdot X_i^*\right)}{\sum_{1}^{50}\left(H_i \cdot X_i^*\right)}$ cross-referenced averaging

5. The batches of 50 were repeated 10^6 times and the error or complex difference between the impedance estimate for each batch and the true impedance calculated.
6. Histograms based on step 5 above were generated for the noise specifications and algorithm of interest.

Appendix B - Spectral estimation testing approach

The impact of different windowing schemes, including Slepian (also known as discrete prolate spheroidal sequences) multi-taper windows (Thomson,1982) and Hanning windows, was tested using the approach described below using the MATLAB technical programming environment:

1. Natural-field EM signal data (electric and magnetic fields) were synthesized to reflect typical real spectral amplitudes and a regular/smooth frequency-dependent impedance character. Data for single output (E) and two inputs (H_a, H_b), and thus two different impedances, were synthesized. A small amount of 50 Hz power-line noise was added to the data, otherwise they were noise-free. The record lengths were 256 s and associated sampling rate was 400 samples-per-second.
2. For a specified frequency-band of interest 0.125 ± 0.0156 Hz and 10 ± 0.5 Hz, the impedances were estimated using frequency-averaging reflecting the frequency-band widths. For the 0.125 Hz data (i.e., 4 periods per ensemble) this equated to no frequency-sample averaging except for that provided by the windowing. For the 10 Hz data, the frequency averaging, with a spectral resolution of 1/32 Hz, spanned 33 frequencies.
3. 256 minute records were rearranged into overlapping ensembles of length 32 s and the offsets removed.
4. The ensembles were windowed, multiple different windows being employed including Slepian sequences, and Fourier transformed (digital Fast-Fourier Transform). In the case of the 0.125 Hz data, a Slepian half-time-bandwidth product of 4 was chosen, and only the first two sequences/windows were employed in the averaging. For the 10 Hz data, a Slepian half-time-bandwidth product of 16 was employed, yielding 32 different and orthogonal windows. However, only the first 29 of those were employed in the median-based averaging (see below).
5. For the given frequency-band of interest, the impedance for each individual frequency within the band was estimated using the least-squares impedance estimation approach (Note: cross-referencing was not employed in these calculations):

   $$E_i = Z_a \cdot H_{a,i} + Z_b \cdot H_{b,i}$$

   While data for a single impedance tensor row (see equation (1)) were synthesized and incorporated in the least-squares solutions, only the primary (Z_a) impedance results are presented in the figures.
6. The multiple Slepian windows were combined by searching for the median result from all windows. Note the specifications indicated in Step 4 above.
7. Results are displayed as the difference between the estimated and true impedances normalized to the magnitude of the true impedance, they are not scaled to percent:

   $$\frac{Z_{est} - Z_{true}}{\left|Z_{true}\right|}$$

8. Steps 1 through 7 were repeated 1000 times to provide the histogram statistics shown in Figure 16 through Figure 19.

Inverting ZTEM data in 3D: Process and Practice

Peter L. Kowalczyk [1] and Patrick B. M. Van Kooten [2]

[1] *Mira Geoscience Ltd., Advanced Geophysical Interpretation Centre, Vancouver, British Columbia, Canada (peterk@mirageoscience.com)*
[2] *Mira Geoscience Ltd., Advanced Geophysical Interpretation Centre, Vancouver, British Columbia, Canada (patrickv@mirageoscience.com)*

Summary

The Z-axis Tipper Electromagnetic system (ZTEM) is an airborne EM system that measures the tipper of natural magnetotelluric (MT) fields at frequencies from 30 Hz to 720 Hz (Legault et al., 2009). It is a passive system that measures both the along-line (X) and cross-line (Y) polarizations of the EM tipper. As such, the survey data are insensitive to flight-line direction.

The principal ZTEM response is from channelling of magnetotelluric (MT) currents through more conductive regions of the survey area (Vozoff, 1972). The system is well suited to mapping regional structures, large breccias and other features of moderate to low-conductivity which would otherwise be poorly mapped by active EM systems.

A plan map of the ZTEM Tipper measurement at a single frequency is intuitively straightforward to understand in that conductive features produce tilt-angle crossovers above the conductive axis of the feature. However, interpretation of these maps for multiple frequencies is less intuitive, since the real and quadrature components for two polarizations of each tipper will produce four maps for each frequency. Nonetheless, this problem is well suited to inversion since this process incorporates a consideration of all of the data acquired by the ZTEM system and will produce a modelled conductivity volume that is immediately useful for interpretation and for targeting drill holes.

We present an example of a ZTEM inversion in conjunction with the integrated interpretation of ZTEM, magnetic and ground-based Titan24 electrical data which has led to the discovery a new buried molybdenum porphyry prospect at the Silver Queen project of New Nadina Exploration Limited.

Introduction

ZTEM data acquired at the Silver Queen Project in northern British Columbia have been inverted to produce a 3D conductivity model. During the acquisition phase of the ZTEM survey, a magnetic data set was also acquired, and this was subsequently inverted to produce a magnetic susceptibility model. The resulting conductivity and susceptibility models were combined with a 3D model of the known vein type mineralization and previous drilling. Integrated interpretation of these results was then used to direct an exploration program comprising a Titan24 electrical survey followed by drilling. The electrical survey targeted blind mineralization in a structurally favourable, yet undrilled location proximal to the known mineralization. This exploration program has led to the discoverer of a significant zone of porphyry-style molybdenum mineralization.

Processing of ZTEM data is straightforward. Our practice is to interpolate ZTEM data as delivered to a grid format and then to inspect for regions of poor data. After deleting noisy or corrupted data, the data are prepared for inversion. We invert ZTEM data using the UBC-GIF group's MT3Dinv code package. This is an MT specific version of the more general UBC EH3Dinv code, with provision made for the plane wave MT source field assumption. We normally invert each frequency by itself and then use one of the results from a single frequency inversion as a starting model for a multi-frequency inversion considering all the data simultaneously.

In the following sections, we describe the process in more detail then illustrate this process applied in practice to aid exploration at a minerals prospect.

Data preparation and inversion

Prior to inversion, the data need to be reviewed, coordinate systems checked, bad data removed, a mesh designed, and errors assigned to the data. Then the data can be inverted, first using single frequency inversions to assess the quality of the data as well as the appropriate errors to assign, and then as a combined multi-frequency inversion done with all frequencies, or a selected subset thereof (Figure 1).

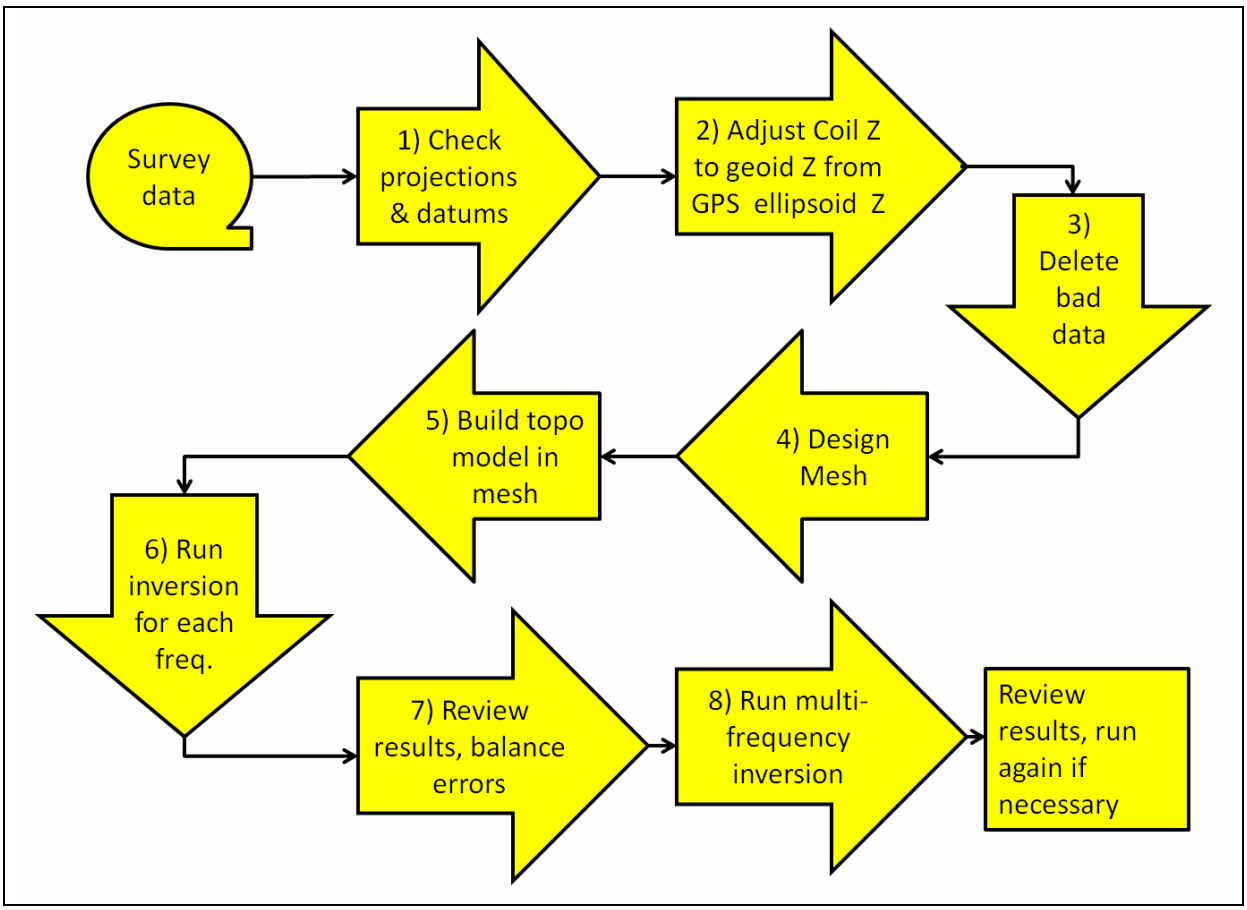

Figure 1. Chart illustrating the process workflow for a ZTEM inversion project. Note that both the single frequency and multi-frequency inversion may be run several times until a satisfactory result is achieved.

Datums and coordinate systems are an ongoing source of trouble. Generally the data are received in WGS84 UTM, with latitude and longitude in the database, and x, y, and z for the ZTEM receiver in the WGS84 UTM projection. However, the data can have the latitude, longitude, and elevation referenced to the WGS84 ellipsoid, and the XY coordinate in another projection (e.g., NAD27). As there are many possible variations, the user must exercise considerable caution. Another source of confusion is elevations. The coil Z is generally referenced to the ellipsoid, while topographic elevations are given with reference to the geoid (mean sea level). Differences in excess of 100 m can exist between elevations referenced to the ellipsoid and those referenced to the geoid. When building a digital elevation model from the GPS record of the aircraft position and the recorded laser/radar altimeter data, the user must ensure that the aircraft position used is an elevation referenced to the geoid. This is very important when building the topographic surface for use in an inversion project as the aircraft GPS position and laser/radar altimeter are often the best data or only data available for this task. When constructing the quantized topographic model, the effect of using large blocks to approximate the topography in steep terrain can result in a topographic model that is not optimum. Considerable differences may exist between the actual ground surface elevation and the top of the model used by the inversion algorithm. This effect is illustrated in Figure 2 and Figure 3.

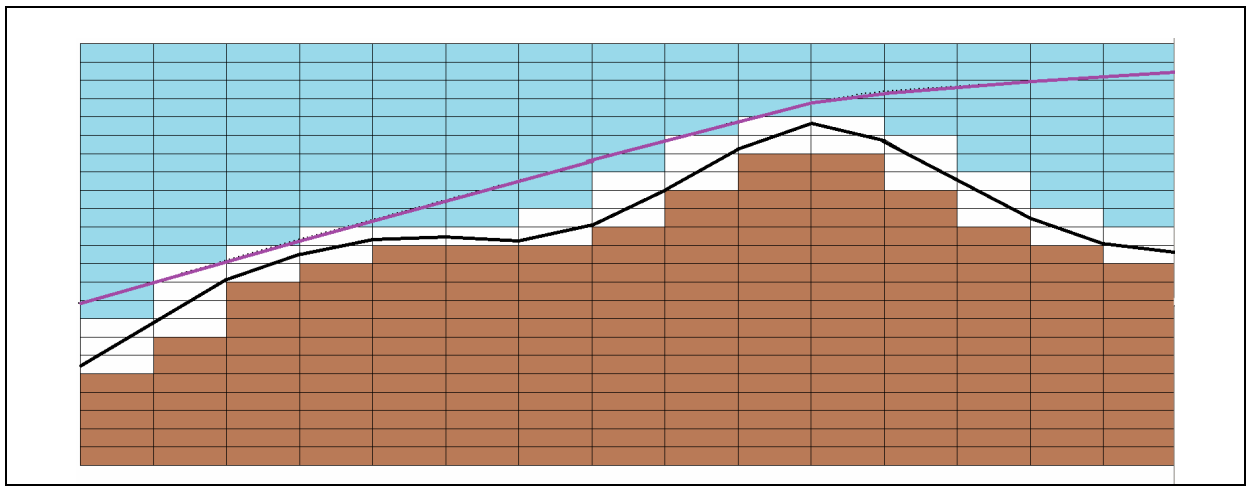

Figure 2. Shown is an example of a real flight (purple) and topographic surface (black) and a topographic model with 200m x 200m x 50m mesh cells. The MT3Dinv code will truncate the surface so no cell extends above the topographic data points supplied as input to the algorithm. Cells fully below the topographic surface are brown, mixed air/ground blocks assigned as air in MT3Dinv are white, and air only blocks are blue. Note that the average flight height off the ground is effectively increased in the inversion block model created by the programme.

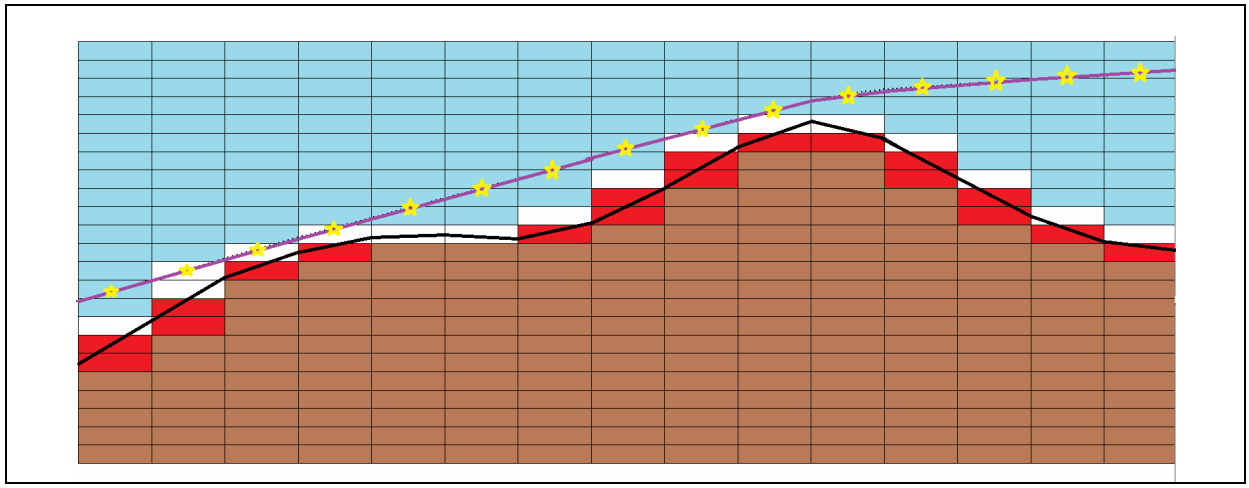

Figure 3. The effect of truncating topography can be reduced if data and topography are only located over the centre of mesh cells and the topography value is rounded up or down to an elevation corresponding to the top of a mesh cell. Red cells shown are added to the inversion model if this process is followed. The resulting cell based model is a better representation of the real topography.

It is essential to review the ZTEM data at all frequencies and both polarizations and to mark or remove bad data. The method we use is to grid the data and then to inspect the power-line monitor maps along with maps of each data field to identify data that are geologically unreasonable. Generally, these are high amplitude short spotty anomalies or anomalies that are correlated with the high values of the power-line monitor and that break up the trends of the map. This is somewhat arbitrary, but has produced the best results for us. If bad data are left in the data sets, they can also be identified later in the workflow if the inversion routine was yet unable to fit these well. This methodology requires an understanding of what tilt-angle anomalies look like and how they are generated by geological features at the frequencies used by the ZTEM system. Comfort with the historical interpretation of tilt-angle anomalies measured with VLF EM receivers such as an EM 16 is very useful. A review of the well-established literature describing VLF EM theory and interpretation is strongly recommended by anybody planning to invert ZTEM data (e.g., Wright, 1988; McNeil and Labson, 1992). The typical form of a tilt angle EM anomaly is shown in Figure 4, whilst data from a ZTEM survey prior to and after the removal of bad data is shown in Figure 5.

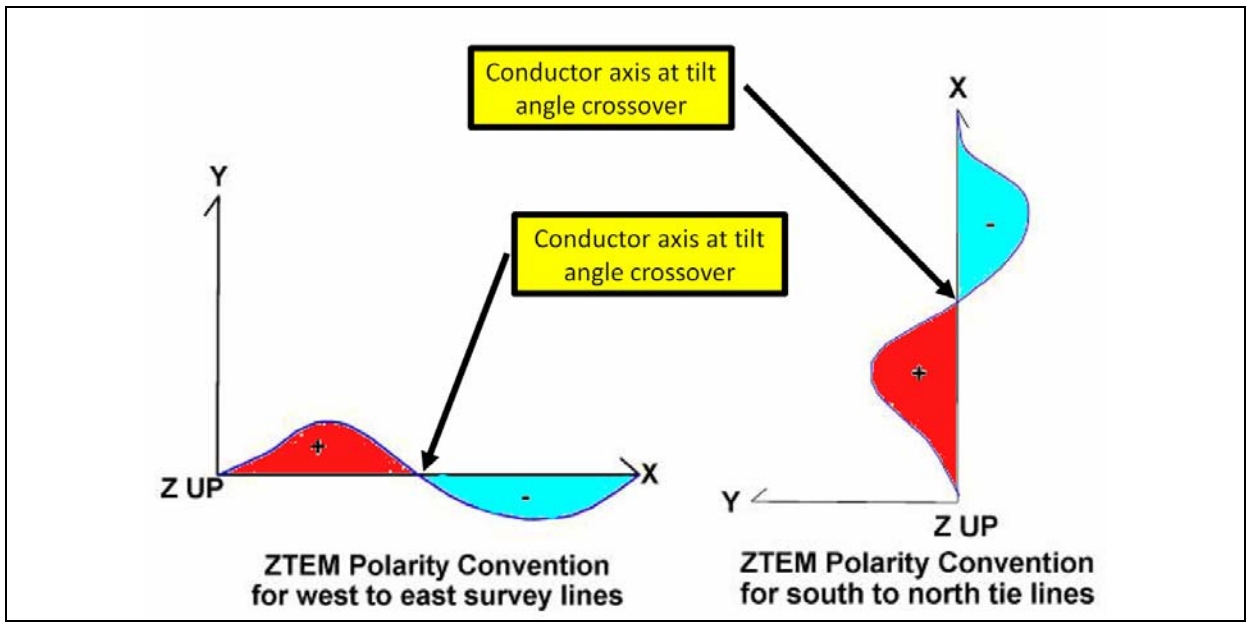

Figure 4. Tilt angle anomaly polarities for a north-south conductive anomaly axis on an east west traverse line, and an east-west anomaly axis on a north-south traverse line using the Geotech ZTEM polarity conventions. This is the typical sign convention used in VLF EM data but is not the EM sign convention used in the MT3Dinv program. ZTEM data needs to be transformed to the MT3Dinv EM sign and polarity conventions prior to use in an inversion.

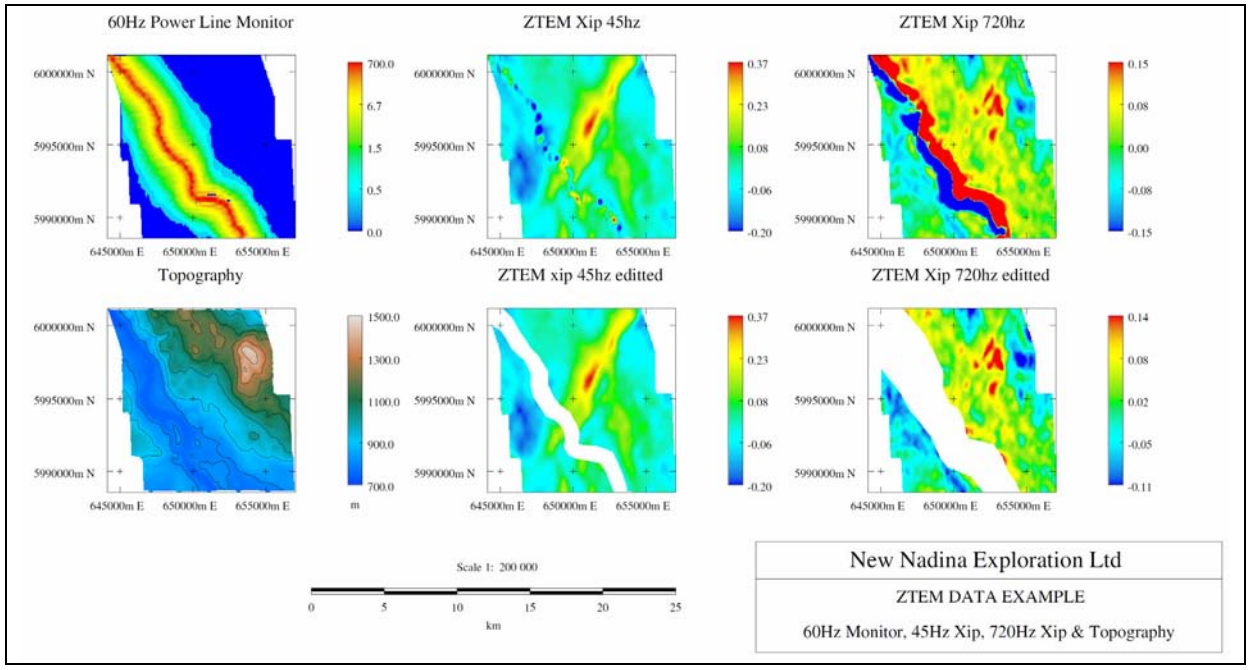

Figure 5. Sample plots illustrating the method used to identity and remove bad ZTEM data. The power line monitor map and project area topography are included for reference. Visual inspection of the gridded data field, in this case the X polarization 45 Hz in-phase and the X polarization 720 Hz in-phase data, shows regions of bad data coinciding with the region of increased power line noise response. The areas of noisy data were identified by inspection and then digitized and flagged as bad. Generally, noisy data are associated with elevated power line response, but it is difficult to remove the bad data using an algorithm. Note the region of bad data at 720 Hz (right side of figure) is considerably larger than the region of bad data removed from the 45 Hz data (centre). Deletion of bad data needs to be done separately for all four parameters of each frequency for best results.

The MT3Dinv program is well documented and a GUI is available to manage inversion runs (Farquharson et al., 2002; Farquharson et al., 2003). We use a Linux 12 core computer (dual Xeon 5660 2.8 GHz) with 48 MB RAM as a computational resource for running the inversions. Typically, a single run might take 3 to 5 days for a model with 6 frequencies and about 1.2 million cells.

Silver Queen project example

A ZTEM survey was flown over the Silver Queen project of New Nadina Exploration Limited. The project area has recorded production of copper, lead, zinc and gold from a past producing underground mine. Considerable drilling has been done around the old mine, including a number of deep holes. The property was recognized to have potential for buried porphyry style mineralization, but no porphyry style mineralization had been encountered in the exploration drill holes.

The magnetic data as well as the ZTEM data were inverted and visualized in 3D to identify the location of an intrusive stock below the Silver Queen mine, and to map large regional structures and the geological domains in the mine area (Figure 6 and Figure 7). Interpretation of these data identified a favourable structural setting for porphyry style mineralization and a Titan24 ground based IP and MT electrical survey was commissioned to find targets for drilling.

The criteria used to identify the favourable area for detailed ground based geophysics are shown in Table 1. These are not complex, but served to focus attention on the area subsequently covered with a ground-based Titan24 electrical survey. The Titan24 induced polarization and resistivity data were inverted and drill targets identified. Thirteen holes were drilled. The first drill hole encountered quartz vein stock-work alteration with copper and molybdenum mineralization (Figure 8). Hole 11-S_13 ended in good porphyry style molybdenum mineralization at 777 m. The ZTEM, Titan24 work and drilling were all done in one short northern Canadian field season.

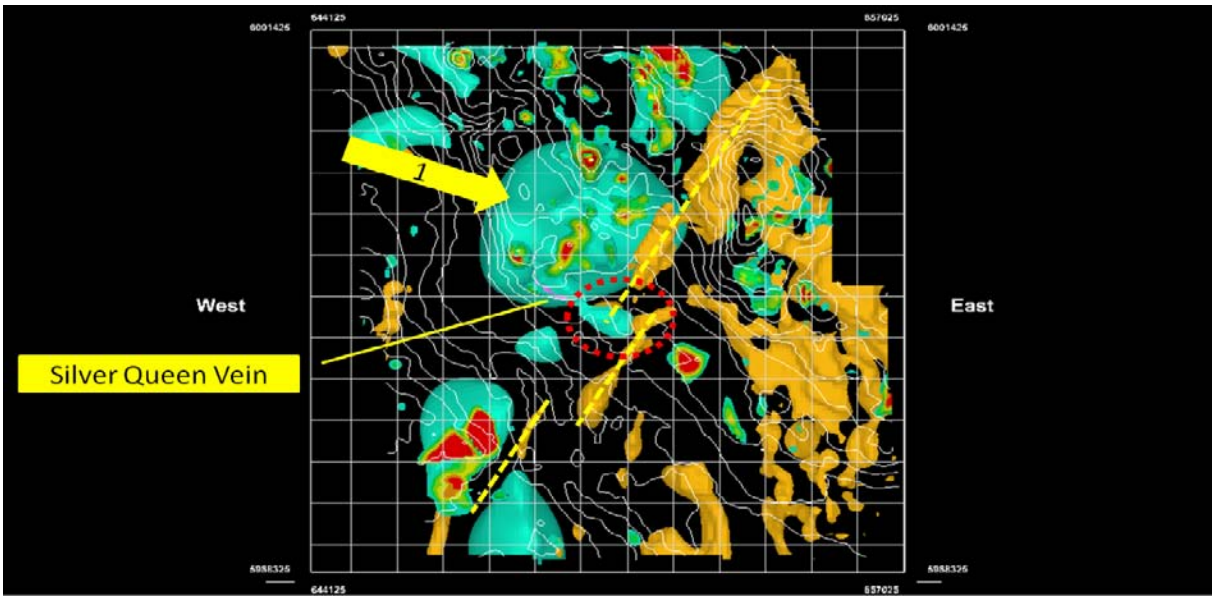

Figure 6. ZTEM inversion results. The 500 ohm-m isosurface (blue) and the 12.5 ohm-m isosurface (brown) from the ZTEM inversion are shown. The Silver Queen Vein system is shown as a small purple body striking NW. The large balloon shaped blue resistive isosurface (marked 1 by the yellow arrow) immediately below and to the north of the Silver Queen Vein system is interpreted to be an intrusive. A yellow dashed line delineates an interpreted NE-SW regional structure. This has been identified based upon the conductive linear feature shown by the brown coloured isosurface. The red ellipse identifies the favourable region close to the intrusive boundary where a zone of structural accommodation exists as movement transfers from the main structure going NE to a parallel arm of the NE-SW fault system that carries on to the SW. A small zone of increased conductivity that may be a breccia is seen below the blue linear resistive feature extending east south-east from the Silver Queen vein system and in the centre of the red ellipse.

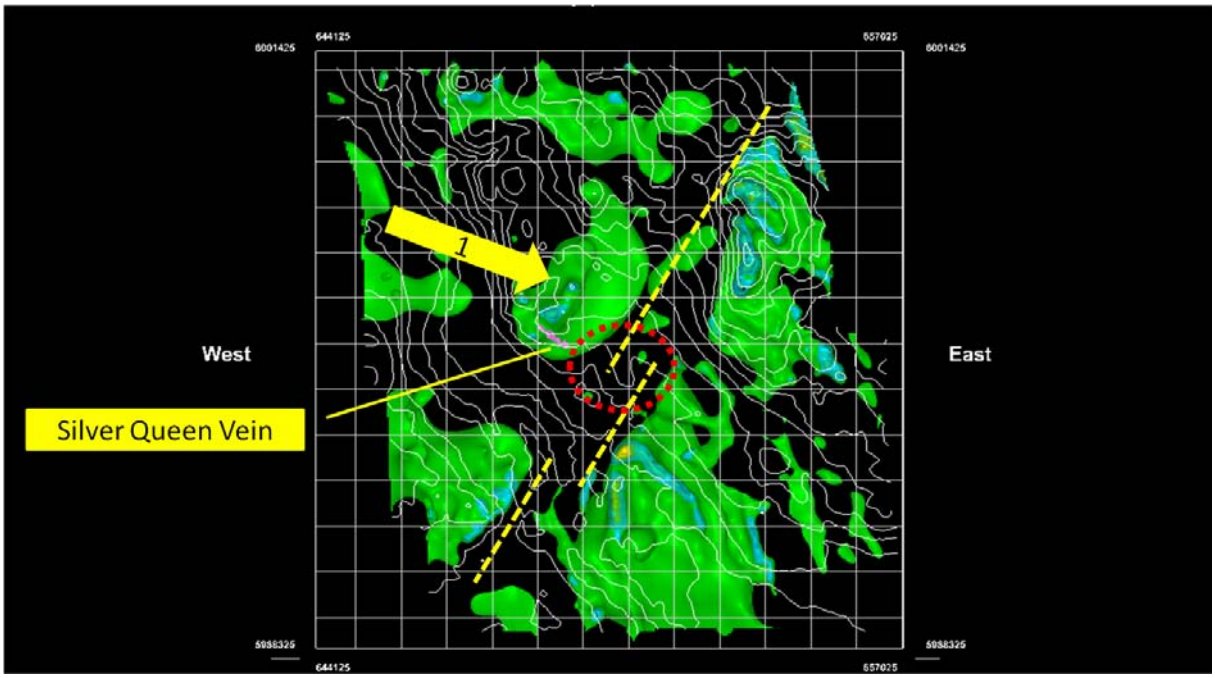

Figure 7. Susceptibility isosurfaces from the magnetic inversion model. The green isosurface is the 0.002 SI surface. This identifies a stock-like body interpreted as a magnetic phase of the intrusive below the Silver Queen vein system. This interpreted intrusive body is marked with the yellow arrow (1). The differing shapes of the inferred intrusives from the ZTEM inversion and the magnetic inversion suggest multiple phases, with magnetic and non-magnetic intrusive phases both being present. The NE-SW structural trend corresponds with a magnetic low. In the SE corner of the project area, magnetic and conductive units exist (green in Figure 7 and brown in Figure 6). This is a region of basalts. The different magnetic and electrical character of this region can be recognized in the ZTEM and magnetic inverted models.

Table 1. Criteria used to identify an area for detailed ground based follow-up using the ZTEM and Magnetic survey inversion results.

Criteria	Source of data
Close to known mineralization.	Old mine workings plotted in 3D, with a corroborating resistive feature seen near surface in the ZTEM inversion.
Close to or in the boundary of intrusive body.	Intrusive boundaries were interpreted using ZTEM inversion conductivity isosurfaces and MAG3DINV susceptibility isosurfaces.
In a regional structure at a thickening of the structure, a kink, or a dilational zone of accommodation transferring movement between parallel structures.	Linear zones of lowered conductivity in ZTEM inversion associated with linear features and magnetic lows in airborne magnetic data were interpreted as zones of brecciation mapping regional structures.
In a zone of increased brecciation.	Interpreted from local zones of increased conductivity indicated by ZTEM inversion.

Figure 8. Core photographs showing molybdenum mineralization and stock-work veining. This mineralization evidenced itself as a zone of moderate to lower resistivity and high chargeability in the induced polarization and resistivity inversion results, respectively. The near-surface zone of increased resistivity seen in Figure 6 as extending into the area of interest in the ZTEM inversion was identified in the 3D resistivity inversion as a near-surface resistive zone.

Conclusions

We have successfully inverted ZTEM data at the Silver Queen project of New Nadina Exploration Ltd. using the UBC-GIF MT3Dinv inversion code package. The inversion model result was interpreted to identify a favourable area for porphyry style mineralization. Ground follow-up work with a Titan24 electrical survey found targets subsequently validated by drilling. The work done has resulted in the discovery of a significant new porphyry molybdenum prospect. The combination of ZTEM and magnetic data, inverted for 3D conductivity and a magnetic susceptibility models, respectively, and then combined with a 3D geological model provided guidance to locate a detailed deep penetrating Titan24 electrical survey on the ground. Follow-up drilling of the induced polarization anomalies identified from the Titan24 survey data intersected a significant and previously unknown mineralized zone. Using the ZTEM data in this process was cost effective as it directed the follow up ground exploration to a smaller area of increased prospectivity and shortened the time necessary to explore the project area.

Acknowledgments

We gratefully acknowledge permission from New Nadina Exploration Ltd., and in particular Ms. Ellen Clements, President, to show these results from the ongoing exploration program at the Silver Queen project.

References

Farquharson, C. G., Oldenburg, D. W., and Haber, E., 2002, An algorithm for the three-dimensional inversion of magnetotelluric data: SEG Expanded Abstracts, 21, 649-652.

Farquharson, C., Haber, E., Shekhtman, R., and Oldenburg, D., 2003, Theoretical Background for the Magnetotelluric Inversion Program MT3Dinv: Unpublished Technical Report, University of British Columbia – Geophysical Inversion Facility.

Legault, J. M., Kumar, H., Milicevic, B., and Hulbert, L., 2009, ZTEM airborne tipper AFMAG test survey over a magmatic copper-nickel target at Axis Lake in northern Sakatchewan: SEG Expanded Abstracts, 28, 1272-1276.

McNeill, J. D., and Labson, V. F., 1992, Geological mapping using VLF radio fields: In Electromagnetic Methods in Applied Geophysics (ed. Misac Nabighian), Vol.2, Society of Exploration Geophysicists, Tulsa, OK, 521-640.

Vozoff, K., 1972, The magnetotelluric method in the exploration of sedimentary basins: Geophysics 37, 98-141.

Wright, J. L., 1988, VLF interpretation manual: EDA Instruments (now Scintrex), Toronto.

An overview of the ZTEM and AirMt systems – A case study from the Nebo-Babel Ni-Cu-PGE deposit, West Musgrave, Western Australia

Jean Legault [1] , Glenn A. Wilson [2] , Alexander V. Gribenko [3] , Michael S. Zhdanov [4] , Shengkai Zhao [5] and Keith Fisk [6]

[1] *Geotech (jean@geotech.ca)*
[2] *TechnoImaging (glenn@technoimaging.com)*
[3] *University of Utah & TechnoImaging (alex@technoimaging.com)*
[4] *University of Utah & TechnoImaging (mzhdanov@technoimaging.com)*
[5] *Geotech (shengkai@geotech.ca)*
[6] *Geotech Airborne (keith@geotechairborne.com)*

Introduction

Over the last decade, airborne electromagnetic (AEM) acquisition systems have evolved, many adopting higher moments to achieve greater depth penetration, whilst sensor calibration and post-acquisition processing technologies have also improved data quality significantly. As an alternative to conventional AEM, the Z-axis Tipper Electromagnetic (ZTEM) and Airborne Magnetic Tensor (AirMt) systems were developed to measure the transfer functions of audio-frequency natural electromagnetic sources from airborne platforms. The ZTEM system measures tipper transfer functions, and the AirMt system measures the rotational invariant of the transfer functions. Ancillary data measured by both systems include radar altimeter, receiver coil altitude, GPS elevation, and total magnetic intensity. For both ZTEM and AirMt, data are typically measured from 25-30 Hz to 600-720 Hz, giving detection depths to 1 km or more, depending on the terrain conductivity. This makes it practical for these systems to be used for mapping large-scale geological structures.

The first commercial surveys for ZTEM were commissioned in 2006, and the first commercial surveys for AirMt were commissioned in 2009. Development of both systems has been aided by Geotech's logistical and technical experience with active-source AEM systems. Presently, eight ZTEM systems and one AirMt system are in operation around the world. ZTEM and AirMt surveys have been flown in Australia, Indonesia, North America, South America, Africa and the Middle East for Sedex, VMS, IOCG, Ni-Cu-PGE, porphyry, uranium and precious metal mineralization systems for numerous major and junior exploration companies. In this paper, we present a case study for the 3D interpretation ZTEM and AirMt surveys flown over the Nebo-Babel Ni-Cu-PGE deposit in Western Australia.

Background

Since the 1950s, magnetotelluric (MT) surveys have been carried out, measuring horizontal electric and magnetic fields induced from ambient (natural) sources, generally assuming that these can be treated as plane electromagnetic waves. The amplitude and phase of the primary field are unknown. By processing the electric and magnetic fields to a complex impedance tensor, the unknown source terms are removed and the transfer functions are dependent only upon frequency and the Earth's conductivity. Magnetovariational (MV) methods are an extension of the MT concept, whereby the transfer functions between the horizontal and vertical magnetic fields:

$$H_z(\mathbf{r}) = W_{zx}(\mathbf{r})H_x(\mathbf{r}) + W_{zy}(\mathbf{r})H_y(\mathbf{r}), \quad (1)$$

form a complex vector often called the Weiss-Parkinson vector, induction vector, or tipper. Similar to the impedance tensor for MT data, the tipper effectively removes otherwise unknown source terms. Since the vertical magnetic field is zero for plane waves vertically propagating into a 1D Earth model, non-zero vertical magnetic fields are directly related to 2D or 3D structures.

This served as the basis for the original development of the audio-frequency magnetic (AFMAG) method (Ward, 1959) whereby two orthogonal coils were towed behind an airborne platform to determine the tilt angle of the plane of polarization of ambient (natural) magnetic fields in the 1 Hz to 20 kHz band. The natural magnetic fields of interest originate from atmospheric thunderstorm activity and propagate over large distances with little attenuation in the Earth-ionosphere waveguide. Given that the tilt angle is zero over a 1D Earth, the AFMAG method produced a non-zero response when crossing conductors. However, the direction and amplitude of the natural magnetic fields randomly varies with time and periodically with season, meaning AFMAG data were not repeatable (Ward et al., 1966). By using MT processing techniques for ground-based orthogonal horizontal magnetic field measurements, Labson et al. (1985) demonstrated that repeatable tipper data could be recovered from measured magnetic fields.

The AFMAG method of Labson et al. (1985) remained largely undeveloped until the recent commercialization of ZTEM (e.g., Legault et al., 2009; Pare and Legault, 2010) (Figure 1) and subsequently, AirMt (e.g., Kaminski et al., 2010) (Figure 2) systems. ZTEM measures the tipper components as the transfer function of a vertical magnetic field measured from an airborne receiver coil to the horizontal components measured at a ground-based reference receiver coil array:

$$H_z(\mathbf{r}) = W_{zx}(\mathbf{r}, \mathbf{r}_0)H_x(\mathbf{r}_0) + W_{zy}(\mathbf{r}, \mathbf{r}_0)H_y(\mathbf{r}_0). \quad (2)$$

AirMt directly measures the rotational invariant of the transfer function for the three magnetic fields measured from an airborne receiver coil array to the three magnetic fields measured at a ground-based (reference) location. Generalizing the Weiss-Parkinson relationship, the three components of a magnetic field measured at a receiver coil array are linearly related to the magnetic fields measured at a ground-based reference receiver coil array:

$$\begin{bmatrix} H_x(\mathbf{r}) \\ H_y(\mathbf{r}) \\ H_z(\mathbf{r}) \end{bmatrix} = \begin{bmatrix} W_{xx}(\mathbf{r}, \mathbf{r}_0) & W_{xy}(\mathbf{r}, \mathbf{r}_0) & 0 \\ W_{yx}(\mathbf{r}, \mathbf{r}_0) & W_{yy}(\mathbf{r}, \mathbf{r}_0) & 0 \\ W_{zx}(\mathbf{r}, \mathbf{r}_0) & W_{zy}(\mathbf{r}, \mathbf{r}_0) & 0 \end{bmatrix} \begin{bmatrix} H_x(\mathbf{r}_0) \\ H_y(\mathbf{r}_0) \\ H_z(\mathbf{r}_0) \end{bmatrix}. \quad (3)$$

If we write $\mathbf{W_1}$ and $\mathbf{W_2}$ as the first and second columns of the transfer function, then we can introduce the variable:

$$\mathbf{K} = \mathbf{W_1} \times \mathbf{W_2} \quad (4)$$

and obtain the complex scalar:

$$K = \mathbf{K} \cdot \frac{Re(\mathbf{K})}{|Re(\mathbf{K})|} \quad (5)$$

called the amplification parameter (AP), which can be shown to be rotationally invariant (Kuzmin et al., 2010; Dodds, 2010, pers. comms.; Wannamaker, 2010, pers. comms.). Since the amplification parameter does not depend on the orientation of the sensor, it negates the post-acquisition need to correct for the sensor orientation with the AirMt system.

For both ZTEM and AirMt systems, the time series of the magnetic fields are recorded at fixed sampling rates, and the data are binned and processed to generate in-phase and quadrature transfer functions in the frequency-domain (i.e., tippers for ZTEM, amplification parameter for AirMt). The lowest frequency of the transfer functions depend upon the speed of the airborne platform, and the highest frequency depends on the sampling rate. For helicopter-borne or fixed-wing ZTEM and helicopter AirMt systems, transfer functions are typically obtained at five or six frequencies from 25 Hz to 600 Hz, giving skin depths ranging between 600 m and 2000 m for typical terrain conductivities.

Instrumentation

For helicopter surveys, the ZTEM and AirMt systems are carried as an external sling load, and are independent of the helicopter (Figure 1 and Figure 2). The ZTEM receiver coil is a 7.4 m diameter air-core loop sensor that measures the vertical magnetic field. The AirMt receiver coil array measures

three components of the magnetic field using three mutually perpendicular, 3.04 m diameter air-core loops. ZTEM and AirMt receiver coils use a patented suspension system mounted inside a fibreglass shell to attenuate the majority of vibrations. The receiver coil arrays are nominally towed from the helicopter by a 90 m long cable, and are flown with a nominal ground clearance of 80 m. Altitude positioning of the receiver coil array is enabled by GPS antennas mounted on the frame in combination with GPS and radar onboard the helicopter. For both ZTEM and AirMt, the magnetic field time-series are measured with a 2 kHz sampling frequency.

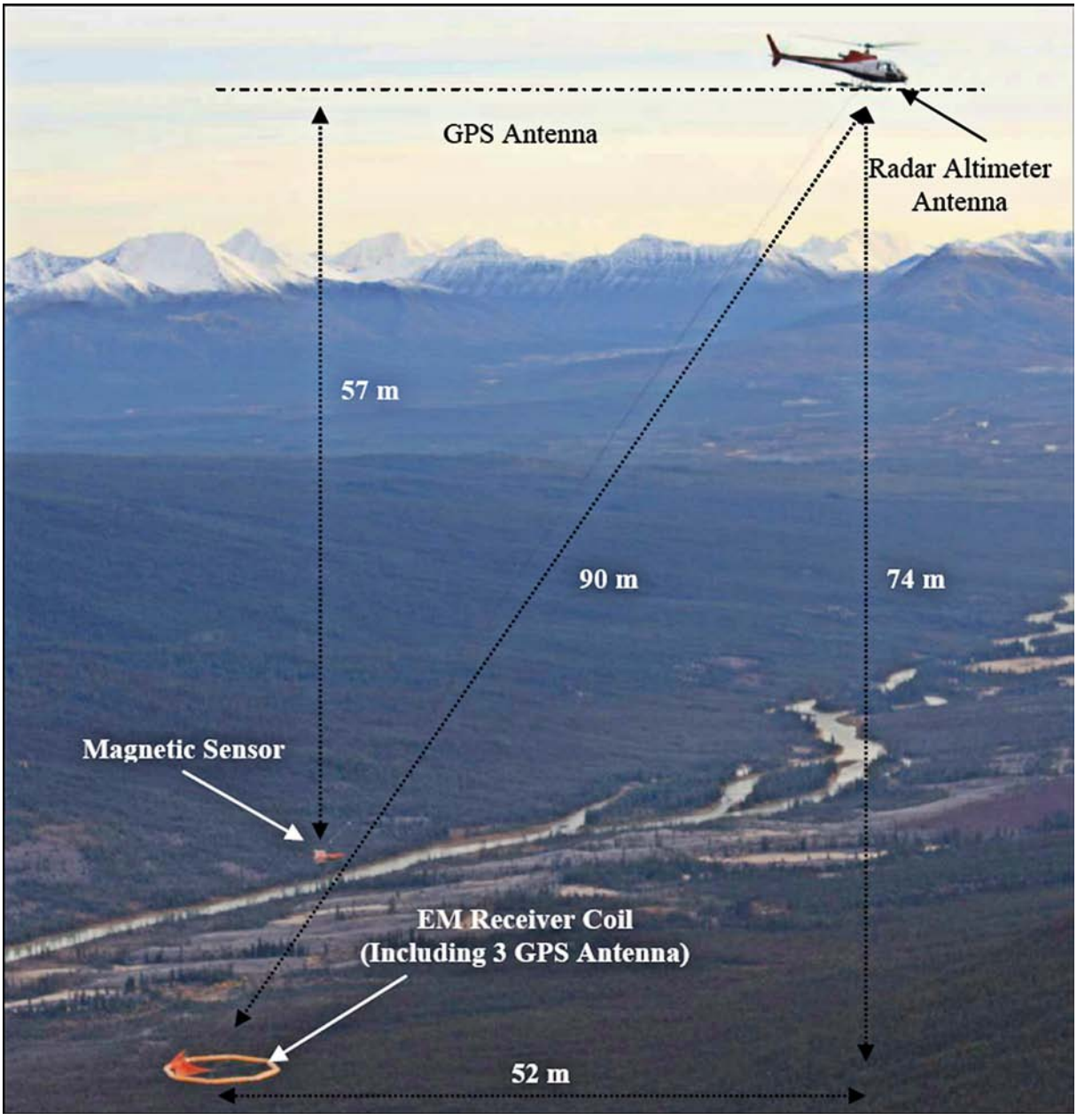

Figure 1. ZTEM (Z-Axis Tipper ElectroMagnetic) system configuration.

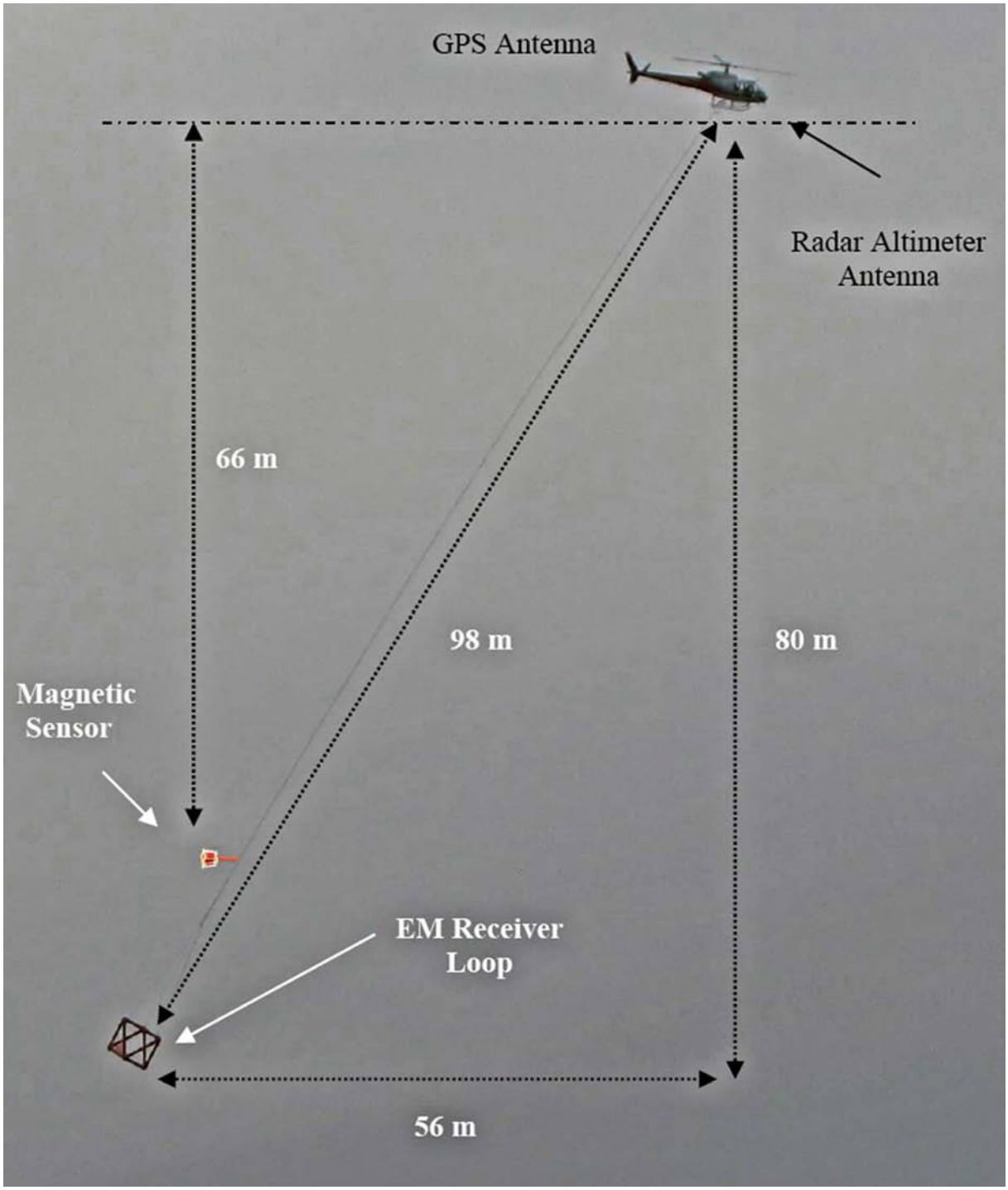

Figure 2. AirMt (Airborne Magnetic Tensor) system configuration.

The base station for these systems is typically the AirMt sensor, consisting of three mutually perpendicular, 3.04 m diameter air-core loops, as shown in Figure 3. The base station provides a reference field which when processed with the airborne receiver coil data, produces the appropriate transfer functions which are output at 2.5 Hz, or approximately 10 m sample intervals.

Figure 3. ZTEM and AirMt base station sensor.

Interpretation

Given the use of the same assumption of plane wave source terms, modelling and inversion for ZTEM and AirMt data is similar to that of MT. However, unlike MT surveys, ZTEM and AirMt surveys typically contain hundreds to thousands of line kilometres of data with measurement locations every few metres, covering areas thousands of square kilometres in size. Geotech's standard products for ZTEM and AirMt include total divergence and phase rotation grids, and 2D Gauss-Newton inversion based upon modifications to algorithms by Wannamaker et al. (1987), de Lugao and Wannamaker (1996), and Tarantola (1987). Third parties provide additional products such as 2D pseudo-sections by Karous-Hjelt filtering (e.g., Sattel et al., 2010) or 2D Occam inversions based on their own modifications of algorithms by Wannamaker et al. (1987) and Constable et al. (1987). Holtham and Oldenburg (2010) introduced 3D ZTEM inversion based on modifications of the 3D MT inversion by Farquharson et al. (2002). In the subsequent case study for both ZTEM and AirMt, our 3D MT inversion analog is that of Zhdanov et al. (2011).

Case study – Nebo-Babel, West Musgrave, Western Australia

Geology

Most world-class deposits of nickel and platinum-group elements (PGE) are found in mafic igneous rocks of Proterozoic age that are part of exceptional large igneous provinces (LIPs). The West Musgrave Block, located in central Australia, is one such example, but one where the most of the prospective ground lies beneath regolith. Access for explorers has been limited in line with the wishes of the traditional landholders. However, access has become more widespread in recent years. One example of early success in the area was WMC's (now BHP Billiton) surface geochemistry-led discovery of the Nebo-Babel Ni-Cu-PGE deposit in 2000 (Groves et al., 2007). The discovery of other large deposits in the West Musgrave region requires the identification, below cover, of the crustal-scale feeder systems of the most voluminous mafic-ultramafic magmatic events. This directly feeds back to the aforementioned need for airborne geophysical techniques capable of deep penetration beneath conductive cover, and 3D imaging of the large-scale data sets acquired.

For Nebo-Babel, drill intersections include 106.5 m at 2.4% Ni, 2.7% Cu, and 0.2g/t PGE; and a resource of about 1 million tonnes contained Ni and 1 million tonnes contained Cu+Co has been released. The Nebo-Babel deposit is hosted within a concentrically-zoned, tube-like gabbronorite intrusion (1078 Ma) that has a 5 km east-west extent, a 1 x 0.5 km plan view cross section, and a shallow WSW-plunge (Figure 4). The gabbro-norite has intruded felsic orthogneissic country rocks of

amplibolite to granulite facies metamorphic grade and is offset along the north-south Jameson Fault, which separates the Babel and Nebo deposits that are of similar morphology. Babel is a large, generally EW to SW striking, mainly low-grade disseminated deposit that subcrops through thin sand cover to the east but plunges under more than 400 m of country rock and remains open to a depth of 600 m (Figure 4b). Nebo, 2 km to the northeast, is buried under a few metres of aeolian dune sand and is smaller than Babel, but contains a number of high grade massive sulphide pods that are mainly found in the upper part of the intrusion. It extends at least 1.8 km east-west, but its eastern limit and lower intrusive contact (inferred at >600 m – Figure 4b) have not yet been drill-defined. The deposits were discovered using deflation lag sampling on a 1 km x 0.5 km grid drill pattern. However, strong magnetic, electromagnetic, and gravity anomalies highlight the massive and disseminated mineralization in the deposit. Nebo-Babel has a number of features in common with other Ni-Cu-PGE deposits hosted in dynamic magma conduits (e.g., Voisey's Bay, Canada), such as multiple magma pulses and sulphide entrainment from depth, rather than in-situ sulphide segregation (Seat et al., 2007, 2009).

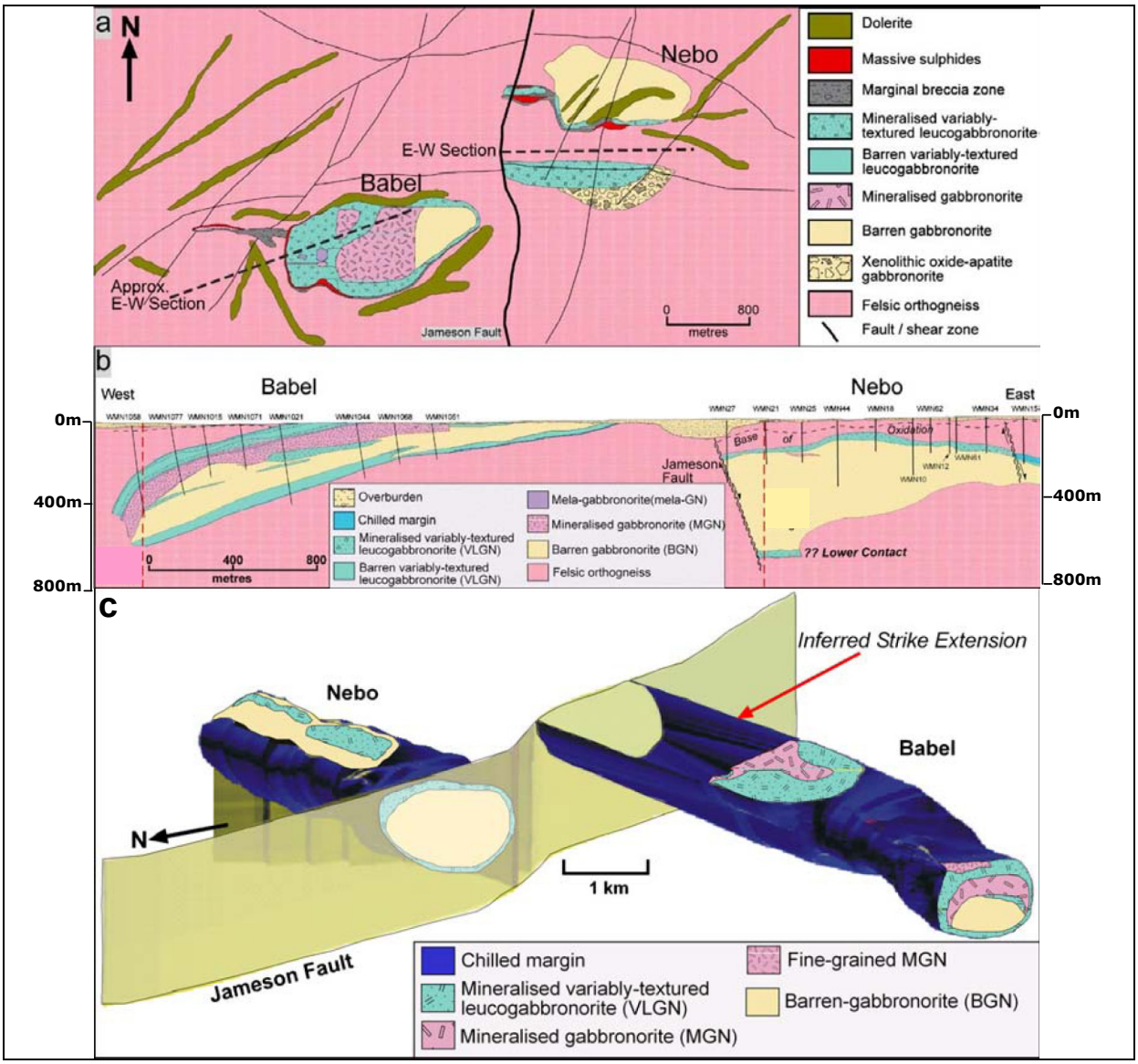

Figure 4. a) Surface projection of the gabbro-norite rock units, mineralized domains, and major structural elements at West Musgrave. b) Longitudinal east–west section through the Nebo–Babel intrusion. c) South–east facing three-dimensional geological model showing spatial and morphological relationships between the Nebo and Babel parts of the intrusion (after Seat et al., 2007).

ZTEM and AirMt Results

Under agreement between Geotech and BHP Billiton, both ZTEM and AirMt surveys were flown over the Nebo-Babel deposit area of West Musgrave (Figure 5 and Figure 6). Previous airborne systems flown over the deposits have included GEOTEM airborne electromagnetics and FALCON airborne gravity gradiometry. A total of 541 line km of ZTEM data and 574 line km of AirMt data were acquired along both east-west and north-south flight lines (Figure 6). The survey area has minimal topographic relief, varying from 460 to 494 m above sea level. The ZTEM receiver coil was flown with a nominal ground clearance of 78 m. ZTEM data were acquired at six frequencies; 25 Hz, 37 Hz, 75 Hz, 150 Hz, 300 Hz, and 600 Hz. The AirMt receiver coil array was flown with a nominal ground clearance of 78 m. AirMt data were acquired at six frequencies; 24 Hz, 38 Hz, 75 Hz, 150 Hz, 300 Hz, and 600 Hz. Total magnetic intensity (TMI) data were also acquired using a caesium magnetometer for both surveys. Figure 7 shows the reduced-to-pole (RTP) magnetic response, which highlights a number of features, including a) a linear NS magnetic low over the Jameson fault, possibly due to alteration or overburden fill, b) NE-trending magnetic lineaments, which mostly correlate with late mafic dolerite dykes (Figure 7), c) a partial ring-like magnetic high centred on a magnetic low over the Babel deposit, that is likely responding to the increased sulphides on the outer perimeter of the intrusive, and d) a broad magnetic high that is largely centred with the Nebo intrusive that likely indicates increased magnetite content in the gabbro-norite body.

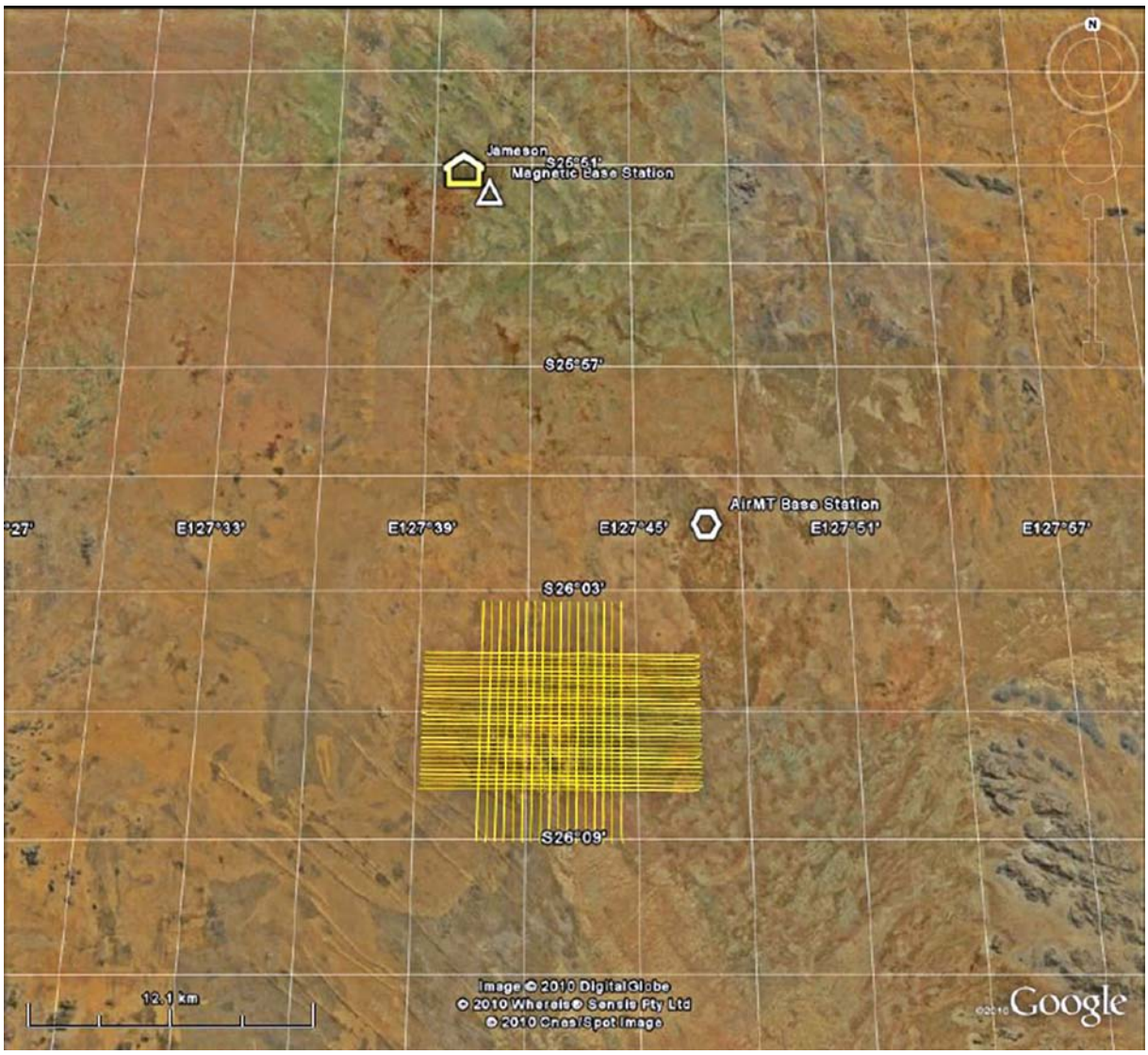

Figure 5. ZTEM and AirMt survey flight lines and base station locations over Nebo-Babel.

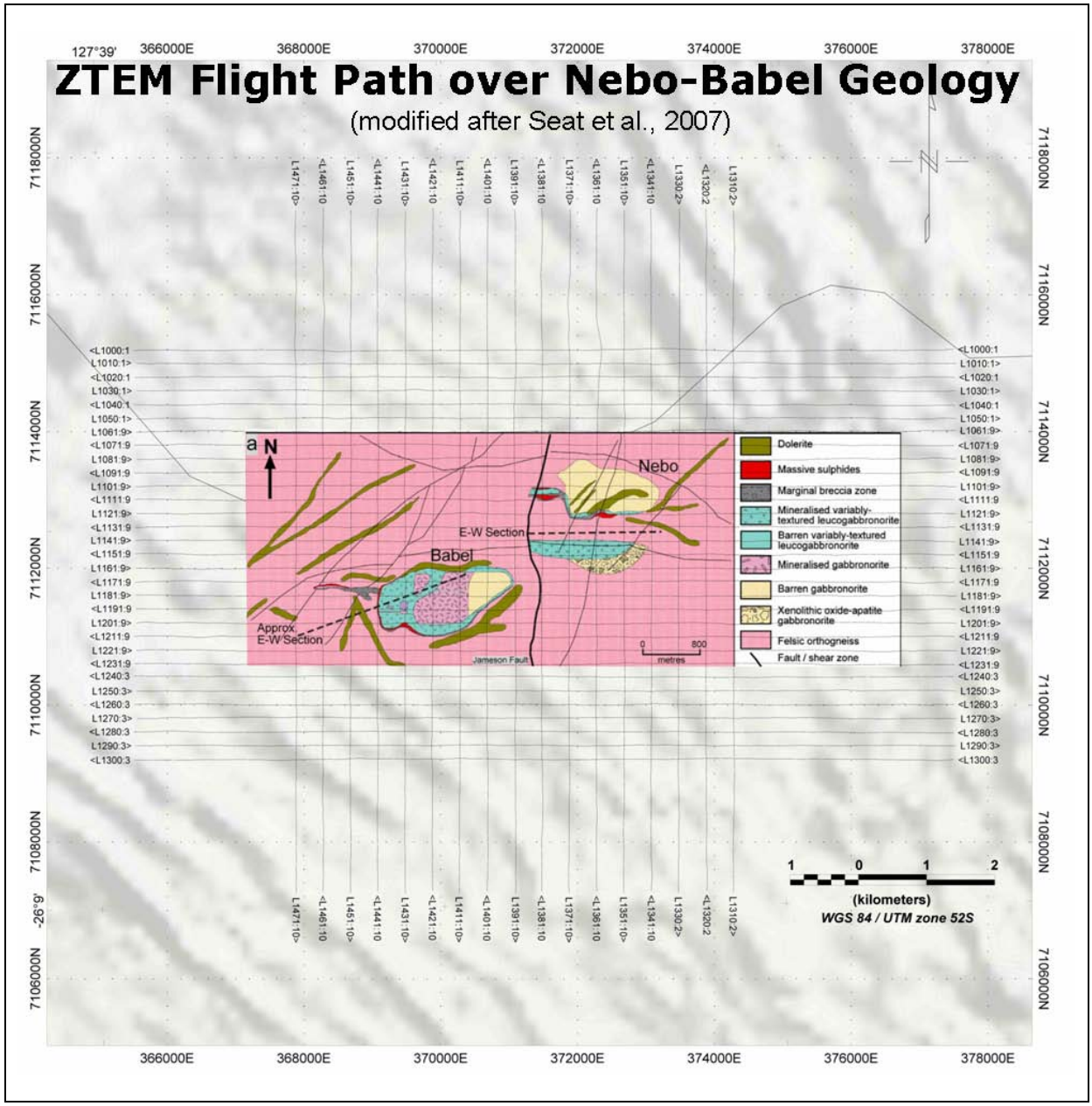

Figure 6. ZTEM and AirMt flight lines over Nebo-Babel geology (modified after Seat et al., 2007).

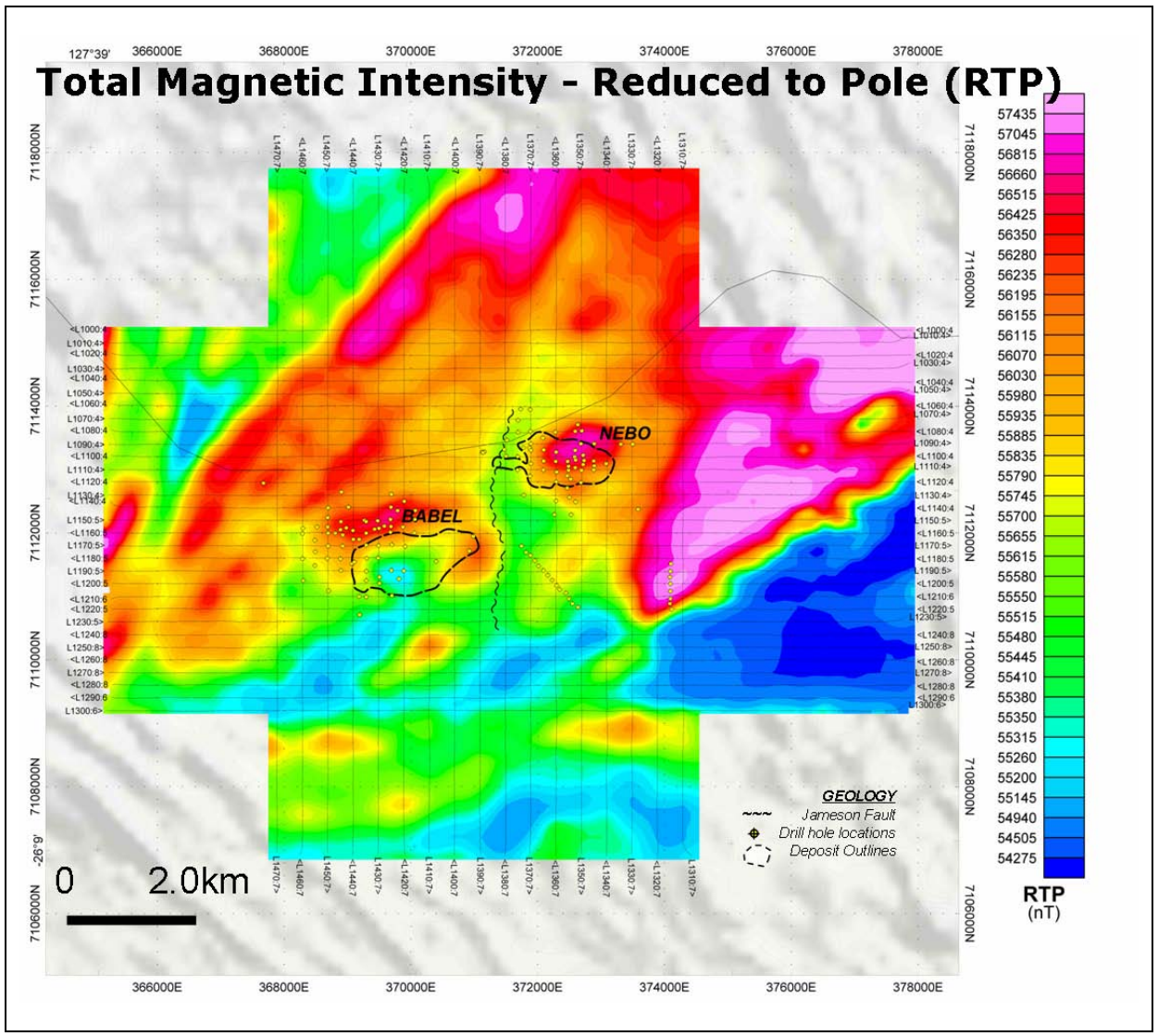

Figure 7. Total magnetic intensity (TMI) – reduced to pole (RTP).

Examples of the 75 Hz ZTEM and AirMt data are shown in plan in Figure 8, Figure 9 and Figure 10. Multi-frequency profiles of the ZTEM and AirMt data are also presented in Figure 11, for a representative north-south flight line (L1430) across the Babel deposit.

To present data from both tipper components in one image, and to compensate for the cross-over nature of ZTEM data (e.g., Figure 11 a and b), the total divergence (DT) is introduced as the horizontal derivatives of the tipper components:

$$DT = \frac{\partial T_{zx}}{\partial x} + \frac{\partial T_{zy}}{\partial y}, \qquad (6)$$

and is derived for each of the in-phase and quadrature components at individual frequencies. These in turn allow for minima-over-conductors and maxima-over-resistive zones. DT grids for each of the extracted frequencies were generated accordingly, using a reverse colour scheme with warm colours over conductors and cool colours over resistors (e.g., Figure 8).

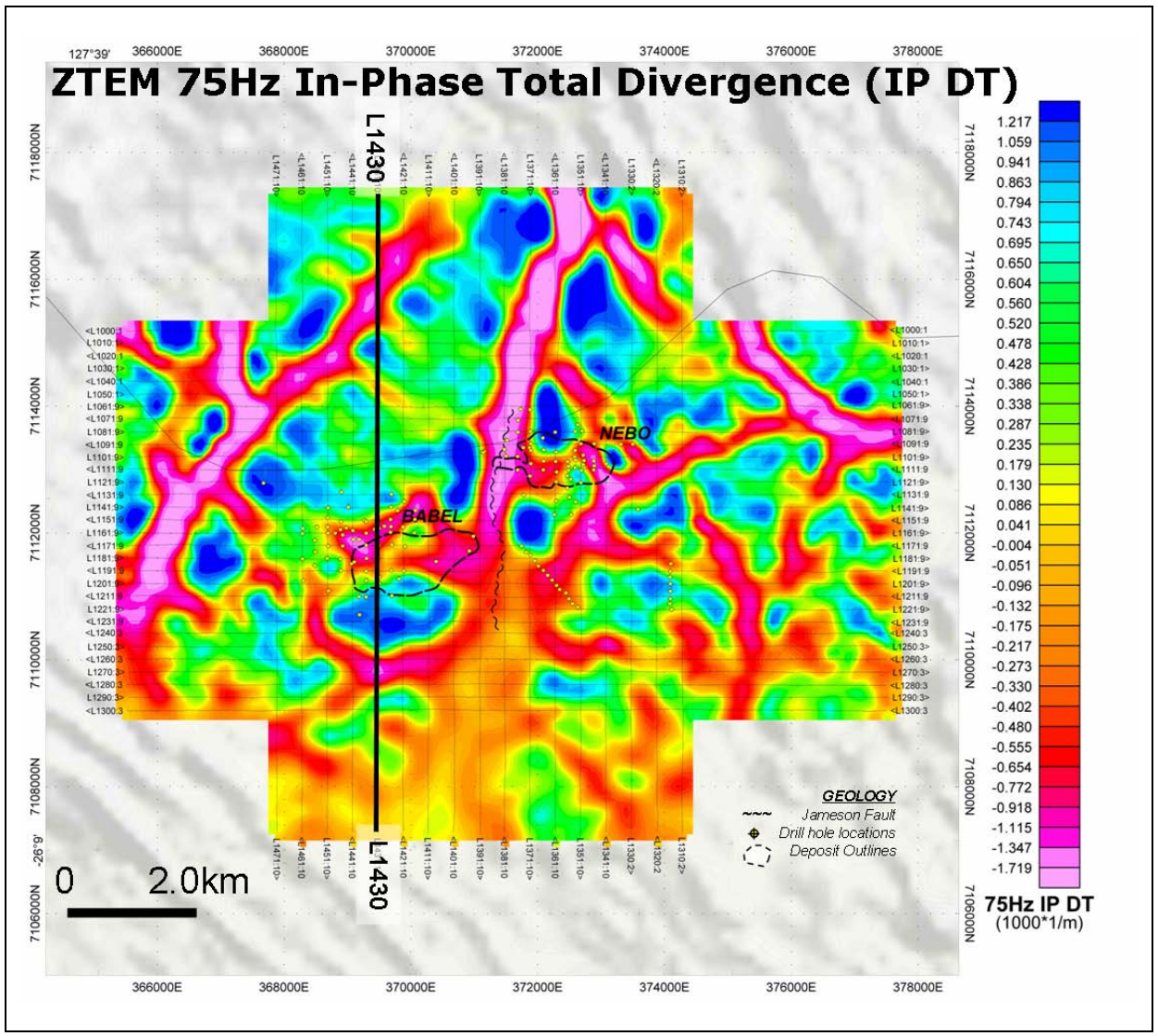

Figure 8. ZTEM 75Hz In-Phase Total Divergence (DT).

Alternatively, a 90 degree phase rotation (PR) can be applied to the grids of each tipper component. This transforms bipolar (i.e., cross-over) anomalies into single pole anomalies with a maximum over conductors, while preserving long wavelength information. The two orthogonal grids are then added together:

$$TPR = PR(T_{zx}) + PR(T_{zy}), \quad (7)$$

to obtain a total phase rotated (TPR) grid for each of the in-phase and quadrature components (e.g., Figure 9).

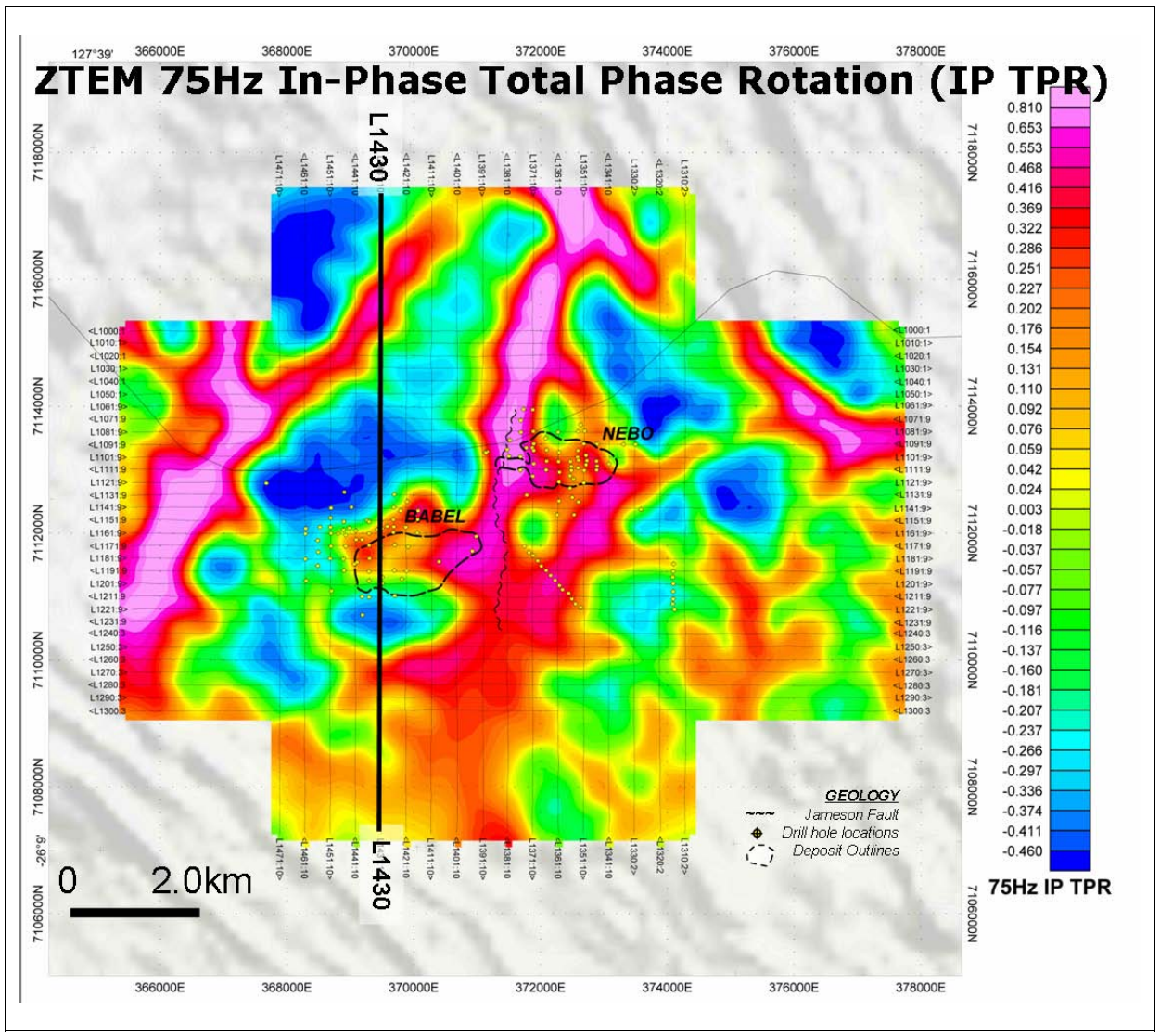

Figure 9. ZTEM 75Hz In-Phase Total Phase Rotation (TPR).

In contrast to the cross-over behaviour demonstrated by ZTEM tipper data, the AirMt amplitude parameter displays peak maxima and minima across conductive and resistive zones, respectively. Hence, no further processing of the AirMt data are required for plan-view presentation, as shown in the 75 Hz AP image in Figure 10.

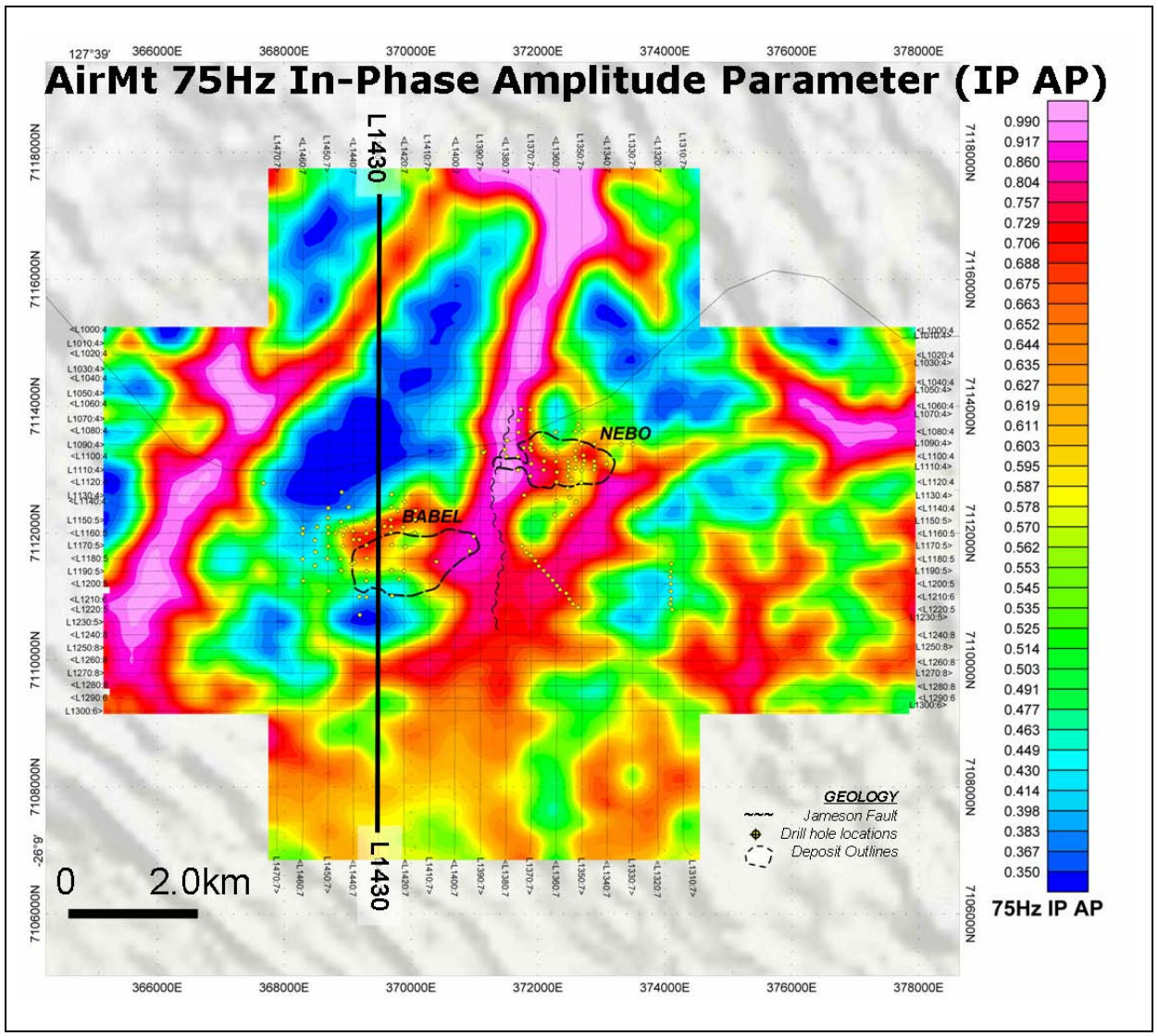

Figure 10. AirMt 75Hz In-Phase Amplitude Parameter (AP).

Comparing the three images in Figure 8, Figure 9, and Figure 10, the ZTEM DT, TPR and AirMt AP results are remarkably consistent and highlight similar geologic features defined in the magnetic results, such as a) the conductive Jameson fault that extends north and south of the survey area, b) a ring-like conductive anomaly that partially coincides with the Babel deposit and, c) a smaller conductive anomaly over Nebo deposit that appears to coincide with the known massive sulphide lenses. Other ZTEM-AirMt conductive lineaments that are defined, in part, appear to correlate with either magnetic linears (e.g., Figure 7) or else mapped faults (Figure 6), and may therefore indicate increased porosity or clay in the faults or possible near-surface paleochannel or overburden relief structures (Greg Walker, 2011, pers. comm.).

What seems clear from these results is that the cross-cutting behaviour in the ZTEM and AirMt clearly points to a 3-dimensional environment at Nebo-Babel. While the DT, TPR and AP grids can be used for qualitative analysis, neither they nor the raw data profiles themselves (Figure 11) are able to easily provide any quantitative information about these 3D structures. For this, inversion modelling is required.

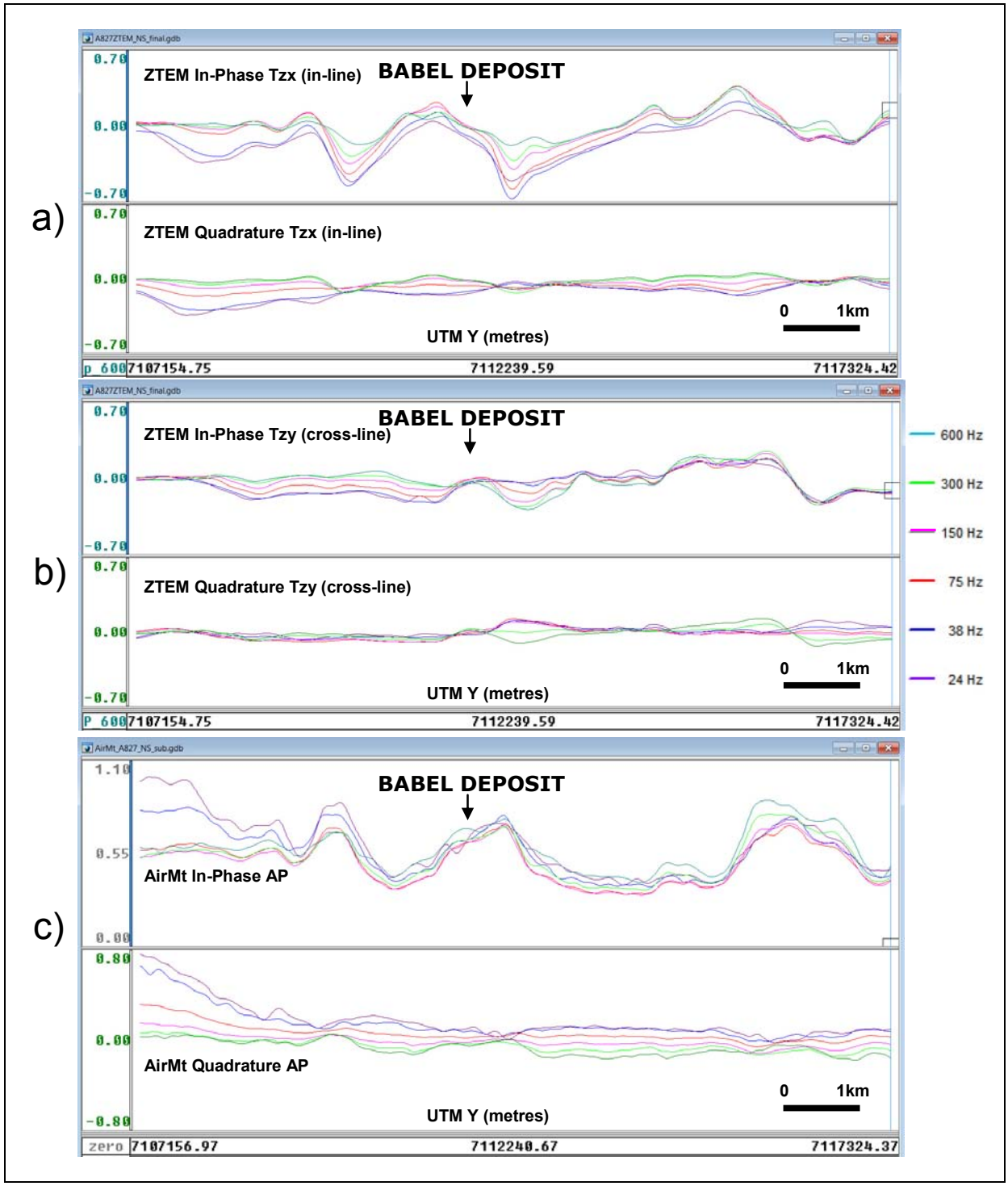

Figure 11. Multi-frequency (24-600Hz) In-Phase and Quadrature data profiles for L1430 a) ZTEM In-line (Tzx) component (XIP & XQD), b) ZTEM Cross-line (Tzy) component (YIP & YQD), and c) AirMt Amplitude Parameter (AIP & AQD).

Geotech's 2D inversion is based on modifications to the MT modelling algorithm of Wannamaker et al. (1987), with sensitivities by de Lugao and Wannamaker (1996) in an iterative Gauss-Newton method (Tarantola, 1987). The algorithm is programmed to operate in serial fashion and runs on desktop computers. Each line is inverted independently. For 2D ZTEM inversion, this software only inverts the inline tipper data and assumes orthogonal and infinite strike length of all targets. For 2D AirMt inversion, the software inverts the amplification parameter assuming orthogonal and infinite strike length of all targets. This approximation is reasonable if the geological structures have strike lengths

orthogonal to the flight line direction in the order of a skin depth; i.e., greater than the footprint or sensitivity of the ZTEM or AirMt systems. In both cases, the 2D ground topography and the air-layer thickness below the receiver coil array are accounted for. The inversions require *a priori* starting models that are reasonably close to the true half-space resistivity. At Nebo-Babel, 300 ohm-m was chosen for the starting half-space resistivity based on available ground AMT survey results provided by BHP Billiton.

For the Nebo-Babel 2D inversions, model convergence RMS fits of 1.0 or less were achieved in 4 to 5 iterations, with data errors of 0.03 to 0.05 for ZTEM whereas considerably higher data errors of 0.1 to 0.22 were required for AirMt data fitting. This relative inability to properly fit the data in 2D is interpreted to reflect the greater sensitivity of AirMt AP measurement to 3D distortion, relative to the ZTEM in-line component data, but also an indication the 3-dimensionality of the Nebo-Babel geologic environment. Similarly, 2D inversions of data along north-south lines appear to best highlight the Nebo and Babel deposit responses, due to their dominant EW strike, with the ZTEM models seemingly more successful than AirMt. On the other hand, neither of the technologies' 2D inversions along east-west lines (not shown) appears to have successfully resolved either deposit, possibly due to the dominance of the Jameson Fault signature. Panels a and b of Figure 12 presents 2D inversions of ZTEM and AirMt data, respectively, along the north-south L1430 profile which crosses the Babel deposit. The approximate outline of the intrusion is also shown.

TechnoImaging's 3D modelling is based on the 3D integral equation method (Hursán and Zhdanov, 2002), and the inversion itself uses a regularized re-weighted conjugate gradient (RRCG) method with focusing stabilizers (Zhdanov, 2002). Unlike smooth regularization, focusing enables the recovery of 3D models with higher contrasts and sharper boundaries. This is an analog of the 3D MT inversion described by Zhdanov et al. (2011). The software is fully parallelized for running on cluster computers, meaning that it can be scaled to invert very large survey areas. Panels d and e of Figure 12 show vertical cross-sections from the 3D inversions of ZTEM and AirMt data, respectively, along the L1430 north-south profile across the Babel deposit.

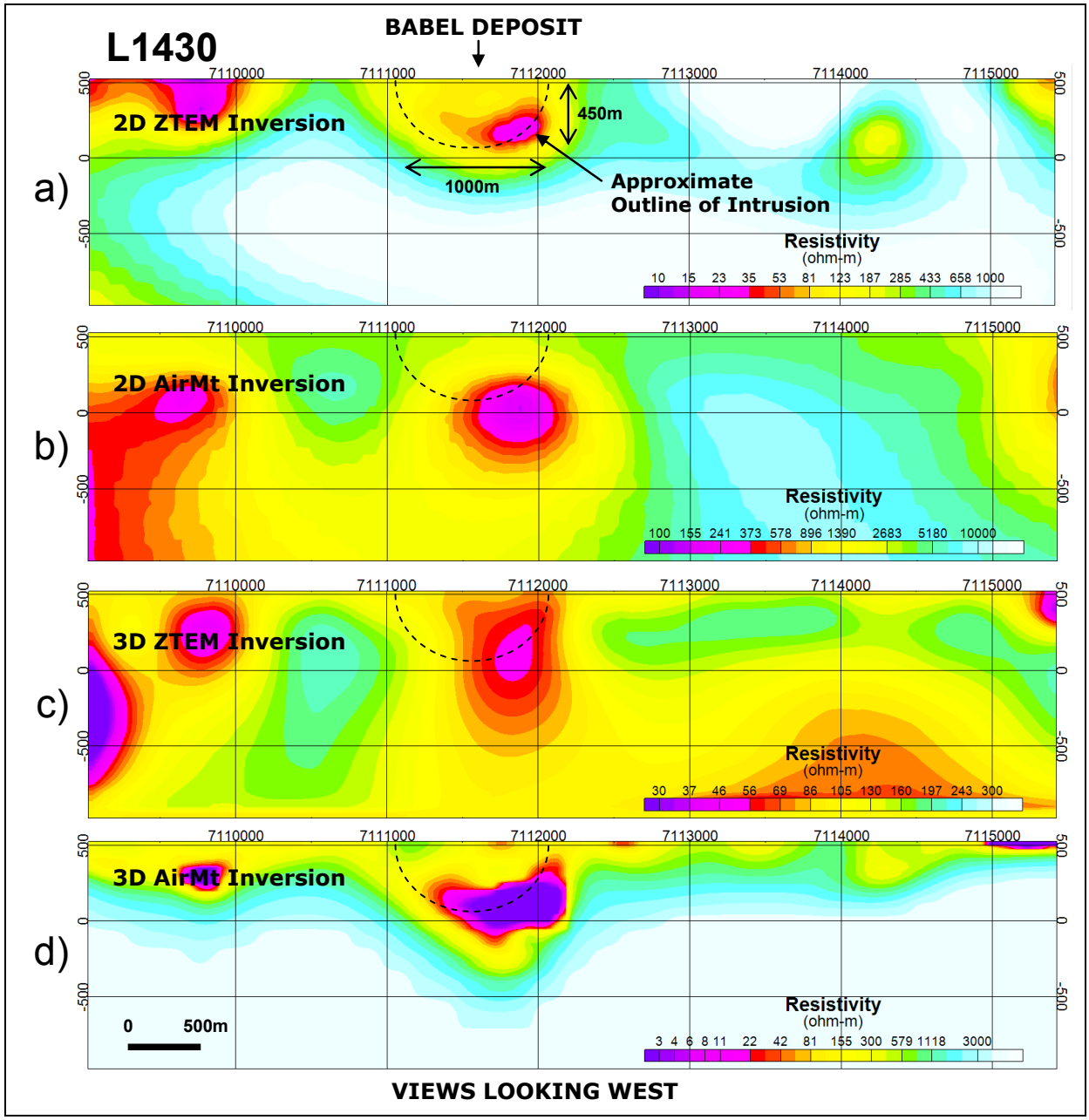

Figure 12. Resistivity cross-sections for L1430 obtained from: a) ZTEM 2D Inversion, b) AirMt 2D Inversion, c) ZTEM 3D Inversion, and d) AirMt 3D Inversion.

Discussion of Results

Comparing the 3D and 2D inversion cross-sections in Figure 12, at first glance, all four appear to show a reasonably well defined anomalous conductive response over the Babel deposit, with the maximum conductivity generally offset towards the north edge and base of the intrusive. Interestingly, this increased conductivity at depth is not easily supported geologically yet is a consistent feature in all 4 models. However, the overall shape and size/extent of the semi-concentric intrusive appear to be better resolved in the 2D ZTEM, and particularly, in the 3D ZTEM and AirMt model images, the lattermost which features the best resolved and most contrasted conductivity anomaly of the four. The generally lower resistivity values found in the gabbro-norite are also consistent with ground AMT results (Greg Walker, 2011, pers. comm.). In contrast, the 2D AirMt model appears to overestimate the target depth, relative to the remaining three inversions, but this may also reflect the poorer quality model-misfits. The increased near-surface conductivity observed in all four model sections that extends south of Babel is consistent with thicker, higher conductance overburden cover that was also observed in ground AMT results.

Figure 13, Figure 14, Figure 15, and Figure 16 provide representative resistivity depth-slices from the 2D and 3D ZTEM and AirMt inversion models for north-south lines over Nebo Babel. Unlike the cross-sectional views, these plan maps clearly highlight the improved imaging of the 3D inversion results as compared to the 2D – in particular: A) Although 2D ZTEM resistivity slice in Figure 13 shows anomalous conductivity over both deposits, across Babel, in particular, the east-west strike length appears to be over-exaggerated, likely due to effects of footprint side-scanning in the 2D inversion; more importantly, the Jameson Fault is not defined, due to fact that it is parallel to the north-south line orientation chosen for the 2D inversions;. B) Although the 2D AirMt resistivity slice in Figure 14 arguably better defines the NNE-SSW Jameson Fault, relative to ZTEM 2D, neither the Babel nor the Nebo deposits are particularly well defined or highlighted in plan; on the other hand, the strike extension of Babel to the southwest is consistent with the geologic plunge of the deposit. C) Of the four images shown, the 3D ZTEM inversion resistivity slice in Figure 15 shows anomalous conductivity that is not only more focused, with shorter strike-lengths indicated, and better centred directly over both Nebo and Babel, but also readily images the Jameson Fault, a result that had been absent in previous 2D inversion results; D) The 3D AirMt inversion resistivity depth-slice in Figure 16 is somewhat coarser than the other 3 inversion images, but nonetheless displays the best contrasted anomalous conductivities over Nebo, Babel and the Jameson Fault; it also appears to be the least impacted of the 3 inversions by the thickening conductive overburden blanket in the south survey area.

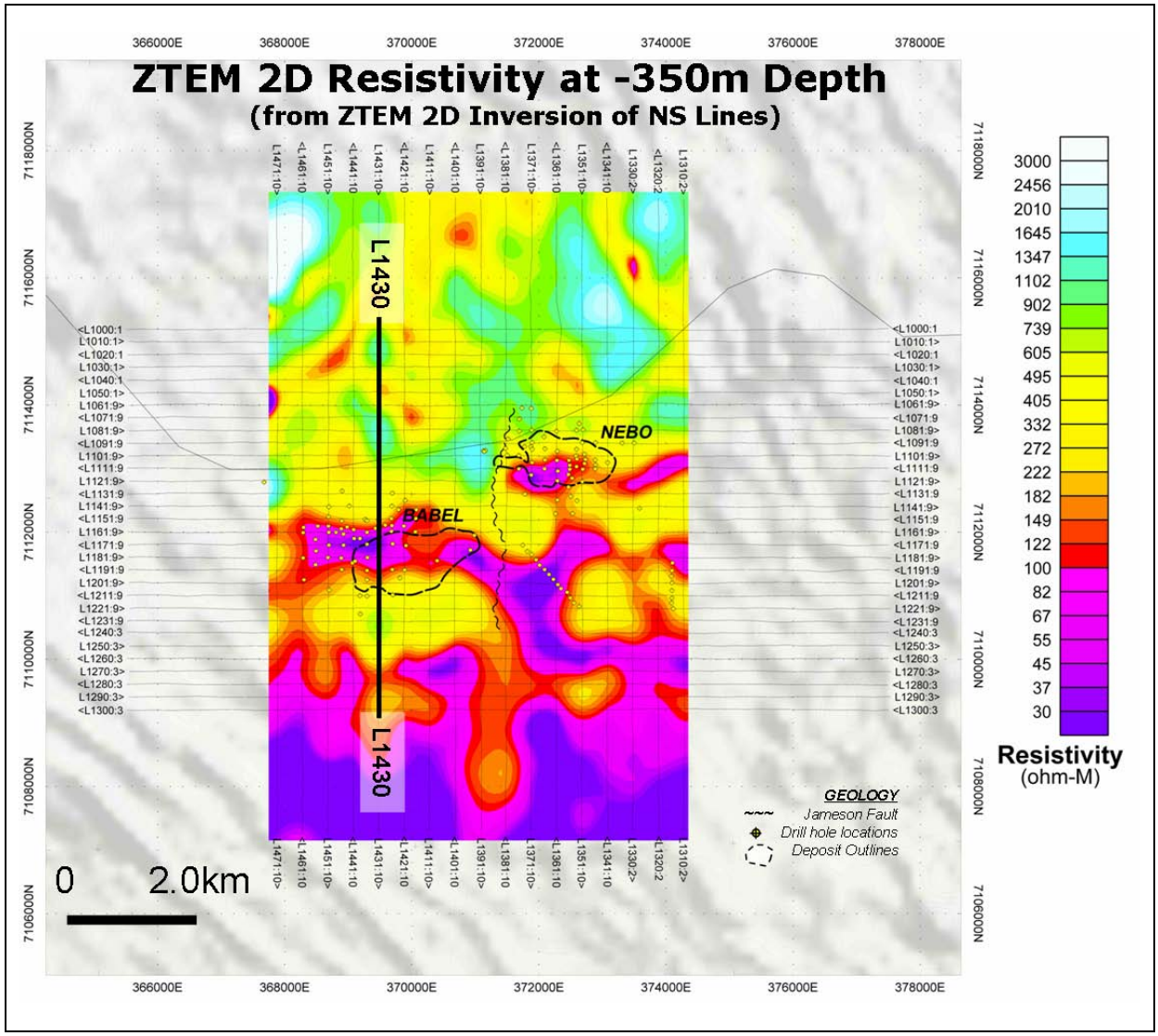

Figure 13. Resistivity depth-slice at -350 m from 2D ZTEM inversions.

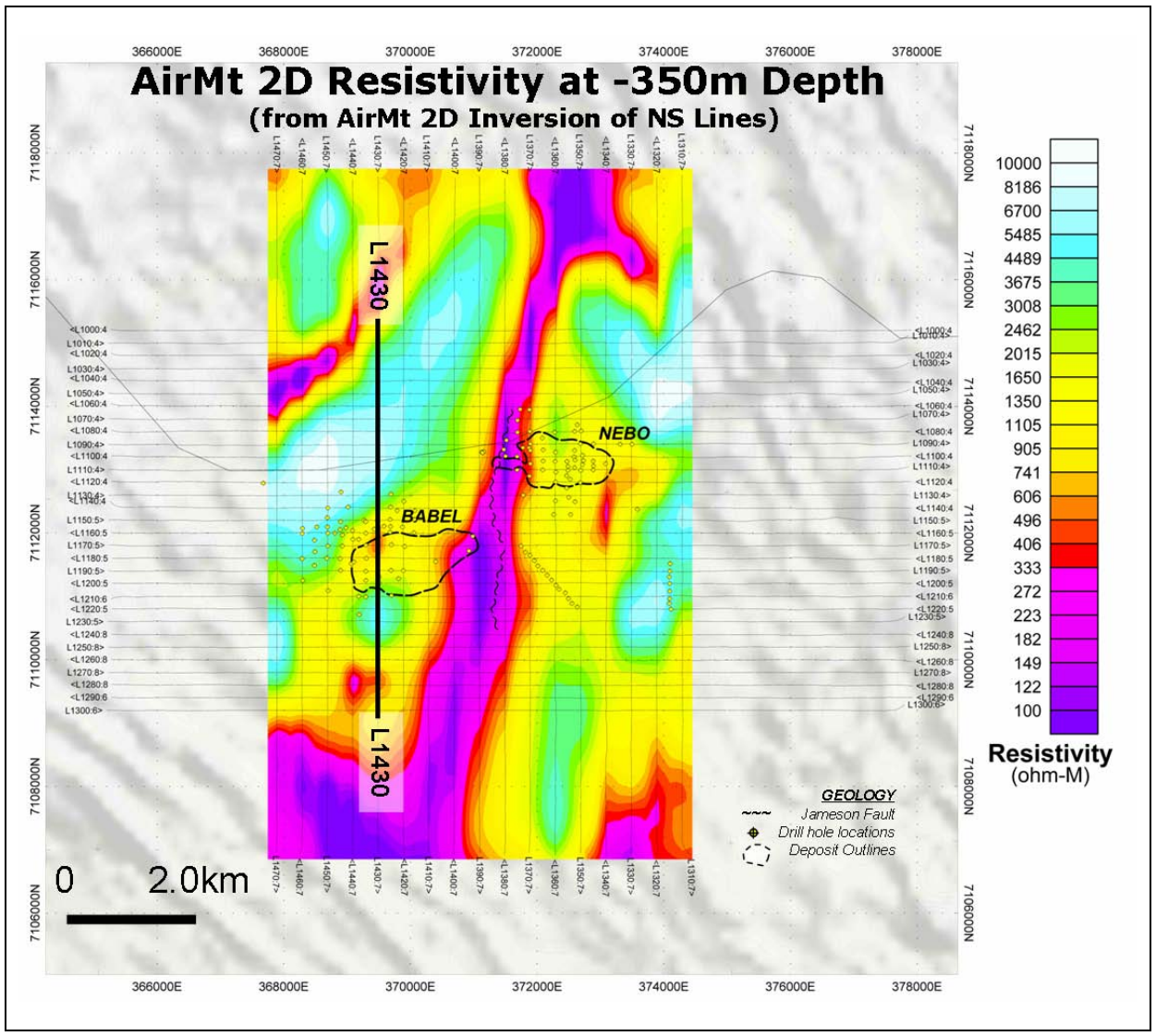

Figure 14. Resistivity depth-slice at -350 m from 2D AirMt inversions.

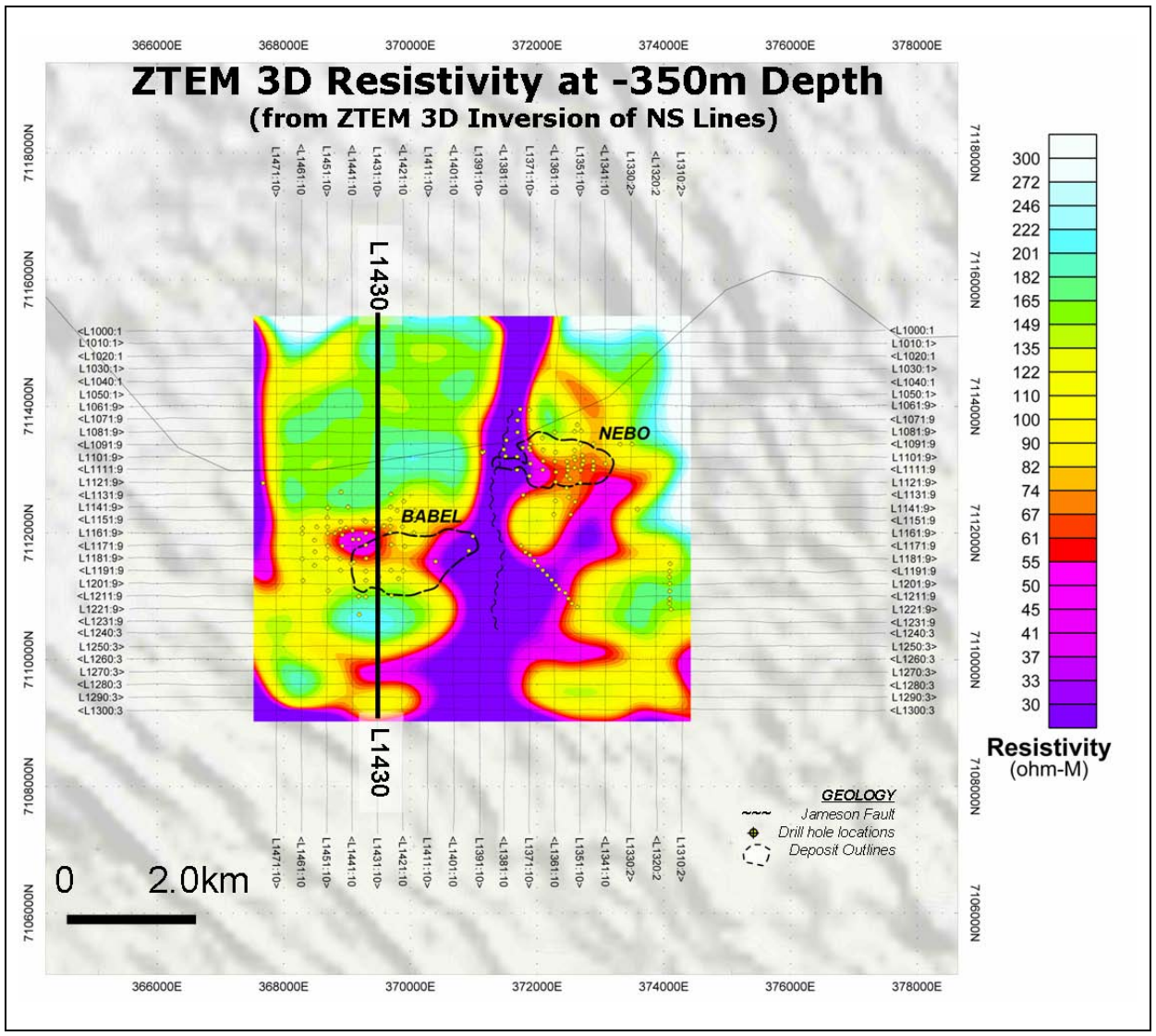

Figure 15. Resistivity depth-slice at -350 m from 3D ZTEM inversion.

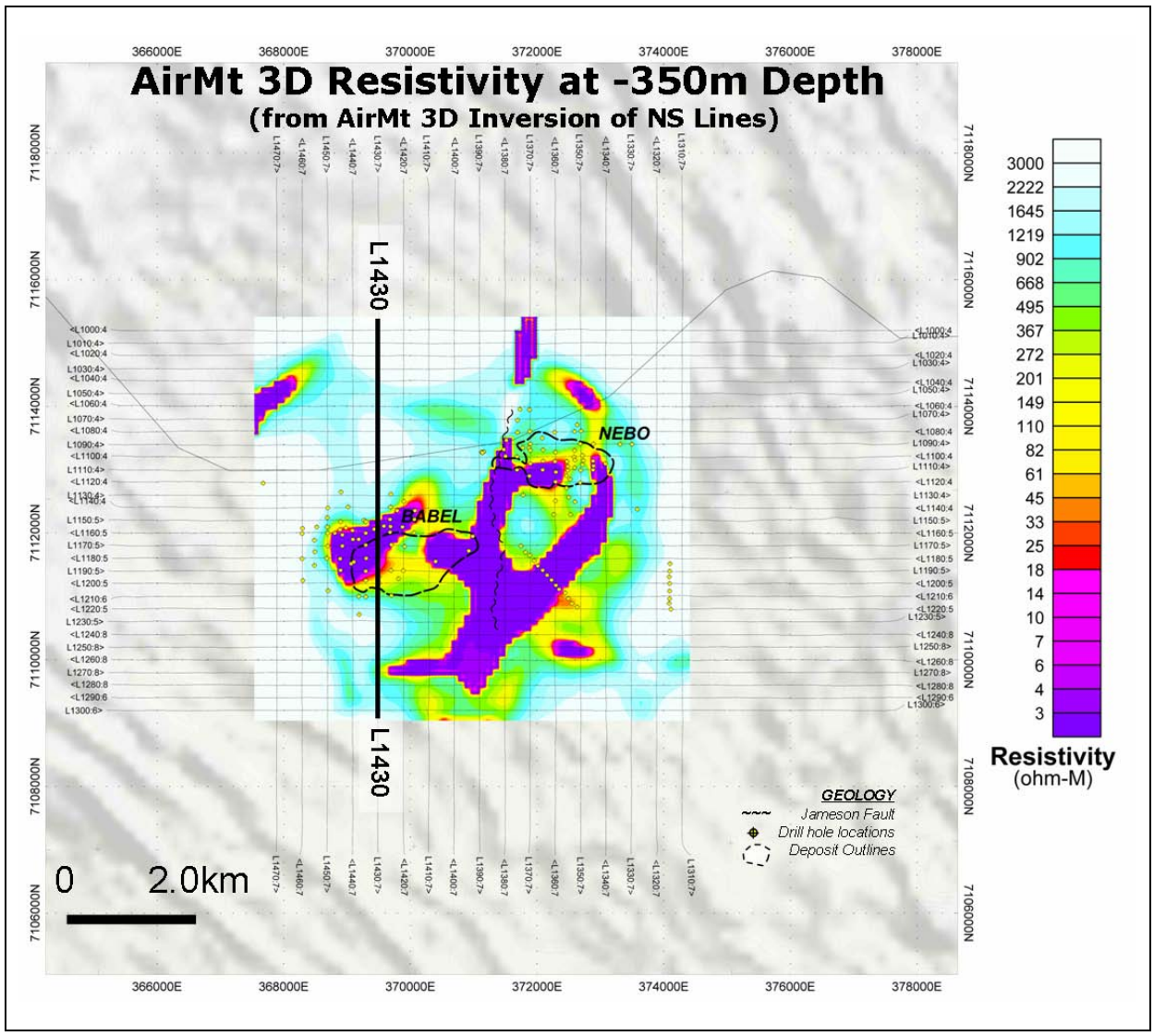

Figure 16. Resistivity depth-slice at -350 m from 3D AirMt inversion.

Conclusions

Given global industry trends towards deeper exploration under cover, ZTEM and AirMt represent practical airborne electromagnetic methods for mapping conductivity to depths in excess of 1 km in terrain of suitable conductivity. As ambient (natural) source electromagnetic methods, allowing a plane wave source to be reasonably assumed in most instances, ZTEM and AirMt data are derived from robust data processing techniques that enable 3D quantitative interpretation. Interpretation of both ZTEM and AirMt data is analogous to magnetovariational (MV) data, and in principle, similar to magnetotelluric (MT) data. We have demonstrated this with a case study involving the interpretation of over 500 line km of both ZTEM and AirMt data from BHP Billiton's Nebo-Babel Ni-Cu-PGE deposit in Western Australia's West Musgrave district.

The analyses of the ZTEM and AirMt survey results and their interpretation using 2D and 3D inversion have shown that both passive EM technologies map the subsurface geology and structure, based on lateral resistivity contrasts, seemingly equally well. Comparisons between ZTEM DT and TPR data images against the AirMt AP data image show strong similarities between both technologies, which is perhaps to be expected. On the other hand, although both ZTEM and AirMt display anomalous responses over the Nebo and Babel deposits, neither appears to resolve or differentiate the increased conductivity associated with the massive sulphides contained in them from more weakly conductive features in the surrounding geology, notably fault-structures and lithological features. This can possibly

be seen as an advantage by some in terms of geologic mapping of mineral deposit environments, or as a disadvantage by others in terms of the direct detection of mineral deposits themselves.

In contrast with visualizing the data on their own, the process of inversion appears to significantly improve the resolution and differentiation of the Nebo and Babel mineral deposits, particularly in cross-section, where the known deposit locations feature well defined conductive anomalies in the 2D and 3D inversion models for both ZTEM and AirMt. The airborne resistivity images also generally agree with those from ground resistivity surveys.

In plan, however, the weaknesses of the 2D inversions are highlighted, notably: a) the directional sensitivity of line orientation to geologic strike that affects the 2D ZTEM inversions to the greatest extent (i.e., Nebo-Babel is only properly imaged in NS lines and the Jameson Fault is only imaged in EW lines); and b) the more weakly contrasted 2D AirMt image that is due, in part, to its inherently smooth behaviour, but also because of lower model-data misfits that are, presumably, a reflection of greater sensitivity of the AirMt AP data measurement to 3D behaviour. In marked comparison to these 2D models, the 3D inversion images in plan appear to more clearly define distinctive anomalies over Nebo and Babel that can also be more easily differentiated from the NS and NE structures that are present. And in the case of ZTEM, the conductive anomalies over Nebo and Babel are better defined in the 3D inversion model; whereas for AirMt, the 3D inversion appears to produce the most contrasted anomalies over the deposits and fault zones, relative to 2D.

The ZTEM and AirMt case-study and inversion comparison at Nebo-Babel has not only served to introduce two new airborne EM survey applications but has also presented field results over a well known ore deposit in a typical Australian regolith environment. It has enabled the current interpretation methodologies to be clearly described and illustrated, including initial plan view data processing, 2D inversion and culminating in the more advanced 3D inversion approaches. This should be of great value to those contemplating similar surveys or those faced with interpretation of acquired data.

Acknowledgements

The authors acknowledge Geotech, TechnoImaging, and BHP Billiton for permission to publish. Gribenko and Zhdanov acknowledge support of the University of Utah's Consortium for Electromagnetic Modeling and Inversion (CEMI).

References

Constable, S. C., Parker, R. L., and Constable, C.G., 1987, Occam's inversion: A practical algorithm for generating smooth models from electromagnetic sounding data: Geophysics, 52, 289-300.

de Lugao, P. P., and Wannamaker, P.E., 1996, Calculating the two-dimensional magnetotelluric Jacobian in finite elements using reciprocity: Geophysical Journal International, 127, 806-810.

Farquharson, C. G., Oldenburg, D. W., Haber, E., and Shekhtman, R., 2002, An algorithm for the three-dimensional inversion of magnetotelluric data: SEG Expanded Abstracts, 21, 649-652.

Groves, D. I., Groves, I. M., Gardoll, S., Maier, W., and Bierlein, F. P., 2007, The West Musgrave – a potential world-class Ni-Cu-PGE sulphide and iron oxide Cu-Au province? Presented at AIG Conference, Perth.

Holtham, E., and Oldenburg, D. W., 2010, Three-dimensional inversion of ZTEM data: Geophysical Journal International, 182, 168-182.

Hursán, G., and Zhdanov, M. S., 2002, Contraction integral equation method in three-dimensional electromagnetic modeling: Radio Science, 37, doi: 10.1029/2001RS002513.

Kaminski, V. F., Kuzmin, P., and Legault, J. M. 2010, AirMt – passive airborne EM system: Presented at 3rd CMOS-CGU Congress, Ottawa.

Kuzmin, P. V., Borel, G., Morrison, E. B., and Dodds, J., 2010, Geophysical prospecting using rotationally invariant parameters of natural electromagnetic fields: WIPO International Patent Application No. PCT/CA2009/001865.

Labson, V. F., Becker, A., Morrison, H. F., and Conti, U., 1985, Geophysical exploration with audiofrequency natural magnetic fields: Geophysics, 50, 656-664.

Legault, J. M., Kumar, H., Milicevic, B., and Hulbert, L., 2009, ZTEM airborne tipper AFMAG test survey over a magmatic copper-nickel target at Axis Lake in northern Saskatchewan: SEG Expanded Abstracts, 28, 1272-1276.

Pare, P., and Legault, J. M., 2010, Ground IP-resistivity and airborne SPECTREM and helicopter ZTEM survey results over Pebble copper-moly-gold porphyry deposit, Alaska: SEG Expanded Abstracts, 29, 1734-1738.

Sattel, D., Thomas, S., and Becken, M., 2010, An analysis of ZTEM data over the Mt Milligan porphyry copper deposit, British Columbia: SEG Expanded Abstracts, 29, 1729-1733.

Seat, Z., Beresford, S. W., Grguric, B. A., Waugh, R. S., Hronsky, J. M. A., Gee, M. A. M., Groves, D. I., and Mathison, C. I., 2007, Architecture and emplacement of the Nebo-Babel gabbronorite-hosted magmatic Ni-Cu-PGE sulphide deposit, West Musgrave, Western Australia: Mineralium Deposita, 42, 551–581.

Seat, Z., Beresford, S. W., Grguric, B. A., Mary Gree, M. A., and Grassineau, N. V., 2009, Re-evaluation of the role of external sulfur addition in the genesis of Ni-Cu-PGE deposits – evidence from the Nebo-Babel Ni-Cu-PGE deposit, West Musgrave, Western Australia: Economic Geology, 104, 521-538.

Tarantola, A., 1987, Inverse problem theory: Elsevier, Amsterdam.

Wannamaker, P. E., Stodt, J. A., and Rijo, L., 1987, A stable finite element solution for two-dimensional magnetotelluric modeling: Geophysical Journal of the Royal Astronomical Society, 88, 277-296.

Ward, S., 1959, AFMAG – airborne and ground: Geophysics, 24, 761-787.

Ward, S. H., O'Donnell, J., Rivera, R., Ware, G. H., and Fraser, D. C., 1966, AFMAG – applications and limitations: Geophysics, 31, 576-605.

Zhdanov, M. S., 2002, Geophysical inverse theory and regularization problems: Elsevier, Amsterdam.

Zhdanov, M. S., Smith, R. B., Gribenko, A., Čuma, M., and Green, A. M., 2011, Three-dimensional inversion of large-scale EarthScope magnetotelluric data based on the integral equation method – geoelectrical imaging of the Yellowstone conductive mantle plume: Geophysical Research Letters, 37, doi:10.1029/2011GL046953.

Natural EM fields from a controlled source perspective

James Macnae [1]

[1] *RMIT University School of Applied Sciences (James.macnae@rmit.edu.au)*

Abstract

From a controlled source exploration perspective, natural EM fields are usually regarded quite simply as unwanted noise, and major efforts are made to get rid of this "noise". The converse is also true.

In textbooks and most research papers, the natural or magnetotelluric (MT) signals are assumed to propagate vertically, with variable horizontal electric field polarizations, and most processing software generally assumes sources are at infinity. Without source information, the horizontal magnetic fields are used as a time (phase) and amplitude reference for horizontal electric field or vertical magnetic field components.

At audio magnetotelluric (AMT) frequencies, the sources are generally "sferics", the fields of distant lightning strikes. We now have extensive lightning and solar wind detection networks in 24 hour operation that define exactly where and when each source "event" occurs, and in theory it is possible to extract the source dipole characteristics from public data. Source information, not conventionally used in MT and AMT, can in concept (a) reduce noise levels, (b) improve our ability to correct static shifts, (c) better map excellent conductors, and (d) identify and assist in the measurement and thus elimination of static shifts.

Introduction

There are many excellent reviews (e.g., Vozoff, 1990; 1991) and some textbooks (e.g., Simpson and Bahr, 2005) on magnetotellurics (MT), whilst geomagnetic deep sounding (GDS) is reviewed by Arora et al., (1999). There are also many others far more qualified than I to describe current methodology in data acquisition and interpretation, and their contributions can be found in this volume. When I was asked to provide a scientific introduction to the Natural Fields Electromagnetics Forum at the 2012 ASEG Conference that would be focused on exploration applications of natural field electromagnetics, and in particular, would be focused on methodologies of the usage of natural fields, I chose to adopt an approach from the perspective of an outsider in the methods.

Since this is an exploration geophysics conference, I am going to focus my discussions on the response of the top 2 km or so, and ignore completely the applications of crustal and deeper sounding. I will also not consider sub-ocean magnetotellurics in this review. With skin-depth δ of an electromagnetic plane-wave in a half-space given (approximately) by $503\sqrt{(\rho/f)}$ where f is frequency in Hz, and ρ is resistivity in Ωm, the 1 Hz to 10 kHz range covers skin depths from 16 to 1600 m in 10 Ωm sedimentary rocks, and 500 m to 50 km in 10,000 Ωm acid volcanic/dry sandstone rocks. It is this "audio" range that is therefore of most interest in direct exploration. Different source mechanisms and considerations apply to natural fields below 1 Hz that are needed for crustal sounding, or for low-resolution studies of the geological environment at mid crustal depths.

Natural source EM methodology

There are four fundamentally different distant source methodologies that can be used with natural electromagnetic data in the 1 Hz to 100 kHz (extended audio frequency) range to predict Earth conductivity variations, listed here in the order of their first published usage. The abbreviations TE and TM refer to wave polarizations (i.e., transverse electric (TE) or transverse magnetic (TM) modes) and will be discussed later in the paper.

(a) The Electrovariational (EV) or electric wavetilt method was introduced for TE mode in theory by Zenneck (1907) and Sommerfeld (1909), and was tested in TM mode by

Barfield (1934) and Norton (1937). This is the basis for the technically successful Barringer E-Phase and RadioPhase systems.

(b) The attenuation (α) method is occasionally used in conductivity mapping via broadcast signal strength analysis (Hack, 1908; Sommerfeld, 1909).

(c) Magnetovariational (MV) methods are used in the AFMAG and ZTEM systems. This method can only indirectly provide resistivity and has no response over a half-space (TM mode), or a small response close to the source (TE mode). This methodology was, to my knowledge, first discussed by Sommerfeld (1909) before being investigated to determine the conductivity of the Earth's core by Chapman (1919) and introduced to geophysical exploration by Ward (1959).

(d) The common Magnetotellurics (MT) method was invented independently in Japan (Rikitake, 1948), Russia (Tikhonov, 1950) and France (Cagniard, 1953).

I will now proceed to discuss the requirements of each of these methods. Note that the MV and attenuation methods were developed for predicting Earth resistivity several years before Wenner (1915) and Schlumberger introduced DC resistivity sounding methods.

Impedance or magnetotelluric method (MT)

Distant source EM data are mostly treated mathematically in the geophysical literature as vertically incident "plane-waves" on a half-space, (McNeill and Labson, 1991 or Ward and Hohmann, 1988, Berdichevsky and Dmitriev, 2008). The half-space resistivity (ρ) extraction method derived under the assumption of vertical plane wave incidence on a half-space is the magnetotelluric (MT) method which involves measuring perpendicular, horizontal E and horizontal H components of the field, and deriving a half-space impedance converted to apparent resistivity ρ through the equation

$$E_x / H_y = E_y / H_x = (1 + j) \sqrt{} (\omega \mu_0 \rho / 2), \qquad (1)$$

where j is $\sqrt{}$-1, ω is the angular frequency and μ_0 is the magnetic permeability of free space. This equation is usually a good approximation and applies to uniform, cylindrical and spherical guided waves. However, at high frequency or resistivity, the approximation breaks down as will be discussed. There is an extensive ground MT literature, with many recent advances covered in the other papers of this volume.

Electric wavetilt method

The first resistivity prediction method invented was the electric wave-tilt method (McNeill and Labson, 1991) where the ratio between the maximum horizontal E_h and the vertical E_z fields for horizontal plane wave incidence (guided transverse magnetic TM mode, Jordan and Balmain, 1968) is given by an almost identical expression to equation 1, specifically:

$$E_h / E_z = (1 + j) \sqrt{} (\omega \varepsilon_0 \rho / 2). \qquad (2)$$

The only change on the right hand side from equation (1) is the replacement of μ_0 by ε_0, the dielectric permittivity of free space. This equation (2) is locally incorrect for spherical guided waves when the rotation due to curvature is significant within one wavelength. Equation (2) is most useful for frequencies greater than 5 kHz where the Earth can be treated as flat within one wavelength (e.g., 30 km at 10 kHz). Comparisons of the magnetotelluric and EV wavetilt amplitudes are shown in Figure 1 to illustrate their equivalence from a signal perspective.

Barringer's E-phase and RadioPhase systems used the physics in equation (2) to compare the horizontal quadrature component of E to the vertical component from VLF and broadcast AM radio respectively. The use of the quadrature component is absolutely necessary because the horizontal E values are usually a very small fraction of the vertical E field, and any sensor rotations would induce a fraction of the vertical component into the horizontal antenna. The EV method has only been geophysically implemented at VLF or higher frequencies, and as a result provided too little penetration to be useful in exploration. It could however have many applications in near-surface geophysics, but no commercial equipment or services are available to my knowledge.

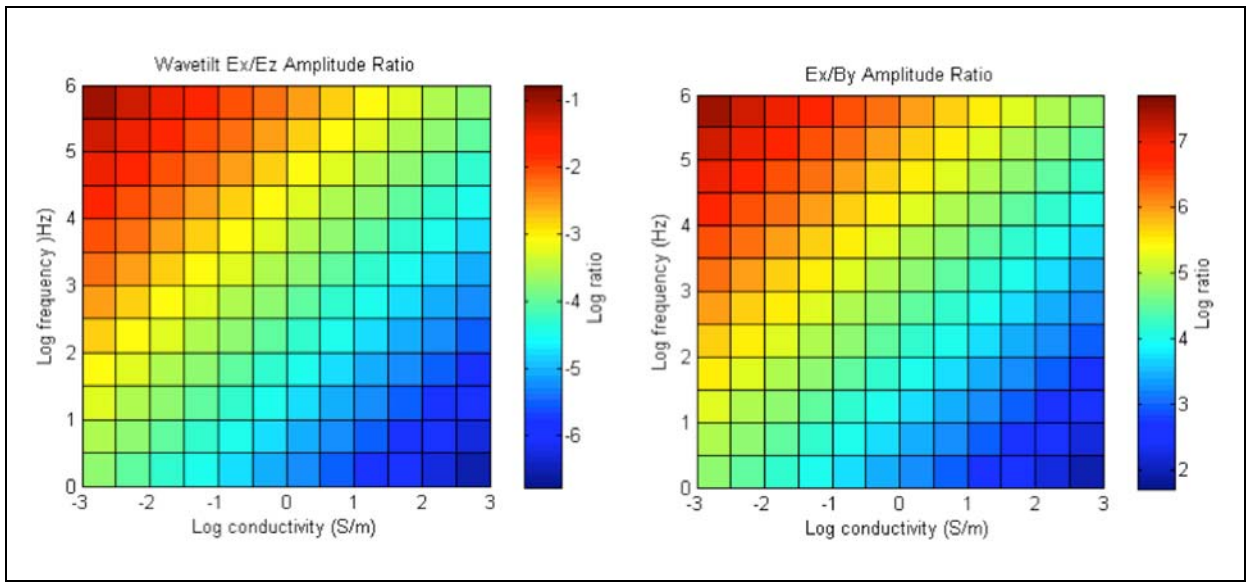

Figure 1. (left panel) Wavetilt amplitude in equation (2) indicates that the horizontal component of E is several orders of magnitude smaller than the vertical component for frequencies less than 10 kHz and Earth resistivity values less than 100 Ωm (> 0.01 S/m). (right panel) MT impedance from equation (1) shows that, with typical Earth resistivity values, the E field has amplitude of the order of nV/m to μV/m or more when the B field is of the order of pT.

Attenuation method

This method is alluded to in the Schumann resonance literature and it forms the basis for conductivity maps used in the antenna installation industry and those derived from AM/FM radio broadcasts (Jordan and Balmain, 1968). I have not, however, found any reference to the use of this method in geophysical exploration. The attenuation method estimates local conductivity using the finite conductivity 'power-loss' as TEM waves propagate in the Earth-ionosphere waveguide, leading to an exponentially decreasing amplitude $e^{-\alpha x}$ where x is the distance in the direction of propagation. Ignoring the spherical expansion and contraction as waves travel around the world, the expression for α at "large" distances from a source can be extracted from Jordan and Balmain (equation 7-46) to be:

$$\alpha = \{ \sqrt{(\omega \mu_0 / \sigma)} + \sqrt{(\omega \mu_0 \rho)} \} / 2h \qquad (3)$$

where h is the Earth-ionosphere separation, ρ is Earth resistivity, and σ is the ionosphere conductivity. Due to day/night ionospheric height and conductivity variations, h and σ are not constant, but representative values can be assumed. The amplitude decline over a 1000 Ωm halfspace would be approximately 40 ppm per km at 1 kHz, and 13 ppm per km at 10 Hz. Over a 10 Ωm halfspace, the attenuation is an order of magnitude smaller. Measurements of individual sferic B or dB/dt amplitudes to such small ppm accuracies of an already very small signal are unrealistic, so local conductivity estimation at airborne survey resolutions would appear to be very difficult if not impossible using this fourth method of attenuation. In addition to this attenuation, there are amplitude effects due to field expansion and contraction which need to be considered. The frequency dependent attenuation (incidentally occurring more in the ionosphere than in the Earth) does cause the dispersion seen in sferics over long baselines, and with a full spherical formulation and appropriate use of specific TM and TEM attenuation factors, could realistically be used to extract average conductivities on, say, a regional 10 to 100 km grid.

Magnetic wavetilt method

A method being used for core conductivity estimates (Chapman, 1919) is the magnetic wavetilt or magnetovariational (MV) method. Its applications in exploration geophysics have been named AFMAG (Ward, 1959) and in crustal geophysics at lower frequencies it has been called Geomagnetic Deep Sounding. MV methods map lateral variations in conductivity rather than the actual conductivity values, but conductivity can be predicted indirectly from spatial variations in the ratio of vertical to horizontal B components. This last approach is taken in Geotech's airborne ZTEM system and several

VLF instruments. Reasonably recent references to MV principles include McNeill and Labson (1991). The severe limitations of AFMAG identified in Ward et al. (1966), specifically, the ambiguity of response with target direction, can now potentially be addressed with 3D inversion or by using the lightning detection networks and local references to separate different source directions.

Limitations of the fundamental assumptions of MT

MT measures Earth impedance Z through the ratio of components E/H, MV uses the ratio of vertical to horizontal magnetic components to locate subsurface currents, and EV estimated impedance from the ratio of vertical to horizontal electric fields in quadrature in the air. MV only provides indirect estimates of Earth impedance; EV and MT are direct measures.

The myth of MT:
The source signal (MT) is a vertically propagating plane wave from directly above the survey site that can be assumed to be uniform. This myth was first independently asserted by Cagniard (1952) and Tikhonov (1950), and has persisted to this day.

The truth about MT:
The majority of useful signal in the 5 kHz to 100 kHz bandwidth comes from “slightly distant” common negative lightning strikes either well within the local hemisphere or at the antipodes. The majority of useful signals in the 1 Hz to 1 kHz band come from occasional worldwide occurrences of positive lightning, sprites and elves. The source signal that is needed for the EV method to work is a sub-horizontally propagating plane wave in the Earth-ionosphere waveguide. Incontrovertible evidence for this comes from existence of the Schumann resonances. These resonances arise at frequencies where the wavelength c/f is an integer multiple of the waveguide circumference and where c is the speed of light and f is frequency.

Why has the myth of vertical MT rather than horizontal source incidence persisted? The answer lies in the physics, expressed mathematically. James Wait, the world’s most modest and prolific ‘electromagnetician’, asserted in 1954 that EM energy is carried in a sub-horizontally propagating wave that is partially reflected and partially refracted into the Earth or out of the ionosphere, with refracted energy travelling sub-vertically except in ‘resistive ground’ (i.e., more than a few thousand Ωm). The angle of refraction depends on polarization (TE or TM), Earth resistivity, relative dielectric permittivity, and frequency. The expressions for TE and TM mode plane wave reflections can be found in many electromagnetic textbooks and in Ward and Hohmann (1989).

Before discussing EM energy propagation in the Earth-ionosphere waveguide, I need to introduce the global current circuit.

The atmospheric circuit and charge balance

The motion of the Sun, planets and moons obey the laws of gravity, which implies they are not strongly charged, which further implies that the solar wind is, on average, neutral. Energy from the Sun and the effects of energetic protons in the electrically neutral solar wind ionize a number of different layers in the atmosphere. Conductivity in these ionized layers is of the order of 1 mS/m, and in the un-ionized atmosphere about 10 fS/m.

There are a number of causes for current flow in the atmosphere, but overall it is a requirement that charge be conserved, and that overall the charge in the “circuit” must balance. Components of the global atmospheric circuit are seen in Figure 2. Although volcanoes, atmospheric nuclear explosions, hurricanes and tornados have associated lightning discharges, these elements of the circuit occur less frequently than thunderstorm activity and are ignored here.

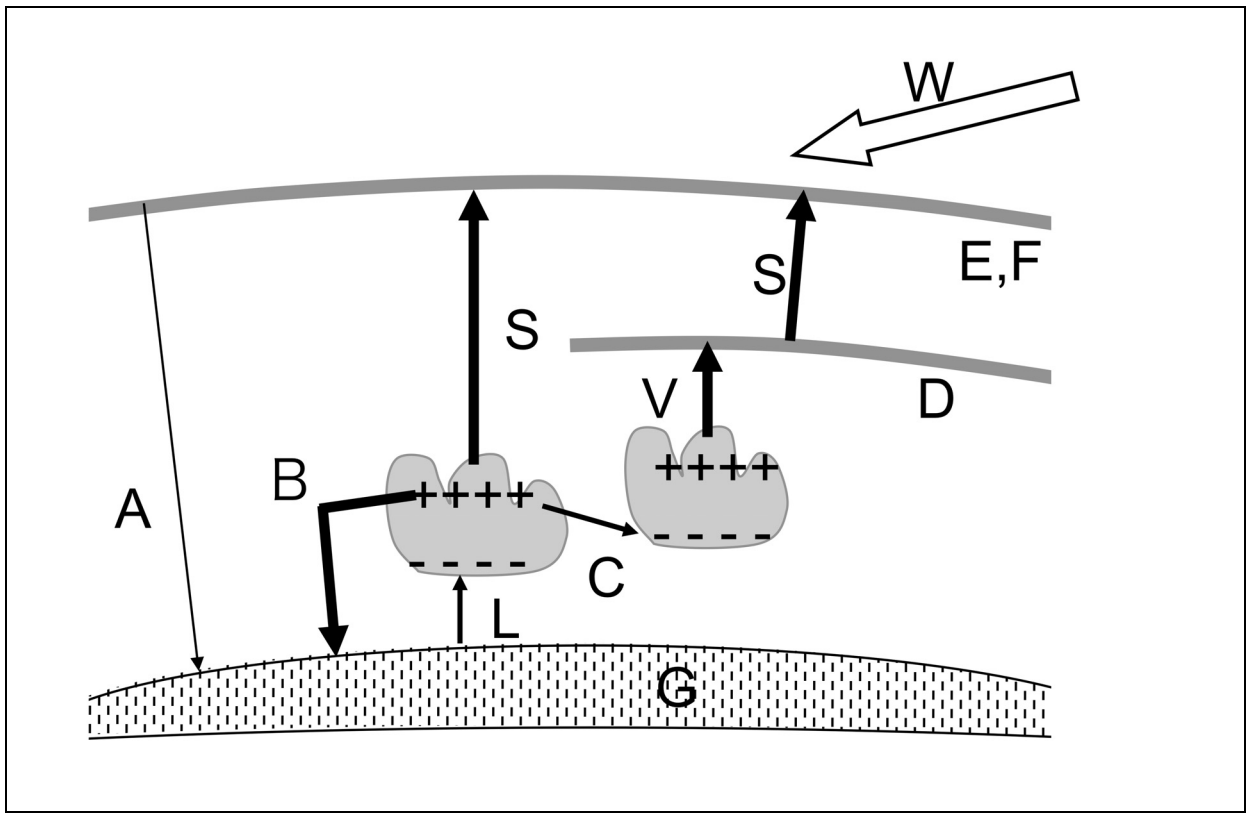

Figure 2. The global atmospheric current circuit at sunset (looking south), consisting of high ionospheric layers E, F and a daytime layer D, all of which are a consequence of solar energy (W); Wind (A) is the fair-weather current; L is normal negative lightning from cloud to ground (G); C is intra and inter-cloud lightning; V are blue jet; S are sprite currents; B is positive lightning.

Fair weather current

Dry air has an electrical conductivity around 10^{-14} S/m. In fair weather, there is observed a vertical electric field of about 100 V/m between the Earth and the ionosphere, which causes a current, the so-called "fair weather current" of about 1 pA/m^2 to flow downwards from the ionosphere to the Earth. In fact, electrons flowing upwards cause most of the current.

Cloud-Earth Lightning

Cloud to Earth lightning is the one component of the global current circuit commonly "seen" by the general public. A typical cloud-to-ground lightning stroke transfers electrons with equivalent current of typically 30 kA for about ten microseconds, radiating energy with a peak frequency in the 10 to 100 kHz range (Figure 3). The spherically radiated EM field from a vertical electric dipole has a cosine amplitude distribution with its peak in the horizontal plane (Figure 4), and energy moves outwards at the speed of light. The peak amplitude of the radiated wave has a vertical electric field component and a horizontal magnetic component. Engineers like to refer the polarisation of a wave with respect to a reference surface, which in this case would be the surface of the Earth. They would recognise that the magnetic component of the EM field is parallel to the surface of the ground and call this a transverse magnetic or TM wave. The occurrence of cloud-to-ground lightning is in the range of 30 to 60 strikes per second worldwide, depending on which reference you choose to believe.

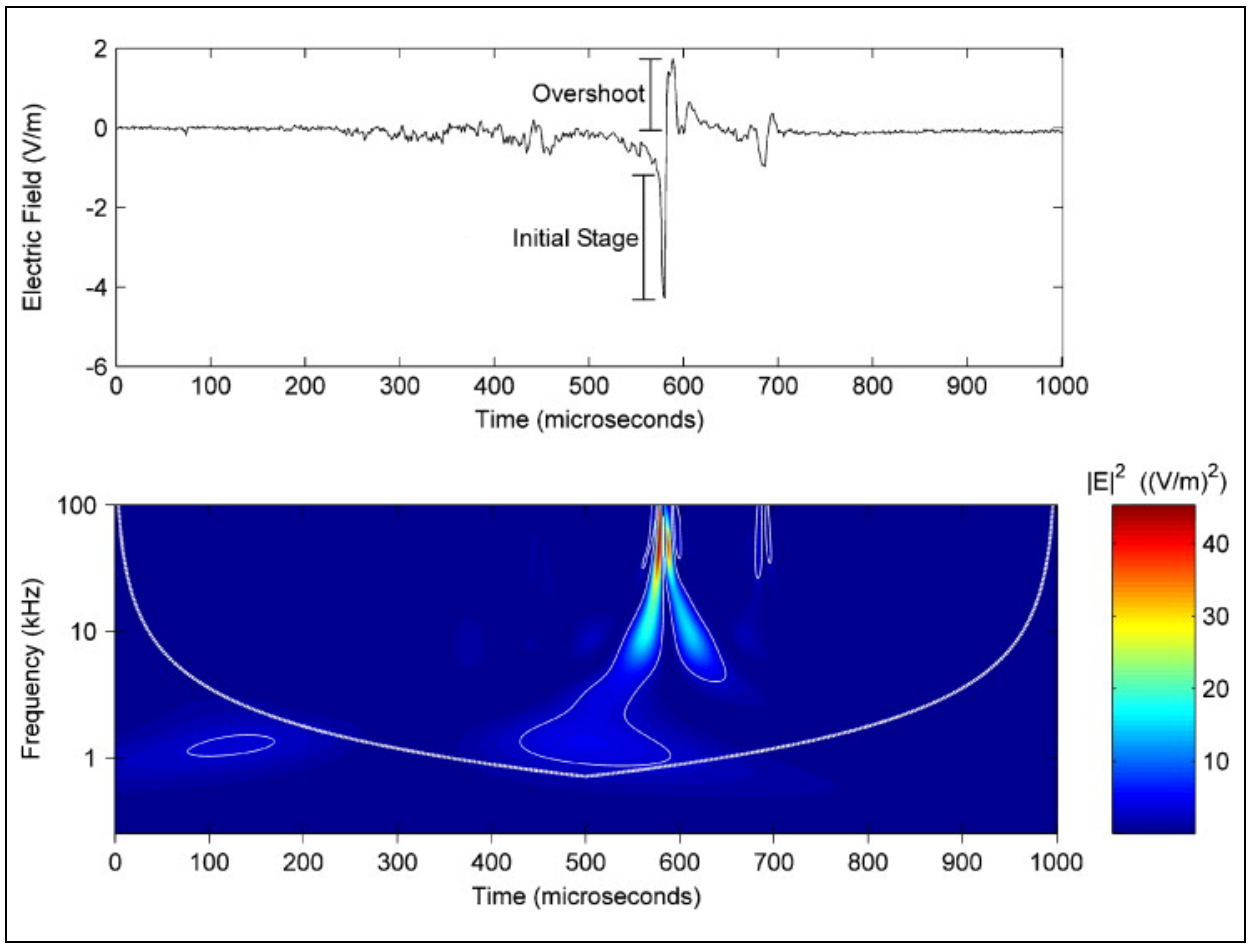

Figure 3. Typical time series and spectrogram collected in the immediate vicinity of a negative lightning strike, with predominantly high-frequency energy due to the short current flow duration (figure from Miranda, 2008).

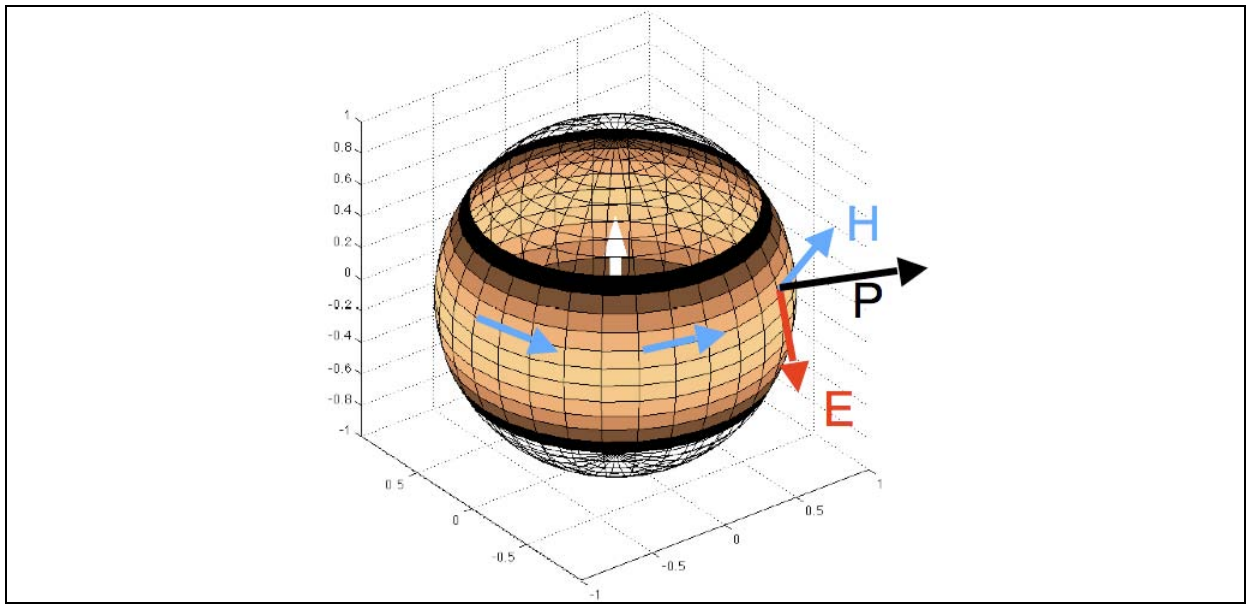

Figure 4. Amplitude in free space of the horizontal magnetic component of the radiated field from a short vertical electric dipole such as cloud-to-Earth or intra-cloud lightning.

Cloud-Cloud lightning

Cloud-to-cloud and intra-cloud lightning is reportedly the most common form of lightning, and is that the component of the global current circuit most commonly heard. The associated flash is often obscured by lower clouds and not seen. Thomas et al. (2001) observe that the highest VHF energy radiation comes from high (5 to 15 km) intra-cloud strikes rather than cloud-to-ground strikes.

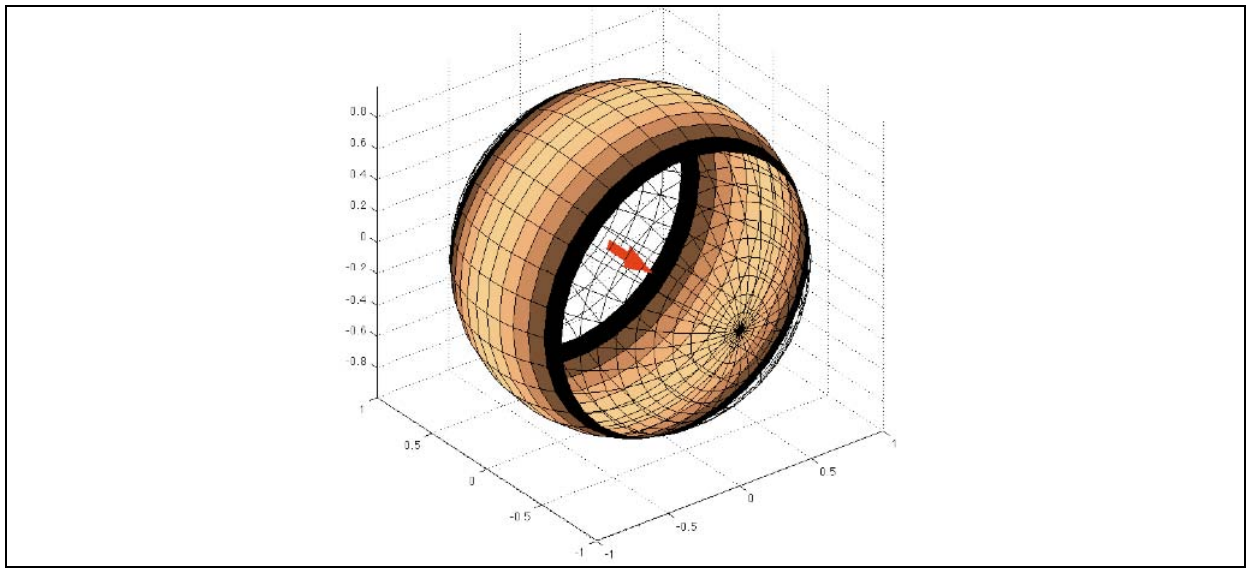

Figure 5. Amplitude in free space of the tangential magnetic component of the radiated field from a short horizontal electric dipole such as cloud-to-cloud lightning.

With a sub-horizontal stroke, the radiated EM field would have a horizontal E component and be classified as transverse Electric or TE mode to an engineer. Significant energy would be radiated only in the direction perpendicular to the lightning stroke. Cloud-to-cloud strokes are typically smaller in both current and stroke-length than cloud-to-ground or intra-cloud strokes. Intra-cloud convection may move charged water-droplets extensively within the cloud without obvious electromagnetic radiation.

Sprites, Elves and Blue Jets

Sprites, Elves and Blue Jets have recently been identified through the correlation of key visual events viewed from space and high-mountain photography with events recorded by lightning detection networks. The accompanying current flow closes the global circuit between clouds and the ionosphere (Reising, 1998). These events are less common than lightning strikes, occurring worldwide at 1 to 10 second intervals. They carry spatially distributed currents with areas of km compared to cm sized lightning bolts. They also have current flow for a longer time than lightning strikes, and are a key part of the global circuit. Figure 6 combines several photographs capturing Elves, Sprites, Blue Jets and normal (i.e., negative base of cloud to ground) lightning.

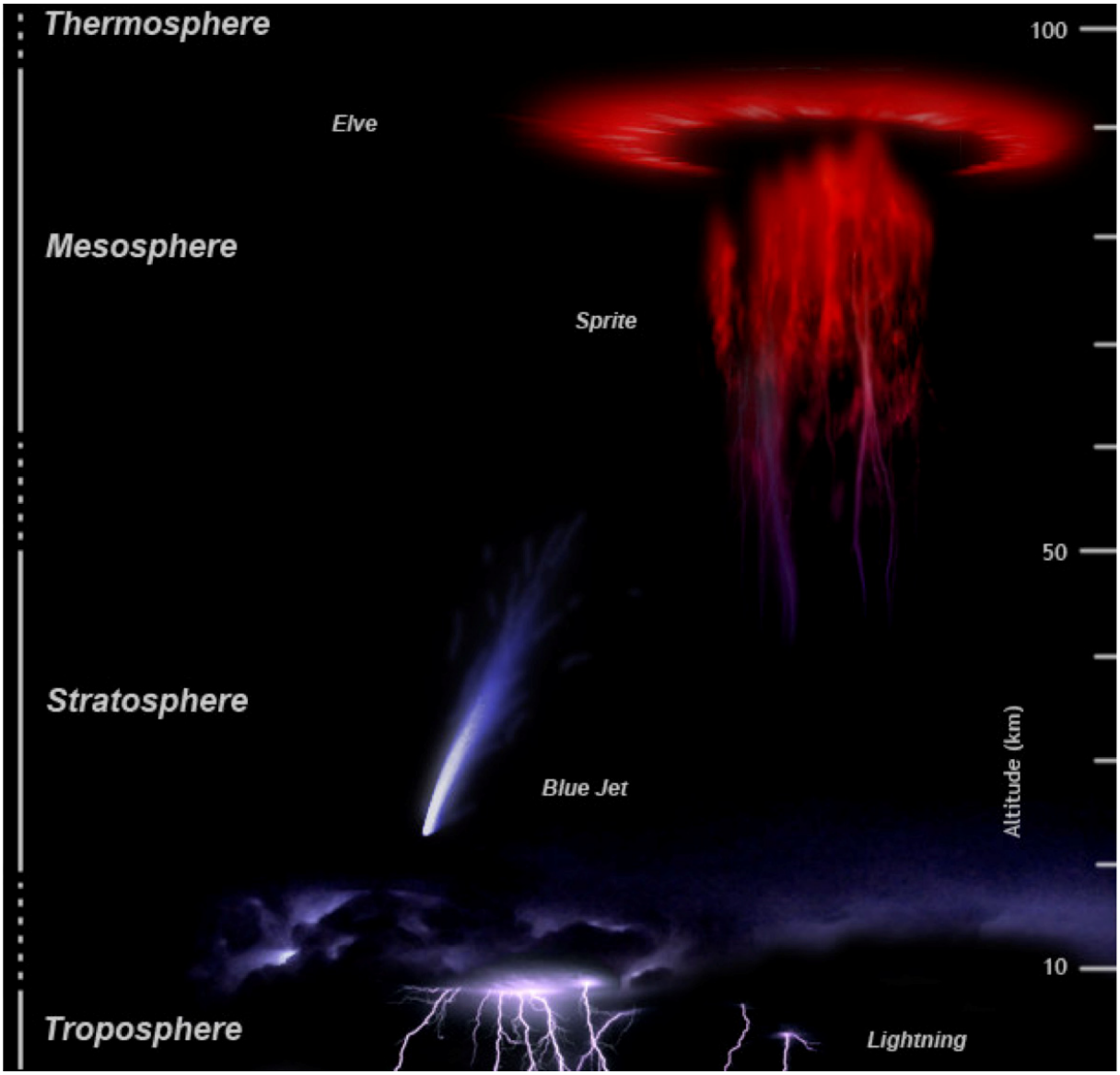

Figure 6. Compilation photograph of night time "visible" components of the global current circuit (Wikipedia commons). The D layer of the ionosphere is located around the visible top of the Blue Jet and bottom of the Sprite.

Bolts from the Blue

Often occurring at the same time as Elves and Sprites is "positive lightning". The direction of current flow can be established from the sign of the associated vertical electric field. These lightning strikes originate from the positive charge at the top of a cloud and strike the ground, often several kilometres away, and at times under locally clear skies (Figure 7). They are thus sometimes called "bolts from the blue". These strikes carry up to 300 kA, or ten times the current of a typical cloud-to-ground lightning strike, and they last for milliseconds rather than tens of microseconds (Figure 8). It is almost certain that these are the source of most low frequency energy (i.e., Schumann resonances that provide ZTEM signals). They have also been reported to be the most common source of forest fires started by lightning due to them having many times greater energy/heat to be dissipated on tree/ground impact, and are almost certainly the source of fulgurites, or fossilized lightning when dry sand is struck.

Figure 7. Over-the-horizon photograph of positive lightning strike from top of cloud. The presence of Venus suggests an early evening timeframe. (Wikipedia commons)

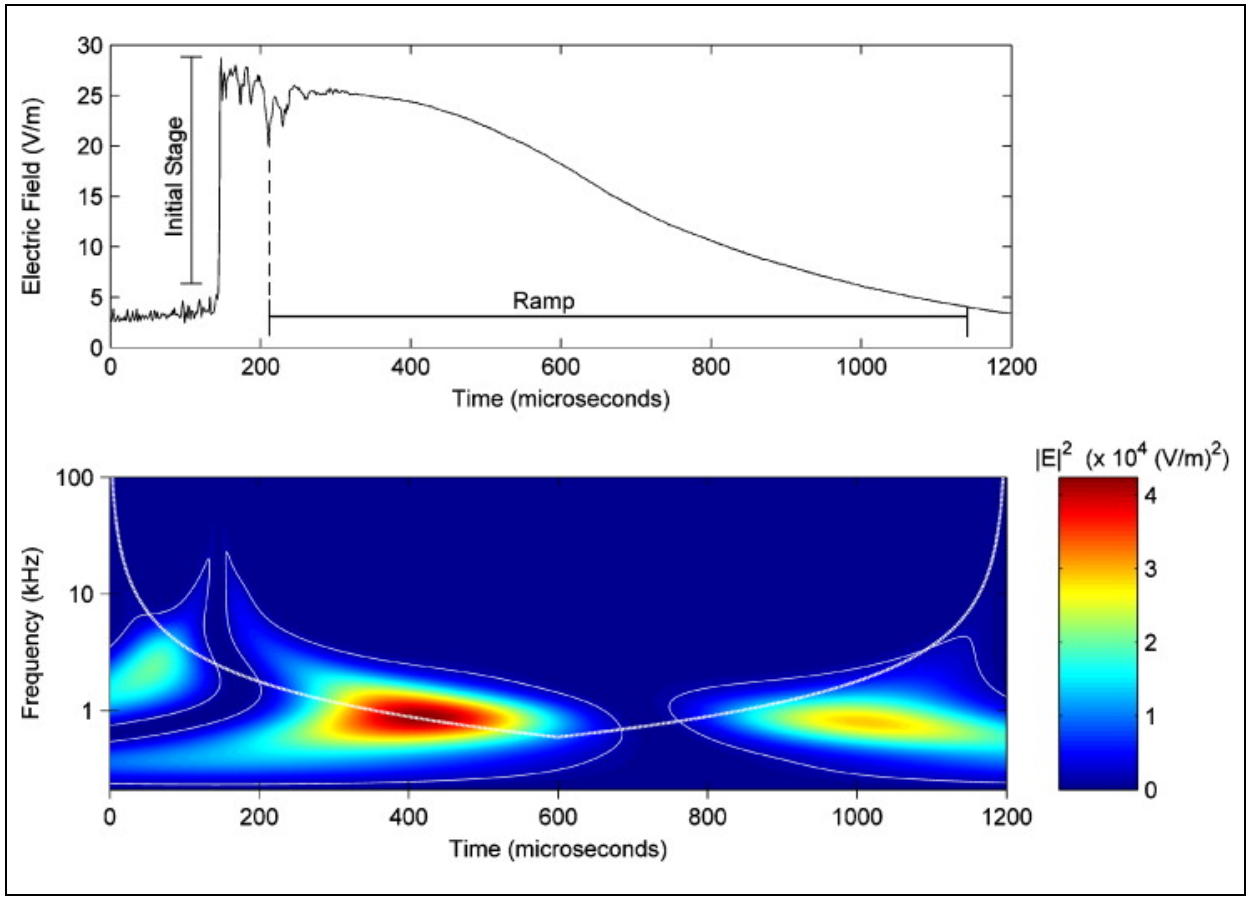

Figure 8. Typical time series and spectrogram collected in the immediate vicinity of a positive lightning strike, with predominantly lower-frequency energy (figure from Miranda, 2008).

EM signals from the sferic source

Wave Propagation

When a sferic EM wave has been launched, it will travel away from the source in the electrically resistive atmosphere. Each time it encounters a boundary, whether ionospheric, at the Earth's surface, or below the surface of the Earth, it will be partially reflected and partially transmitted into the conductor. Using a ray-optics approximation and the Earth-ionosphere geometry, it is possible to predict the minimum number of reflections required to travel a certain distance, and the appropriate angles of reflection.

Figure 9 and Figure 10 schematically show TM and TE reflections. Incident angle ψ is around 15° for maximum travel without reflection assuming an ionosphere at 90 km above an Earth with 6378 km radius. For the frequency range 1 to 100 kHz, and Earth conductivity greater than 0.001 S/m, it is safe to assume that φ is 0 and that the refracted (MT) wave travels vertically. In the TM propagation case, there is a strong vertical component of electric field in the air that is inconsistent with the "standard" assumption of an EM source at the azimuth. Provided that the wave can be assumed to be planar (true for distant sferics), the MT approximation (equation 1) holds in the ground, whether the excitation is TM or TE.

TE mode waves (Figure 10) attenuate faster than TM modes waves (i.e., the values for f and F are larger), and as mentioned tend to have smaller dipole moments and can be ignored in most cases.

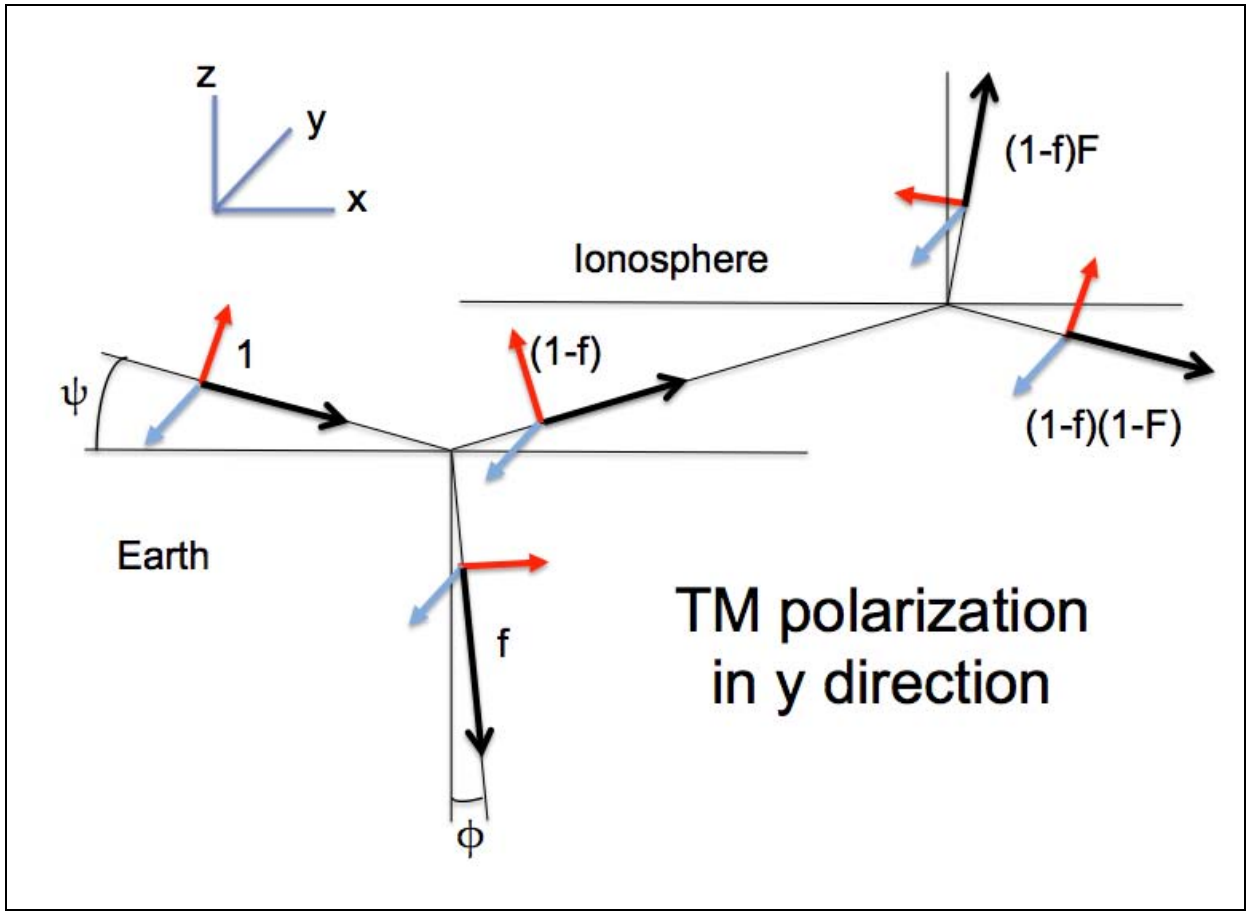

Figure 9. TM reflection fraction f and refraction fraction F of incident power are directed into the Earth and ionosphere respectively. Red vectors show E field direction, Blue H field and Black direction of power radiation (ray tracing). The H field maintains a constant direction.

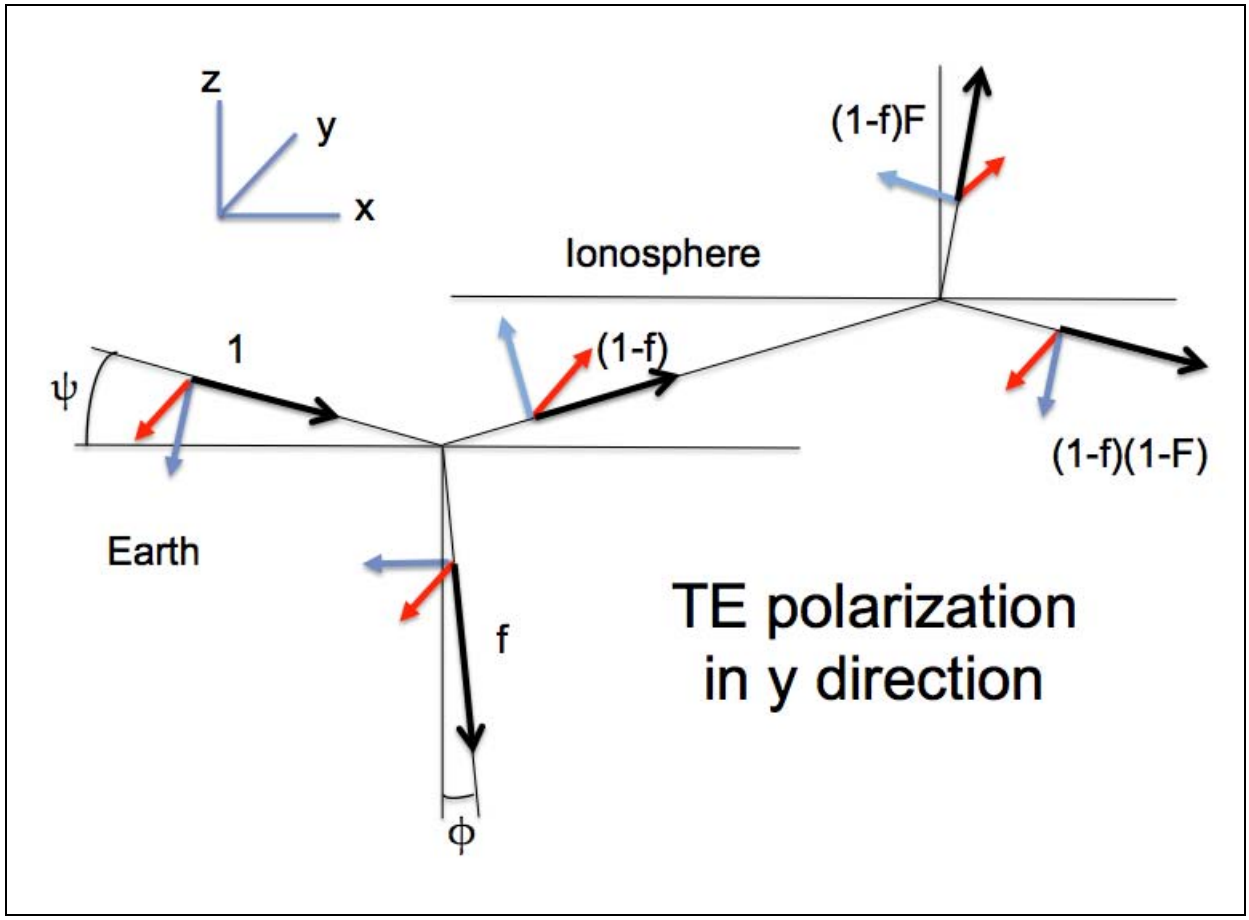

Figure 10. TE reflection fraction f and refraction fraction F of incident power are directed into the Earth and ionosphere respectively. Red vectors show E field direction, Blue H field and Black direction of power radiation (ray tracing). Note the sign reversal in E after reflection and the direction changes in H fields after either reflection or refraction at each boundary. TE mode waves at any distance form the source are strongly reduced by interference effects.

Lightning strike polarity can be unambiguously determined by noting that TM waves (Figure 4 have a constant sign of E_z. Tables of refraction power fraction and refraction angle φ are presented below, calculated for a relative dielectric permittivity of 8, typical of Earth materials. When the Earth conductivity is less than 1 mS/m, for example in sandstone rocks or in acid volcanic rocks that can exhibit conductivities as low as 10 μS/m, the refraction angle φ can be as much as 15 to 20° off vertical, implying that the MT approximation is poor and that the response will be source-direction dependent and have vertical electric fields in the Earth. If the down-going wave encounters a more conductive horizontal conductor at depth, additional refraction will cause the wave to travel in the vertical plane below that horizontal layer.

Table 1. TM mode refraction power fraction values as a function of frequency and conductivity.

Frequency Conductivity	1 Hz	10 Hz	100 Hz	1 kHz	10 kHz	100 kHz
10 S/m	0.00003	0.00006	0.0003	0.0008	0.003	0.008
1 S/m	0.00006	0.0003	0.0008	0.003	0.008	0.03
100 mS/m	0.0003	0.0008	0.003	0.008	0.03	0.08
10 mS/m	0.0008	0.003	0.008	0.03	0.08	0.22
1 mS/m	0.003	0.008	0.03	0.08	0.22	0.55
0.1 mS/m	0.008	0.03	0.08	0.22	0.55	0.91
0.01 mS/m	0.03	0.08	0.22	0.55	0.91	0.98

Table 2. TE mode refraction power fraction values as a function of frequency and conductivity.

Frequency Conductivity	1 Hz	10 Hz	100 Hz	1 kHz	10 kHz	100 kHz
10 S/m	0.000002	0.000005	0.00002	0.00005	0.0002	0.0005
1 S/m	0.000005	0.00002	0.00005	0.0002	0.0005	0.002
100 mS/m	0.00002	0.00005	0.0002	0.0005	0.002	0.005
10 mS/m	0.00005	0.0002	0.0005	0.002	0.005	0.002
1 mS/m	0.0002	0.0005	0.002	0.005	0.002	0.05
0.1 mS/m	0.0005	0.002	0.005	0.002	0.05	0.2
0.01 mS/m	0.002	0.005	0.002	0.05	0.2	0.3

Table 3. Refraction angle φ values for TM and TE mode as a function of frequency and conductivity.

Frequency Conductivity	1 Hz	10 Hz	100 Hz	1 kHz	10 kHz	100 kHz
10 S/m	0.0	0.0	0.0	0.0	0.0	0.1
1 S/m	0.0	0.0	0.0	0.0	0.1	0.2
100 mS/m	0.0	0.0	0.0	0.1	0.2	0.6
10 mS/m	0.0	0.0	0.1	0.2	0.6	1.8
1 mS/m	0.0	0.1	0.2	0.6	1.8	5.7
0.1 mS/m	0.1	0.2	0.6	1.8	5.7	14.9
0.01 mS/m	0.2	0.6	1.8	5.7	14.9	19.8

Highlighted colours indicate the range on conductivity and frequency values where the MT approximation is invalid since propagation will be significantly off vertical. Interestingly, it is at the point where the MT approximation does not hold that maximum power is refracted into the ground. Power

loss into the ionosphere can be estimated from the 1 mS/m row, as relative permittivity is not an important parameter at this frequency.

James Wait performed an analysis that was mathematically correct for this oblique incidence geometry, and published a mild criticism of MT in 1974, repeated in his textbook (Wait, 1982). Wait conceded that vertical incidence and oblique horizontal incidence gave rise to the MT approximation (equation 1) provided that lateral variations were not too big, and the sphericity of the Earth was unimportant at the scales of interest and the scales of diffusion wavelengths of EM in the ground. It is my impression that many in the MT community have dismissed this criticism out of hand. Fortunately, the assumption of vertical incidence does not affect most MT modelling with two exceptions; (1) at high frequency and/or high conductivity, or (2) when the electric field in the air (TM mode) and the magnetic field in the air (TE mode) are incompatible with vertical incidence. Basically, the common MT modelling assumption is completely wrong in the air, but usually valid in the ground.

With a plane-wave approximation, the radiated EM energy will follow a set of “straight rays” which successively reflect and circle the Earth. Evidence that this ray approximation is valid comes from comparing the azimuth of EM energy received in Antarctica with the segmented great circle path ray from sferics of known location launched in North America (Figure 11).

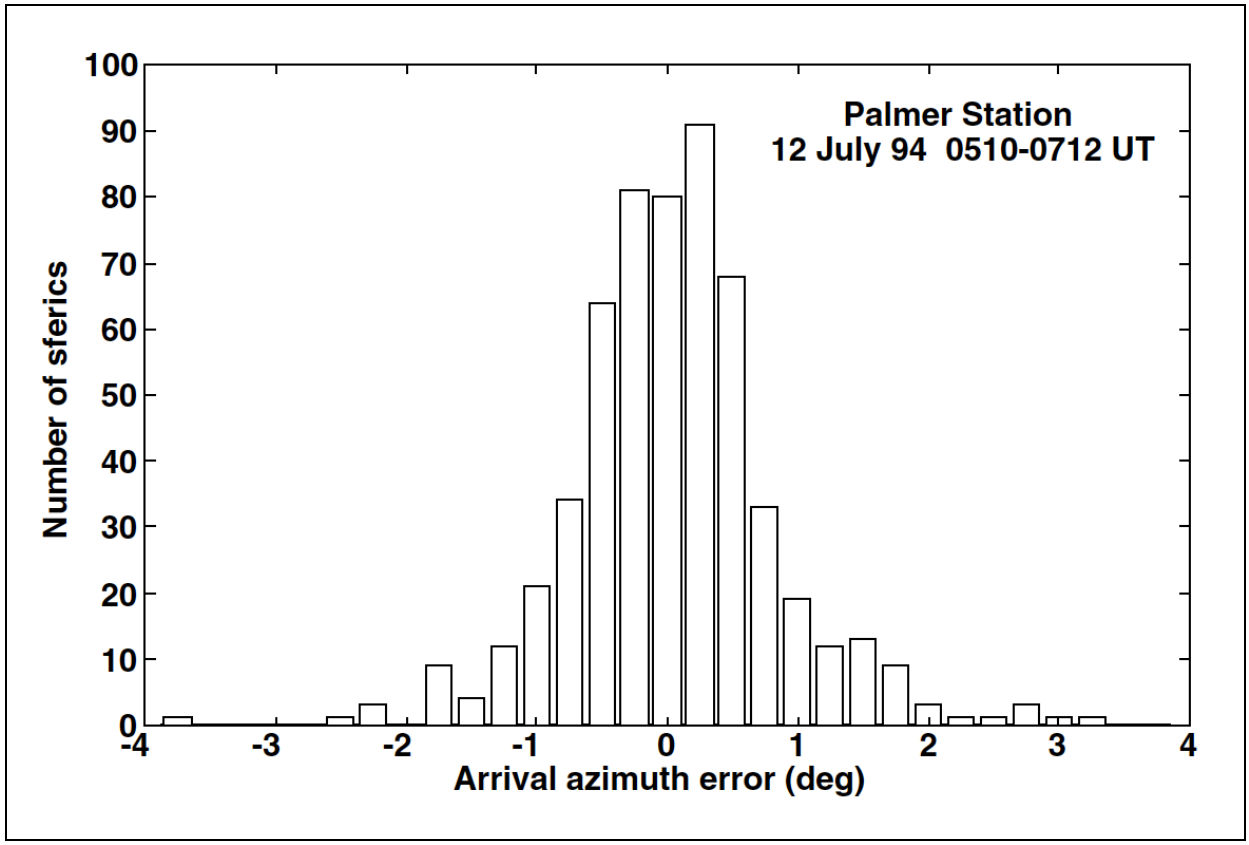

Figure 11. The measured Antarctic arrival azimuth error for single sferics, referred to a great-circle path. Sferics can be assumed to travel great circle paths. Figure reproduced from Reising, (1998).

Sferics can be seen at great distances, with examples in Figure 12 measured in Antarctica from sferics of origin in North America.

If an EM wave were perfectly reflected at the Earth and ionosphere, its power would remain constant in the waveguide and its amplitude would therefore decrease and then increase, with amplitude inversely proportional to the square root of distance from either the point of origin or its antipodean pole. This behaviour is illustrated in Figure 13.

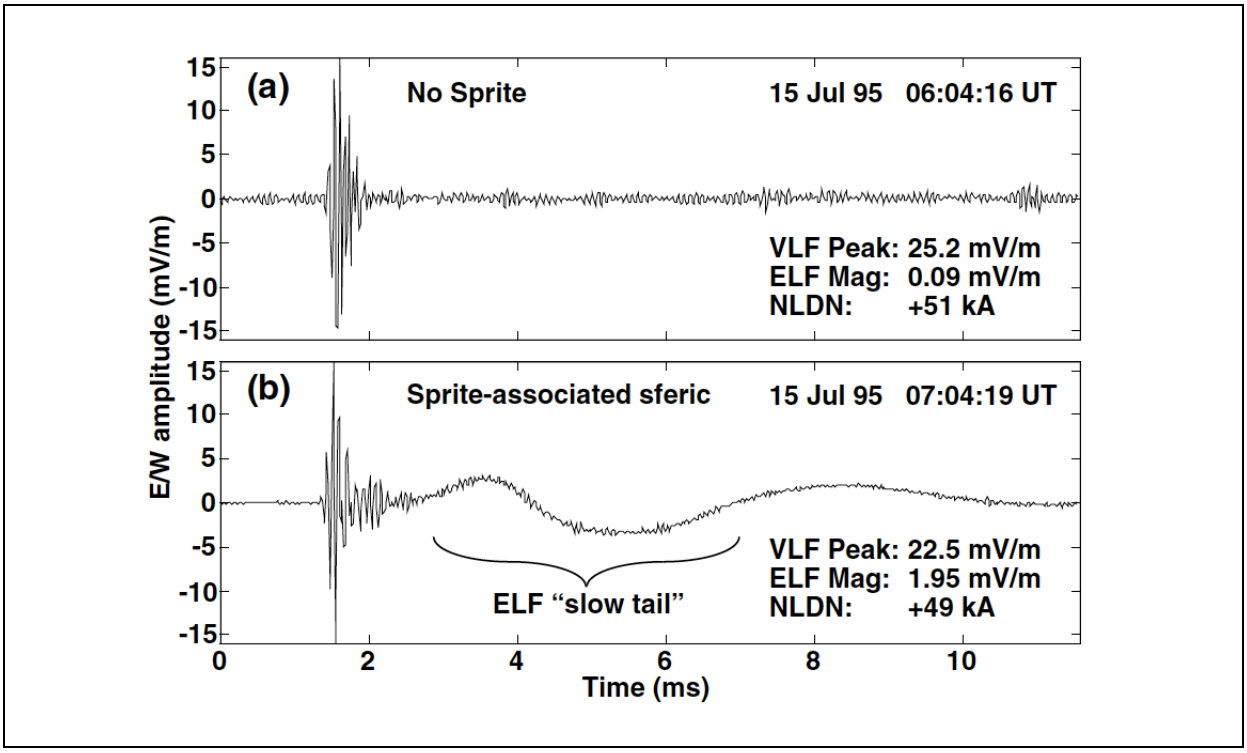

Figure 12. Sample time series of similar peak amplitude sferics launched from the same storm in North America and measured close to the antipodes (Antarctica). (a) Sferic from a normal strike, and (b) sferic from a strike/Sprite combination.

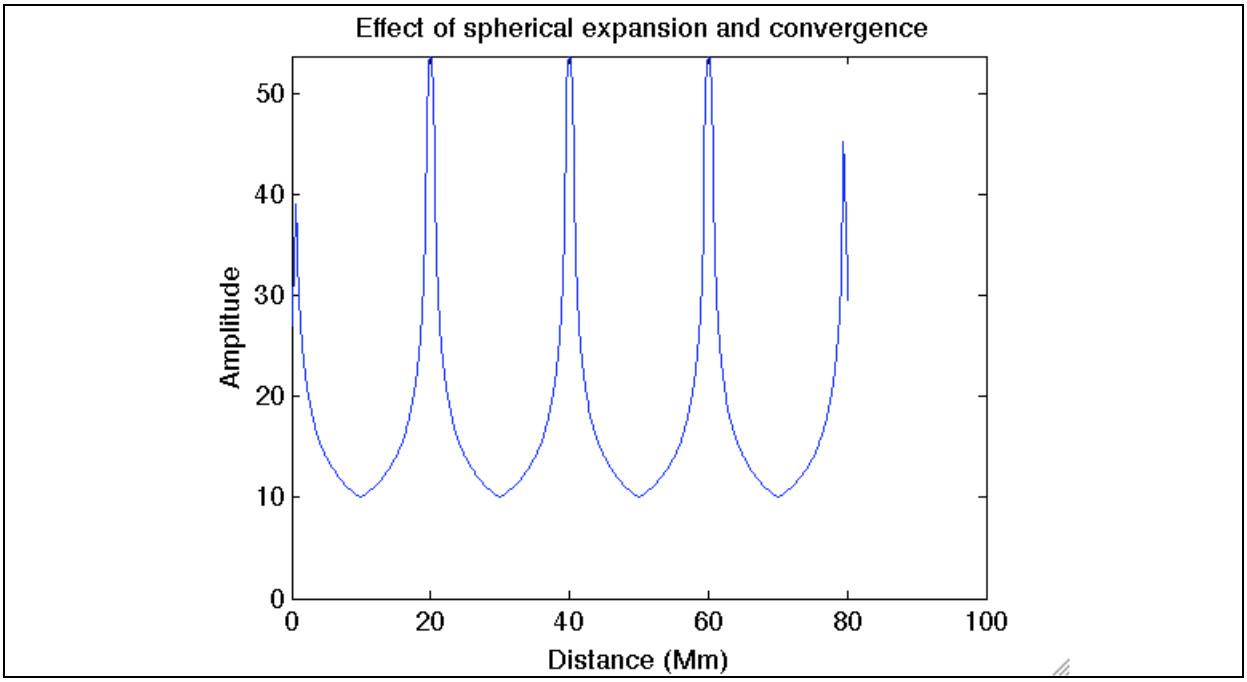

Figure 13. The effect on electric or magnetic amplitude of expansion and convergence after launch of an EM wave from a point into a perfectly reflecting spherical waveguide of the size of the Earth, with distance measured from the point the wave was launched. Peak amplitudes have been limited for display. With the circumference of the Earth at 40 Mm, this plot shows 2.5 circulations around the Earth.

EM plane-waves that are incident on a flat boundary are partially reflected and partially refracted. The relative energy split between refraction and reflection is a function of conductivity, dielectric constant, frequency and polarization. Table 1 shows the reflected fraction of the power. Figure 14 and Figure 15 show an approximation to expected amplitudes under the assumptions of either (a) a purely day-time or night-time path, (b) a constant Earth or sea conductivity under the path, (c) a sequence of plane-wave reflections at defined boundaries, i.e., when there is no topography, (d) no atmospheric dispersion / absorption, or (e) interference effects are ignored. It is clear that at 100 Hz under these assumptions, the signal could make several circuits of the globe. In practice, attenuation is higher than assumed here.

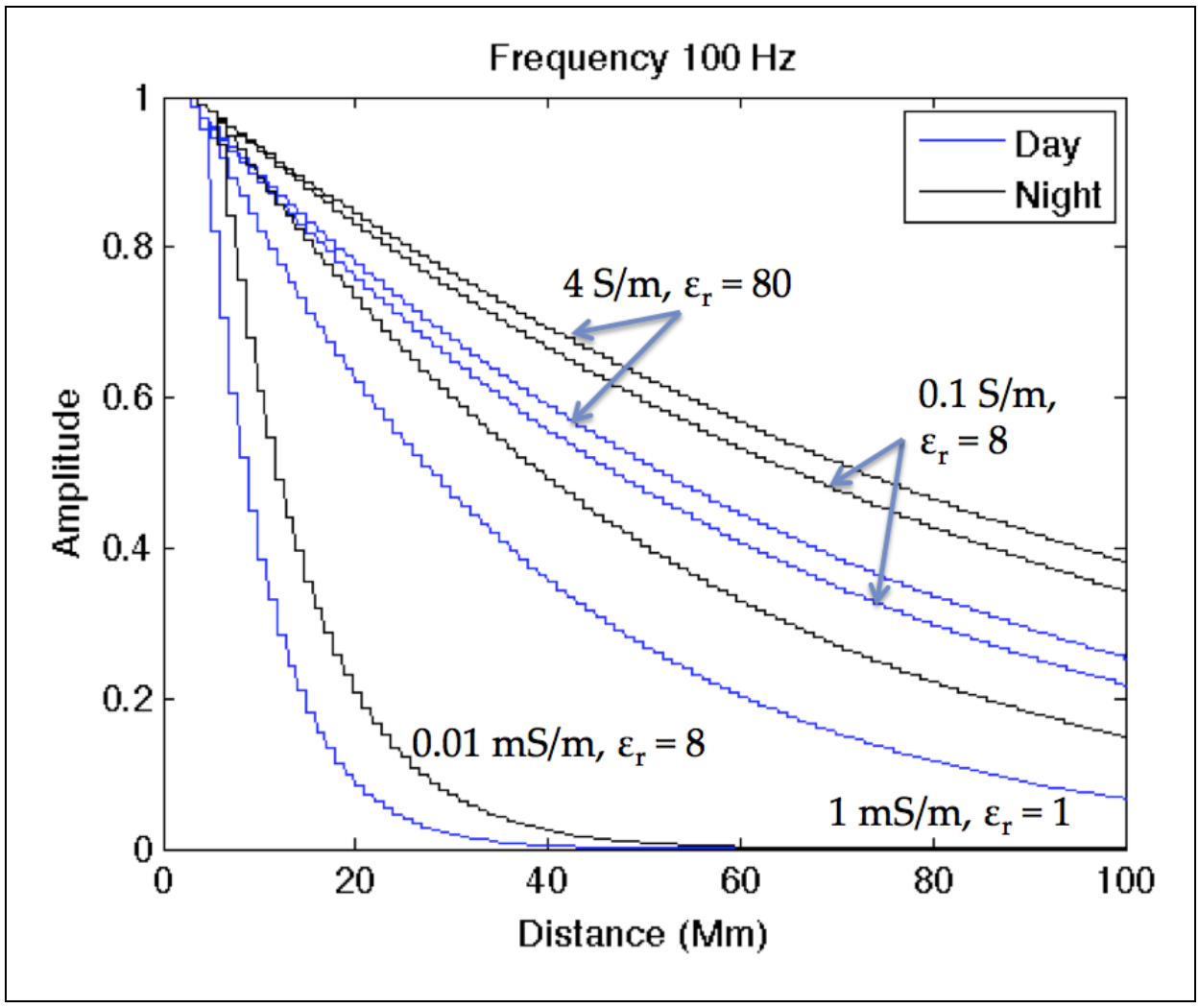

Figure 14. The day-time and night-time attenuation effects (y-axis) under a ray-trace approximation of multiple reflection losses in TM mode propagation as EM signals circulate in the Earth-ionosphere waveguide as a function of distances to the source (x-axis) for different values of conductivity and dielectric constant.

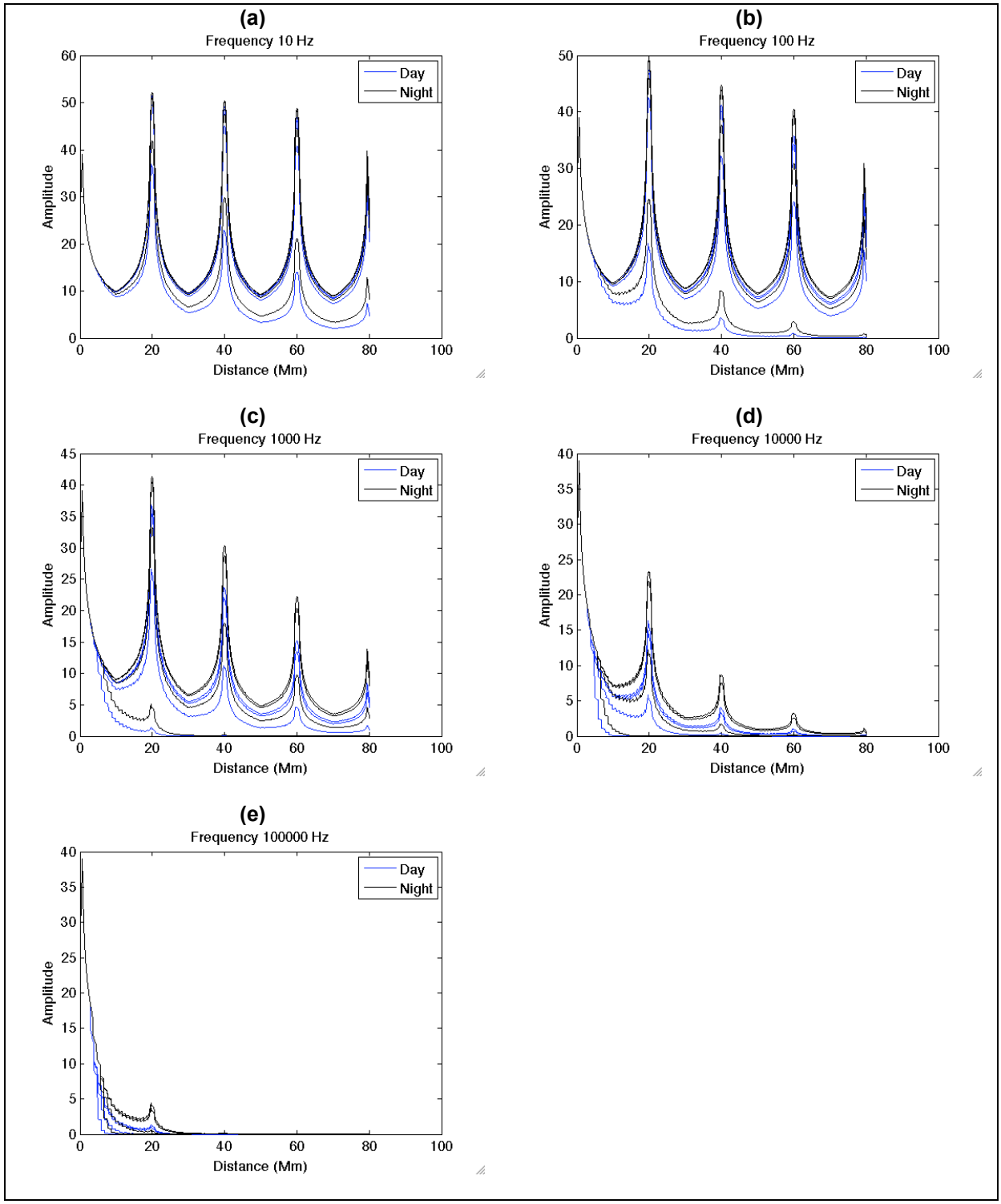

Figure 15. Plots of synthetic ray-trace amplitude of sferic energy as a function of distance from the source, using a spherical layer waveguide with ionospheric leakage over an Earth with constant surface conductivity. Different curves correspond to the conductivity values illustrated in Figure 14. The x-axis covers 2.5 trips around the world. Plots (a) to (e) cover frequency values from 10 Hz to 100 kHz.

Lightning Detection Networks

Lightning detection networks (LDN) are sprouting around the world. Existing networks include the US Precision Lightning Network with over 100 stations and 250 m accuracy with 95% detection, the sparser North American Precision Lightning Network, the commercial Global LDN, and the academic

World Wide Lightning Location Network. There are also country and continent-based local networks, such as the European EUCLID, Strike Star and Central Europe LDN. Detection efficiency is variously claimed to be between 30% and 80% for the global networks, with claims of up to 95% in Asia, Europe Australia and North America. Location is generally claimed to be within 1 km at worst. The commercial networks are focused on continental events for commercial reasons. Lightning is also monitored from space.

Known source EM compared to MT

MT conventionally takes the observed horizontal fields as the 'reference' or 'substitute primary' field. In the case of ZTEM, this reference is taken at some distance from the airborne vertical component receiver coil. Without getting into quantitative modelling, it is worth considering the potential advantages of having a known, or at least well-predicted, source location rather than a reference measurement taken as primary. I will list 4 potential advantages of using source locations and dipole moments.

Let us assume then that, using GPS timing, we can identify the "launch point" of each sferic detected in our measured MT data series. There are several things we could usefully test to see if they improve data statistics. At high frequencies, we could include data only within a couple of milliseconds of each predicted sferic arrival, thus reducing noise power in our overall stack whilst still recovering all signal energy. We could further predict a "time correction" for the conventional synchronised remote reference to allow this technique to work at high frequencies. Advantage 1 with the use of LDN locations and timing should be better signal/noise ratios, particularly for high frequency data.

There are a number of methods (e.g., Groom and Bailey, 1989; chapter 5 in Simpson and Bahr, 2005) that attempt to separate the effects of regional structures, static shifts, and other effects on MT data. I will not be reviewing these, but it seems very reasonable that, if either the electric or magnetic field direction is different from that expected using a great-circle path, then regional or local effects have affected the MT response. Known source azimuth values would allow for characterisation of this distortion as a function of incident angle. Bailey et al. (1974) introduced a methodology they called hypothetical event analysis to determine how geological structures might affect local MT and tipper data. This method computes model responses as a function of source azimuth. Now that source azimuth is, in theory, known, direct rather than indirect interpretation could be attempted using this modelling methodology. This is potential advantage 2 using a known azimuth from a LDN.

I therefore assert we are likely to have better data which can be binned and processed as a function of source azimuth. Let us next assume that our survey crosses a very good conductor (e.g., Ni sulphides) that has a large secondary magnetic field at all frequencies. We could uniquely extract the component of the secondary field perpendicular to the expected sferic azimuth, and ultimately if the source dipole moment and waveform were extracted from the LDN, could predict, using a global conductivity model, the primary component amplitude as well as its direction. Thus, we could get a "complete" secondary field without the need for statistical analysis, and further, could directly detect anomalies in the horizontal component as is done in simultaneous geomagnetic depth sounding. Local distortions of the magnetic components, ignored in conventional MT, can in concept be used with source locations and dipole moments to detect and locate the "perfect conductors" that are often the targets of low-frequency, controlled source EM. At Schumann resonance frequencies, the signal consists of many overlapping response arriving from direct and antipodal paths. However, it may be possible to isolate distinct signals from an occasional positive strike/Sprite with exceptional energy which would be useful in achieving this advantage 3, i.e., better detection of magnetic anomalies.

I finally assert without proof or discussion that other common "problems" of MT such as static shift would also be improved if source azimuth were known rather than assumed. If the observed magnetic field is consistent with the source azimuth, then any E fields not perpendicular to it arise from geological structures and static shift. Such considerations could be used, for example, to quickly determine if the base station used for MT or ZTEM remote references recorded undistorted E and H fields without local anisotropy affecting azimuths.

Conclusions

From a controlled source exploration perspective, natural EM fields are usually regarded as unwanted noise, and major efforts expended to get rid of this “noise”. The converse is also true. Without source information, the horizontal magnetic fields are used as a time (phase) and amplitude reference for horizontal Electric field or vertical magnetic field components.

At AMT frequencies, the sources are generally “sferics”, the fields of distant lightning strikes. We now have extensive lightning detection networks in 24 hour operation that define exactly where and when almost every large source “event” occurs, and in theory it is possible to extract the source dipole characteristics from public data. Source information, not conventionally used in MT and AMT, can in concept (a) reduce noise levels, (b) improve our ability to correct static shifts, (c) better map excellent conductors, and (d) identify and assist in the measurement, and thus elimination of static shift.

References

Arora, B. R., Padilha, A. L., Vitorello, Í., Trivedi, N. B., Fontes, S. L., Rigoti, A., and Chamalaun, F. H., 1999, 2-D geoelectrical model for the Parnaíba Basin conductivity anomaly of northeast Brazil and tectonic implications: Tectonophysics, 302, 57-69.

Bailey, R. C., Edwards, R. N., Garland, G. D., and Greenhouse, J. P., 1974, Electrical conductivity studies over a tectonically active area in eastern Canada: J. Geomagn. Geoelectr., 26, 125-146.

Barfield, R., 1934, Some measurements on the electrical constants of the ground at short wavelengths by the wave-tilt method: J. IEEE., 75, 214.

Berdichevsky, M., and Dmitriev, V., 2008, Models and methods of magnetotellurics: Springer.

Cagniard, L., 1953, Basic theory of the magneto-telluric method of geophysical prospecting: Geophysics, 18, 605-635.

Chapman, S., 1919, The solar and lunar diurnal variations of terrestrial magnetism: Phil. Trans. R. Soc. Lond. A, 218, 1-118, doi:10.1098/rsta.1919.0001.

Groom, R., and Bailey, R., 1989, Decomposition of Magnetotelluric Impedance Tensors in the Presence of Local Three-Dimensional Galvanic Distortion: J. G. R., 94 B2, 1913-1925.

Hack, F., 1908, the propagation of electromagnetic waves over a plane conductor: Ann. Phys., 27, 43-45.

Jordan, E., and Balmain, K., 1968, Electromagnetic waves and radiating systems: Prentics Hall.

McNeill, J. D., and Labson, V., 1991, Geological Mapping using VLF radio fields: In Electromagnetic methods in applied geophysics – Applications (edited by M. Nabighian), Society of Exploration Geophysicists, 521-640.

Miranda, F., 2008, Wavelet analysis of lightning return stroke: Journal of Atmospheric and Solar-Terrestrial Physics, 70, 1401-1407.

Norton, K. A., 1937, The propagation of radio waves over the surface of the Earth and in the upper atmosphere: Proc. Inst. Radio Eng., 25, 1203.

Reising, S., 1998, Remote Sensing Of The Electrodynamic Coupling Between Thunderstorm Systems and The Mesosphere / Lower Ionosphere: Unpublished PhD thesis, Stanford.

Rikitake, T., 1948, Notes on the electromagnetic induction within the Earth: Earthquake Research Institute, Japan. (Accessible on mtnet.dias.ie)

Simpson, F., and Bahr, K., 2005, Practical Magnetotellurics: Cambridge University Press.

Sommerfeld, A., 1909, The propagation of waves in wireless telegraphy: Ann. Der physik, 28, 665-736.

Thomas, R., Krehbiel, P. R., Rison, W., Hamlin, T., Harlin, J., and Shown, D., 2001, Observations of VHF Source Powers Radiated by Lightning: Geophysical Research Letters, 28, 143-146.

Tikhonov, A. N., 1950, The determination of the electrical properties of deep layers of the Earth's crust: Dokl. Acad. Nauk. SSR, 73, 295-297.

Vozoff, K., 1990, Magnetotellurics: principles and practice: Proc. Indian Acad. Sci., 99, 441-471.

Vozoff, K., 1991, The magnetotelluric method: In Electromagnetic methods in applied geophysics – Applications (edited by M. Nabighian), Society of Exploration Geophysicists, 641-711.

Wait, J., 1982, Geo-electromagnetism: Academic Press.

Ward, S., 1959, AFMAG - airborne and ground: Geophysics, 24, 761-789.

Ward, S., and Hohmann, G., 1989, Electromagnetic theory for geophysical applications: In Electromagnetic methods in applied geophysics – Theory (edited by M. Nabighian), Society of Exploration Geophysicists, 131-310.

Ward, S., O'Donnell, J., Rivera, R., Ware, G., and Fraser, D., 1966, AFMAG - Applications and limitations: Geophysics, 31, 576-605.

Wenner, F., 1915, A method of measuring Earth resistivity: Bull. National Bureau of Standards, 12(4) 258, 478-496.

Zenneck, J., 1907, Uber die fortflanzung ebner electromagnetischer wellen - Einer ebenen letterflache und ilire beziehung zur drahtlosen telegrapie: Ann. Phys., Series 4, 23, 846-850.

Improving sub-salt imaging by incorporating magnetotelluric data in a 3D Earth model building workflow - A case history, Walker Ridge, Gulf of Mexico

Elena Medina [1] , Andrea Lovatini [2] , Federico Golfré Andreasi [3] , Simone Re [4] , and Fred Snyder [5]

[1] *Integrated EM Center of Excellence, WesternGeco, Milan (EMedina8@exchange.slb.com)*
[2] *Integrated EM Center of Excellence, WesternGeco, Milan (ALovatini@exchange.slb.com)*
[3] *Integrated EM Center of Excellence, WesternGeco, Milan (FAndreasi@exchange.slb.com)*
[4] *Integrated EM Center of Excellence, WesternGeco, Milan (SRe@exchange.slb.com)*
[5] *Earth Model Building Center of Excellence, WesternGeco, Houston (FSnyder@exchange.slb.com)*

Introduction

The inclusion of non-seismic data, such as magnetotelluric (MT), to augment seismic methods in petroleum applications is not a new concept. Various 2D and 3D integrated inversion approaches have been discussed and published since the early 1990s. The power of a linked multi-domain approach has long been attractive and lies in the relational as well as the independent nature of the data: independent in that the electromagnetic (EM) data are sampling a completely unique source, frequency and spectral bandwidth, while at the same time attempting to resolve exactly the same object as the other data. And although the EM data are inherently lower in resolution, when included as part of a 3D simultaneous joint inversion (SJI) workflow in combination with seismic or other data, their contribution is complementary and effectively enhanced. This proves very useful for improving Earth models, particularly in complex salt provinces where the SJI method can leverage the differences between salt and sediment resistivity as well as between seismic velocity and density.

Magnetotelluric data

In 2007-2008, WesternGeco acquired MT data at more than two thousand marine receiver sites in the deep water northern Gulf of Mexico. The goal was to use these data in conjunction with seismic data processing to improve the Earth model, and thereby the final seismic image, in challenging salt-imaging areas. The measured electric and magnetic field continuous time series data were originally processed on board the acquisition vessel with a remote reference approach (Egbert, 1997), and then modelled using 3D MT blind inversions.

Simultaneous Joint Inversion

In 2009, Simultaneous Joint Inversion (SJI) (De Stefano et al., 2011) pilot tests were performed over two blocks, one around the Walker Ridge Block 52 area encompassing Anadarko's Shenandoah Lower-Tertiary discovery well (Figure 1). The results were very promising and a larger 1,200 km^2 production project surrounding the same area was planned and initiated in 2010. The objective of this new project was to refine the base of salt interpretation, to improve sub-salt imaging, and to understand the deeper salt structure from a petroleum system stand-point.

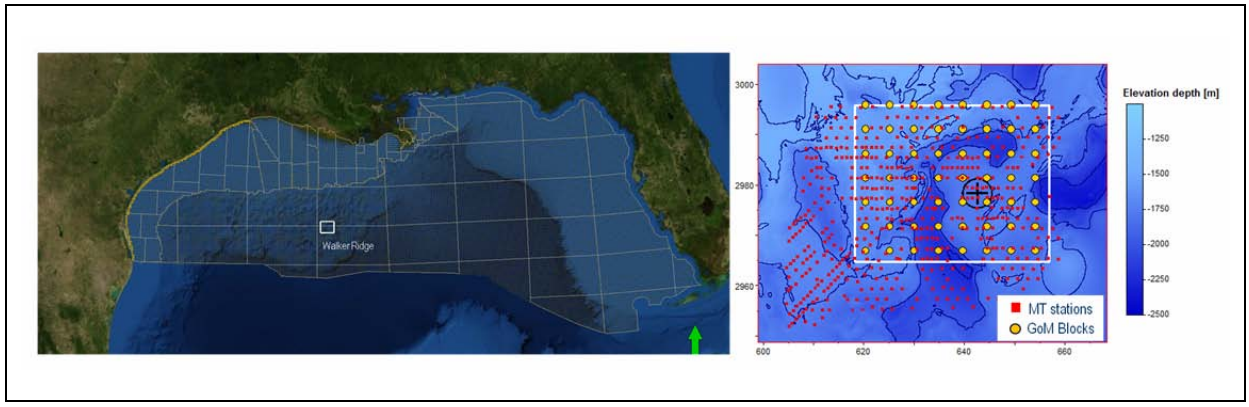

Figure 1. (Left) Location of the Walker Ridge area in the Gulf of Mexico. (Right) Map of the Block 52 area showing the location of the MT stations (red squares) and GoM blocks (yellow circles) relevant to this project. In both pictures, the white rectangular outline represents the Block 52 area boundary and the black symbol in the right hand panel shows the position of the Shenandoah well.

Common image point (CIP) residuals were obtained through anisotropic migration of the 3D wide azimuth seismic data, using a velocity salt-for-sure model. To build this model, two main horizons were used: the interpreted top of salt and salt-for-sure horizon, the latter being a layer interpreted as an intra-salt horizon with a high level of reliability thanks to previous imaging efforts. Only the region between these two horizons was characterized by salt properties. A heterogeneous salt velocity was used ("dirty salt") to account for possible sediments and inclusions within the salt bodies, causing relative acoustic impedance variation within the bodies themselves (Figure 2). To flatten the residual move-out on these data, a correct base of salt interpretation and subsalt velocity field are necessary.

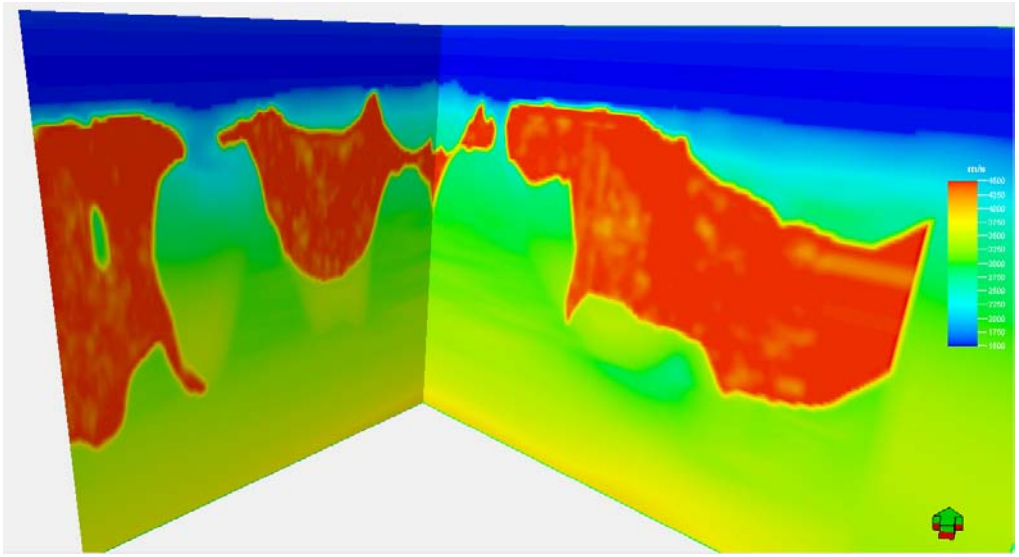

Figure 2. Velocity model slices showing the heterogeneous salt velocity values in the salt-for-sure bodies.

It would be difficult to reconstruct such a model using CIP tomography because of the weakness of the signal below salt. SJI is thought to compensate for this lack of seismic signal feeding the inversion by using the MT data as well and by simultaneously updating velocity and resistivity model to fit the MT impendence tensor components as well as flattening the CIP residuals. In this project, MT data for 485 marine stations covering an area of approximately 3300 km^2 were inverted. The padded resistivity model covered an area of more than 100,000 km^2, whilst the velocity model covered an area of approximately 4500 km^2.

The initial step of the SJI process was to carry out separate single domain MT inversions and CIP tomographies to define an optimal parameter set for each domain. As far as the 3D MT inversion is concerned, these initial investigations focussed on aspects of the starting model and inversion penalization scheme. The starting MT resistivity model geometry was built re-sampling the finely gridded 3D velocity model into a mesh of adequate dimensions to solve the MT forward and inverse problem. Models with increasing complexity were tested as starting point, integrating the available seismic interpretation, to assess the inversion output stability. These models ranged from a simple salt-flood model, where all the cells below the top of salt horizons were "flooded" with high resistivity values associated with salt (Figure 3), to more complex salt models, where the salt body geometries from previous seismic imaging were used (Figure 4). Different minimization schemes were also tested, in combination with the starting model tests: from a simple scheme searching for the smoothest variations within the output model or with respect to a reference model, to a constrained approach where the same salt-for-sure region excluded from the inversion domain in the acoustic domain, was softly "locked" (i.e., resistivity variations were more penalized in the inversion process). Integrating the MT data into the inversion process has the benefit of compensating for some of the illumination problems in the seismic data. Conversely, the seismic data enable a higher resolution Earth model to be constructed than would be possible using the MT data alone given the inherent reduced resolution of this diffusive method, and the lack of high frequency information that is available in the MT data due to the low-pass effects of the conductive water column.

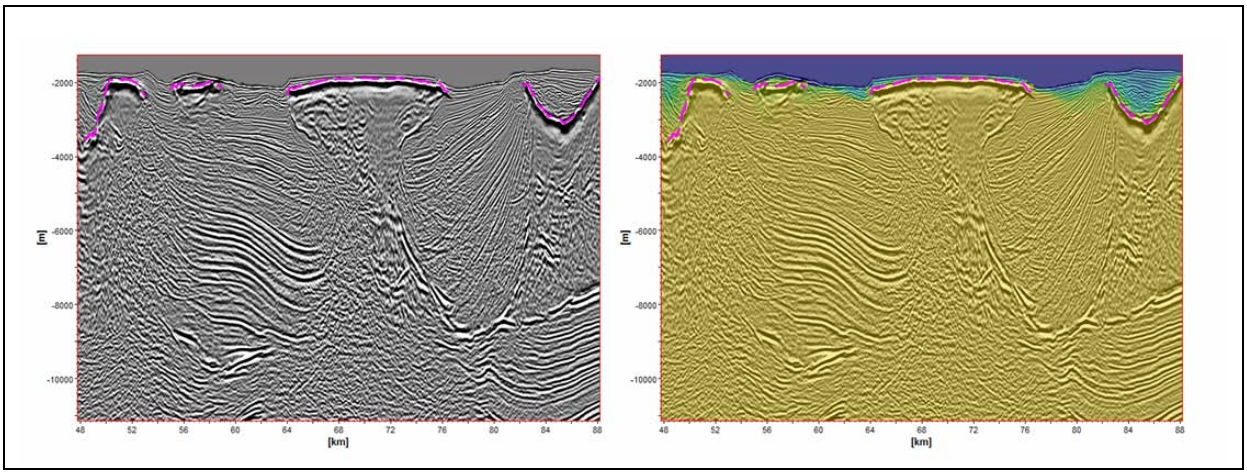

Figure 3. Benchmark reverse time migration (RTM) sections; from left to right: Top of Salt horizon (pink stippled line) on InLine 4555; Salt-flood resistivity model along InLine 4555 co-rendering with seismic and Top of Salt horizon.

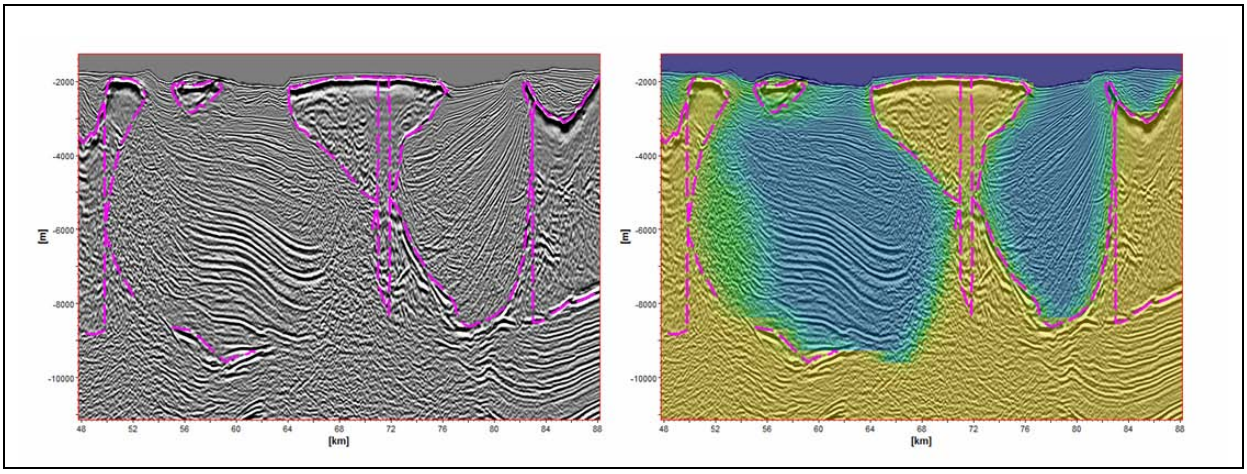

Figure 4. Benchmark reverse time migration (RTM) sections; from left to right: Top of Salt horizon and salt body geometries from previous seismic imaging (pink stippled lines) on Inline 4555; Resistivity model populated using seismic horizons along InLine 4555 co-rendering with seismic and seismic horizons.

SJI allows different data types to be jointly inverted whilst also providing a linking function between different properties that is either petrophysical or geometrical (De Stefano et al., 2011). In this case, the relationship between resistivity and velocity models was a petrophysical space, with different lithologies giving rise to different properties in this space. For subsalt sediments, an empirical relationship between velocity and resistivity was inferred from sonic and resistivity logs in the core study area. For the region covering approximately the zone from salt-for-sure horizon to the legacy interpretation of the base of salt, a petrophysical relationship based on well logs as well as results of single domain inversion was used. This spatially varying linking function between multiple properties constitutes the third data flow whose residual is minimized in the inversion itself.

Once the three streams were parameterized, they were jointly inverted thus providing a multi-property Earth model, fitting MT data, flattening residual move outs and following the empirical relationship between resistivity and velocity. These output models were used to reinterpret the base of salt and deep feeders between the allochthonous salt bodies and the deeper autochthonous one (Figure 5 and Figure 6). As a final step, a reverse time migration (RTM) was carried out using a new velocity model that was based on the new interpretation from the SJI output.

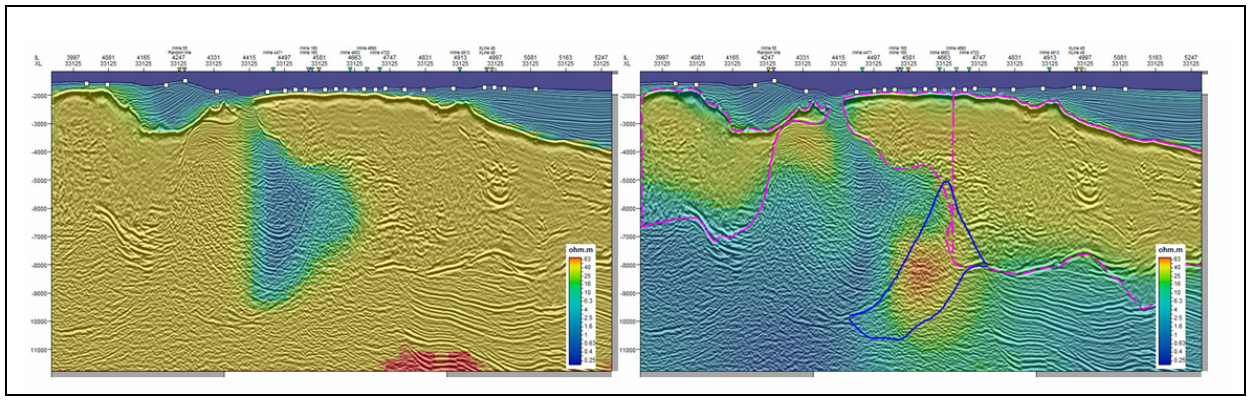

Figure 5. 3D Simultaneous Joint Inversion input (on the left) and output (on the right) resistivity model along XLine 33125 co-rendered with benchmark reverse time migration (RTM) seismic cube data; Pink horizons on the right section are the salt body geometry from the previous seismic imaging whilst the blue horizons came from the post-SJI interpretation.

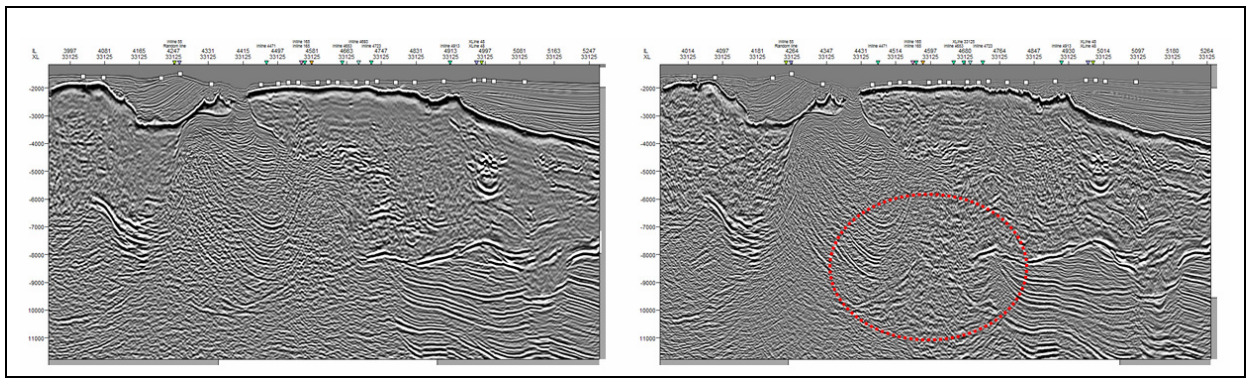

Figure 6. From left to right: Benchmark reverse time migration (RTM) section along XLine 33125; Post-SJI reverse time migration (RTM) section along XLine 33125. The red circle marks the main portion of the section which showed greatest improvement in the post-SJI reverse time migration (RTM) data volume.

Conclusions

By rigorously integrating wide azimuth seismic data (WAZ), SJI processing workflows, careful Earth model interpretation, “dirty salt” velocity compensation, and RTM migration, a clearer picture of the salt and sub-salt structures emerged. In addition, the work has helped to increase confidence in earlier theories as to the nature and extent of several deep autochthonous salt feeders, as well as better explain the overall salt tectonic development in the area. This new understanding of the salt volumetrics is of essential importance to rank the exploration potentials of the area under investigation.

References

Egbert, G., 1997, Robust multiple-station magnetotelluric data processing: Geophysical Journal International, 130, 475-496.

De Stefano, M., Golfre Andreasi, F., Re, S., Virgilio, M., and Snyder, F., 2011, Multiple-domain, simultaneous joint inversion of geophysical data with application to subsalt imaging: Geophysics, 76, R69-R80.

Magnetotellurics in mining applications

Trent Retallick [1] and Rob Hearst [2]

[1] *Quantec Geoscience (tretallick@quantecgeoscience.com)*
[2] *Quantec Geoscience*

Abstract

The search for mineral resources has moved from the near-surface (e.g., upper 500 m) to ever greater depths. Along with this increased depth for detection of mineral resources, exploration has moved to more challenging and difficult terrains, often into areas where geophysical surveys can be difficult to perform (e.g., large deep lakes, desert areas, mountainous terrains, etc.). This has resulted, in part, to the re-emergence of geophysical technologies such as magnetotellurics (MT) for obtaining geophysical images of the Earth's subsurface at depth.

Traditionally, the MT method has most often been applied to deep crustal studies, geothermal prospecting and the search for hydrocarbons. Developments in instrumentation (i.e., improved sensor calibration, higher sampling rates, greater S/N), computer inversion software and computer hardware has resulted in improved data acquisition methodologies, data processing and interpretation through inversion processes.

In this paper, we look at the application of MT in two different, but challenging, geologic settings for the detection of potentially economic mineralized systems. In the first example, we illustrate the use of MT in the detection of vertical basement conductors at depth below a large and deep freshwater lake, necessitating the acquisition of the MT data under challenging winter conditions on a frozen lake. The depth to the target horizon was a minimum of 600 m, and current airborne and ground EM techniques where unable to adequately penetrate the depth of the water column and sedimentary sequence below. The second example illustrates the use of high spatial sampling MT to map and detect a vein system in the near-surface associated with a porphyry at depth.

Introduction

The magnetotelluric method was proposed by Cagniard in 1953 as an entirely new method of exploration in which the magnetic fields induced by changes in the Earth's telluric currents would be measured simultaneously with the voltage changes recorded between electrodes placed on the surface (Cagniard, 1953). Through the calculation of the ratio of the measured amplitude of the electric and associated magnetic fields, and plotting these ratios as a function of frequency, Cagniard demonstrated that it was possible determine the resistivity of the Earth as a function of depth. As these magnetic and electric telluric fields penetrate deep into the Earth, the method has the status of being the deepest penetrating electrical method. This is particularly appealing as it allows for imaging of the resistivity structure of the sub-surface to great depths. Since these early days, the development of the magnetotelluric (MT) method has been such that it is now an accepted method of exploration, not only for hydrocarbons and geothermal resources, but also for mining applications.

Developments such of 24-bit recording systems with low S/N and high memory capability, use of multi-channel distributed recording systems, and improved data processing, and interpretation techniques has resulted in higher quality data interpretations being carried out which, in turn, has created greater demand for more sensitive and better calibrated systems to be able to resolve more subtle, and deeper anomalous features.

Instrumentation and typical field procedures

The current state-of-the-art in MT acquisition systems from the major manufacturers is for 24-bit digital capture and recording of the telluric signals. A typical set of ground MT equipment required for field acquisition is illustrated by Figure 1. The electric field dipoles are deployed in the horizontal plane at right angles to each other to capture the horizontal telluric electric field signals. Magnetic coils are deployed to measure the rate of change of the magnetic field associated with the electric telluric field.

These coils are generally buried in the ground, and arranged to measure the magnetic field in three dimensions using two horizontal orthogonal coils and a vertically-oriented coil. The physical layout of the MT equipment at a field location is illustrated in Figure 2. In order to extract the maximum amount of information from the magnetic coils, it is necessary to accurately calibrate the coils across the entire frequency range being utilised. To ensure this, Quantec Geoscience has built and operates a calibration chamber through which all magnetic coils are tested and calibrated (Figure 3).

Figure 1. Typical equipment required for ground MT acquisition. Equipment includes horizontal magnetic field coils (long white cylinders), vertical field coil (short black cylinder), electrode connections, coil connectors, data logger, and battery power supply.

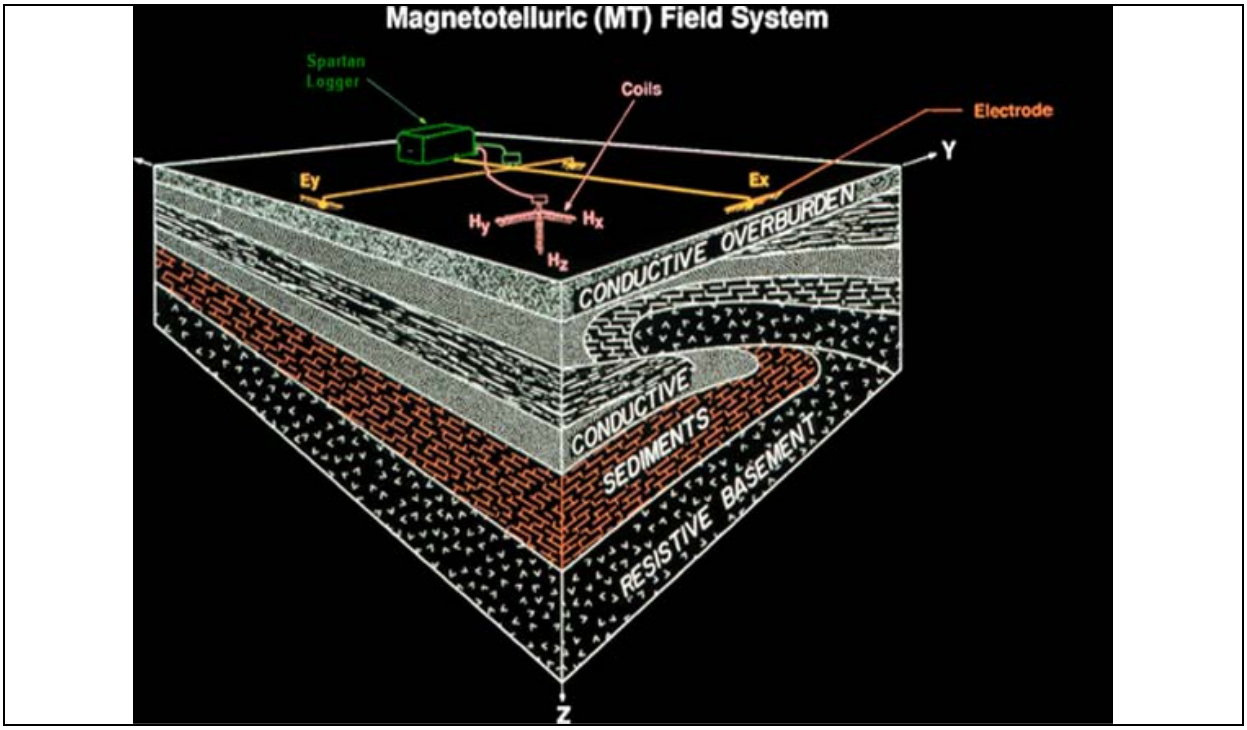

Figure 2. Cartoon of a typical MT site setup. The electric dipoles for measuring the electric telluric current are illustrated in yellow and labelled as Ey and Ex. Magnetic coils are illustrated in pink and labelled as Hx, Hy and Hz. The electric and the magnetic sensors are connected via cables

to a battery-powered data logging unit. By measuring the telluric electric field and associated magnetic field it is possible to calculate a resistivity depth section and determine the resistivity structure of the subsurface.

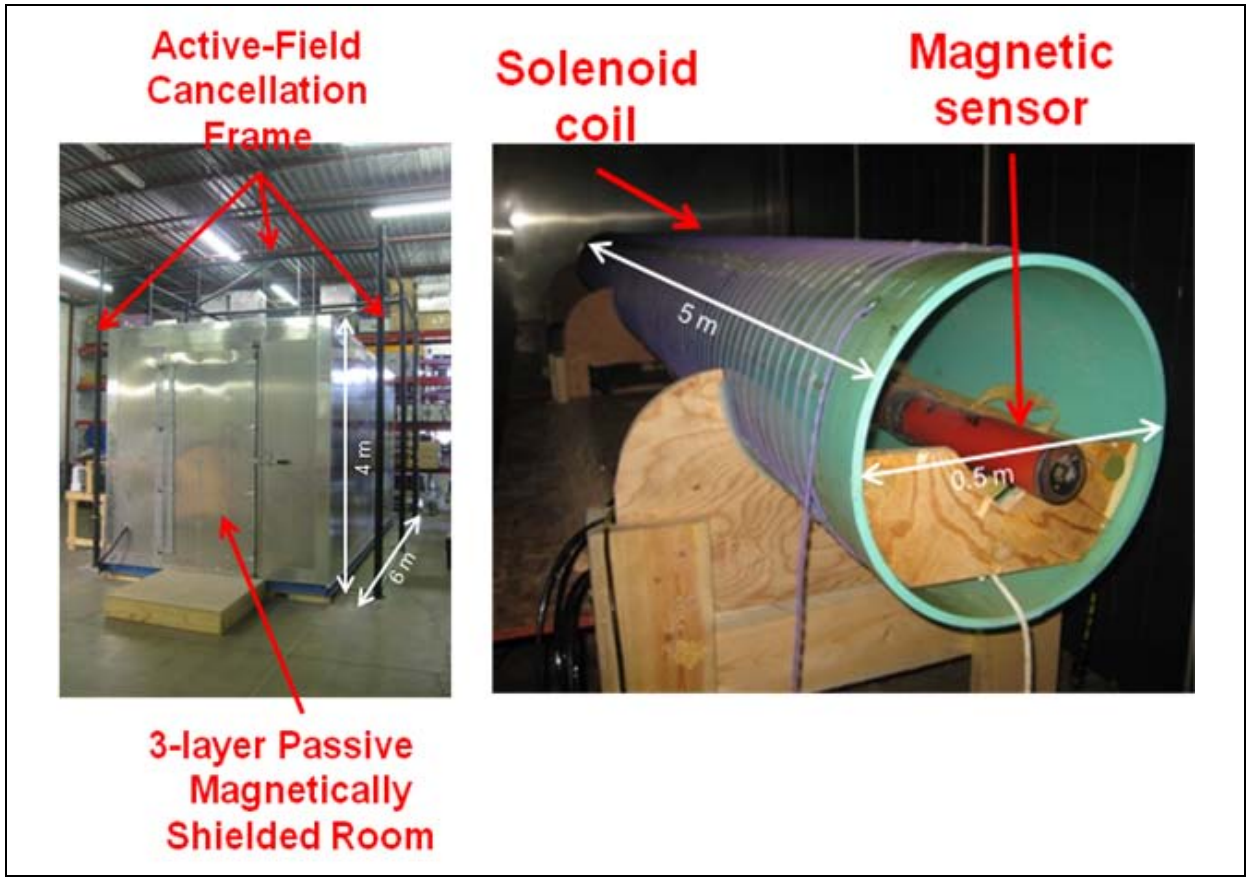

Figure 3. Magnetic coil calibration chamber that provides a 3-layer passive shielded and active field cancellation facility for achieving a high-sensitivity calibration of the magnetic coils used on MT surveys.

Application of MT in challenging geologic environments

In this section, we examine the application and adaptation of the MT method in two very different and challenging geological and geophysical situations. In the first example, we illustrate the use of MT in the detection of vertical basement conductors at depth below a large and deep freshwater lake, necessitating the acquisition of the MT under winter conditions on a frozen lake. The second example illustrates the use of high spatial sampling MT to map and detect a vein system in the near-surface associated with a porphyry at depth.

Example 1 – Uranium unconformity

A conceptual model of an unconformity type uranium deposit is illustrated in Figure 4. The geological model is characterized by a uranium deposit than is surrounded by an alteration zone within the sandstone basin, commencing at the unconformity extending towards the surface. This alteration zone, consisting predominantly of sericite – kaolinite - chlorite +/- silicification, is generally spatially associated with graphite fault zones in the basement. Typical resistivity values for these units are presented in Figure 4, indicating that the alteration zones can be either resistive or conductive relative to the resistive sandstone basin, but that basement graphite is a highly conductive sub-vertical zone hosted in a more resistive basement environment. This type of conceptual model suggests that mapping of resistivity anomalies in the sandstone basin that are associated with conductive zones in the basement will highlight favourable areas for uranium deposits.

In the example to be presented here, the sandstone layer that is presented in Figure 4 as a uniform resistive layer is actually a more conductive layer at depth consisting of a sandstone/mudstone unit.

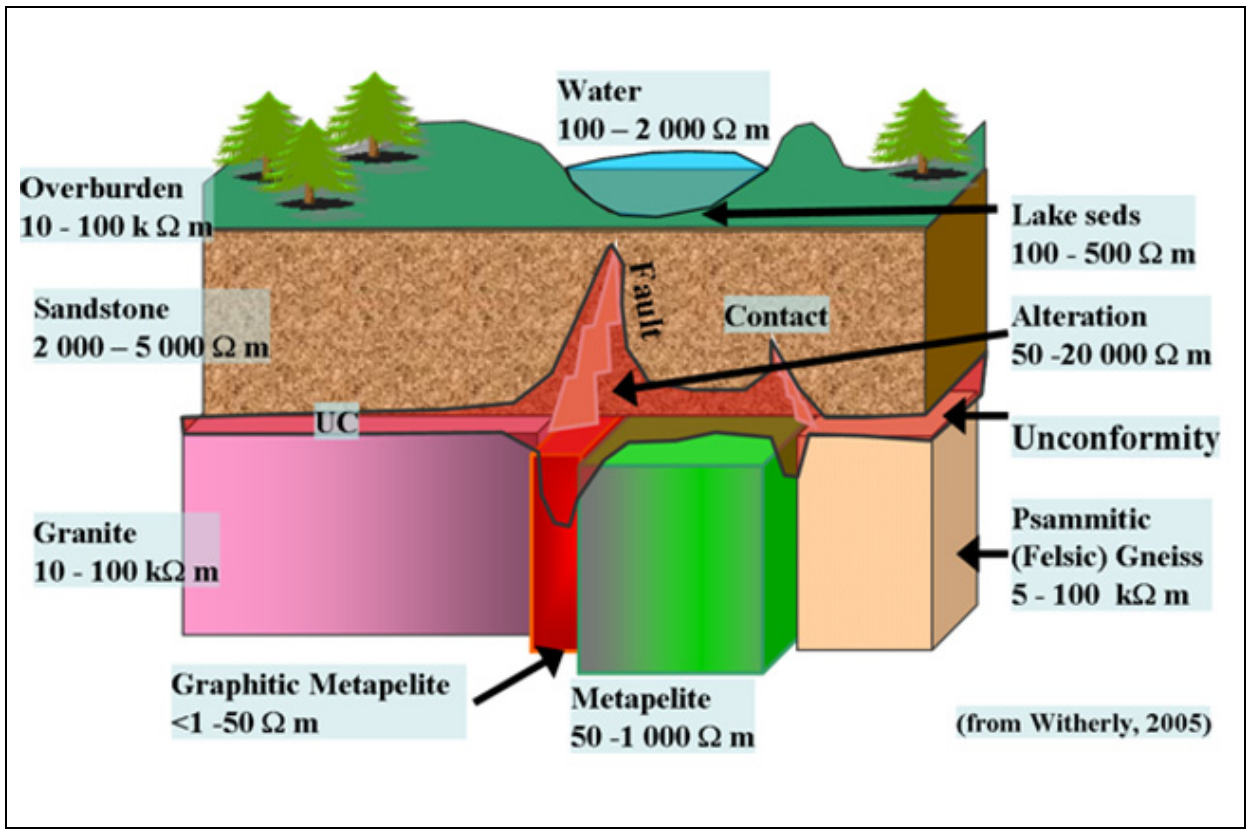

Figure 4. Conceptual geological model and typical geophysical resistivity parameters for unconformity uranium deposits (after Witherly, 2005).

Example 1 - Exploration environment and survey methodology

The principal survey objective was to penetrate below thick conductive lake bottom sediments and conductive sandstone/mudstone sediments that have hampered conventional ground and airborne methods in order to detect deeper geophysical signatures associated with unconformity-type uranium deposits. More specifically, the objective was to define and to delineate graphitic meta-sedimentary rocks and with fault structures in the basement below the unconformity as well as alteration zones, potentially related to uranium mineralization, in the sediments above the unconformity.

The survey was almost exclusively to occur over a lake, with a reference base station located on a small island central to the survey area. This necessitated the survey being completed in winter, when the lake was frozen over, under conditions of extreme cold weather, high winds and low visibility (Figure 5). The detection of the potential graphitic conductors at depths of 600 m and more required that a high degree of lateral resolution be obtained in addition to sufficiently clean data being acquired to “see” below the shallower conductive horizons.

To complete the survey, Quantec Geoscience employed the company’s proprietary Spartan MT in a unique semi-array configuration whereby multiple continuous electric dipoles were deployed in conjunction with magnetic coils (Figure 6). This allowed for acquisition of high density lateral resolution electric and magnetic data in an efficient and safe manner despite the harsh operating conditions of the area.

Figure 5. Harsh environment of Lake Athabasca, Northern Saskatchewan, where the MT survey needed to be completed on ice, dealing with cold temperatures (often below -40°C), low visibility, high winds, pressure ridges in the ice, and other complications from working on a large lake ice sheet.

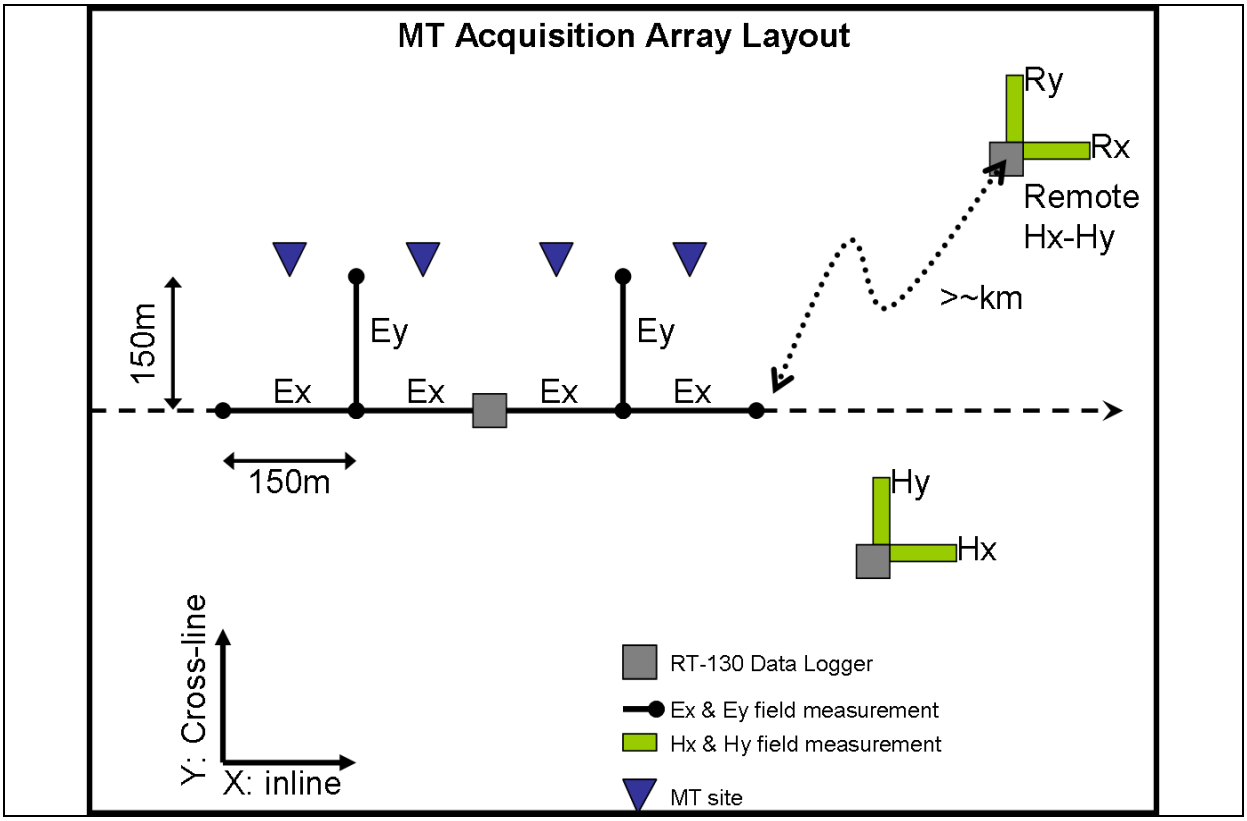

Figure 6. MT acquisition array layout utilized for the survey.

Example 1 - Data results

This use of MT in this harsh environment and subsequent interpretation (Figure 7) resulted in the definition of the following:

- A transition zone at approximately 700 m in depth from a sub-horizontal layered conductive unit to sub-vertical structures, which is interpreted to be the transition between the sandstone sediments and the basement, i.e., the unconformity;
- Several low resistivity zones in the sandstone sediments that appear to represent alteration zones above the inferred unconformity, possibly corresponding to disseminated sulphide/uranium mineralization zones;
- Different conductive zones in the basement that might represent graphitic horizons; and
- A clear association between several low resistivity zones in the sandstone sediments and conductive features in the basement.

Subsequent drilling and follow-up by the client encountered mineralization and confirmed the theorized geologic setting and the effectiveness of the MT method in this environment.

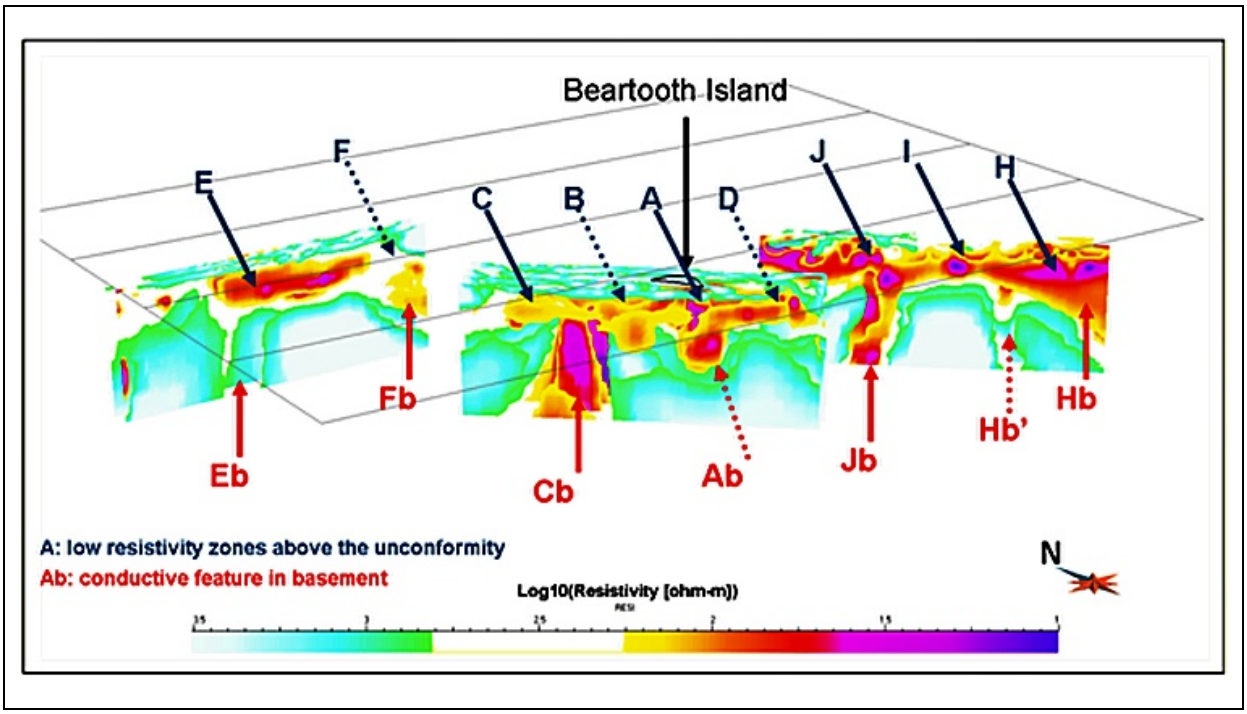

Figure 7. 3D perspective view of the resistivity values obtained from the MT survey data acquired on Lake Athabasca in the vicinity of Beartooth Island. The correlation of the vertical basement conductors defined on the MT resistivity sections with conductive "halos" in the overlying sediments confirming the geologic model and provided confidence that future exploration based on this model should be continued.

Example 2 – Vein porphyry system

The Silver Queen project area is located in Central British Columbia, Canada, and lies within a series of volcanic and intrusive rocks. The volcanic formations consist mainly of dacites and dacitic andesites which likely form a part of the Upper Cretaceous-Eocene Endako Group. A sill-like body of micro-diorite intrudes these volcanic rocks and is referred to as the Mine Hill Micro-diorite. It is part of the Bukley intrusions. The volcanic rocks and the micro-diorite have been intruded by dikes and sills of porphyritic felsites and by basalt dykes (Figure 8).

Approximately 20 mineralized veins have been discovered to date. The average width of the veins is approximately 1 m to 5 m. The veins appear to be controlled by NW striking fractures that cut all geological formations. Widespread alteration on the property is visible. Pyrite-sphalerite-chalcopyrite and sphalerite-galena are the two general types of sulphide mineralization occurring within the vein systems. Moderate to high grades of Ag and Au are generally associated with the chalcopyrite-

sphalerite veins. Other sulphide minerals include pyrite, tetrahedrite and tennantite. The gangue is mainly cherty quartz, carbonate minerals, and some barite. Local intense alteration of the wall rock along veins and fissures has resulted in a mixture of clay and carbonate minerals, some chlorite, minor epidote and disseminated pyrite.

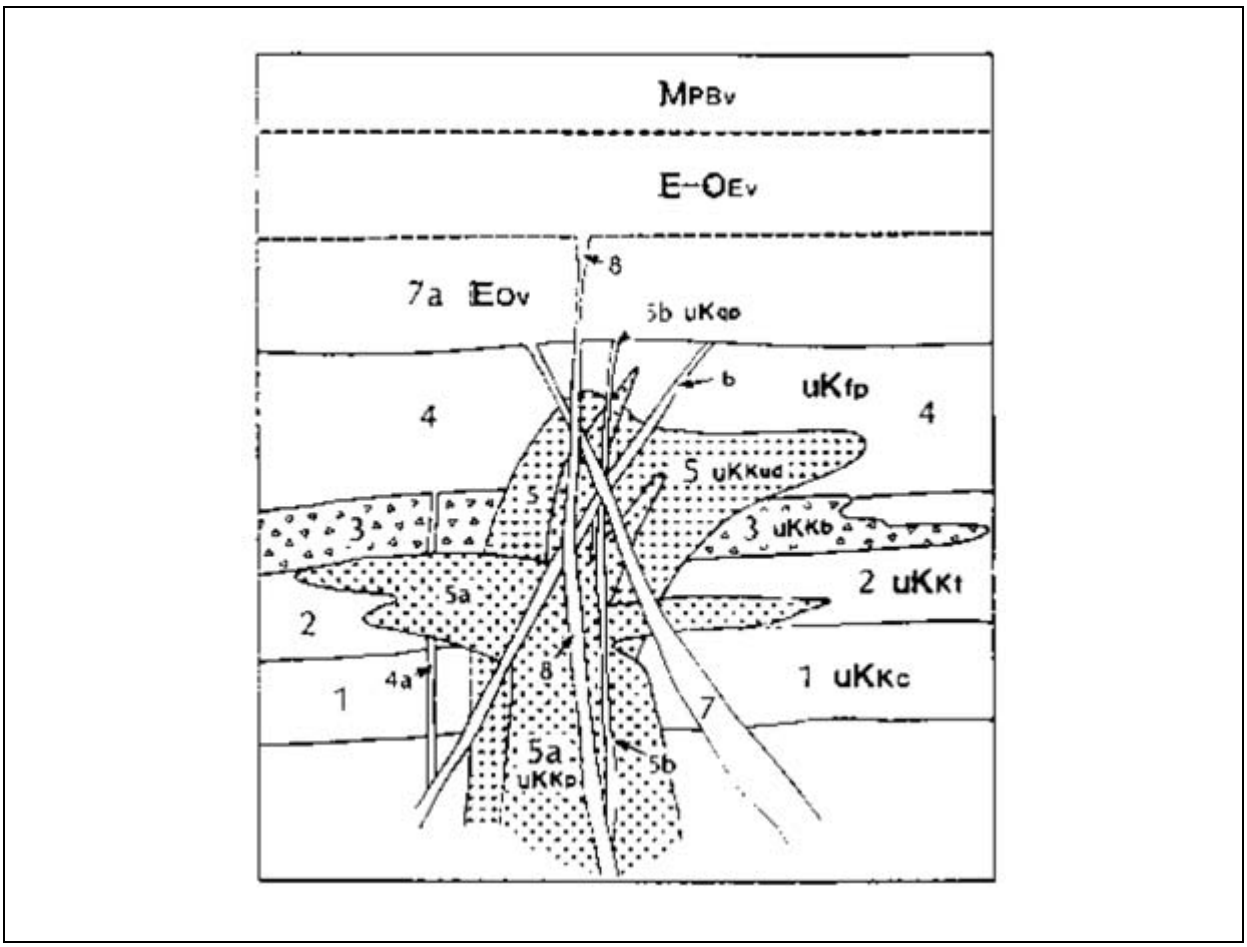

Figure 8. Schematic diagram of the stratigraphic and intrusive units present on the Silver Queen Property. MPBv – olivine basalt; EOEv-8 – basalt, diabase dykes; EOv-7a – trachy-andesite basalt; 7- feldspar porphyry dykes, 6- amygdular dykes; uKgp-5b – qtz-rhyolite dikes, stocks; uKKp-5a – intrusive porphyry sills, stocks; 4 – feldspar porphyry; uKKb-3 – medium to coarse tuff-breccia; uKKt-2 – crystal tuff, local lapilli tuff, 2a – fine ash tuff; uKKc-1 – basal conglomerate, sandstone and shale interbeds. (after JDS Energy and Mining, 2011).

Example 2 - Exploration environment and survey methodology

The Silver Queen property is located in the rugged and mountainous terrain of Central British Columbia in Canada. The property area consists of areas of open cattle pasture, rugged scarp slopes and heavily forested terrain (Figure 9). Low topographic areas are typically very wet and swampy.

The survey method selected for this exploration target was the Quantec Titan DC resistivity, IP chargeability and magnetotelluric system. The Titan system allowed for the rapid acquisition of MT data over a tightly spaced array of 24 MT sites simultaneously (Figure 10). The MT data were acquired as a complementary dataset to the DCIP data, allowing for the extension of zones identified in the near-surface by the DCIP to great depths through use of the MT. The MT allowed for the determination of potential source material related to the vein systems observed in the surface geology, previous mining activity, and DCIP portion of the survey.

Figure 9. View of the topographic setting and environment of the Silver Queen Prospect, Central British Columbia, Canada.

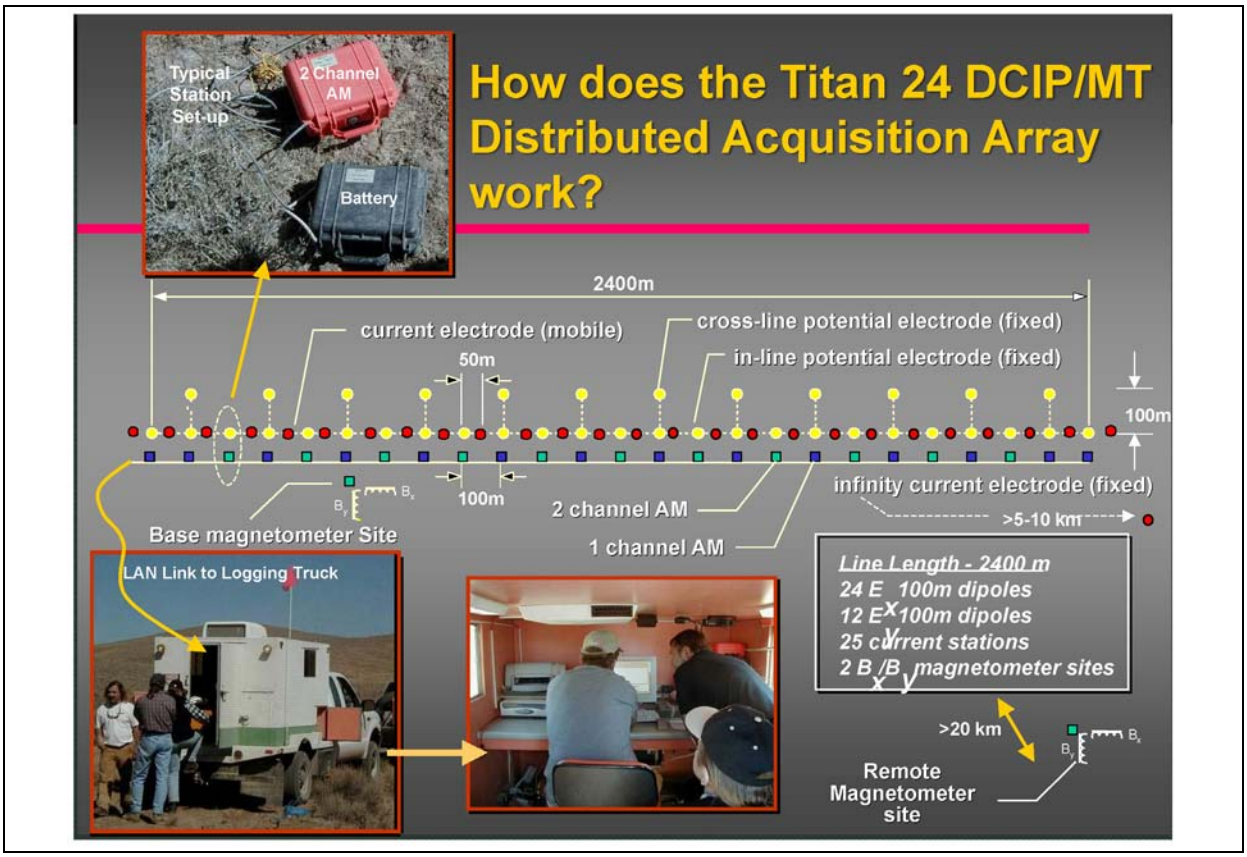

Figure 10. Conceptual diagram of the Titan 24 DCIP & MT data acquisition system. The MT acquisition utilizes electric dipoles (yellow) in both in-line and cross-line orientations as well as magnetic coils that are deployed along the array. Depending on the application and requirement, multiple sets of magnetic coils or a single coil set may be deployed. All MT data is remote referenced.

Example 2 – Data results

The Titan MT data were better suited and subsequently proved to indeed be better than the data from other surficial methods or airborne systems for locating and defining a potential conductive source at depth. This is in part due to the high spatial resolution and wide bandwidth of the MT data acquisition carried out. In the vicinity of the Silver Queen vein system, a large, potential porphyritic target was identified from the MT survey data. This target is located at a depth of 400 m below surface and extends to approximately 800 m below surface (Figure 11). Subsequent diamond drilling by New Nadina Explorations of this target has confirmed the presence of the vein system in the near-surface and deep seated porphyry as identified from the MT survey data. The porphyry contains significant visible molybdenum in addition to elevated silver.

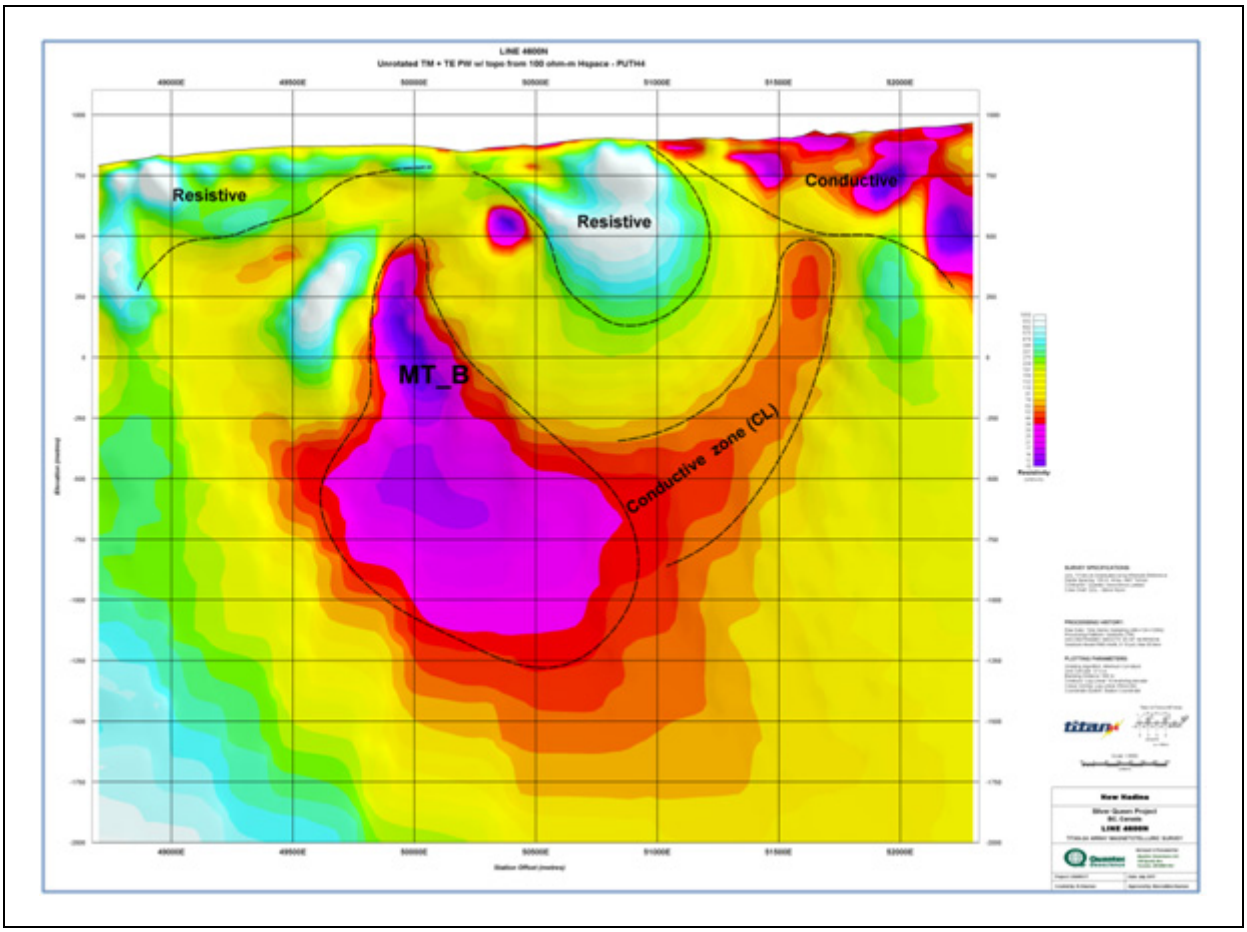

Figure 11. Conductive anomaly related to the Silver Queen vein system that was identified using the MT data and inversion methods.

Inverting the MT data in 3D and overlaying the results from the DCIP component of the Titan survey illustrates the relationship between the Silver Queen vein system and the features defined by the DCIP data and between the deep seated porphyry system identified by the MT component of the survey and subsequently proven through diamond drilling (Figure 12).

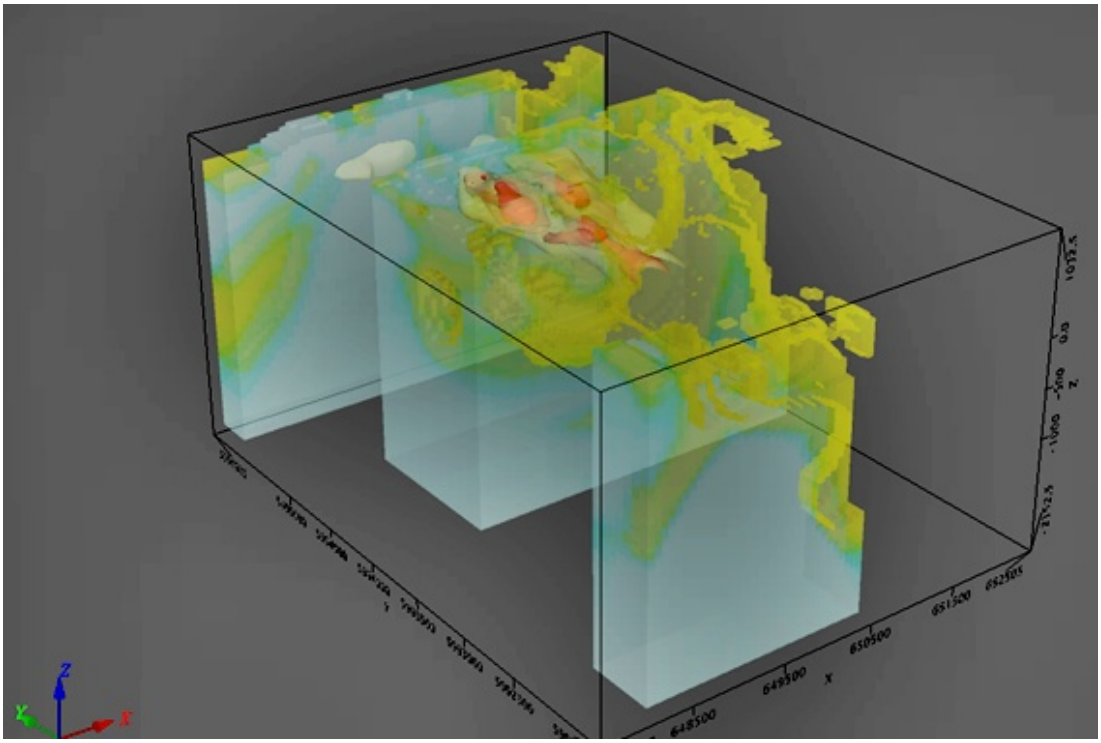

Figure 12. Silver Queen vein system identified by the DCIP component (red/orange iso-surfaces) superimposed on the results of the 3D MT inverted data identifying the deep porphyry system contained within a more resistive host rock environment.

Conclusions

The acquisition of high spatial sampling, high resolution MT data using the present generation of acquisition technology and inversion methods demonstrates the practicality and usefulness of the methodology in the search for deep-seated mineral resources. Targets of relatively small size can be detected and defined if sufficient resistivity contrast with the surround rocks exists. These types of targets can be identified in harsh climatic conditions, harsh environmental conditions, and complex geological environments. Key to the method being effective is a high spatial sampling rate, high resolution electronics (e.g., 24-bit recording systems) and well calibrated magnetic coils, all of which contribute to being able to discriminate between areas of varying resistivity with depth.

Acknowledgements

The hard work and efforts of the field acquisition crews and interpretation group of Quantec Geoscience Ltd. has made the presentation and success of the programs possible. Permission to share the survey results and geologic considerations from Golden Valley Mines Inc. and Joint Venture Partner Ditem Explorations Inc. for the Lake Athabasca MT survey data and from Ellen Clements of New Nadina Explorations Inc. is gratefully acknowledged.

References

Cagniard, L., 1953, Basic Theory of the Magneto-telluric Method of Geophysical Prospecting: Geophysics, 18, 605-635.

JDS Energy and Mining Inc., 2011, http://jdsmining.ca/Default.aspx : Accessed 14 February 2012.

Witherly, K., 2005, Advances in Airborne and Ground EM: Acquisition and Processing: Unpublished notes from “Athabasca Uranium Short Course”, Saskatchewan Geological Survey Open House.

An overview of ZTEM data interpretation tools

Daniel Sattel [1] and Ken Witherly [2]

[1] *EM Solutions, USA (dsattel@earthlink.net)*
[2] *Condor Consulting, Inc., USA (ken@condorconsult.com)*

Abstract

The airborne AFMAG-style data acquired with the ZTEM system can be modelled and interpreted with software originally developed for the interpretation of VLF and MT data. With most surveys covering large areas, image products, including apparent conductivity, phase-rotated response and the VLF peaker allow for a rapid initial assessment of the data to be carried out. Pseudo-sections can be derived with the Karous-Hjelt filter, which offer some indication for the distribution of conductivity with depth. More reliable conductivity-depth sections are derived with 2D and 3D inversion algorithms.

The latter are also used for the computation of synthetic data. ZTEM response values across contacts and fault zones were computed with a 2D algorithm. The results across these features were different, but it can be very difficult to correctly identify the differences when viewed as grid products.

For the modelling and interpretation of ZTEM data in mountainous terrain, it is crucial to take into account the topography of the survey area. It is shown that the ZTEM data acquired across a section of rugged terrain primarily reflects the topographic character of the terrain.

ZTEM data acquired at the Forrestania test site in Western Australia were modelled with 2D and 3D inversion algorithms. Since the survey was flown in two different flight line directions, we were able to evaluate the repeatability of the survey data, which turned out to be excellent. Separate inversion results for the two data sets are very consistent for the 3D algorithm and somewhat consistent for the 2D algorithm.

Introduction

The ZTEM system, built and operated by Geotech Ltd., measures the AFMAG-style magnetic field response (Ward, 1959) of naturally occurring subsurface currents, predominantly those induced by distant lightning discharges (Legault et al., 2009). The vertical component of the time rate of change of the magnetic field is measured with a receiver loop slung below a moving helicopter platform, while the horizontal components of the time rate of change of the magnetic field are recorded on the ground at a base station. The ZTEM tipper responses are extracted from the recorded dB/dt time series at discrete frequencies in the range 25-600 Hz or 30-720 Hz for survey areas with 50 and 60 Hz electric power grids, respectively.

Products originally developed for the interpretation of VLF and MT data have been adapted for application with ZTEM data. These include image products such as phase-rotated response, the VLF peaker (Pedersen et al., 1994) and apparent conductivity and phase (Becken and Pedersen, 2003). Karous-Hjelt pseudo-sections (Karous and Hjelt, 1983) can be derived to obtain some vague conductivity-depth information from ZTEM data. More reliable conductivity-depth sections are derived with 2D and 3D inversions (Holtham and Oldenburg, 2010; Legault et al., 2009; Sattel et al., 2010). In scenarios where current channelling can be ignored, the response of discrete conductors energized by vortex currents can be modelled with MAXWELL (Duncan, 1987).

2D and 3D algorithms can be used to produce forward model synthetic ZTEM profiles across conductivity scenarios of interest, and can be used to evaluate the effect of topography and survey elevation on ZTEM response.

After a brief discussion of the 2D and 3D algorithms used, ZTEM response profiles and derived image products are shown for contact and fault zone models as an interpretation aid to help distinguish these

two conductivity scenarios. The effect of topography is then demonstrated for a ZTEM data set acquired across rugged terrain.

Finally, image and section products derived from a ZTEM data set from Forrestania, Western Australia (WA) are shown. These products demonstrate the contribution of each product to the interpretation of the survey data. The acquisition of data in different flight directions allowed for a consistency check of the inversion algorithms and the survey data to be performed.

Model algorithms

The 2D algorithm used for forward modelling and inverting ZTEM data is based on a 2D MT algorithm developed by Constable and Wannamaker (deGroot-Hedlin and Constable, 1990; Wannamaker at al., 1987; deLugao and Wannamaker, 1996). The algorithm derives the in-line (Tzx) tipper profiles from the computed transverse electric (TE) response. The finite-element algorithm models the effect of topography (Wannamaker et al., 1986) and takes into account the terrain clearance of the airborne platform along the flight line. An example of the model mesh is illustrated in Figure 1.

The 3D inversion algorithm applied to the Forrestania survey data has been developed by Holtham and Oldenburg (2010), and is based on earlier work by Farquharson et al. (2002). Rather than invert individual Tzx profiles, the 3D inversion simultaneously inverts the in-line Tzx and across-line Tzy data of multiple flight lines using a Gauss-Newton approach.

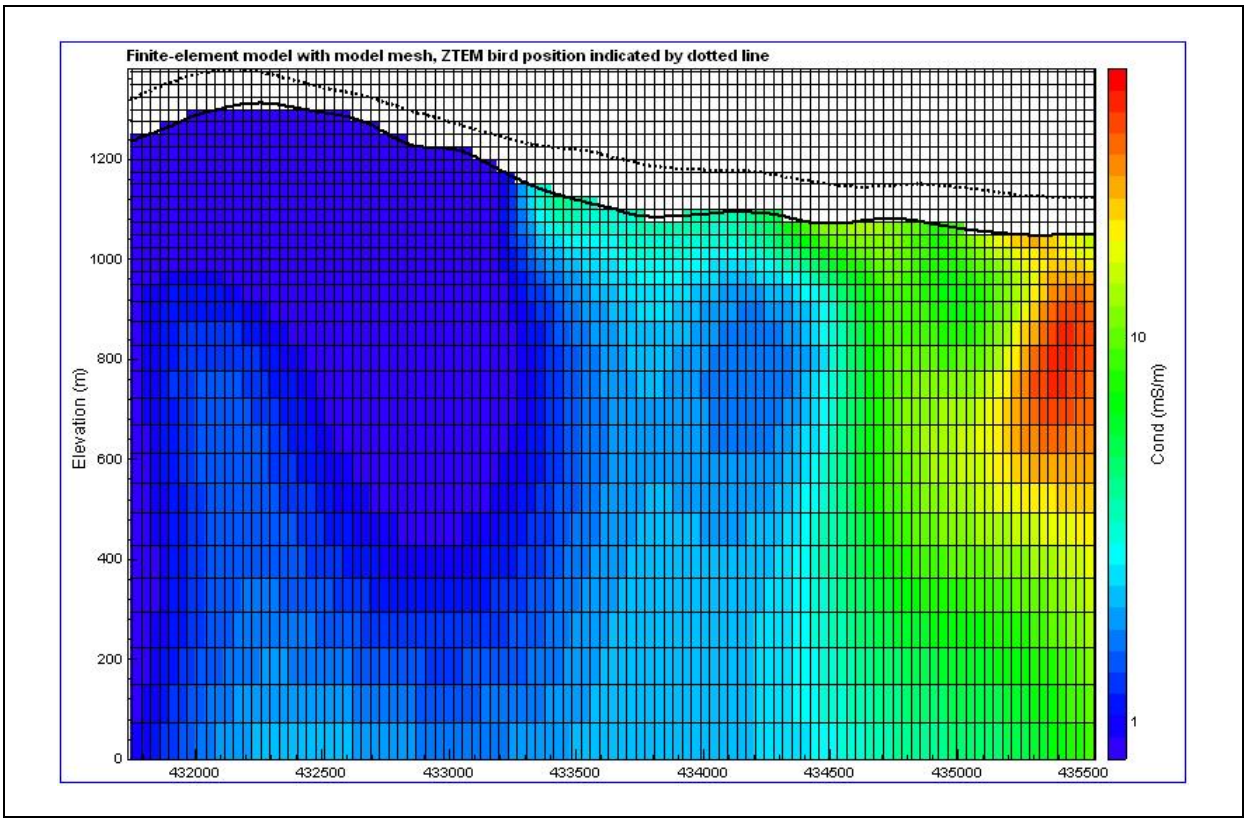

Figure 1. Illustration of a model mesh used for 2D inversion. Since the algorithm takes into account the topography and ZTEM bird terrain clearance along each line, air cells are an integral part of the finite-element model.

Synthetic ZTEM data

Contact model

The inphase response across a vertical contact is shown in Figure 2. Also shown are phase-rotated profiles obtained by reduction-to-pole (RTP) filtering and Hilbert transformation. Profiles of the horizontal derivative and apparent conductivity (Becken and Pedersen, 2003) are also shown.

For the 2D case, the horizontal derivative is equivalent to the Peaker (Pedersen et al., 1994) and the total divergence (Lo and Zang, 2008). Grids of the phase-rotated data and the total divergence are standard products supplied by Geotech with ZTEM survey data. The phase-rotated profiles of Figure 2 indicate little difference between the RTP-filtered and the Hilbert-transformed profiles.

Assuming a 2D conductivity structure, the north-south oriented profiles of Figure 2 were replicated in east and west directions to produce the images shown in Figure 3. The results of Figure 2 and Figure 3 indicate that for the contact model, all observed and derived data show a peak or a crossover at the contact. The width of the response is a function of the conductivity contrast across the contact. Unless the appropriate colour stretch is used, it can be difficult to distinguish a crossover from a peak.

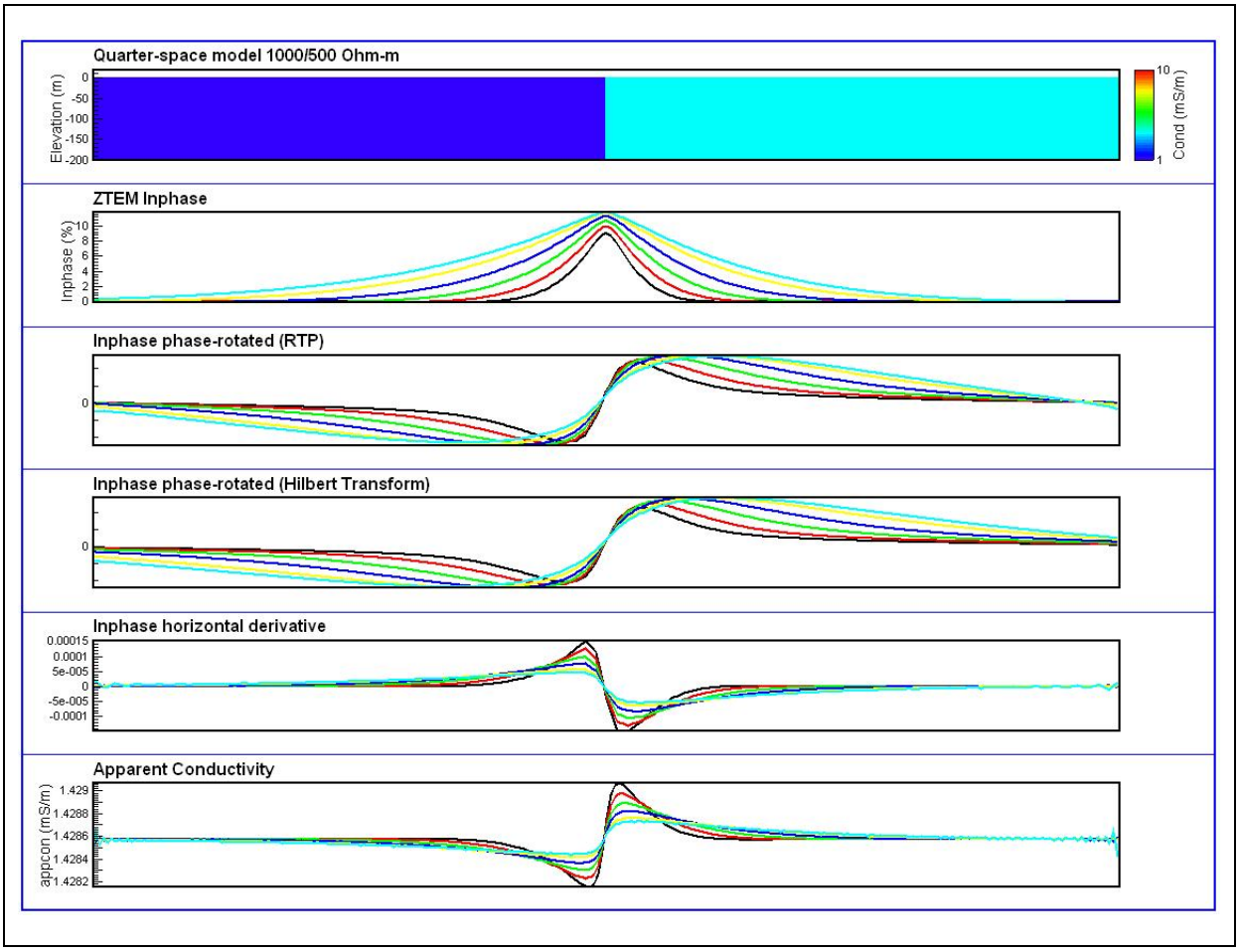

Figure 2. The ZTEM response and derived profiles across a contact, juxtaposing quarter-spaces of 1,000 and 500 ohm-m, respectively. The conductivity model, the inphase response, the phase-rotated inphase response derived by RTP filtering and Hilbert transformation, respectively, the horizontal derivative of the inphase profile and the apparent conductivity profile are shown.

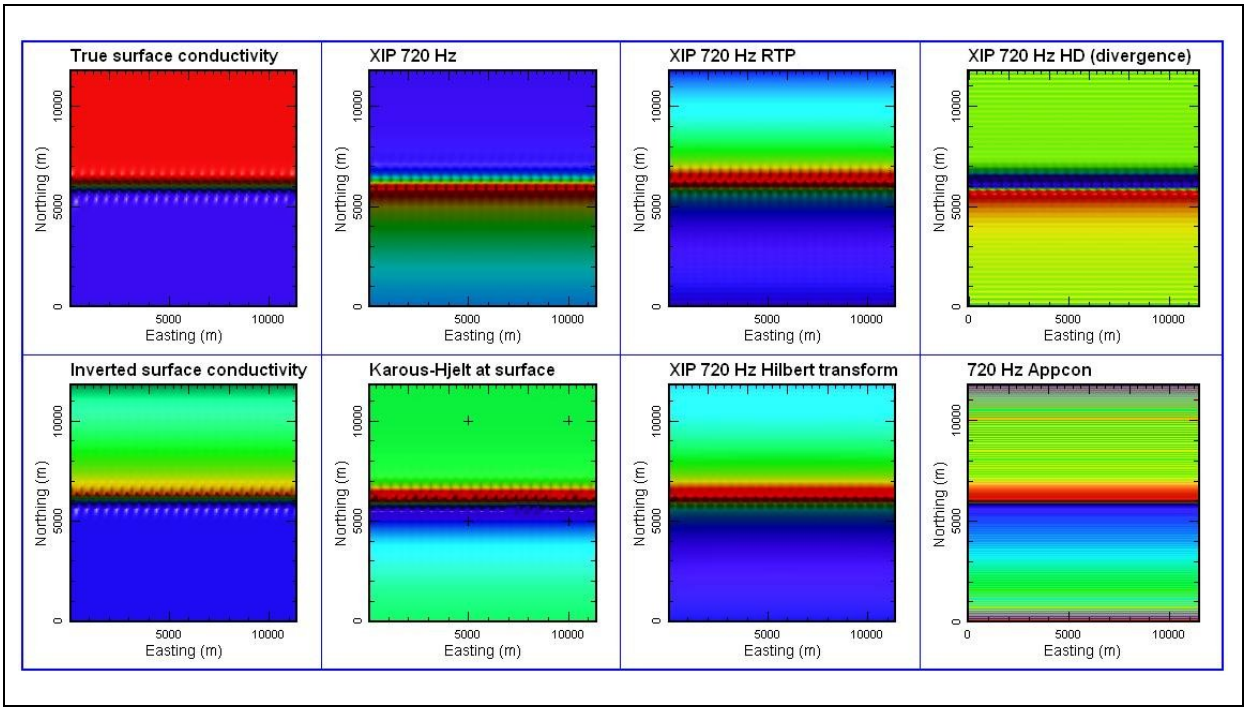

Figure 3. Grids derived from the data shown in Figure 2. Shown in the top row: the true conductivity model, the 720 Hz inphase response, the phase-rotated 720 Hz inphase response (RTP), the horizontal derivative of the 720 Hz inphase response (total divergence grid), and in the bottom row: the conductivity model recovered by 2D inversion, the near-surface Karous-Hjelt filter result of the 720 Hz inphase response, the phase-rotated 720 Hz inphase response (Hilbert transform) and the 720 Hz apparent conductivity grid.

Fault zone model

The inphase response across a conductive fault zone is shown in Figure 4. Also shown are phase-rotated profiles, horizontal derivative and apparent conductivity profiles. The corresponding grid products are shown in Figure 5. The results indicate that for the fault zone model, all observed and derived data show a peak or a crossover at the fault zone. The amplitude of the response is a function of the conductivity contrast between the host material and the fault zone, and the fault zone width.

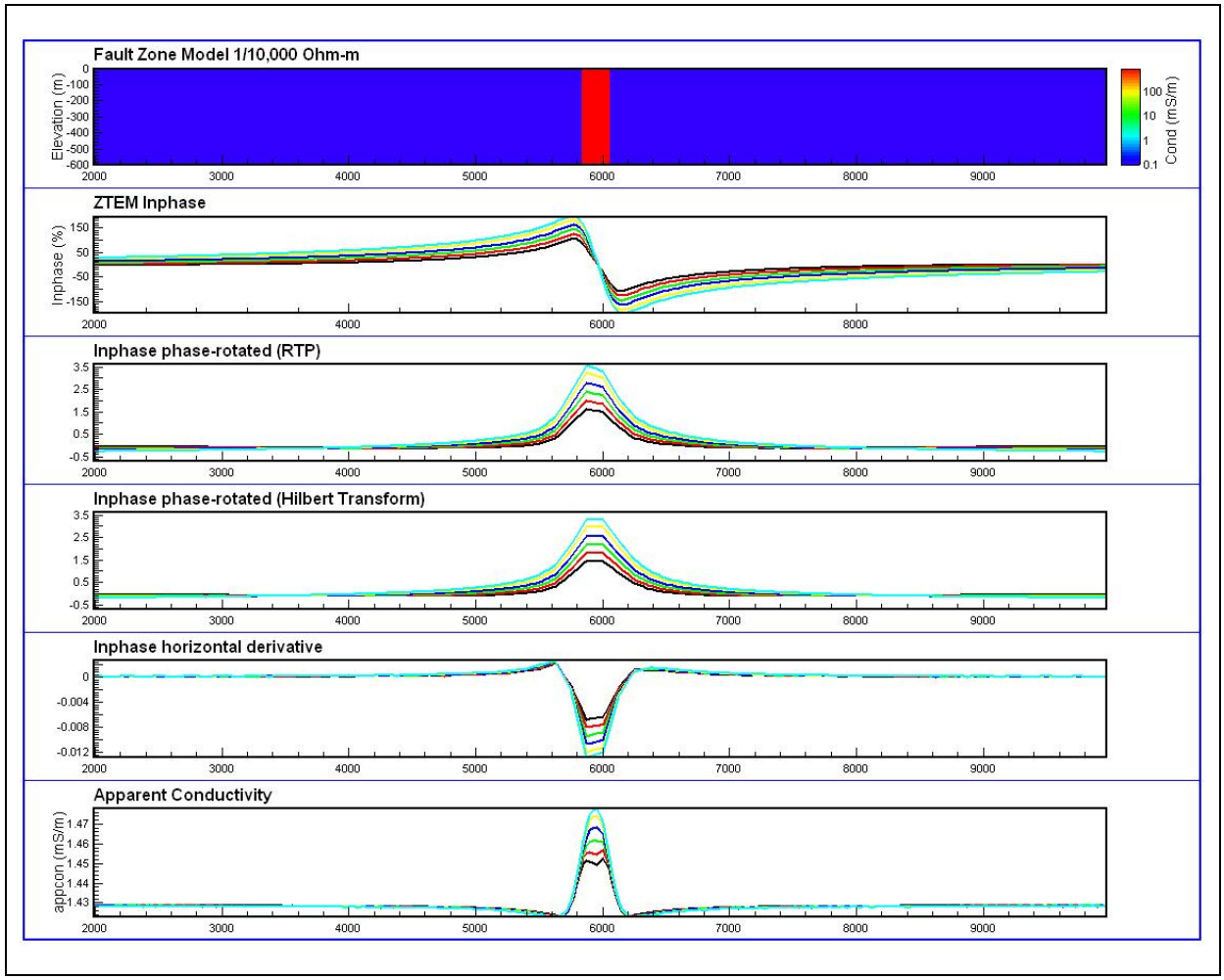

Figure 4. The ZTEM response and derived profiles across a 1 ohm-m fault zone in a 10,000 ohm-m host. The conductivity model, the inphase response, the phase-rotated inphase response derived by RTP filtering and Hilbert transformation, respectively, the horizontal derivative and the apparent conductivity profile are shown.

Even though the profiles of Figure 2 and Figure 4 are very different (i.e., where a crossover anomaly form is present for one model, a peak or trough anomaly form is present for the other model), the responses are much harder to distinguish on the grids. In both cases, a strong change in response occurs in a restricted region in close lateral proximity to the contact or conductor.

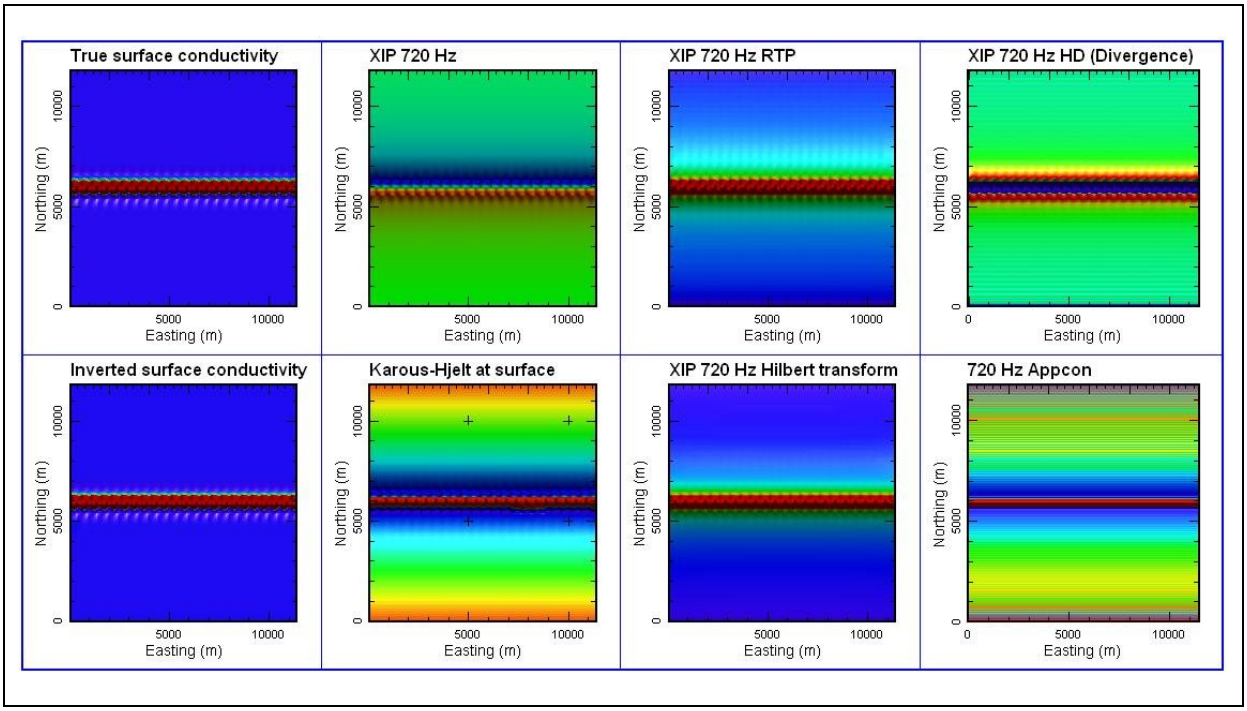

Figure 5. Grids derived from the data shown in Figure 4. Shown in the top row: the true conductivity model, the 720 Hz inphase response, the phase-rotated 720 Hz inphase response (RTP), the horizontal derivative of the 720 Hz inphase response (total divergence grid), and in the bottom row: the conductivity model recovered by 2D inversion, the near-surface Karous-Hjelt filter result of the 720 Hz inphase response, the phase-rotated 720 Hz inphase response (Hilbert Transform) and the 720 apparent conductivity grid.

The effect of topography

Although survey data can be corrected for the effect of varying receiver elevation by analytic continuation (Watts, 1975), application of a topographic correction, as discussed for VLF and MT data by Eppelbaum (1991) and Schwalenberg and Edwards (2004) appears less reliable. Correcting the data for terrain effects and the sensor elevation would allow for a less ambiguous interpretation of the various filtered image products. However, such a correction is unnecessary for the inversions, since the survey topography and the receiver elevation are taken into account by the algorithms, as illustrated in Figure 1.

Sattel and Witherly (2012) show synthetic ZTEM profiles across a hill and a depression. Their results indicate that the ZTEM response of hills and depressions can be confused with the responses of conductors and resistors, respectively, if the topography is not taken into account during a qualitative interpretation of various products or when the data are subjected to quantitative processing such as inverse modelling. Figure 6 shows images of the topography and acquired Tzx data for a ZTEM survey across mountainous terrain. The vertical relief in the survey area is approximately 2 km. Using the observed topography, Tzx responses were predicted for 100 and 1,000 ohm-m half-spaces, respectively, and are shown in Figure 6. The observed and predicted data have been phase-rotated to align peaks with conductors and troughs with resistors. A comparison of the images shows strong agreement between the observed and predicted data; this confirms that it is essential to take into account topography for the interpretation of ZTEM data in mountainous terrain.

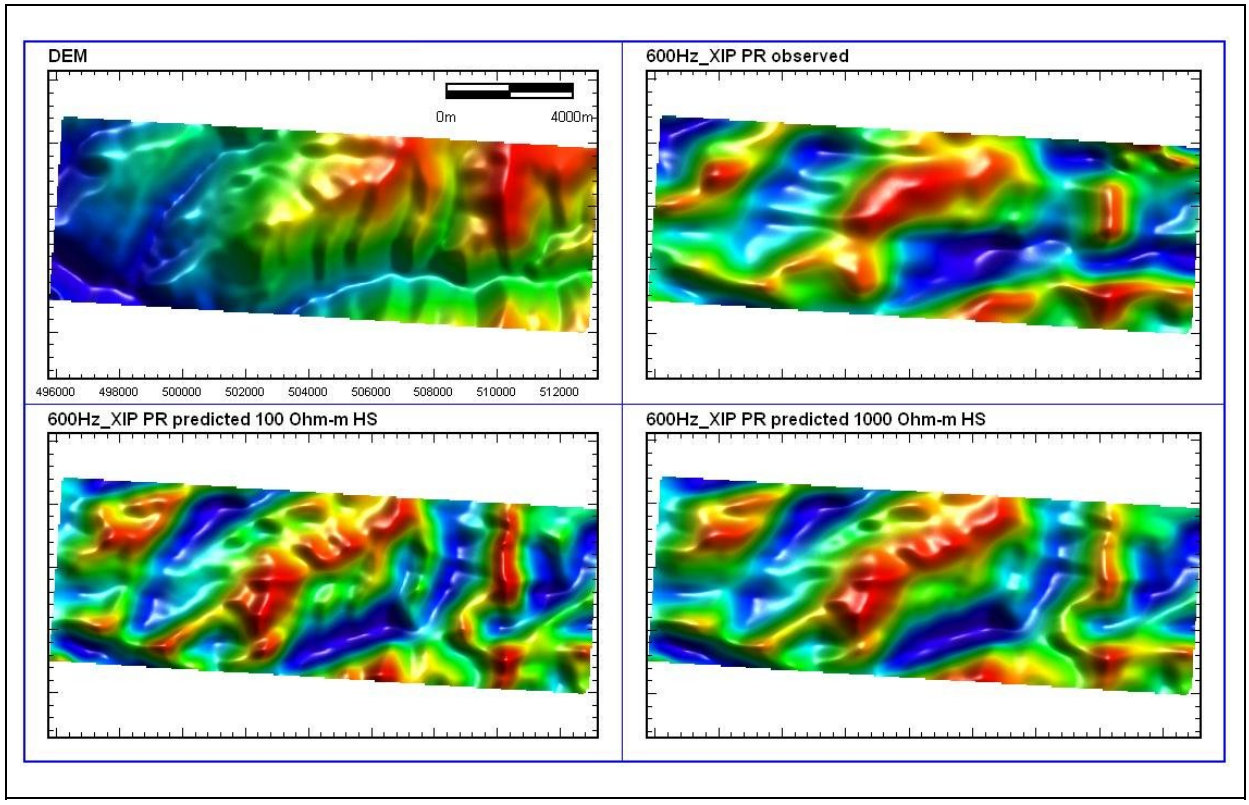

Figure 6. ZTEM response in mountainous terrain. Shown clockwise from the upper left: the survey topography, the observed 600 Hz phase-rotated Tzx inphase data, and the same data predicted for 1,000 and 100 ohm-m half-spaces, respectively. The high degree of agreement between observed and predicted data show that the response is dominated by the topographic response of the survey area.

Forrestania Survey

Figure 7 shows the flight lines of a survey flown at the Forrestania, WA, EM test range, which is described on the website of Southern Geoscience Consultants (www.sgc.com.au). The ground covered by the ZTEM survey includes two drilled, barren, semi-massive to massive sulphides (IR2 and IR4), hosted in highly resistive bedrock under a conductive overburden (10-20 S). IR2 is described as shallow (<100 m), highly conductive (>7,000 S), small (<75x75 m) and dipping 30-40 degrees to the north. It is well defined by surface, downhole and some airborne EM systems. Conductor IR4 is described as deep (>300 m), highly conductive (5,000-10,000 S), extensive in strike and plunge extent (>500 m), limited in depth extent (100-150 m) and dipping 30-40 degrees to the north. East-west and north-south lines were flown over the IR2 and IR4 bodies which allowed repeatability and consistency between the two data sets to be assessed. The terrain is flat with less than 60 m of vertical relief across the survey area, and it was thought that ZTEM response variations related to the topography would be very unlikely.

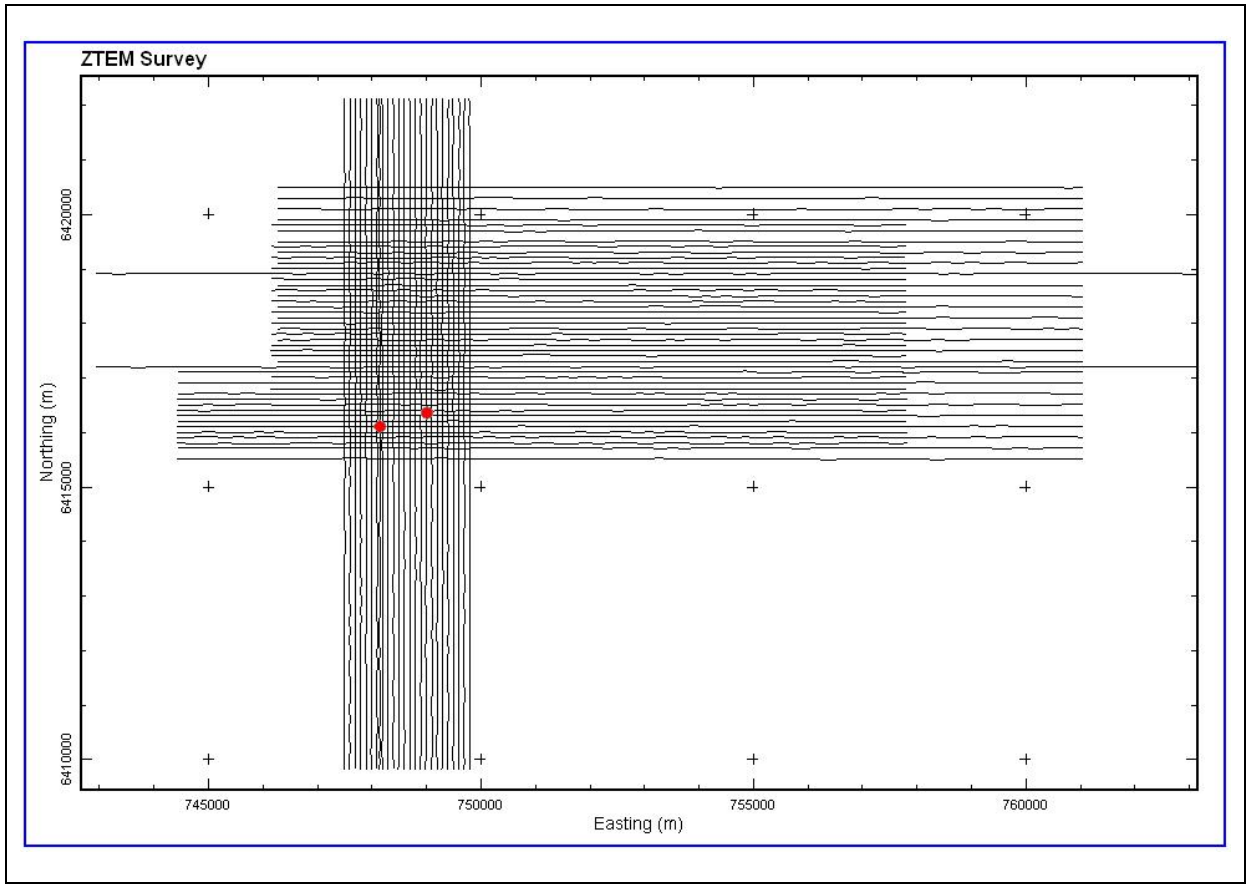

Figure 7. Flight lines from the ZTEM survey at Forrestania, WA. The locations of sulphides IR2 and IR4 are indicated by red dots.

Image products of data from the north-south lines are shown in Figure 8 to Figure 12. The Tzx and Tzy inphase data shown in Figure 8 indicate the sensitivity of the data to cross-striking structures. The corresponding phase-rotated grids of these responses are shown in Figure 9. These Tzx and Tzy inphase grids were then combined to form the total phase-rotated inphase grids shown in Figure 10. These grids show high values over cross-striking conductors and show structures striking in many directions. Total divergence grids are also shown in Figure 10. Since these are a product of the spatial derivatives, they highlight the spatial variation of the data. The apparent conductivity grids shown in Figure 11 are derived from the Tzx and Tzy data and show a close resemblance to the total phase-rotated grids in Figure 10. The corresponding phase grids are more difficult to interpret. According to Becken and Pedersen (2003), lower and higher values indicate conductivity to be decreasing and increasing, respectively, with depth.

Karous-Hjelt near-surface grids as shown in Figure 12 are another way to apply a phase rotation to the data, while also attempting to extract some depth information.

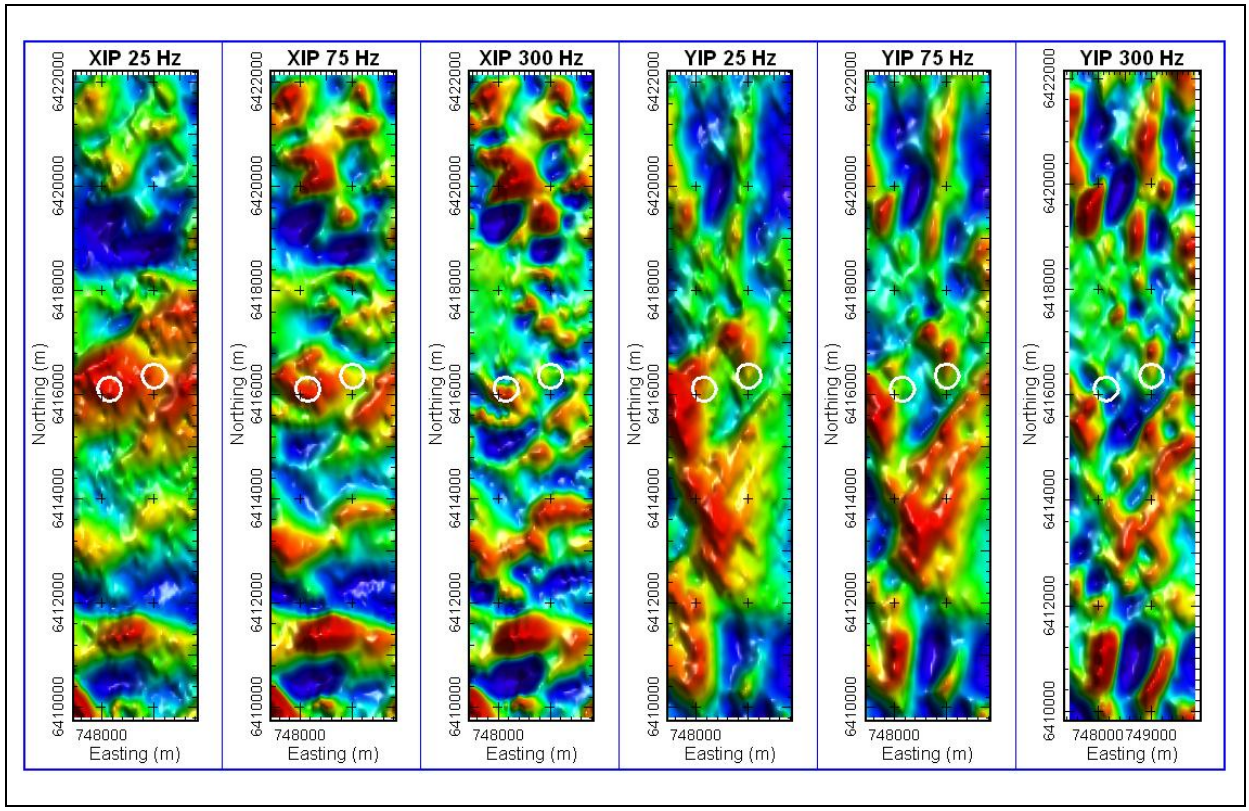

Figure 8. Grids of selected frequencies of Tzx (left panels) and Tzy (right panels) data from north-south survey lines provided by Geotech. The locations of the known sulphides IR2 and IR4 are indicated by white circles.

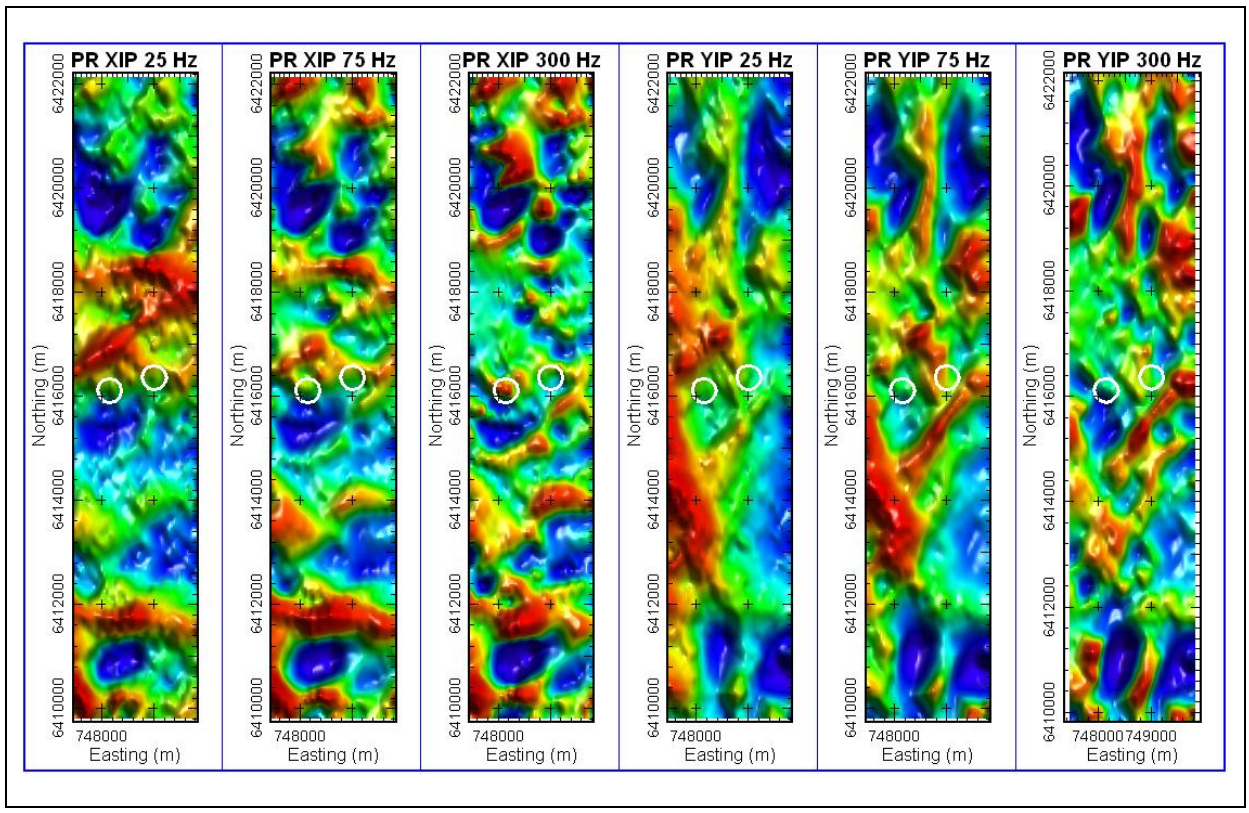

Figure 9. Phase rotated grids for the data shown in Figure 8 provided by Geotech.

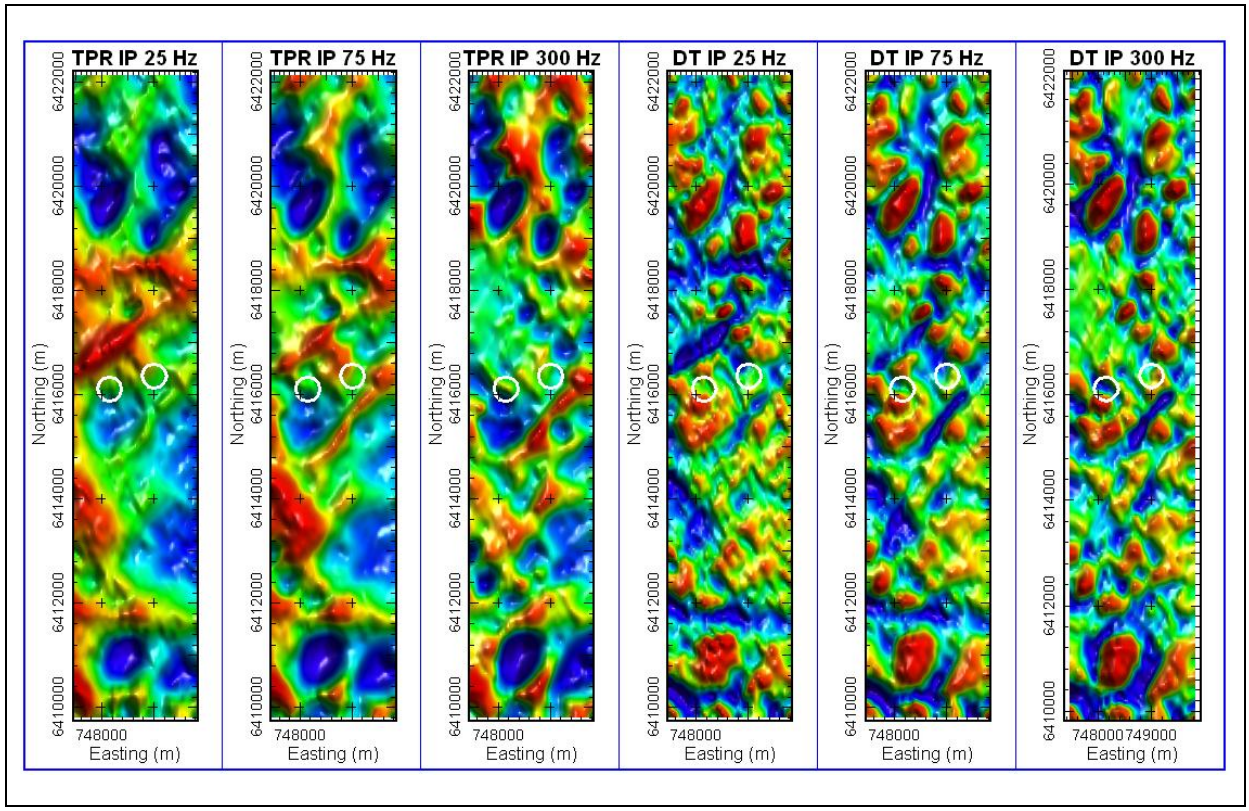

Figure 10. Total phase rotated grids (left panels) and total divergence grids (right panels) provided by Geotech.

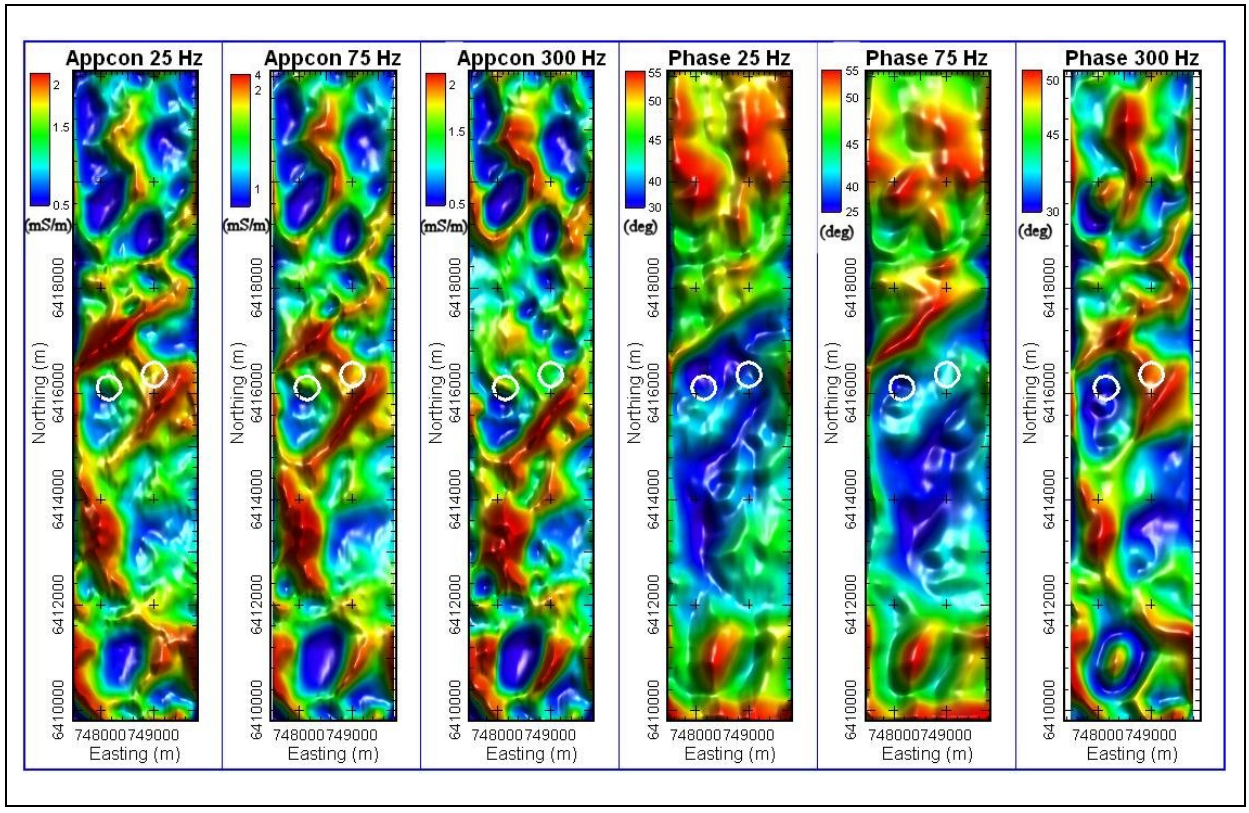

Figure 11. Apparent conductivity (left panels) and phase (right panels) grids.

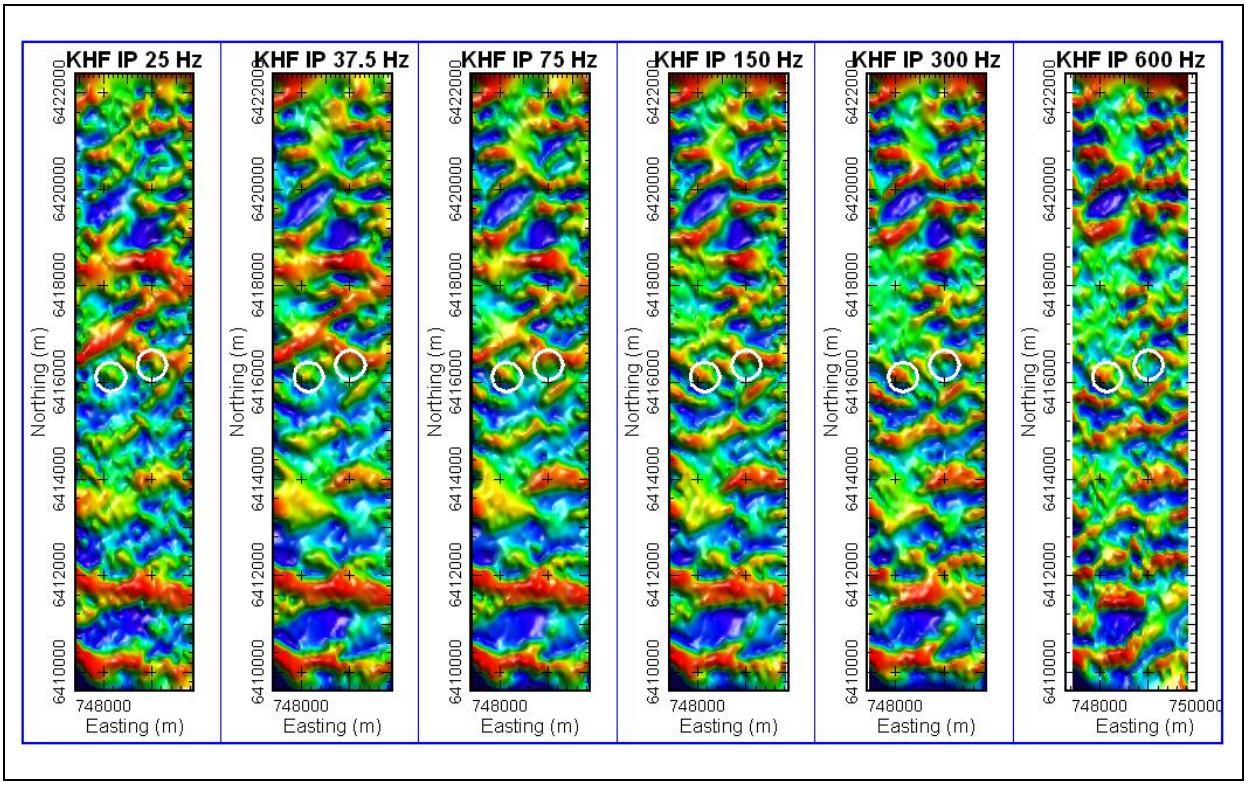

Figure 12. Karous-Hjelt near-surface grids derived from the Tzx in-phase (left panels) and quadrature (right panels) data.

Karous-Hjelt pseudo-sections derived from the Tzx in-phase data acquired across conductor IR2 are shown in Figure 13. A different section is derived for each frequency and a composite model is generated from the averaged sections of all frequencies. The location of sulphide IR2 is indicated by elevated current density values at the surface. Even though the depth information is not reliable, these pseudo-sections give some indication of the spatial distribution of the most prominent conductors and resistors. Hence, these sections can help to interpret conductors mapped on 2D or 3D inversion conductivity-depth sections that might be related to data over-fitting.

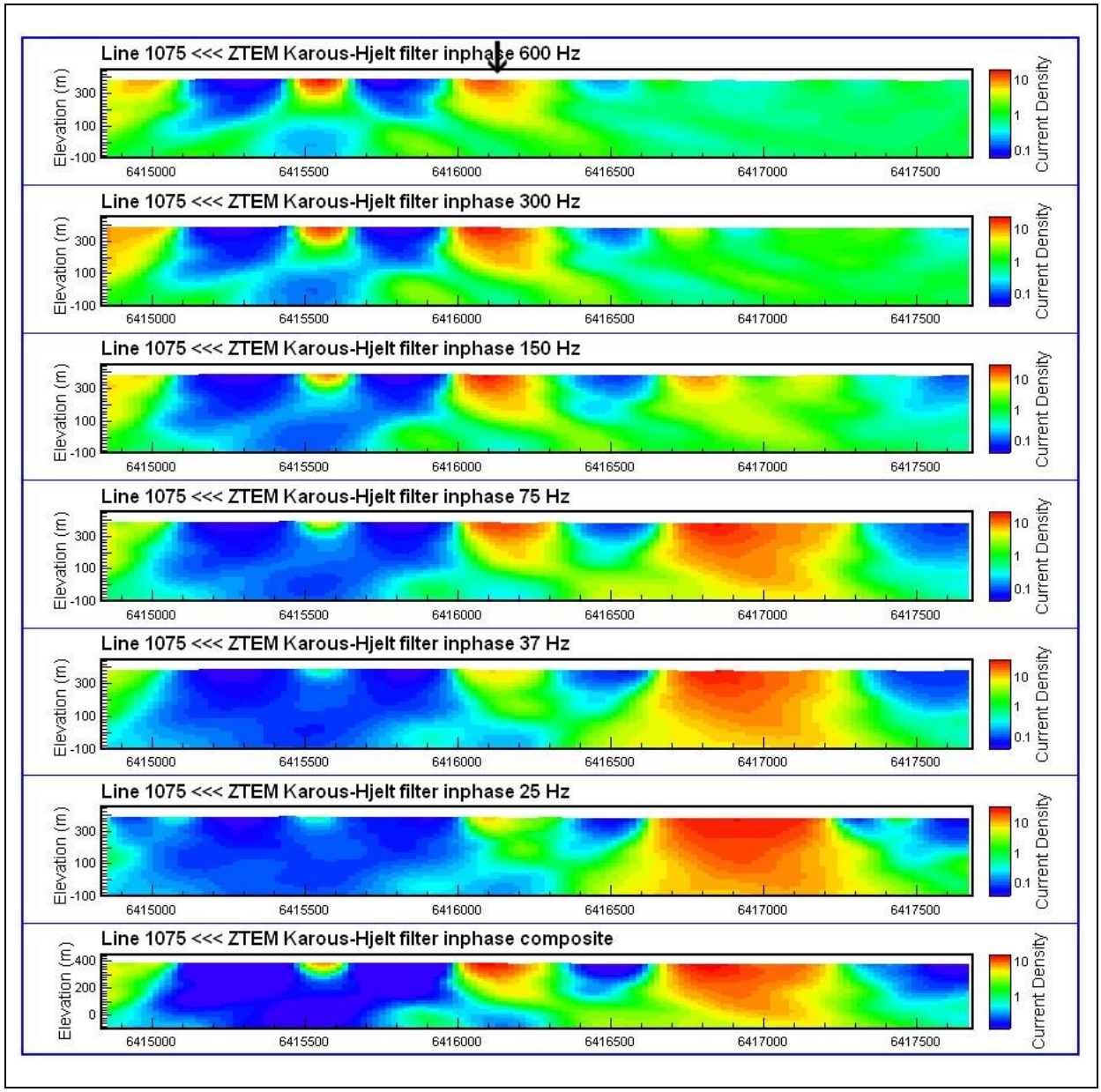

Figure 13. Sections for north-south line 1075. Karous-Hjelt sections derived from inphase ZTEM profiles with decreasing frequency from top to bottom and a composite section of all frequencies at the very bottom. The location of conductor IR2 is indicated by an arrow.

The 2D inversion result of the same line shown in Figure 14 indicates a conductive structure at the location of IR2. Due to the limited strike length of the sulphide zone, a strong response was not expected. It should be noted that the response might be due to a geological structure with long strike length that hosts the sulphide.

The 2D inversion result of the east-west line across IR2 (not shown) does not give any indication of the presence of the conductor. For a more appropriate comparison between the east-west and north-south data sets, Tzy data from the east-west data set were extracted to derive a profile of in-line tipper values directed north-south. For this step, each east-west line contributes one point to the pseudo north-south line, and the data spacing on the pseudo profile is determined by the line spacing of the east-west data set. Due to the close flight-line spacing of the Forrestania survey (mostly 100 m) the anomaly shape is recovered well and the derived conductivity structure agrees very well with the result from the north-south data. This indicates great consistency and repeatability between the two data sets flown at different flight line directions and acquired at different times.

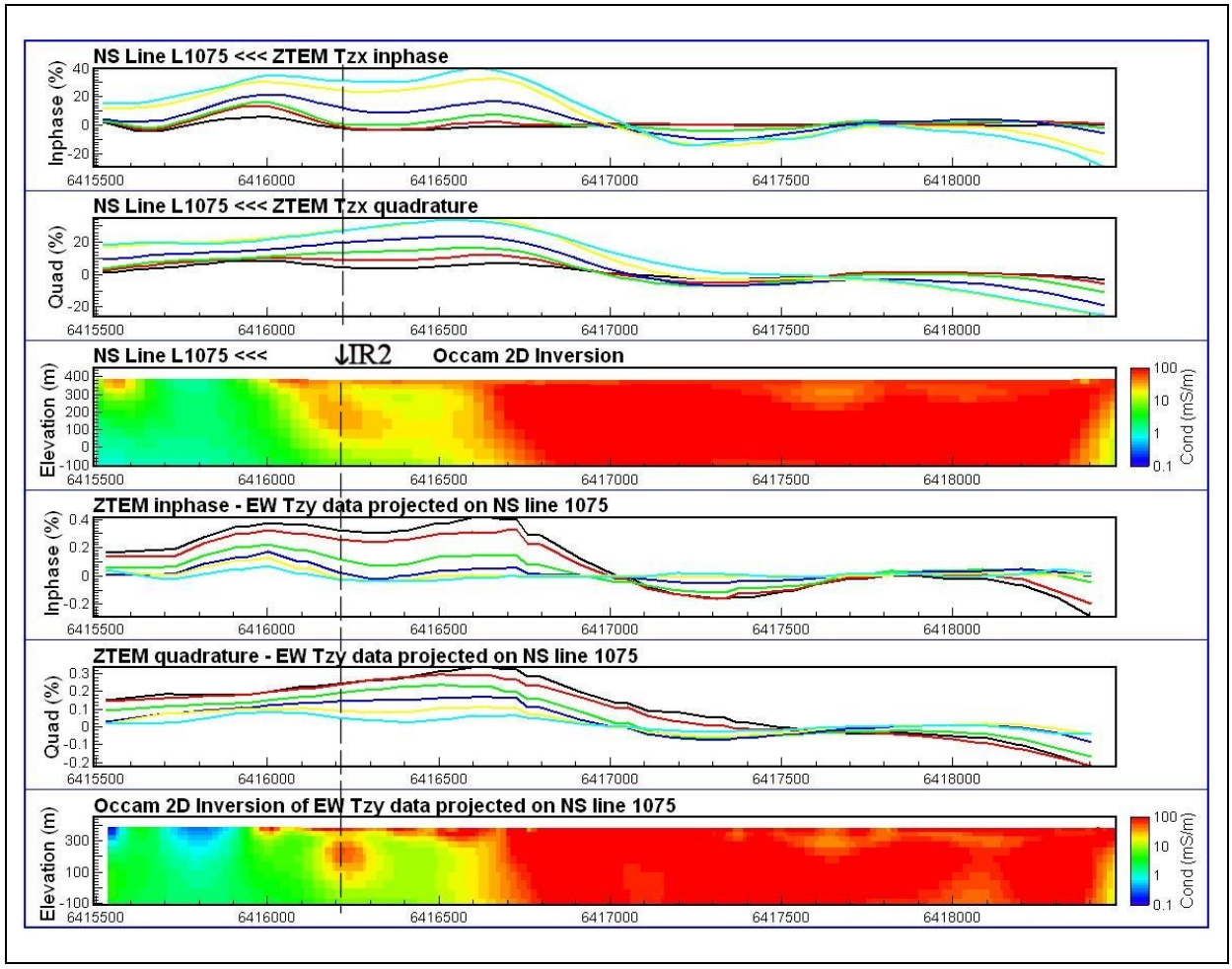

Figure 14. ZTEM profiles across sulphide IR2, indicated by a dashed line, with corresponding inversion results. A portion of Tzx profiles of north-south line 1075 are shown in the top panels; the profiles derived from the Tzy data of the east-west lines are shown in the bottom panels.

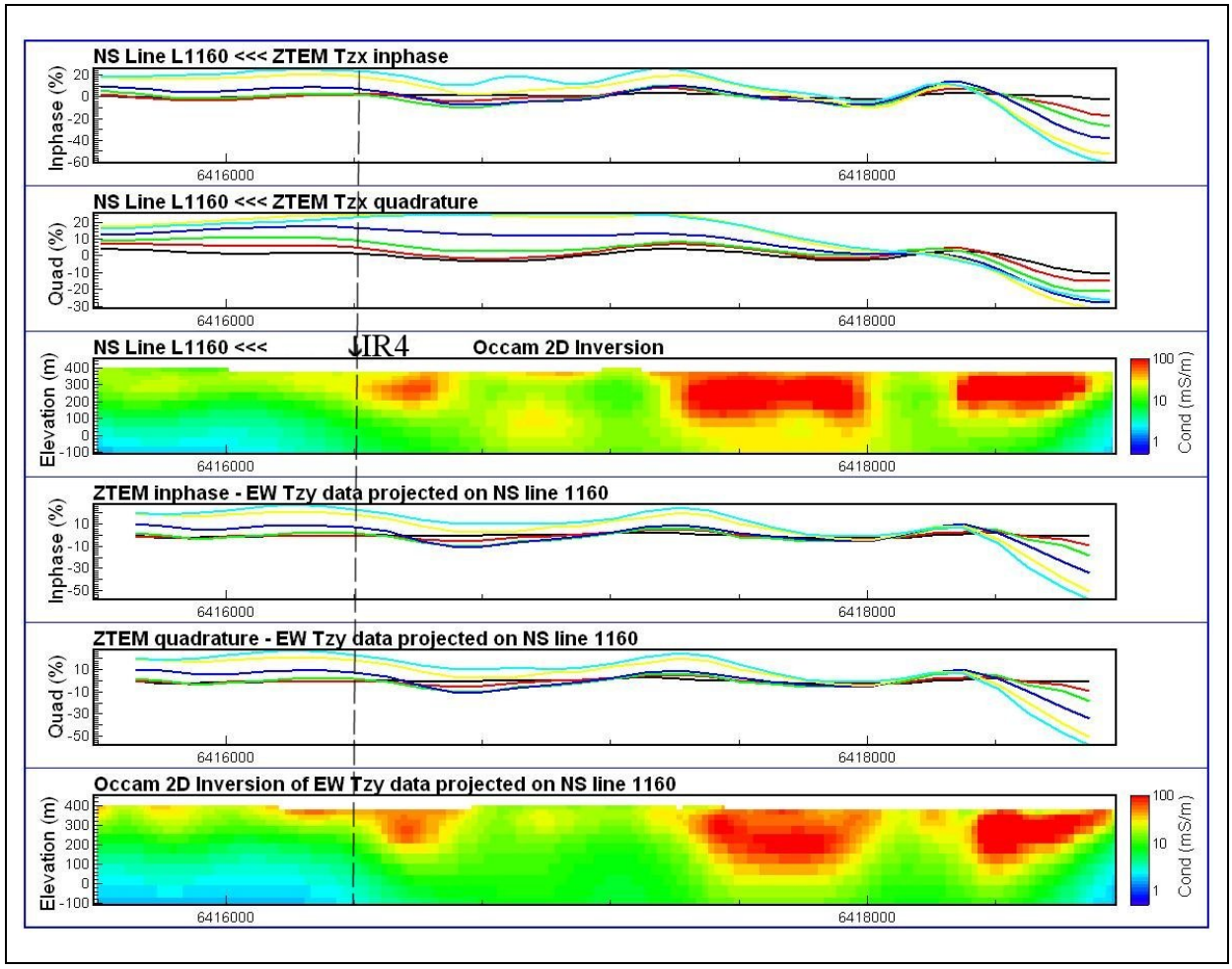

Figure 15. ZTEM profiles across the location of sulphide IR4, indicated by a dashed line, with corresponding inversion results. A portion of Tzx profiles of north-south line 1160 are shown in the top panels; the profiles derived from the Tzy data of the east-west lines are shown in the bottom panels.

The 2D inversion results of data acquired across IR4 are shown in Figure 15. The original north-south data are shown along with projected data from the east-west survey. The two data sets show excellent agreement again. The conductivity-depth sections indicate a near-surface conductor near IR4, but probably too shallow to correspond to the target sulphide body.

These results also suggest that for 2D inversions to extract the maximum information of some structures, survey data might have to be projected and rotated into profiles with more appropriate flight-line directions. Since Tzx and Tzy are available for the entire survey, any angle can be chosen for reprojecting the data. However, in complex terrain such as Forrestania, a 3D inversion is expected to give more reliable results than 2D inversions. For the 3D inversion, the entire NS survey area was inverted using horizontal cell sizes of 100x100 m, and the sub-area, corresponding to the region of overlap of the east-west and north-south surveys, was inverted with 50x50 m cells.

The north-south and east-west survey data of the sub-area were independently modelled by the 3D-inversion. The conductivity values recovered from both data sets across IR2 and IR4 are shown in Figure 16 and Figure 17. These sections are quite similar to the 2D inversion results from Figure 14 and Figure 15. The inversion results mostly agree that a shallow conductor at the location of IR2 is dipping north, agreeing with the known geometry of IR2. Near the location of IR4, the 3D inversions indicate a broad conductor with significant depth extent, whereas the 2D inversions indicate near-surface conductive material only. Since IR4 is known to be 300 m below surface and dipping north, the modelled conductive material might not correspond to the sulphide body. The profiles of predicted response for the 3D model match the observed data quite well. A better fit would have been

achievable, but at the expense of the models' smoothness which was not considered to be justified in this instance.

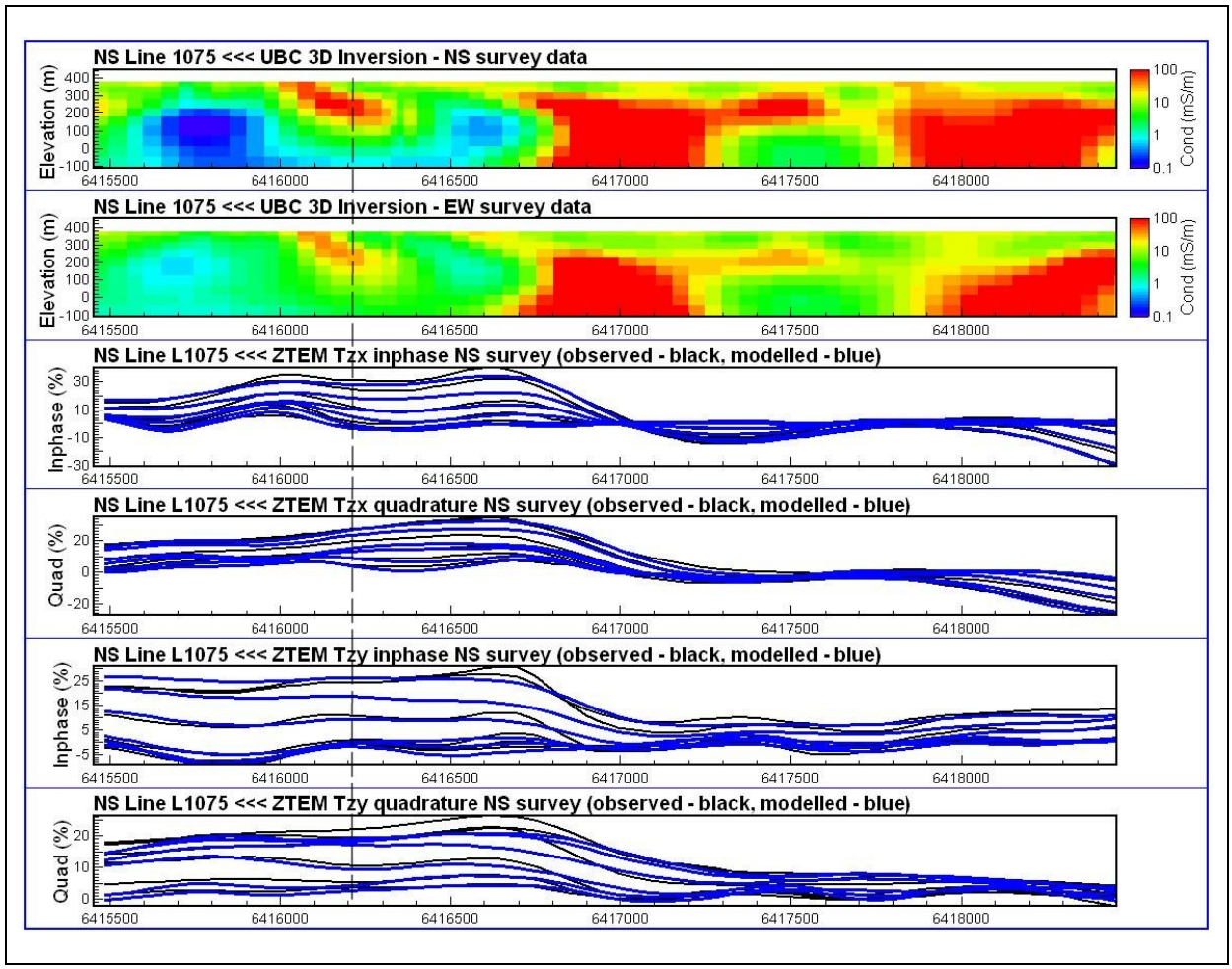

Figure 16. 3D inversion results across sulphide IR2, indicated by a dashed line. Shown are the conductivity-depth sections derived from the north-south and east-west data, respectively, and a comparison of the observed and modelled Tzx and Tzy profiles for the north-south data. Compare to 2D inversion results of Figure 14.

A comparison of conductivity slices derived from the 2D and 3D inversions for the north-south survey data is shown in Figure 18. The generation of east-west pseudo-lines allowed for the 2D inversion of the Tzy data. To capture the results of both 2D inversions, the conductivity grids of the Tzx and Tzy data were merged. As shown in Figure 18, the results of the merged grids look reasonable, and appear to have successfully combined the information of the individual results.

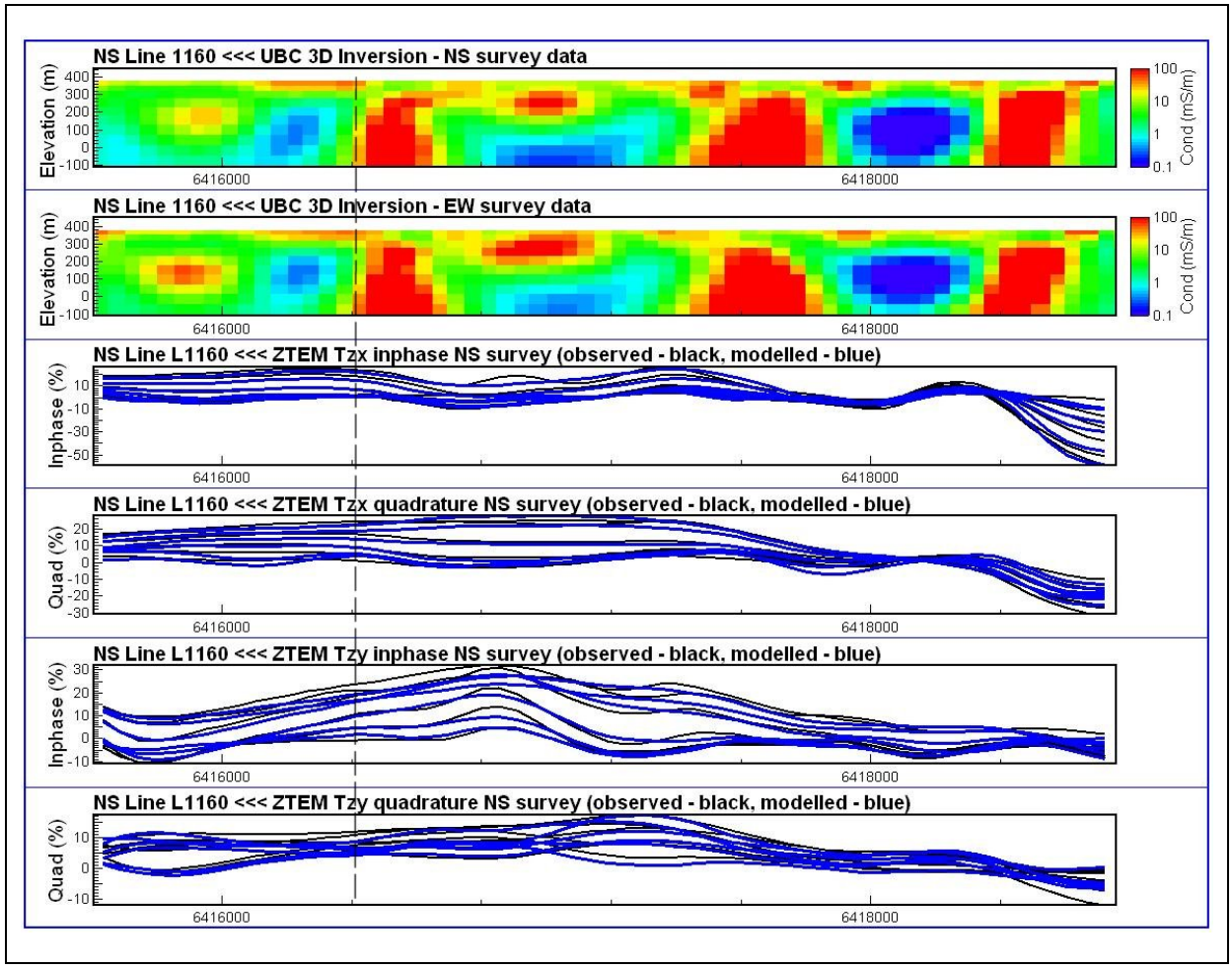

Figure 17. 3D inversion results across the location of sulphide IR4, indicated by a dashed line. Shown are the conductivity-depth sections derived from the north-south and east-west data, respectively, and a comparison of the observed and modelled Tzx and Tzy profiles for the north-south data. Compare to 2D inversion results of Figure 15.

The 3D inversion results shown in Figure 18 confirm the complexity of the conductivity structure and indicate that the strike direction is quite variable across the survey area, the latter indicating that the to results from 2D inversions are likely to be less reliable. Nevertheless, the 2D and 3D results are fairly similar. The conductivity slices derived from the 2D inversion actually have better spatial resolution due to a much smaller horizontal cell size (10 m) having been used. However, it is unclear if some of the structures, shown on the 2D conductivity grids but absent on the corresponding 3D grids, are real or an artefact of the 2D processing.

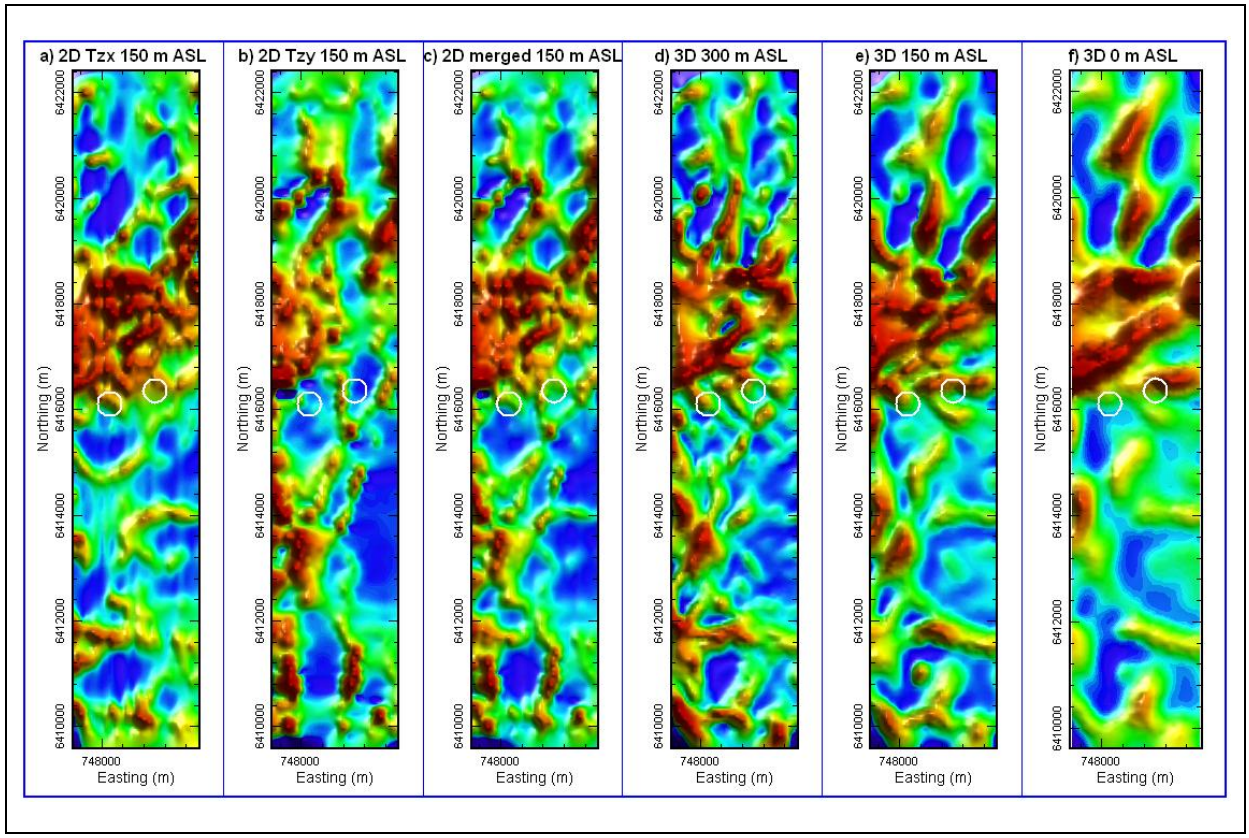

Figure 18. Conductivity-elevation slices derived from the Forrestania north-south survey data, from left to right: a) 2D inversion result of Tzx data at 150 m ASL, b) 2D inversion result of Tzy data at 150 m ASL, c) merge of a) and b), d-f) 3D inversion results at 300, 150 and 0 m ASL, respectively.

A summary of the modelling results across the two known sulphide bodies is shown in Figure 19. Since this is the area of overlap between the north-south and east-west surveys, results are shown for both data sets. The results of the total phase-rotated 150 Hz responses are quite similar between the two data sets, indicating excellent data repeatability. The former as well as the 150 Hz apparent conductivity values indicate the sulphides IR2 and IR4 to be located along northwest-southeast trending, conductive lineaments. The conductivity slices derived from the 2D inversions show great similarity where expected: 1) between the slices derived from the north-south Tzx and the east-west pseudo-line Tzy data (both being sensitive to structures striking east-west) and 2) between the slices derived from the east-west Tzx and the north-south pseudo-line Tzy data (both being sensitive to structures striking north-south). The conductivity slices derived from the 3D inversion of the two data sets show excellent agreement and map the locations of the sulphides near conductive lineaments. The conductor mapped at the location of sulphide IR2, as shown in Figure 14 and Figure 16, not being mapped as a discrete conductor in any of the images of Figure 19 suggests that IR2 is likely connected to a more extended structure, as suggested by the 3D result. Being connected to an extended structure increases current channelling into the sulphide, boosting its EM response and enabling its detection by an AFMAG method.

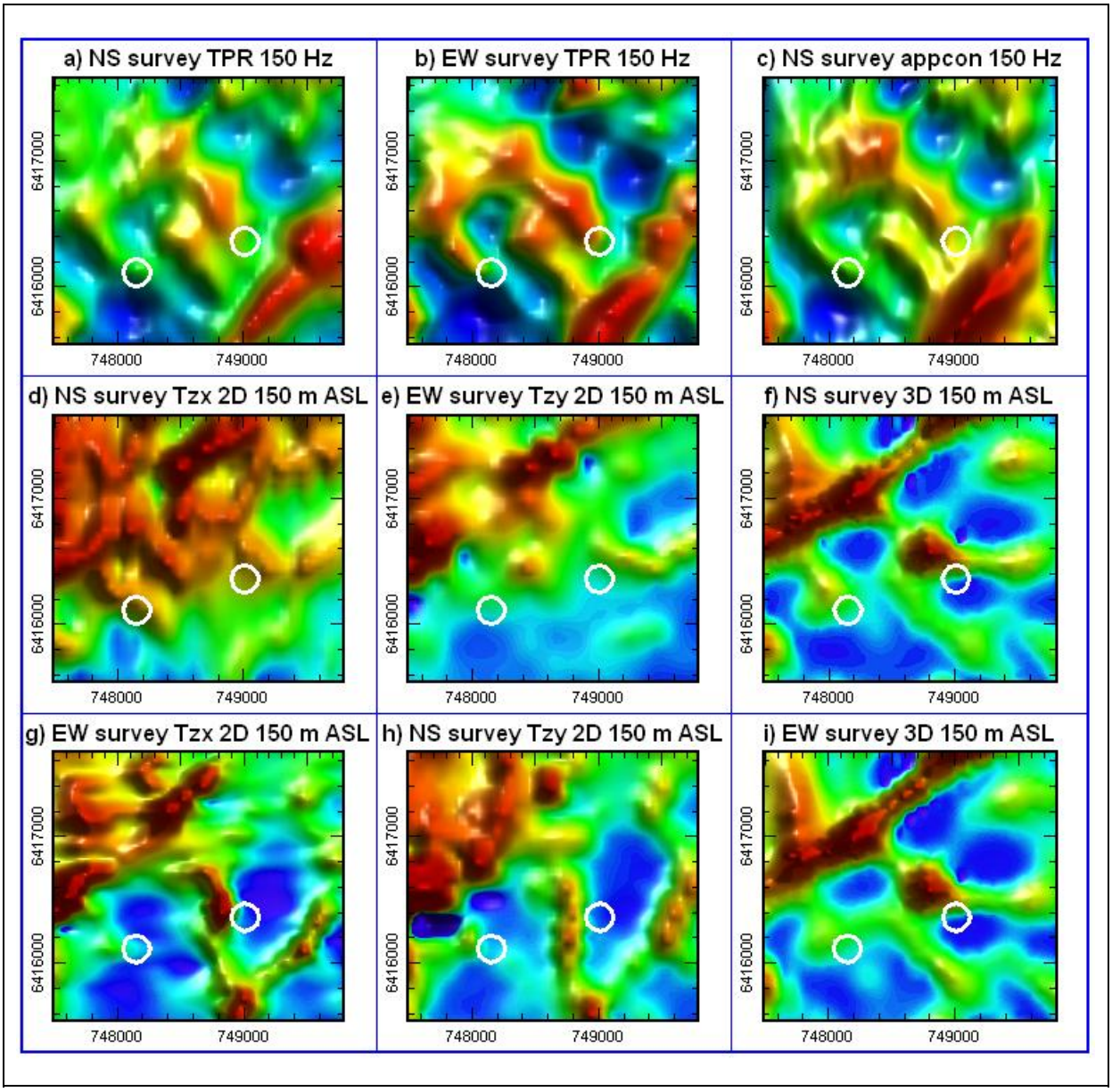

Figure 19. Summary of processing and modelling results of both surveys in the area of overlap around sulphides IR2 and IR4. In the top row: a) 150 Hz total phase-rotated inphase response for north-south lines, b) same as a) for east-west line data, c) apparent conductivity values derived from the 150 Hz north-south line data; in the center and bottom row: conductivity slices at 150 m ASL derived from d) 2D inversion of north-south Tzx data, e) 2D inversion of east-west Tzy data, f) 3D inversion of north-south data, g) 2D inversion of east-west Tzx data, h) 2D inversion of north-south Tzy data, i) 3D inversion of east-west data. Note the similarities between d) and e), g) and h), and f) and i).

Conclusions

Products originally developed for the interpretation of VLF data, such as phase-rotated response, apparent conductivity, the VLF peaker and Karous-Hjelt filtering can be applied to ZTEM data for rapid initial data assessment. For more reliable results, 2D and 3D inversion algorithms can be used. The latter can also be used to forward model conductivity scenarios and predict the response due to the topography of a survey area.

The results from synthetic models indicate that even though contacts and fault zone models produce quite different ZTEM profiles, it is difficult to distinguish them using grid products.

A brief analysis of ZTEM data acquired across rugged terrain indicates that it is essential to take into account topography for the inversion of ZTEM data in such an environment.

The analysis of ZTEM data at Forrestania, WA, has shown excellent repeatability between two data sets flown in different flight line directions and acquired at different times. The derivation of ZTEM profiles along pseudo-lines allowed suitably oriented 2D inversions to be produced for structures that were oriented in directions other than perpendicular to the survey flight-line direction. However, in terrain of complex geology and conductivity structure such as at Forrestania, 3D inversions are necessary to derive reliable conductivity-depth information from the data.

Acknowledgments

We would like to thank Doug Oldenburg and Elliot Holtham for use of their 3D inversion algorithm ZTEM_MT3Dinv, and Geotech Airborne Pty Ltd for releasing the Forrestania data shown in this publication.

References

Becken, M., and Pedersen, L. B., 2003, Transformation of VLF anomaly maps into apparent resistivity and phase: Geophysics, 68, 497-505.

DeGroot-Hedlin, C. and Constable, S., 1990, Occam's inversion to generate smooth two-dimensional models from magnetotelluric data: Geophysics, 55, 1613-1624.

De Lugao, P. P., and Wannamaker, P., 1996, Calculating the two-dimensional magnetotelluric Jacobian in finite elements using reciprocity: Geophysical Journal International, 127, 806-810.

Duncan, A. C., 1987, Interpretation of down-hole transient EM data using current filaments: Exploration Geophysics, 18, 36-39.

Eppelbaum, L. V., 1991, Examples of Terrain Corrections in the VLF-method in the Caucasian Region, USSR: Geoexploration, 28, 67-75.

Farquharson, C. G., Oldenburg, D. W, Haber, E., and Shekhtman, R., 2002, An algorithm for the three-dimensional inversion of magnetotelluric data: SEG Expanded Abstracts, 21, 649-652.

Holtham, E., and Oldenburg, D. W., 2010, Three-dimensional inversion of ZTEM data: Geophysical Journal International, 182, 168-182.

Karous, M., and Hjelt, S. E., 1983, Linear filtering of VLF dip-angle measurements: Geophysical Prospecting, 31, 782-794.

Legault, J. M., Kumar, H., Milicevic, B., and Wannamaker, P., 2009, ZTEM tipper AFMAG and 2D inversion results over an unconformity target in northern Sakatchewan: SEG Expanded Abstracts, 28, 1277-1281.

Lo, B., and Zang, M., 2008, Numerical modelling of Z-TEM (airborne AFMAG) responses to guide exploration strategies: SEG Expanded Abstracts, 27, 1098-1102.

Pedersen, L. B., Qian, W., Dynesius, L., and Zhang, P., 1994, An airborne tensor VLF system. From concept to realization: Geophysical Prospecting, 42, 863-883.

Sattel, D., Witherly, K., and Becken, M., 2010, A brief analysis of ZTEM data from the Forrestania test site, WA: 21st International Geophysical Conference and Exhibition, ASEG, Extended Abstracts.

Sattel, D., and Witherly, K., 2012, Extracting information from ZTEM data with 2D inversions: 22nd International Geophysical Conference and Exhibition, ASEG, Extended Abstracts.

Schwalenberg, K., and Edwards, R. N., 2004, The effect of seafloor topography on magnetotelluric fields: an analytical formulation confirmed with numerical results: Geophysical Journal International, 159, 607-621.

Wannamaker, P. E., Stodt, J. A., and Rijo, L., 1986, Two-dimensional topographic responses in magnetotellurics modelled using finite elements: Geophysics, 51, 2131-2144.

Wannamaker, P. E., Stodt, J. A., and Rijo, L., 1987, A stable finite-element solution for two-dimensional magnetotelluric modelling: Geophysical Journal of the Royal Astronomical Society, 88, 277-296.

Ward, S., 1959, AFMAG - Airborne and Ground: Geophysics, 24, 761-787.

Watts, R. D., 1975, A Fortran IV program for analytic continuation of VLF electromagnetic data: U.S. Geological Survey Open-File Report 75-159, 28 p.

Full Field Array Electromagnetics: Advanced EM from the surface to the borehole, exploration to reservoir monitoring

Kurt Strack [1] and Azizuddin Aziz [2]

[1] *KMS Technologies – KJT Enterprises, Inc., USA (kurtstrack@me.com)*
[2] *University of Houston, Texas, USA (aabdulaziz@uh.edu)*

Abstract

Achieving greater production efficiency and monitoring water/steam/CO_2 movements are key issues for hydrocarbon production and geothermal reservoir monitoring. Similar technical issues exist for CO_2 storage applications. They can be addressed to some degree with borehole and surface electromagnetic (EM) measurements, which are sensitive to fluid variations in the pore space. Linking the EM information to 3D surface and borehole seismic data permits extrapolation to the inter-well space. Evaluating several reservoir dynamic monitoring methods and technologies leads to a practical concept of Full Field Fluid Monitoring with EM. Our implementation includes marine and land sources and receivers, surface-to-borehole arrays. The concept envisions a single well system being used to look tens or even hundreds of metres around the wellbore and ahead of the drill bit.

On land, we distinguish between exploration and production applications. For exploration, it is essential to distinguish resistive and conductive targets equally well. To do this, we can use natural field magnetotelluric methods (MT) for conductive targets like sediment thickness or geothermal targets. For resistive targets such as hydrocarbon reservoirs, we add Controlled Source ElectroMagnetics (CSEM) with a dipole transmitter.

In the marine environment, the receiver sensors are included in seismic spreads, with fluxgate sensors used for the low frequency MT field, and induction coils for the high frequency component. CSEM is only needed when the resistive strata are thin. Multi-component acquisition and dense station spacing are essential to measure anisotropy and lateral structural changes, and to extend the application from exploration to production.

For borehole application, we combine EM sensor packages with a borehole seismic acquisition system or build special purpose Logging While Drilling (LWD) sub-assemblies. So far, we have built the various critical components for an integrated land and borehole monitoring experiment based on a commercial seismic acquisition system.

One of the major outcomes of the various projects was that surface electromagnetic methods alone are ambiguous if they are not used in combination with surface-to-borehole measurements. The reason lies in the up-scaling associated with the inherent averaging nature of EM methods.

Introduction

Electromagnetic (EM) methods are some of the oldest geophysical methods. In the mining industry they are well accepted as key technology while in the hydrocarbon industry, they are still used for trial purposes in exploration only (Nabighian and Macnae, 2005). There has been some progress with marine electromagnetic methods, and demand has stabilized in the market place but at much lower levels than expected. This is somewhat difficult to understand, since borehole environment electromagnetic logging tools are the most important of all and in most cases used for reserve estimates.

The issue clearly lies in the diffusive nature of electromagnetic field methods; there is a loss of sensitivity with distance between the source and the object of investigation. Thus, with increasing depth, the volume of investigation for surface methods becomes larger and fuzzier. Mining industry targets are relatively shallow and mostly conductive, whilst hydrocarbon targets are normally deep and resistive, requiring the use of electric field sensors (Passalacqua, 1983; Eadie, 1980; Strack et al., 1988; Eidesmo

et al., 2002). Unfortunately, electric field source and receiver systems are only customary in the marine environment as high power systems are dangerous to operate onshore. In addition, the cost of a high power system goes up quadratically as generator costs rise linearly with output current and power is a function of the square of the current. In the 1980s, megawatt sources and superconducting receiver sensors were used for geothermal exploration (Keller et al., 1984). Today, we can achieve the same or better results with less exotic technology due to electronic control of the source waveform, improved signal-to-noise receivers and data processing (Strack and Vozoff, 1996; Strack, 1992). New versions of these concepts using today's low power, low drift electronics and exclusively digital filters are refining this even further.

Anisotropy has been an ongoing issue. Our understanding of the electrical anisotropy of the subsurface has improved now that we are able to measure 3 component induction logs (Kriegshaeuser et al., 2000). We can now better integrate sub-surface and surface EM measurements by calibrating horizontal and vertical resistivity values correctly.

From the hardware side, EM systems have always had high cost per channel and bulky equipment. While a significant instrumentation downsizing effort would likely require funds beyond the business value of the technology, there is sufficient room for improvements by linking seismic concepts and experience, and by coordinating seismic and EM acquisition. This would address the cost reduction from an operational side. It would mean that multiple measurements could be carried out together and the logistics cost, which is usually the biggest part, would be covered by seismic operations. Thus incremental cost of the EM measurements would be reduced. This is a "must" for larger-scale field operations.

As long as only small amounts of data are being acquired on land, the value of EM will be limited since the lateral resolution of EM is not as good as that of seismic methods. In the offshore environment, where the business models are completely different, this is not the case. Here, any additional information that can contribute to de-risking a drilling decision can help. The contribution of marine electromagnetic methods to the exploration portfolio has shown this (Eidesmo et al., 2002). Their real value lies in the extension of the technology usage to additional parts of the reservoir life cycle, namely production.

The success of marine developments has fuelled improvements in the land methods. A new array acquisition system that we have developed is a 24-bit version of our 32-bit marine node, and our land transmitter design benefits from our marine transition-zone transmitter.

Full Field Array EM

The Full Field Array EM concept is the generation of a 3D data cube that has as many calibration points as possible and allows the user to extrapolate the calibrated information into an interpretation of the non-calibrated space. Figure 1 shows an artists rendition of such a cube. Here we can see several high value problems facing the oil industry:
Geosteering - placing the borehole in the right location in the subsurface,
Monitoring - observing fluid movement with permanent and semi-permanent sensors, and
Defining reserves that are left behind - exploring and monitoring from the surface (onshore and offshore) and linking the information to the 3D data cube.

EM sensors are represented by coils, symbolizing magnetic sensors (H), whilst the coordinate indicator represents electric field measurements (E) as well as tensors measurements for both E and H.

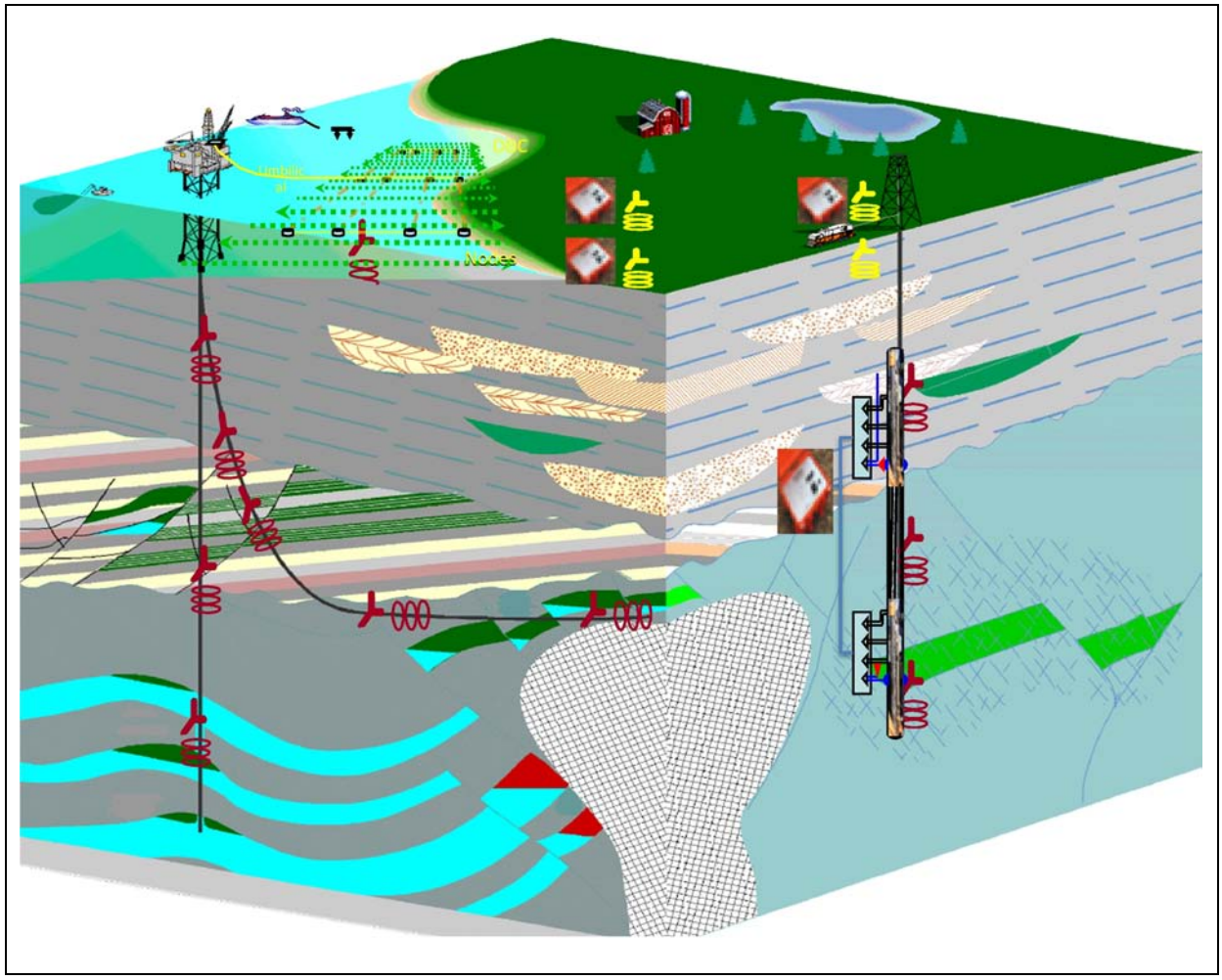

Figure 1. Artists rendition of components of the Full Field Array EM concept. Sensors placed inside the borehole as well as on the surface (onshore and offshore) are shown.

The problems with populating this 3D cube are the cost of data acquisition, the inherent resolution of the EM methods, and the information value that would be returned. Since EM methods and equipment are in many cases custom made, the cost is still many times higher than for surface seismic methods. Our array system is the second attempt (Rueter et al., 1995) to reduce the cost of EM hardware. For borehole measurements, the cost is a secondary issue because the information value of placing a borehole in the subsurface is significantly higher than the EM measurement cost. Here, the remaining issue is the change of business model of the service companies as assets are owned by the oil field owner and only limited services are required. As the marine exploration costs were already very high, EM methods had a chance to break into a high-risk market with limited (compared to other geophysical methods) but unique risk mitigation value.

The drivers for the integration need to be the oil companies or geothermal producers as they are the ultimate beneficiaries of the technology integration value. In all cases attempted to date, data density has been too low. Since the time when this vision of technical integration was outlined in 1996 (Strack and Vozoff, 1996), two necessary improvements have taken place. (1) Significant progress has been made with respect to hardware and electromagnetic data can now be acquired with fairly broadband systems that have, at the same time, long-term-stability, low noise, and are significantly cheaper than electromagnetic systems were 20 years ago. Issues such as synchronization, data formats, and data storage are well in the past. The surface observation points shown in Figure 2 look more like a typical seismic layout, with a mixture semi-regular grids linked by more irregular arrays patterns in rougher terrain where nodes are carried or helicopter-deployed. (2) Borehole anisotropy measurements are more generally available as both of the two largest service companies provide them. In addition, borehole seismic systems are today often manufactured by 3rd party vendors, which allow us to more easily integrate EM methods add-ons.

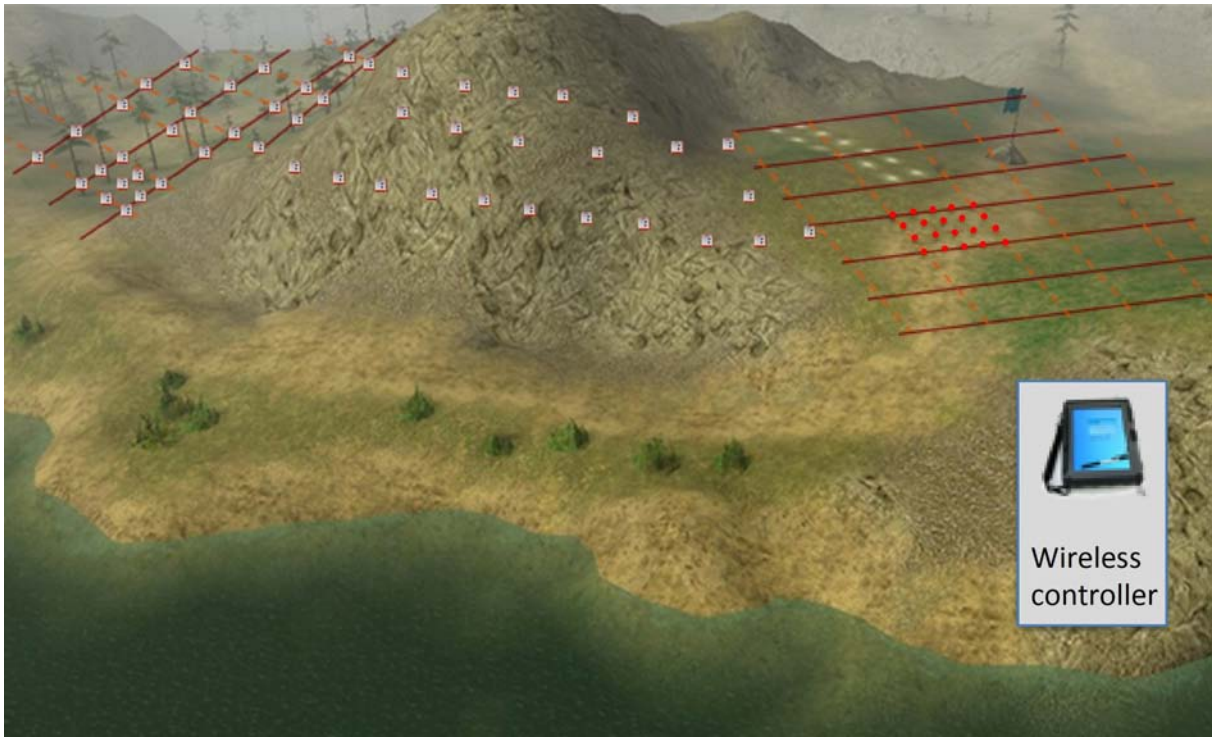

Figure 2. Seismic-style layout example of an electromagnetic survey using wireless nodes in a semi-regular grid layout and also in irregular lines.

Technology components

Figure 3 shows an example of a 3D induction log interpretation. The 3D induction-logging tool was developed by Baker Atlas under the mentorship and funding of Shell (Kriegshaeuser et al., 2000, Strack et al., 2000). It allows the measurement in a vertical borehole of horizontal and vertical resistivity values. In a borehole with more general orientation, the tool can be used to determine the tensor resistivity. The motivation lies in a large amount of resistive oil trapped in thin laminations between conductive shales. Standard induction logs only yield horizontal resistivity values, which are dominated by the shales (Yu et al., 2002), resulting in a significant underestimation of the hydrocarbon reserves. Obviously, use of this tool need not be restricted to applications involving thin laminations but also to any dispersed shales. When coupled with the appropriate petrophysical analysis, interpretation can yield tensor saturation values. Higher transverse isotropic resistivity values (i.e., where resistivity values are approximately the same for horizontal directions but different in the vertical direction) result in most cases in higher vertical resistivity values and thus higher hydrocarbon saturation or more oil. This justified the development of this tool. In Figure 3, we have a natural gamma ray log on the left, indicating shale content. To the right are gamma-gamma density and neutron density curves followed by 2D inverted resistivity values (vertical, Rv, and horizontal, Rh). Together with the porosity track that follows and the appropriate petrophysical equation, oil saturation can be calculated. Note that the oil saturation is significantly higher when the vertical resistivity values are high. When we carry out controlled source EM (CSEM) measurements with a grounded dipole, we measure predominantly the vertical resistivity. With the development of logging tools that can resolve vertical and horizontal resistivity values, we can better calibrate and link surface dipole CSEM measurements with borehole values than was previously possible.

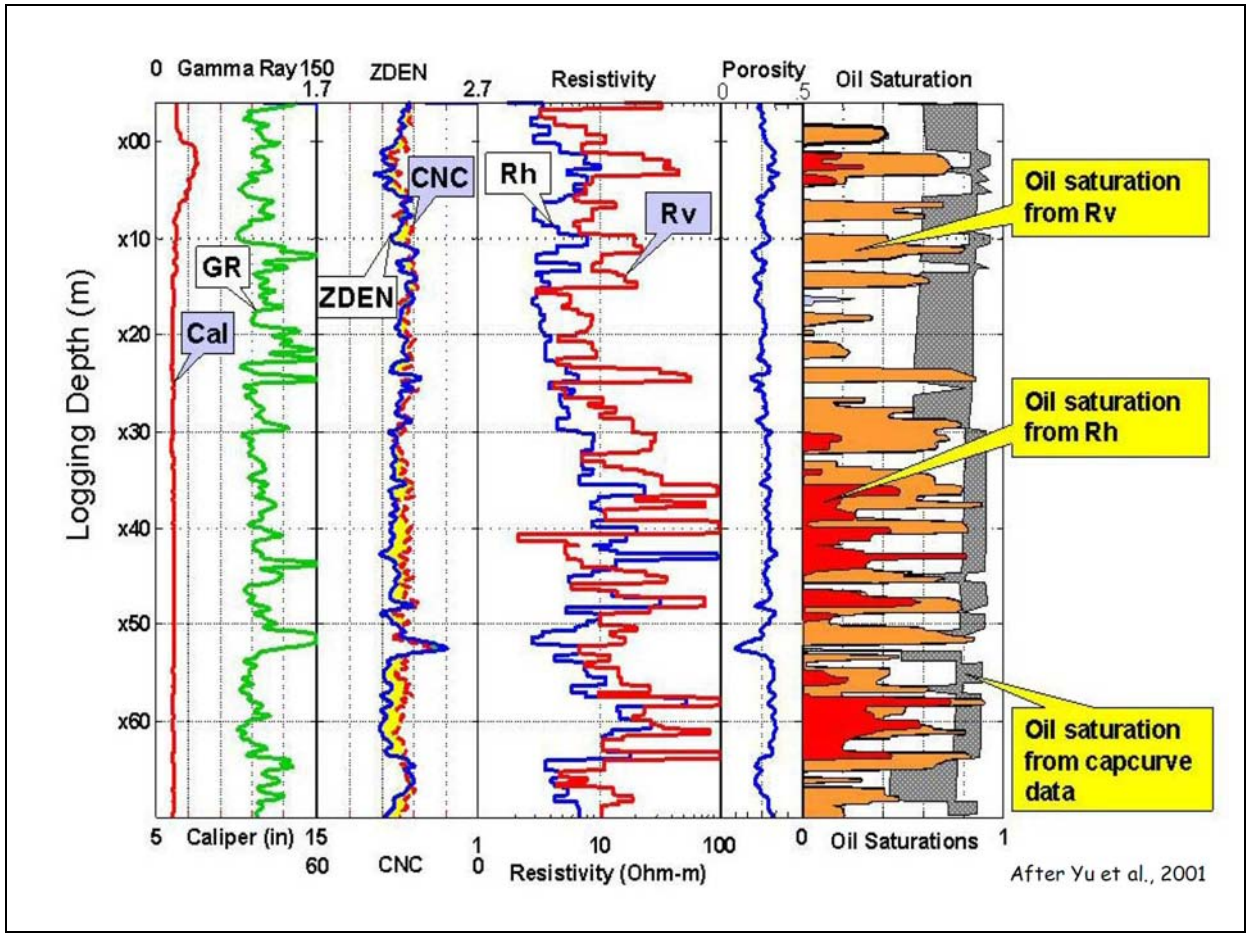

Figure 3. Example of an interpretation incorporating information from 3D induction logs (Yu et al., 2001). The tracks from left to right show: natural gamma ray for shale content, gamma-gamma density and neutron density for gas zone indicators, 2D inverted vertical and horizontal resistivity values, interpreted porosity and interpreted oil saturation.

Given that most sedimentary basins show electrical anisotropy (as do fractured carbonate units for that matter), one could assume that most of our prior log calibrations are inadequate and many of our interpretations should be revisited. Fortunately, this was already recognized in the1960s by Keller who developed simple rules of log reduction to deal with the common anisotropy in the oil field environment (Keller and Frischknecht, 1967). He systematically studied the effect of electrical anisotropy on logs. In summary, he derived limiting equivalent resistivity rules using the fact that inductive methods are biased towards conductors and galvanic methods are biased towards resistors. In the 1960s, the group around Keller used resistivity logs for vertical resistivity values and induction logs for the horizontal one. From a normal induction log, we can obtain the limiting equivalent resistivity values by using the cumulative conductance (i.e., thickness multiplied with conductivity, or thickness divided by resistivity) for the lower bound and the cumulative transverse resistance (i.e., resistivity multiplied with thickness) for the upper bound. Figure 4 shows a graphic display of a log with the cumulative conductance values and transverse resistance values on the right. Graphically, you can point to the layer boundaries, calculate the cumulative values, and fit a straight line between the boundaries to determine the horizontal and vertical resistivity values for that layer. These values are then superimposed on the log on the left. In this way, we can calibrate our logs for the purpose of linking them to magnetotelluric data via the horizontal resistivity values, and to grounded dipole CSEM data via vertical resistivity values.

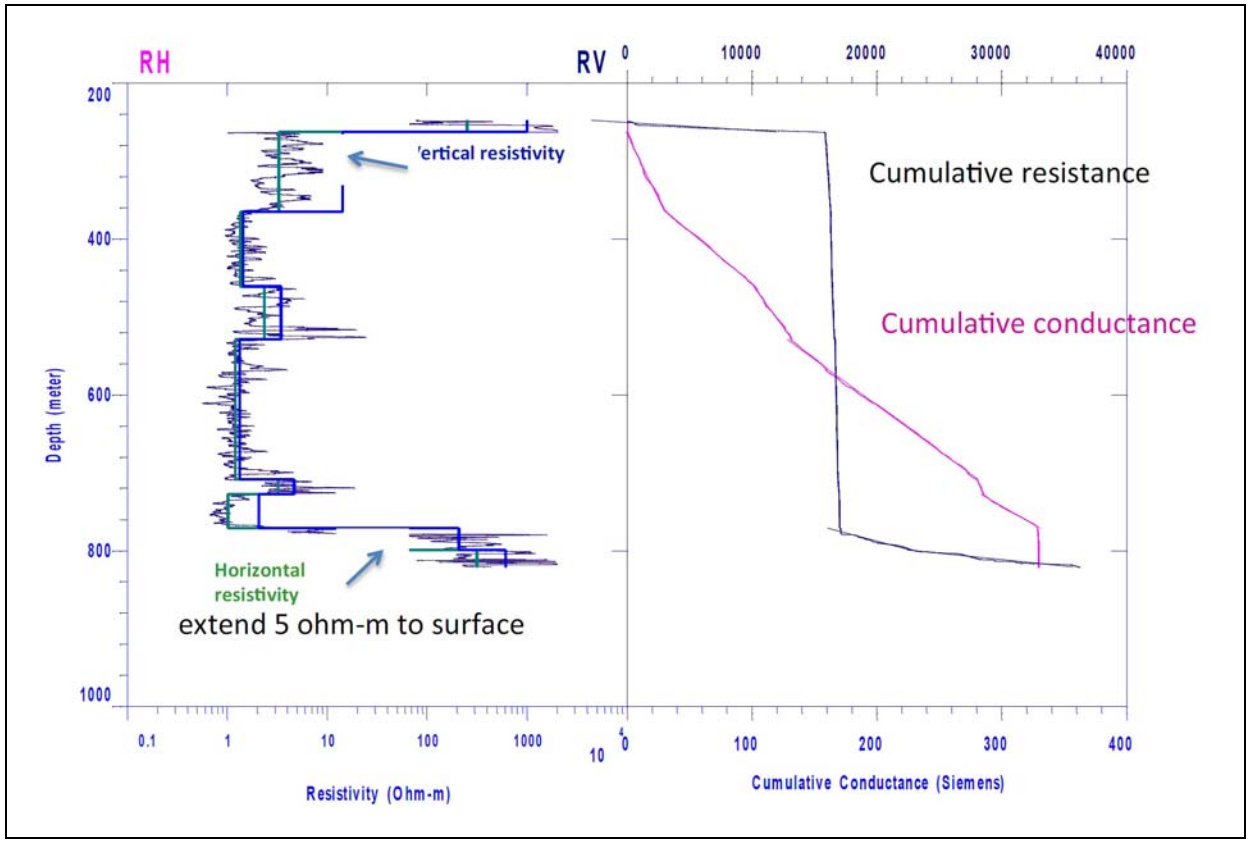

Figure 4. Example of a method for deriving vertical and horizontal resistivity from an induction log. The induction log is shown on the left. The equivalent piecewise linear block values that have been superimposed on the log were derived from the cumulative conductance and cumulative transverse resistance values shown on the right by fitting lines between layer boundaries. The layer boundaries were interactively picked by the user. The plot was generated with IX1D by Interpex Ltd. (www.interpex.com).

This technical progress was incorporated in the fast growth, subsequent fall and now stabilization of the marine EM exploration industry. Technically, this was a result of the consequences of the "thin resistive layer effect", recognized first on land (Eadie, 1980; Passalacqua, 1988; Strack et al., 1988) and subsequently pioneered offshore by Eidesmo et al. (2002). An early example is shown in Figure 5 from the Troll field, Norway (Johnstad et al., 2005). We can see in the top part of Figure 5 a normalized amplitude plot, which is the measured amplitude over reference background amplitude outside of the hydrocarbon reservoir. Clearly, an anomaly can be seen which coincides with the seismic image with superimposed interpreted anomaly in the middle as well as the interpreted structure of the reservoir shown at the bottom of Figure 5.

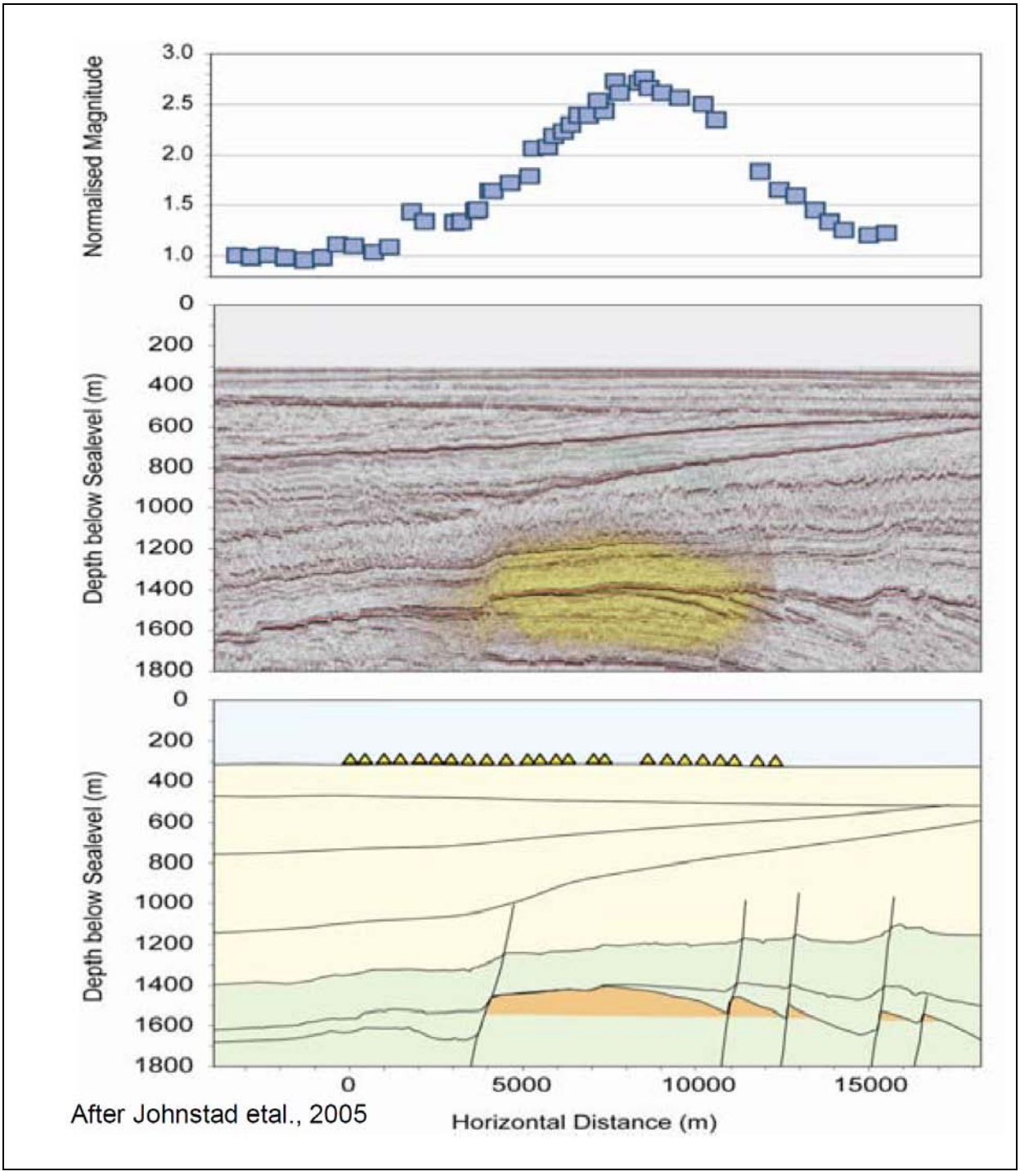

Figure 5. Example of a marine CSEM interpretation for the Troll field, Norway (after Johnstad et al., 2005). The top panel shows a magnitude versus offset curve, which exhibits an anomaly directly over the reservoir.

The next step in the marine environment will be – as on land – to reduce the acquisition hardware cost and to acquire denser data. Automatically, one would try to image the data directly as raw data as shown in Figure 6. This figure is for synthetic data but these concepts were confirmed in several proprietary data sets (Thomsen et al., 2007). The figure shows a common-source gather, where the curves are at increasing offsets from the left. In the top of the figure we have the unprocessed data displayed with automatic gain control. The vertical axis is diffusion time after current turn off. One can clearly see first the ocean wave arriving, which is the initial strong response part that does not spread out that much with time. Following is the subsurface response, which includes the target and the rest of the subsurface. It

clearly smears over larger time with increasing offset. As the target is resistive, its contribution arrives earlier than the rest of the response at larger offsets. The bottom of the figure shows the target response that has been isolated from the remainder of the response, using an automatic gain controlled scaling. The target move-out response behaves like a refracted seismic wave. This leads to the need for closer spacing and more data as well as time domain processing with marine data. It would allow direct imaging of the data and thus more operational decisions could be made and the technology would be utilised to a greater degree in the reservoir life cycle.

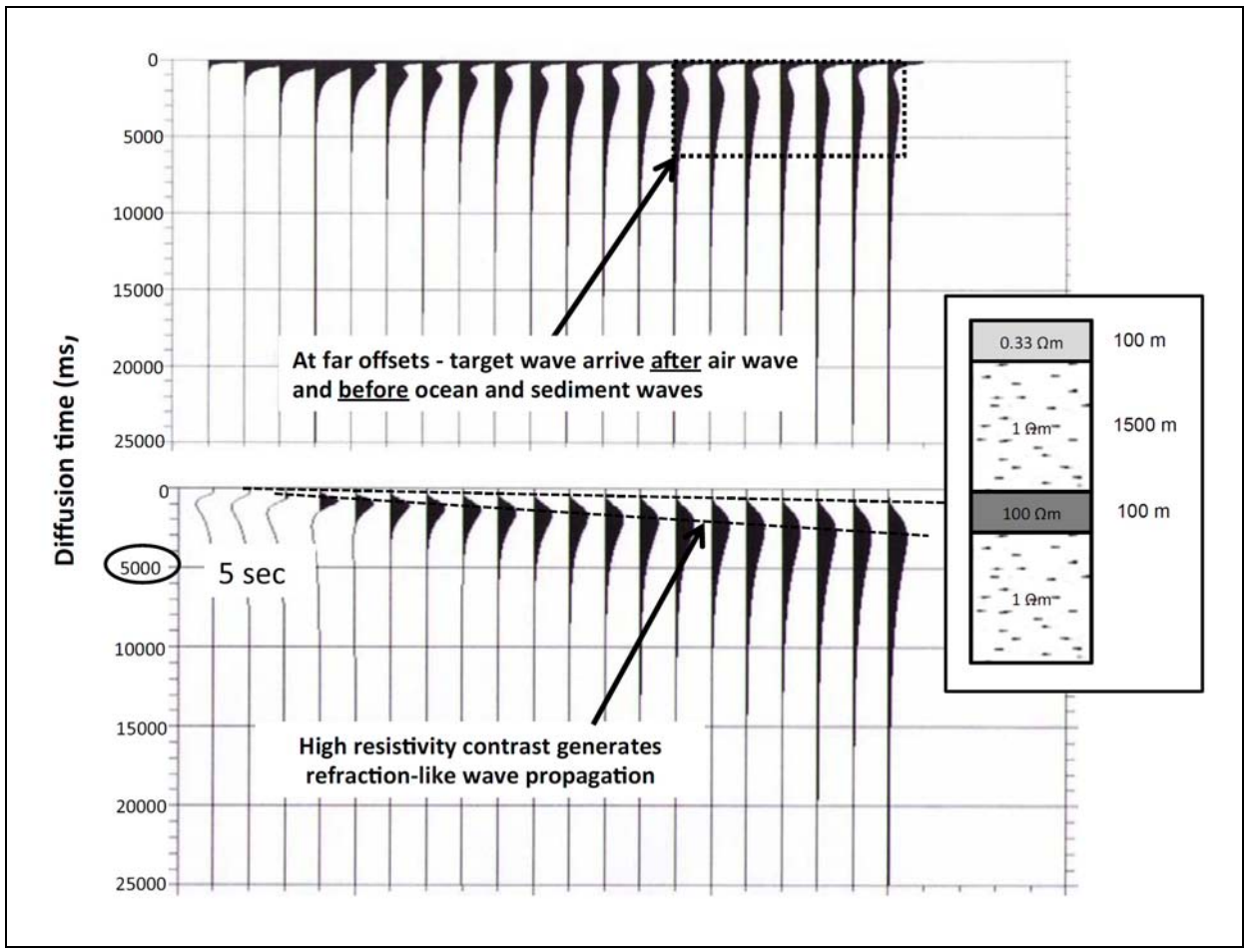

Figure 6. Common-source gathers for the impulse response of an inline electric field marine tCSEM™ setup. The normalized traces represent different offsets between source and receiver. The display shows the measured voltages. The Earth model has an oil reservoir at 1,500 m depth below the seafloor. The top gather contains all wave components (air wave, ocean wave, sediment wave, and target wave). The bottom gather only contains the reservoir response after removal of all other components. (after Allegar et al., 2008).

Technology examples

After demonstrating that denser or array data is needed from the technology side, we now look at two examples of difficult, but typical exploration problems where much denser data would be beneficial. The first example is a sub-salt exploration problem where an additional drilling location around a salt dome was to be determined (Buehnemann et al., 2002; Zerilli et al., 2002). The issue was that reflection seismic data could not determine top of salt for the salt flanks or the structure below the salt. No electrical logs were available except for those in a water bore. The producing well site was to be used to use to drill a deviated well through the salt into a target area sub-salt (for environmental reasons). The survey location was near several major German cities and thus extremely electromagnetically noisy. Over a period of 2 months, more than 300 sites were acquired, some of them at 50 m spacing to control cultural noise (i.e., those sites near railroads and through villages). This time included 2 weeks of survey operational parameter testing. A remote reference site was located several hundreds kilometres away.

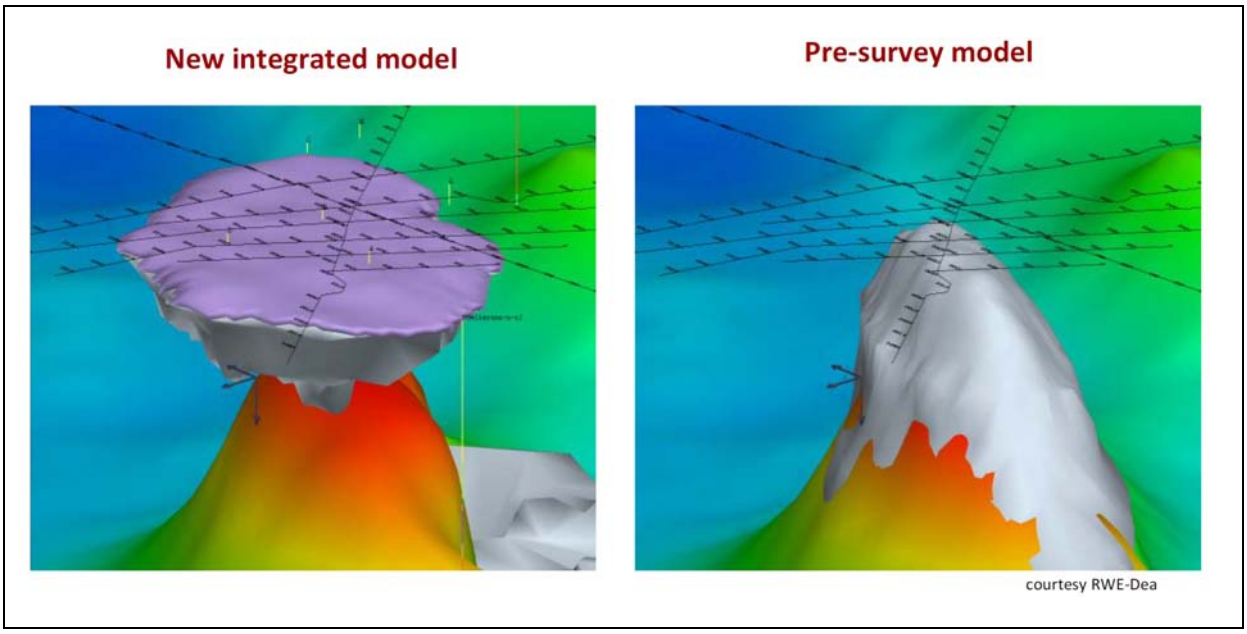

Figure 7. Interpreted images of a sub-salt exploration survey in Northern Germany. The interpretation integrates magnetotelluric data with gravity and seismic data (Buehneman et al., 2002). On the left is the interpretation after acquiring and integrating the MT data, whilst the interpretation before the MT survey data was used is shown on the right.

More detailed description can be found in Buehnemann et al. (2002) and Zerilli et al. (2002). Here, we only show a summary slide of the pre-survey and post-survey interpretation in Figure 7. The survey lines are indicated on the figure. The cross lines are the lines with 50 m spacing, with the other lines using 100 m spacing. Clearly, this would result would not have been possible with wider spacing, which is again a supporting argument for the use of larger channel counts and array measurements.

The next example is a success story from a reconnaissance geothermal exploration survey in Hungary. Here, MT and gravity were combined with existing seismic data to define early drilling locations (Yu et al., 2009). MT was done at low frequency and high frequency (audio-magnetotelluric or AMT) modes. The data were inverted twice; first independently and then in combination with the gravity inversion. Subsequent interpretation with the geology yielded a combined model where a low resistivity and low-density anomaly coincided. For the entire survey throughout Hungary, over 40 targets were defined in such a fashion. Next, the vintage (i.e., existing) seismic data were integrated with the EM and gravity data and the inversions were re-done several times as the structural interpretation changed. This yielded the final interpretation shown at the top of Figure 8. Subsequent drilling produced a 4 MW geothermal well with suitable temperatures encountered at approximately 1700 m depth.

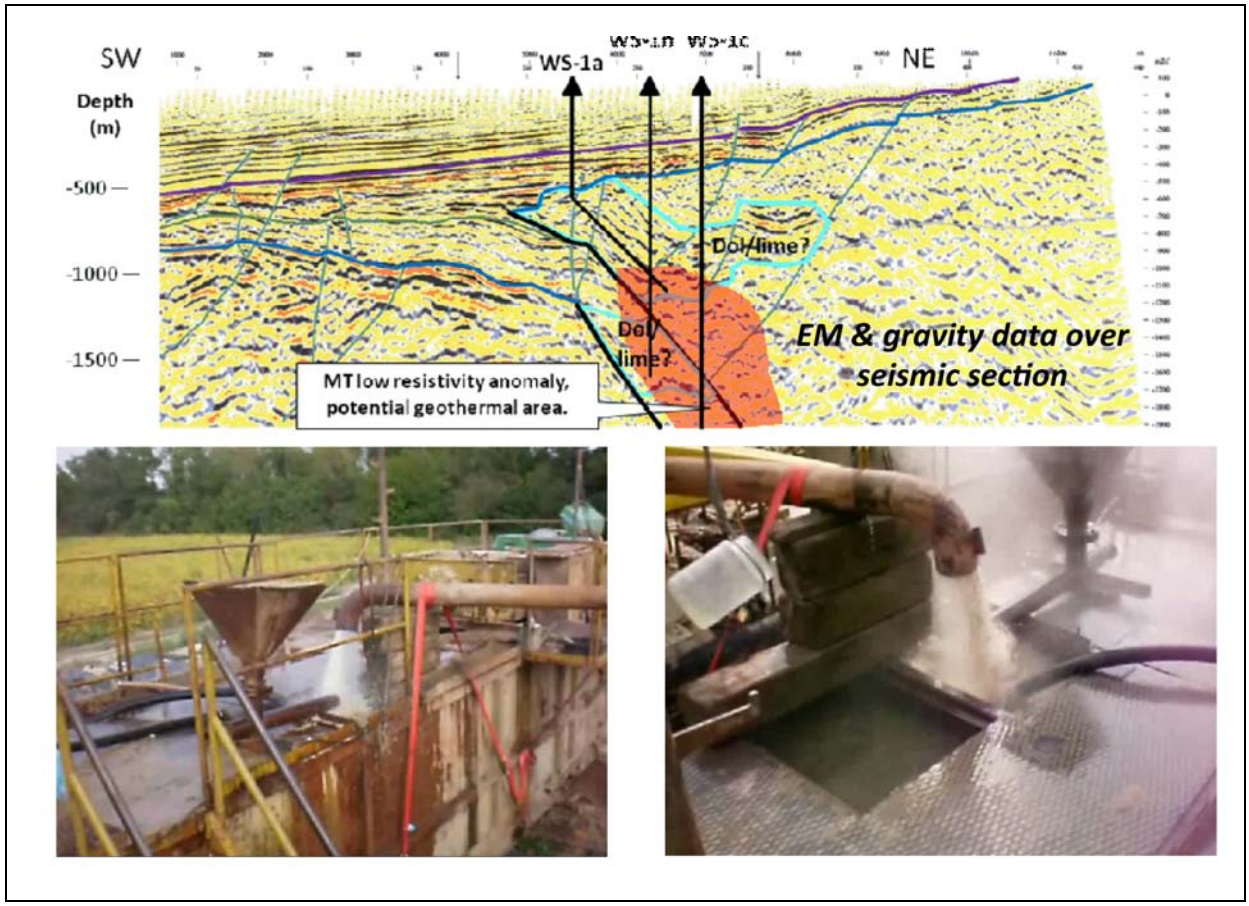

Figure 8. Integrated interpretation results from an integrated geothermal exploration project in Hungary (Yu et al., 2009). The top panel of the figure shows the seismic section ("vintage" or existing data) with a structural interpretation and resistivity anomaly superimposed. The bottom 2 pictures are from the initial flow test of the successful 3 MW geothermal well.

While this was done with vintage MT systems and larger spacing, the re-runs of the interpretation and resulting lateral shifts of the anomaly clearly tell us that denser data or smaller array setups would have delivered the results faster. Now, when the power plant is being developed, more wells will have to be drilled, and denser measurements will be required as the resolution capabilities of the existing sparse distribution of stations is not sufficient for interpretation at this finer scale.

Reservoir monitoring

Over the past 15 years the need for permanent sensors has become clear to the industry. Unfortunately, due to the existing business model, it has been difficult to adapt so as to make permanent sensors a viable business. Only recently have the large service companies been able to have profitable sensor deployments, mostly in temperature and pressure measurements and completion hardware. Feed forward or predictive geophysical sensors are still in their infant stages although the need is becoming more obvious (see First Break, Sept. 2011, for a report on reservoir monitoring). Among the proposed sensors are seismic, gravity and electromagnetic sensors. Here, we focus on electromagnetic sensors and assume that seismic sensors will automatically be included as the data needs to be integrated into the 3D seismic cube. Gravity sensors are less important as the density is intrinsically included in the seismic impedance (Strack, 2010).

Our original concept included starting with natural field and then adding, as needed, controlled source and borehole measurements (Strack, 2004). We have since deviated from this concept as we have learned from feasibilities that surface EM measurements, in general, has low resolution for detection of deeper reservoir changes. Natural fields will have even lower sensitivity than controlled sources. In addition, the time-lapse changes in a reservoir are mostly three-dimensional and thus the corresponding

anomaly is even about one decade smaller than would be the case for 2D, or more dramatically, for a 1D source feature.

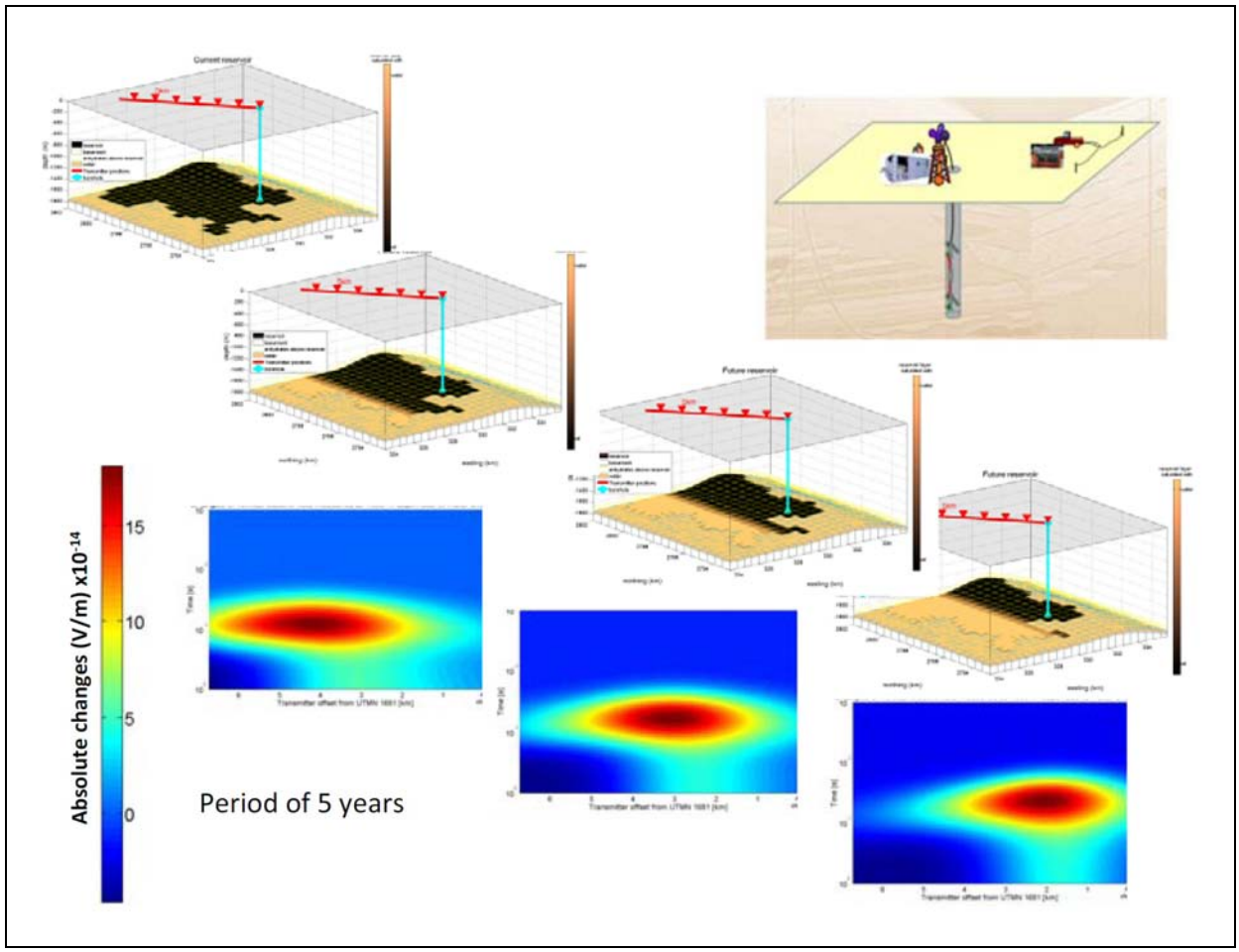

Figure 9. Simulated response of surface-to-borehole EM for 4 time steps over a period of 5 years (Colombo et al., 2010). Differences relative to the initial measurements are shown for the latter 3 measurements.

Figure 9 shows an example from a feasibility study carried out in the Middle East (Colombo et al. 2010). Here, the time-lapse model was derived from different reservoir simulator time steps and appropriate fluid substitution in the induction logs. Using different time steps and building the differences yielded a difference model of 'removed oil'. This model was then used to model surface-to-borehole and surface-to-surface measurements. Only the surface-to-borehole measurements gave reasonable anomalies as the target was located below an anhydrite layer.

In the figure, we see the survey layout on the top right. A transmitter loop with several tens of amperes was simulated (though for modelling purposes, everything was normalized to unity values). The receiver array is at about 1900 m depth below an anhydrite layer. The feasibility is for the Ghawar field test site. Source positions are placed in a circular array with a walk away test. The 3 images are for this walk away test. The four beige and dark brown horizontal slices are reservoir simulator-driven removed oil projections, which build the underlying models for the colour images. We can see that with increasing time the oil in this depth slice is getting less and we also see that the images reflect this (the red anomaly is moving to the right). The anomaly is still relatively low, which is why the test has so far not been carried out.

Conclusions

We started out stating that the real value of electromagnetic methods in petroleum and geothermal applications currently lies in reservoir monitoring and explored why this has not made more progress in the past 20 years. We have outlined several reasons why EM methods have not made progress in the past, and why this may no longer be a valid way to look at the subject.

Technical deficiencies of the acquisition methods have made hardware costs and commercial survey costs too high. For surface measurements, this has been shown onshore as well as offshore to no longer be the case.
Lack of integration between various EM measurements with calibration data such as well logs. This has been technically solved with the commercialization of the 3D induction log that now allows proper up-scaling as is customary during field studies.
Last, but not least, the cost reduction in hardware allows more and denser measurements and imaging techniques with faster turn-around time to be implemented.

Several feasibility studies have shown that these solutions, together with proper reservoir analysis and sensor technology, allow us to take this integrated technology (i.e., EM combined with seismic methods) to a real field trial. However, while surface data will give us the integration in the 3D cube and inter-well space, it will inherently still have low resolution, and surface-to-borehole measurements are required.

Acknowledgements

We herewith acknowledge the contribution of our colleagues at KMS Technologies and Western Atlas/Baker Atlas. In addition, we acknowledge our clients (BP, USA, Saudi Aramco, Dahran and RWE-Dea, Hamburg) and thank their organizations for their support. The list of the individuals is too long to be included here, but every one of them surely counted. I (KMS) would like to especially thank my mentor of the past 30 years, Keeva Vozoff, for his continued support and encouragement to the vision and for enlisting others into it. It is an honour to be able to do this when sharing the new version of our vision from the 1980s with my own students.

References

Allegar, N. A., Strack, K. M., Mittet, R., and Petrov, A., 2008, Marine time domain CSEM - The first two years of experience: 70th Conference & Exhibition, European Association Geoscientists & Engineers, Rome, Italy, abstract volume.

Bekker, R., and Danielsen, J., 2011, The future of Marine CSEM: First Break, 29, 77-81.

Buehnemann, J., Henke, C. H., Mueller, C., Krieger, M. H., Zerilli, A., and Strack, K. M., 2002, Bringing complex salt structures into focus - a novel integrated approach: SEG Expanded Abstracts, 21, 446-449.

Colombo, D., Dasgupta, S., Strack, K. M., and Yu, G., 2010, Feasibility study of surface-to-borehole CSEM for oil-water fluid substitution in Ghawar field, Saudi Arabia: Geo 2010, poster.

Eadie, T., 1980, Detection of hydrocarbon accumulations by surface electrical methods - a feasibility study: Unpublished M. Sc. Thesis, University of Toronto.

Eidesmo, T., Ellingsrud, S., MacGregor, L. M., Constable, S., Sinha, M. C., Johansen, S., Kong, F. N., and Westerdahl, H., 2002, Sea Bed Logging (SBL), a new method for remote and direct identification of hydrocarbon filled layers in deep water areas: First Break, 20, 144-152.

Johnstad, S. E., Farrelly, B. A., and Ringstad, C., 2005, EM seabed logging on the troll field: 67th Conference & Exhibition, European Association Geoscientists & Engineers, Madrid, Spain, abstract volume.

Keller, G. V., and Frischknecht, F. C., 1967, Electrical methods in geophysical prospecting: Pergamon Press.

Keller, G. V., Pritchard, J. I., Jacobson, J. J., and Harthill, N., 1984, Mega source time-domain electromagnetic sounding methods: Geophysics, 49, 993-1009.

Kriegshäuser, B., Fanini, O., Forgang, S., Mollison, R. A., Yu, L., Gupta, P. K., Koelman, J. M. V., and van Popta, J., 2000, Increased oil-in-place in low-resistivity reservoirs from multi-component induction log data: SPWLA annual meeting transactions vol., Paper A.

Nabighian, M., and Macnae, J., 2005, Electrical and EM methods: The Leading Edge, 24, 42-45.

Passalacqua, H., 1983, Electromagnetic fields due to a thin resistive layer: Geophysical Prospecting, 31, 945-976.

Rueter, H., and Strack, K. M., 1995, Method of processing transient electromagnetic measurements in geophysical analysis: U.S. Patent 5 467 018.

Strack, K. M., 1992, Exploration with deep transient electromagnetics: Elsevier, 373 pp (reprinted 1999).

Strack, K. M., 2004, Surface and borehole integrated electromagnetic apparatus to determine reservoir fluid properties: U.S. Patent 06739165.

Strack, K. M., 2010, Advances in electromagnetics for reservoir monitoring: Geohorizons, June 2010, 15-18.

Strack, K. M., LeBrocq, K., Moss, D. C., Petry, H., Vozoff, K., and Wolfgram, P. A., 1988, Resolving resistive layers with LOTEM in hydrocarbon exploration: Case Histories Paper 4-23, 50th Annual Meeting, European Association for Exploration Geophysicists, The Hague, abstract vol., 158.

Strack, K. M., and Vozoff, K., 1996, Integrating long-offset transient electromagnetics (LOTEM) with seismics in an exploration environment: Geophysical Prospecting, 44, 99-101.

Yu, L., Fanini, O. N., Kriegshaeuser, B. F., Koelman, J. M. V., and van Popta, J., 2001, Enhanced evaluation of low-resistivity reservoirs using new multi-component induction log data: Petrophysics, 42, 611-623.

Yu, G., He, Z. X., Hu, Z. Z., Porbergsdóttir, I. M., Strack, K. M., and Tulinius, H., 2009, Geothermal exploration using MT and gravity techniques at Szentlõrinc area in Hungary: SEG Expanded Abstracts, 28, 4333-4338.

Zerilli, A., Buehnemann, J., Henke, C., Krieger, M., Mueller, C., and Strack, K. M., 2002, Bringing complex structure into focus - A novel integrated approach: 72nd Society of Exploration Geophysicists' Annual Meeting and International Exposition, Invited presentation in the “Recent Advances and Road Ahead” session.

3D magnetotelluric inversion using cloud computing

Stephan Thiel [1] , Graham Heinson [2] , Craig Mudge [3] , Pinaki Chandrasekhar [4] and Brad Alexander [5]

[1] *TRaX, School of Earth and Environmental Sciences, University of Adelaide, Adelaide, SA (stephan.thiel@adelaide.edu.au)*
[2] *TRaX, School of Earth and Environmental Sciences, University of Adelaide, Adelaide, SA (graham.heinson@adelaide.edu.au)*
[3] *C3L, School of Computer Sciences, University of Adelaide, Adelaide, SA (craig.mudge@adelaide.edu.au)*
[4] *C3L, School of Computer Sciences, University of Adelaide, Adelaide, SA (pinaki.chandrasekhar@adelaide.edu.au)*
[5] *C3L, School of Computer Sciences, University of Adelaide, Adelaide, SA (brad.alexander@adelaide.edu.au)*

Abstract

Magnetotelluric methods (MT) have been applied to regions where the subsurface targets show a varying degree of complexity and the ability to model for three-dimensional (3D) structure is crucial in these situations. This form of modelling has been applied to MT data across varying scales, and in our own experience we have tackled regional projects across the Gawler Craton as well as more local studies for geothermal targeting.

The challenges for magnetotelluric modelling are two-fold: (1) large matrices are used, and operations performed on these can be computationally expensive in terms of time and memory, and (2) the inclusion of complex surfaces in terms of topographic effects and complex-shaped bodies places demands on the way that the user interacts with these models and the numerical methods that must be used to stabilise modelling operations. In order to address the computational needs, we have ported a parallelised version of the 3D code to a facility in the cloud. This solution has proven useful in both enlarging the modelling and data domain sizes as well as reducing computation time by a factor of 5. We have been encouraged by the results to date, and are looking to trial non-deterministic modelling approaches and genetic algorithms in this environment in the future.

A more extensive treatment of this trial use of a cloud computing facility for 3D inverse modelling of magnetotelluric data can be found in Mudge et al. (2011).

Introduction

An increase in the number of magnetotelluric soundings being acquired in a typical project has led to an improved understanding of the subsurface structure ranging from Craton-scale studies across arrays of hundreds of kilometres down to only a few square kilometres for mineral exploration and geothermal targeting. Two-dimensional modelling approximations are not appropriate for many of these projects and three-dimensional modelling algorithms are required. Magnetotelluric modelling and inversion algorithms are typically non-linear leading to the need for large-sized matrix operations. In order to address the necessary model and data sizes, both computation time and memory issues arise, and these cannot be adequately addressed with single conventional 32-bit or low-cost 64-bit machines.

Local computer networks have been used as a solution for many similar sized problems. We chose instead to trial the use of cloud computing architectures consisting of low-cost chips in data centres of public cloud service providers, such as Microsoft, Amazon and Google, to solve the magnetotelluric inverse problem. The usage is demonstrated on a deterministic 3D MT inverse code. Based on this experience, we are now considering the use of non-deterministic modelling approaches that may be better suited to the extreme scalability of the cloud computing facilities.

We show results of 3D MT inversions imaging the lithospheric structure of the Gawler Craton and sedimentary basin structure across a geothermal area.

Method and results

The MT method involves the use of recordings of naturally occurring magnetic and electric fields at the surface of the Earth (Cagniard, 1953). A primary magnetic field will induce a secondary electric field in the Earth, which through Ohm's Law, causes large-scale eddy currents. The depths of the induced electric field are proportional to the frequency of the magnetic field signals, a relationship also known as the "skin-depth relationship". Since the MT method is sensitive to a volumetric half-space, the resolution decreases with increasing skin-depth, i.e., longer period events (lower frequency signals) sense deeper but with less resolution. The Earth's response is contained in the complex, frequency dependent impedance tensor Z, which relates the measured electric (E) and magnetic field (B) components at the surface.

$$E = Z \cdot B \quad (1)$$

The 3D inversion algorithm that we have used (Siripunvaraporn et al., 2005) is a data-space method based on the Occam approach (de Groot-Hedlin and Constable, 1990). Due to the non-uniqueness of the magnetotelluric inverse problem, a penalty function φ is minimised:

$$\varphi = \varphi_m + \lambda^{-1}\varphi_d \rightarrow min, \quad (2)$$

where φ_m is the model structure functional and φ_d is the data functional. The Lagrange multiplier λ controls the trade-off between fitting the data and producing a smooth model. The Occam-style inversion is a two-stage approach where firstly the Lagrange multiplier is used as both a step length control and a smoothing parameter. In the second stage, the smoothness is maximised once the desired misfit is reached. In three-dimensional space, the data space dimensions are usually smaller than the model dimensions leading to the use of a data-space Occam inversion.

Cloud computing

Cloud computing facilities provide a user with compute and storage resources in an easy-to-use, flexible pay-per-use manner. Because of the huge scale of the data centres owned by public cloud service providers, the cost of resources and storage is less than that of on-premises infrastructure, up to a factor-of-seven cheaper (Armbrust et al., 2009; Hamilton, 2011). In addition, the fault tolerance provided by the operations software of the major cloud services providers is an important bonus when looking to use long-running inversion programs in this type of environment.

The most common parallelisation strategy, termed "Message Passing Interface" (MPI), has been used in a variety of parallel modelling codes. In cases involving frequent message passing, MPI routines are poorly suited to a cloud architecture because of its low cost interconnect between processors within a data centre.

The approach taken here has been to use declarative languages, examples of which include MapReduce, Hadoop, LINQ and DryadLINQ. MapReduce works well for highly distributable problems, which require minimal or no communication. In such an approach, a single large problem is "mapped and reduced" into many smaller data-independent computation sub-elements which can easily be mapped onto thousands of CPU's simultaneously.

We currently use the Windows Azure cloud, a public cloud service provider, since it provides the best option for the scale-driven effects of cost reduction and fault tolerance. The large scalability, with the availability of thousands of CPU's, provides better scaling potential compared to local clouds or other computer networks.

Implementation of magnetotelluric inversions

We begin with implementing existing inversion codes. Figure 1 shows the computing architecture that was used. We parallelise an existing 3D MT inversion code WSINV3DMT (Siripunvaraporn et al., 2005) by frequency and submit each frequency computation as a "Job".

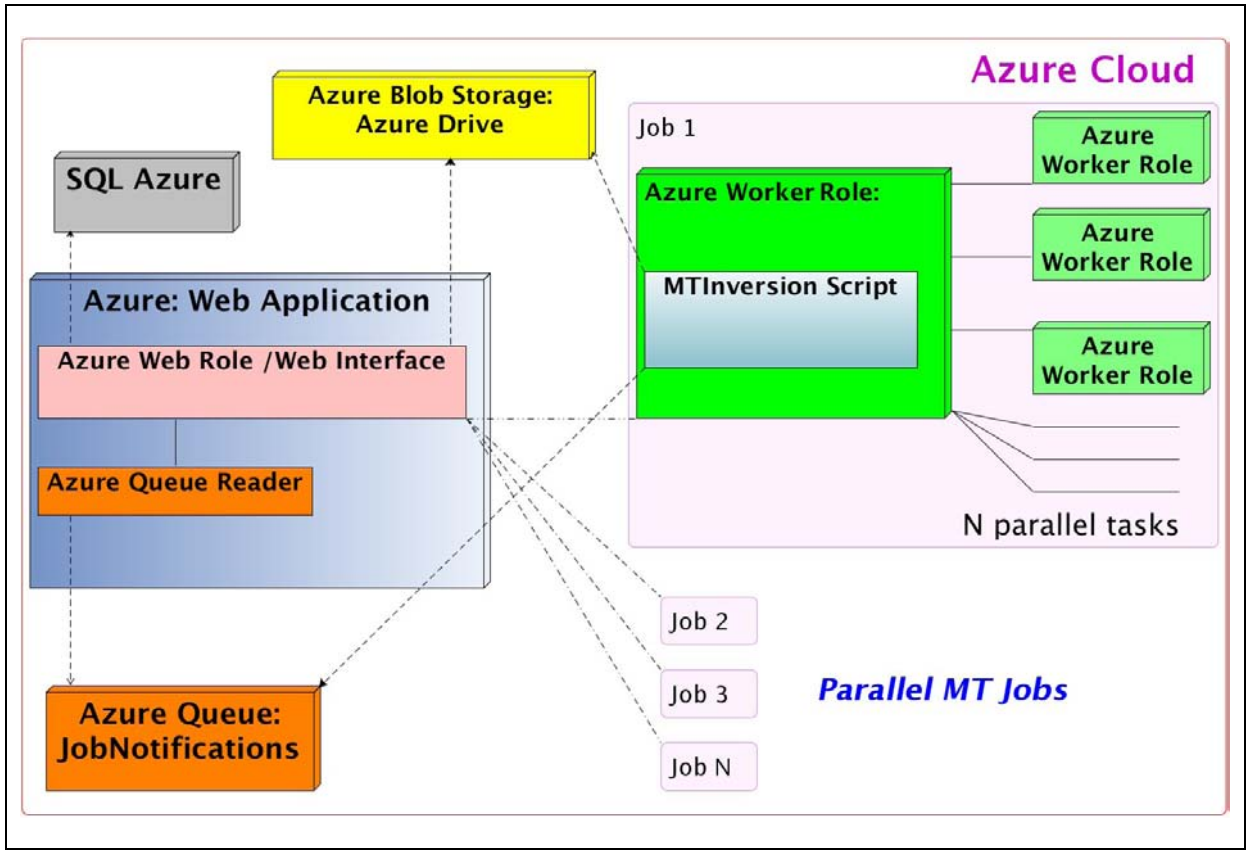

Figure 1. Architectural overview of the MT modelling routine running on Microsoft Azure Cloud. The cloud infrastructure is accessed through a web application and the task is split across n processors, where n is the number of frequencies (or periods) used.

Figure 2 shows the speed-up curve observed when modelling a geothermal data set for models involving between 5 and 15 frequencies. The speed-up approaches a factor of 5 times faster compared to the serial version of the 3D inversion code for the larger models.

On the Windows Azure cloud the maximum RAM size per node is limited to 13.8 Gb, and this defines the maximum problem size that is allowed to run. The biggest influence on storage for MT modelling is the size of the full sensitivity matrix of the forward operator. Its size is determined by the number of model parameters, M, equal to the product of the matrix dimensions in x, y and z dimensions, and the number of data parameters, N, equal to the product of the number of stations, Ns, the number of periods Np, and the number of elements of the full impedance tensor, NE, where NE is equal to 8 in this application. The final memory size of the sensitivity matrix, RAM, is roughly given by:

$$RAM = 1.2 \cdot \left(8N^2 + 8NM\right). \quad (3)$$

Since each unit in the cloud is made of low-cost parts with slow clock speeds and interfacing speeds, deterministic codes such as WSINV3DMT can achieve quicker convergence on local computer clusters. However, we have shown that a speed-up is still achievable within a cloud computing environment (Figure 2).

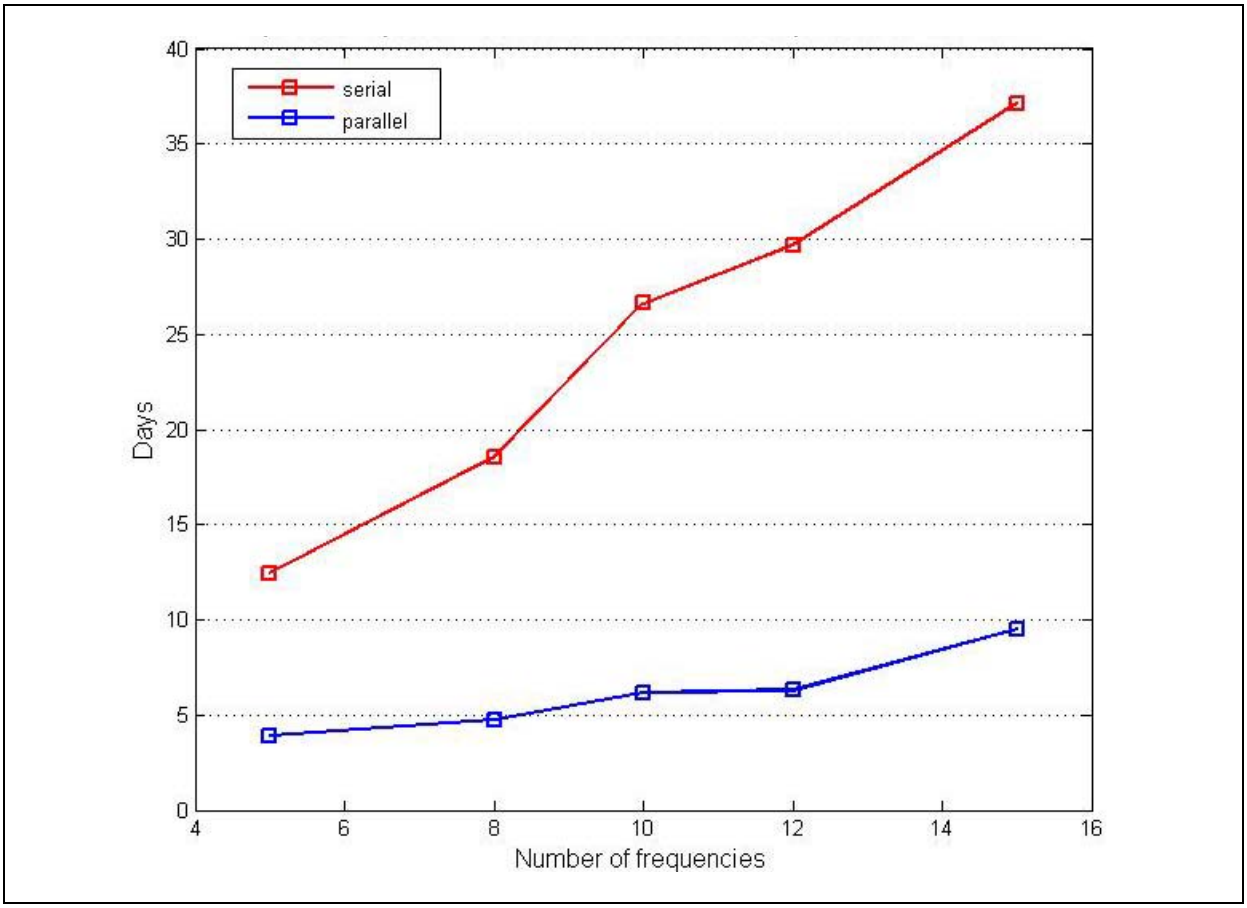

Figure 2. Computation time of the 3D inversion code for the serial solution (red) and the parallel version (blue). The speedup increases with the number of frequencies.

The structure of the cloud, its attractiveness for non-deterministic modelling codes and its extreme scalability makes it possible to pursue stochastic approaches such as Monte Carlo searches and genetic algorithms. While pure Monte Carlo searches across a discretised modelling domain for the MT problem may still require a larger infrastructure, guided evolutionary algorithms are a viable alternative. We present early results of a genetic algorithm using ellipsoids. Good fitting models are found using a three-stage approach of dropping, priming and evolving. The priming process is highly suited to cloud implementation.

3D modelling examples

The cloud-based 3D MT inversion has been applied to a data subset from the Gawler Craton in South Australia and a smaller scale area across the Paralana hot dry rock site, also in South Australia. The Gawler Craton model involved a data set from 54 MT stations with 8 inverted periods between 30 s and 4000 s (Figure 3). The data error floors were set to 5% and 50% for the off-diagonal and diagonal elements, respectively. The model dimensions were 35 x 49 x 42 cells and contain fixed resistivity values for cells assigned to the oceans. Sedimentary layers were included as *a priori* model values but these were not held fixed during the inversion. The smoothness parameter, τ, was set equal to 5 and the model length scales were reduced from δ equal to 0.3 in the beginning to 0.1 for the final result. The rms error of the final model was 5.16%.

The results at depths greater than 10km were vey similar for inversions with different error floors and static shift settings, indicating that these model elements were sensitive to the data rather than the *a priori* information or inversion settings. Shallow features at depths less than 10 km were strongly dependent on the starting model (i.e., geometry and resistivity information of the sedimentary basins in the *a priori* model). A deep conductor with resistivity less than 10 Ωm is visible beneath the postulated Achaean core of the Gawler Craton, commencing at a depth of approximately 80 km (Figure 3).

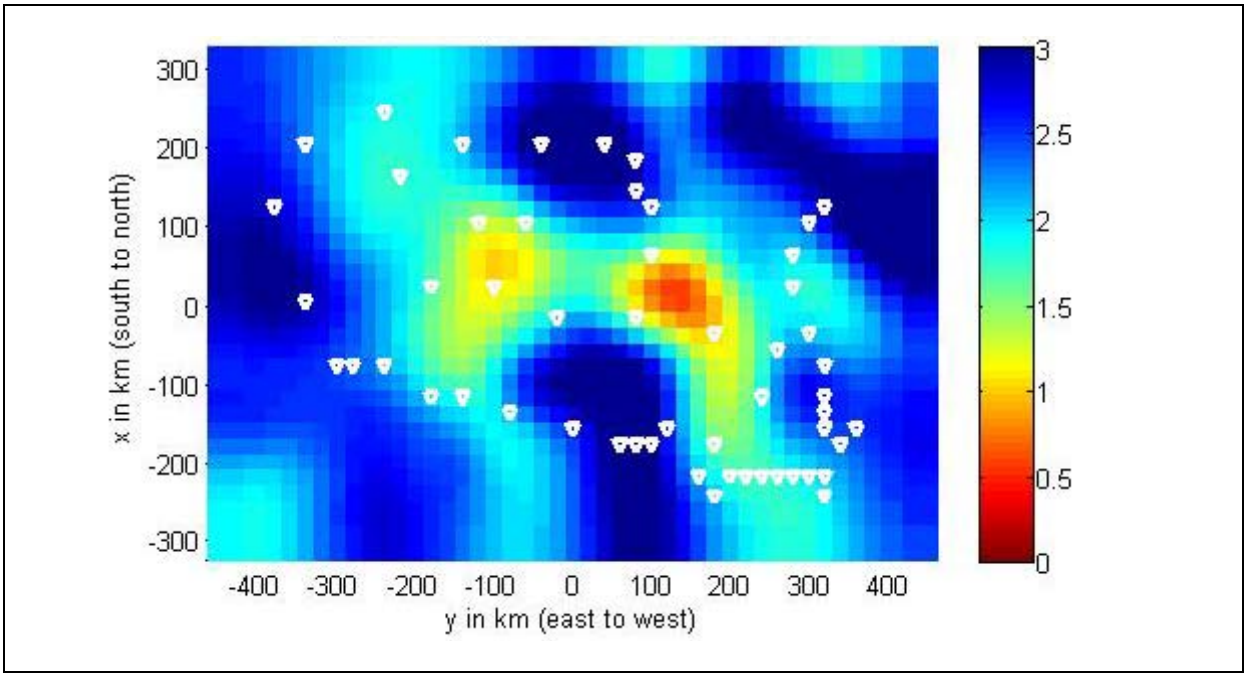

Figure 3. Plan view 3D model slice from the Gawler Craton resistivity model at a depth of 80 km. A log10 colour scale has been used for the resistivity values. An upper mantle conductor at a depth of 80 km is present in this model across the centre of the Gawler Craton.

Conclusions

Three-dimensional modelling of magnetotelluric data provides a significant challenge in memory size and computation time. We have shown that cloud computing is an interesting alternative to common local cluster use and has great potential for non-deterministic modelling approaches. The 3D modelling execution time is reduced by a factor of 5 and is shown on examples of the Gawler Craton and other small-scale surveys.

Acknowledgments

Financial support came from a Jim Gray Seed Grant from Microsoft Research. Other funding has been from IMER (Institute for Minerals and Energy Research, University of Adelaide); South Australian Centre for Geothermal Energy Research; and Primary Industries Resources (SA). Wei Wang helped with systems programming expertise on Windows and Windows Azure, and Jared Peacock had input into MT processing and discussions on non-deterministic approaches. Andrew Wendelborn improved the systems aspects.

References

Armbrust, M., Fox, A., Griffith, R., Joseph, A. D., Katz, R. H., Konwinski, A., Lee, G., Patterson, D. A., Rabkin, A., Stoica, I., and Zaharia, M., 2009, Above the Clouds: A Berkeley View of Cloud Computing: UC Berkeley Technical Report No. UCB/EECS-2009-28, accessed on 22 June 2010 at http://www.eecs.berkeley.edu/Pubs/TechRpts/2009/EECS-2009-28.htmlck.

Cagniard, L., 1953, Basic theory of the magneto-telluric method of geophysical prospecting: Geophysics, 18, 605-635.

deGroot-Hedlin, C., and Constable, S., 1990, Occam's inversion to generate smooth, two-dimensional models from magnetotelluric data: Geophysics, 55, 1613-1624.

James Hamilton, 2011, Internet Scale Storage: Keynote address delivered at SIGMOD 2011. Slides available at http://mvdirona.com/jrh/TalksAndPapers/JamesHamilton_Sigmod2011Keynote.pdf.

Mudge, J. C., Heinson, G. S., Thiel, S., and Chandrasekhar, P., 2011, Evolving Inversion Methods in Geophysics with Cloud Computing - a case study of an eScience collaboration: In Proceedings of IEEE eScience 2011, Stockholm, December 2011.

Siripunvaraporn, W., Egbert, G., Lenbury, Y., and Uyeshima, M., 2005, Three-dimensional magnetotelluric inversion: data-space method: Physics of The Earth and Planetary Interiors, 150, 3-14.

Reflections on natural field EM methods

M. Don Watts [1]

[1] *Consultant, Milan, Italy (mdwatts1@gmail.com)*

Abstract

In common with all geophysical methods, natural field EM (NFEM) techniques suffer from uncertainty and noise in data, often both unquantified and unknown. Inversion tends to use non-geological concepts (e.g., minimum structure) which, together with limitations of the data give rise to resistivity images which at times are of unknown value.

The conclusion, based on experience and reflected in Tarantola's classic review (2006), is that data-driven inversion should largely be replaced by hypothesis-testing, in which all *a priori* data are considered as well as the reliability of the data.

Introduction

In 1968, one of the first commercial magnetotelluric (MT) surveys was carried out in the Canning Basin (Australian Aquitaine, 1968). The cost per station was A$1600 (about A$16,000 in 2011 dollars). At that time, seismic data were of poor quality and very little was known about the geology of central Australia, so the high price was nevertheless justified in that it gave additional information.

In the subsequent 40+ years, the unit costs have come down, due in large part to the impact of the PC. Data processing has improved somewhat and for modelling, 1D "inversion" is still in regular use. The MT technique has been extended to the marine environment, primarily for sub-salt and sub-basalt exploration, and the 1950's airborne technique, AFMAG, has been revived.

Data Processing

Data processing in 1968 was by use of a Fourier transform; in 2011, the FFT (or DFT) remains the favoured technique, although improvements in the processing of data in the audio-magnetotelluric (AMT) band around 1 to 5 kHz using wavelet transforms have been demonstrated by Garcia and Jones (2008). Robust, remote-reference processing is the norm (e.g., Larsen et al., 1996; Egbert, 1997; Smirnov, 2003; Chave and Thomson, 2004). At AMT frequencies – characterized by erratic signal levels – Goldak and Goldak (2001) have shown that selective stacking of transients improves S/N notably. Many regions of the world are characterized by a high level of anthropogenic noise (e.g., power lines, machinery, cathodically-protected pipelines, DC trains) and by man-made conductors in an otherwise resistive environment. At high latitudes and near the geomagnetic equator (i.e., close to the electrojets), signal may not be plane-wave, and indeed may correspond to a moving sheet-source (Pulkkinen and Engels, 2005). With a few academic exceptions (e.g., Engels, 2001), these complications are rarely accounted for in processing and interpretation, but have the effect of under or over estimating apparent resistivity depending on position at high latitudes.

Interpretation

Interpretation of MT data is largely at the level of circa 1990, that is, minimum-structure 2 and 3-D inversion (e.g., Jupp and Vozoff, 1977; Madden and Mackie, 1989; Smith and Booker, 1991; Mackie and Madden, 1993). The resultant smooth resistivity volumes pose several problems: they are largely dependent on *ad hoc* inversion and smoothing parameters, and usually present non-geological images which have to be interpreted in light of other data. The seismic method, in contrast, at least in the oil industry, has achieved technological growth of another order of magnitude, improving very substantially the imaging of sub-salt and even-sub-basalt sediments, making the application of MT in these environments of limited value without external constraints. Although progress has been made on 2- and 3-D inversion using discrete, closed bodies (Abubakar et al., 2009), these function primarily when physical properties are well-known and then only on a sub-set of the model interfaces (e.g. Zerilli et al., 2011). Alternative imaging techniques have been suggested, such as Gibert et al. (1994), who

linked diffusive EM fields to their propagative equivalent hoping then to use seismic techniques. These fail, unfortunately, because of noisy and incomplete data.

In the high-enthalpy geothermal environment, regularized inversion of MT data remains a valid and largely uncontested tool, since it indirectly maps a parameter closely associated with targets: electrically-conductive smectite alteration (Cumming et al., 2000). The added value of MT is well established.

The mining industry has seen large improvements in deep-penetrating AEM systems over the last decade, such as MEGATEM and VTEM. Under average conditions, these have a depth of penetration of the order of 750 m. Ground-based natural field techniques (i.e., AMT or MT) are usually the most cost-efficient for exploration to greater depth (2 to 3 km), but are expensive by the standards of this industry. Airborne natural field techniques, dating back to AFMAG (Ward, 1959), are showing something of a revival but are inherently limited to high frequencies and modest resolution. Conventional inversion techniques are useful but do not provide images of the resolution needed to accurately locate drill-holes over typical massive sulphide targets.

Imaging reliability

The sequence extending from data collection to a final resistivity image is subject to noise and uncertainty at each step (e.g., Johnson et al 1977). Only recently has this problem been addressed (Meju, 2009; Tompkins, submitted 2011). These uncertainties are rarely incorporated in the final assessment of the reliability of the image, partially because of the large computational cost. Tompkins et al. (2011, figure 16), consider the range of possible solutions fitting a given CSEM data set to a given misfit without specifically addressing data uncertainty, and show a disconcertingly large range of equi-feasible but dissimilar models. When data uncertainty is included, the range becomes even greater (Tompkins, pers. comm.).

Further limitations on the validity of inversion models come from a multitude of underlying assumptions (e.g., model smoothness, model dimensionality, anisotropy, etc.), and through the simplification of input data (e.g., the down-weighting of on-diagonal MT data or the exclusion of the vertical magnetic field transfer functions). The starting and reference models used for inversion clearly have a significant impact, e.g., beginning with a conductive *a priori* leaves the model unchanged at a depth where there is little sensitivity to the data, leading to the erroneous conclusion that a conductor is present (e.g., the base of salt hydrocarbon exploration).

Conclusions

The late Albert Tarantola, after a lifetime dedicated to the philosophy as well as the mathematics of inversion, concluded that, given the complexity of the Earth models we are seeking, rather than using inversion to find the “best” – usually lowest rms misfit – solution, it is better to use geophysical data to test hypotheses. This in turn implies close cooperation between geologists, data processors, and geophysicists (rather than treating each step as an independent operation), to create a priori models. More sophisticated inversion techniques, in which components of a geologically-valid model can vary (e.g., through the use of geostatistical stabilizers - Rodi and Mackie, 2010) may offer an interpretation strategy, which, in conjunction with uncertainty analysis, will result in a meaningful earth model with associated reliability estimates.

Acknowledgments

My thanks go to Randy Mackie for his insights over the last twenty years into the topics of ‘inversion techniques’ and ‘significance’, and to Graeme Cairns for drawing my attention to Albert Tarantola’s Nature Physics paper.

References

Abubakar, A., Habashy, T. M., Li, M., and Liu, J., 2009, Inversion algorithms for large-scale geophysical electromagnetic measurements: Inverse Problems, 25, no. 12, 123012.

Australian Aquitaine Pty. Ltd., 1968, Terry Range (WA) Magneto-Telluric Survey, Permits 151H, 152H, and 205 H, Canning Baisn: WA Geol Survey ID IDS000236.

Chave, A., and Thompson, D., 2004, Bounded influence magnetotelluric response function estimation: GJI, 157, 988-1006.

Cumming, W., Nordquist, G., and Astra, D., 2000, Geophysical exploration for geothermal resources: an application for combined MT-TDEM: SEG Expanded Abstracts, 19, 1071-1074.

Egbert, G., 1997, Robust multiple-station magnetotelluric data processing: GJI, 130, 475-496.

Engels, M., 2001, On Multisheet and Volume-3D Modelling of the Baltic Shield: Kolloquium Elektromagnetische Tiefenforschung, Burg Ludwigstein.

Garcia, X., and Jones, A. G., 2008, Robust processing of magnetotelluric data in the AMT dead band using the continuous wavelet transform: Geophysics, 73, F223–F234.

Gibert, D., Tournerie, B., and Virieux, J., 1994, High-resolution electromagnetic imaging of the conductive Earth interior: Inverse Problems, 10 341-351.

Goldak, D. K., and Goldak, S. M., 2001, Transient Magnetotellurics with Adaptive Polarization Stacking: SEG Expanded Abstracts, 20, 1509-1512.

Johnson, B. D., Jupp, D. L. B., and van Klinken, G., 1977, Arbitrariness, uniqueness and optimization: Bull. ASEG, 8, 103-105.

Jupp, D., and Vozoff, K., 1977, Two-dimensional magnetotelluric inversion: Geophys. J. R. Astr. Soc., 50, 333-352.

Larsen, J. C., Mackie, R. L., Manzella, A., Fiordelisi, A., and Rieven, S., 1996, Robust smooth magnetotelluric transfer functions: Geophys. J. Int., 124, 801–819.

Mackie, R., and Madden, T. R., 1993, Three-dimensional magnetotelluric inversion using conjugate gradients: Geophys. J. Int., 115, 215-229.

Madden, T. R., and Mackie, R. L., 1989, Three-dimensional magnetotelluric modeling and inversion: Proceedings of the IEEE, 77, 318-333.

Meju, M. A., 2009, Regularized extremal bounds analysis (REBA): An approach to quantifying uncertainty in nonlinear geophysical inverse problems: Geophysical Research Letters, 36, L03304.

Pulkkinen, A., and Engels, M., 2005, The role of 3-D geomagnetic induction in the determination of the ionospheric currents from the ground geomagnetic data: Annales Geophysicae, 23, 909–917.

Rodi, W., and Mackie, R., 2010, Geophysical inversion with geostatistical regularization: Paper presented at PIERS 2010 Cambridge - Progress in Electromagnetics Research Symposium, July 5–8, 2010, Cambridge, USA. Abstract available from http://piers.org/piers2010cambridge/submit/get_testpdf.php?status=valid&id=091220192424&pdffilename=091220192424.pdf (website visited 9 February 2012).

Smirnov, M., 2003, Magnetotelluric data processing with a robust statistical procedure having a high breakdown point: Geophys. J. Int., 152, 1–7.

Smith, J. T., and Booker, J. R., 1991, Rapid inversion of two- and three-dimensional magnetotelluric data: J. Geophys. Res., 96, 3905-3922.

Tarantola, A., 2006, Popper, Bayes and the inverse problem: Nature Physics, 2, 492-494.

Tompkins, M. J., Fernandez Martınez, J. L., Alumbaugh, D., and Mukerji, T., 2011, Scalable uncertainty estimation for nonlinear inverse problems using parameter reduction, constraint mapping, and geometric sampling: Marine controlled-source electromagnetic examples: Geophysics, 76, F263–F281.

Tompkins, M. J., 2011, Comparison of Maximally-Sparse Stochastic Collocation and Monte-Carlo Integration in Posterior Model Covariance Estimation: submitted to Geophysics.

Ward, S. H., 1959, AFMG - Airborne and ground: Geophysics, 24, 761-789.

Zerilli, A., Labruzzo, T., Buonora, M. and Abubakar, A., 2011, Joint inversion of marine CSEM and MT data using a “structure” ‐ based approach: SEG Expanded Abstracts, 30, 604-608.

3D mega-cell inversion of land, marine, and airborne natural field EM data

Michael S. Zhdanov [1] , Alexander V. Gribenko [2] , Martin Čuma [3] and Glenn A. Wilson [4]

[1] *University of Utah & TechnoImaging (mzhdanov@mines.utah.edu)*
[2] *University of Utah & TechnoImaging (alex@technoimaging.com)*
[3] *University of Utah & TechnoImaging (martin@technoimaging.com)*
[4] *TechnoImaging (glenn@technoimaging.com)*

Introduction

Natural field electromagnetic (EM) methods use plane wave EM fields that diffuse into the Earth, generating predominantly horizontal current flow. These methods came into use during the 1960's, following the theoretical basis proposed by Andrei N. Tikhonov (1950) in the USSR, Louis Cagniard (1953) in France, and Tsuneji Rikitake (1950) in Japan. Yet, knowledge of telluric currents is far from recent. As early as 1868, Sir George Biddell Airy made the first coordinated study of telluric currents and their relationship to magnetic variations (Airy, 1868). In 1862, one of the first experiments to measure telluric currents was carried out by Lamont (1862) in the Alps. Terada (1917) appears to have been the first to measure the dependence of the magnetic field relationships on the conductivity of the ground. The Schlumberger brothers also documented observing telluric currents during their experiments with DC measurements. They were the first to suggest that telluric currents could be used for oil and gas exploration. However, practical measurements showed significant variations and instability in telluric current behaviour, which made it difficult to develop any reasonable interpretation methods. The main sources of this instability were associated with complex processes in the ionosphere and magnetosphere, which were unknown at the time.

The primary discovery made independently by Tikhonov and Cagniard was that the effect of ionospheric and magnetospheric processes could be cancelled if the electric and magnetic field components of the telluric currents were normalized as a surface impedance. At the time, this was a revolutionary idea because it enabled geophysicists to transform measured data into estimates of the Earth's resistivity. As early as 1934, Hirayama found the explicit form for the surface impedance of a plane wave (Hirayama, 1934), and Hatakayama (1938) even used tensor conductivities to explain differences in principle impedances. However, Tikhonov and Cagniard should be credited with creating the solid geophysical foundation upon which the magnetotelluric (MT) method was later developed for imaging the Earth's conductivity over the past 60 years. In the former Soviet Union, MT methods were the primary methods used for oil and gas exploration during the 1960's and 1970's, and can be attributed with the discovery of many of the giant Siberian oil and gas fields that remain in production to this day. Originally, the MT data were interpreted using a catalogue of 1D Earth models. This made it easy to provide MT sounding curves as plots of apparent resistivity versus the period or the square root of the period (which is proportional to skin depth). Since the world is 3D, distortions in the MT soundings were later falsely interpreted for oil and gas reservoirs. The development of 2D and 3D modelling in the 1980's and 1990's, and 2D and 3D inversion in the 1990's and 2000's has expanded the opportunities for MT and other natural field EM methods in exploration. We are now able to invert various forms of natural field EM data for mega-cell 3D Earth models, and this paper will review recent examples by the authors for land, marine and airborne surveys.

Magnetotellurics

In the following example, we review a classic application of MT methods for continental-scale imaging, and how 3D inversion of MT and magnetovariational (MV) data has revised thinking toward some Earth processes. First, we need to introduce EarthScope, which is a US National Science Foundation program intended to explore the structure and evolution of the North American continent, and to further understand the processes controlling earthquakes and volcanoes. A major part of the EarthScope project is the USArray of seismic, MT, and geodetic instruments that are being deployed over the current decade across the entire continental US. This transportable array of geophysical

instruments provides an unparalleled means to study the crust and mantle geology of the US through seismology and MT data. EMScope is the MT component of the USArray program, and is managed by Oregon State University on behalf of Incorporated Research Institutions for Seismology (IRIS). EMScope comprises long-period MT measurements at hundreds of sites, in addition to a number of long-period backbone MT stations. By mid-2011, MT data had been collected throughout Washington, Oregon, Idaho, Wyoming, Montana, and northern California, Nevada, Utah and Colorado.

In the example we present here (Figure 1), we focus our attention on the MT data acquired in Montana, Idaho, and Wyoming. The unique geological setting of the western US, including plate boundary transform faulting, subduction, intraplate extension of the Basin Range, and the active Yellowstone hotspot, is very important, both for its geodynamic history, and for understanding the physical processes of earthquakes and volcanoes. It is a tectonically active region, with the subducting Juan de Fuca plate and volcanically important from the effects of the Juan de Fuca and Gorda plates moving over a mantle plume currently located beneath Yellowstone National Park (YNP). For such a complex region, definitive structural interpretations based purely on seismological observations are not complete. Conductivity has a significant role in determining tectonic activities, primarily because it is sensitive to temperature, the presence of interstitial fluids, melts, volatiles, and bulk composition.

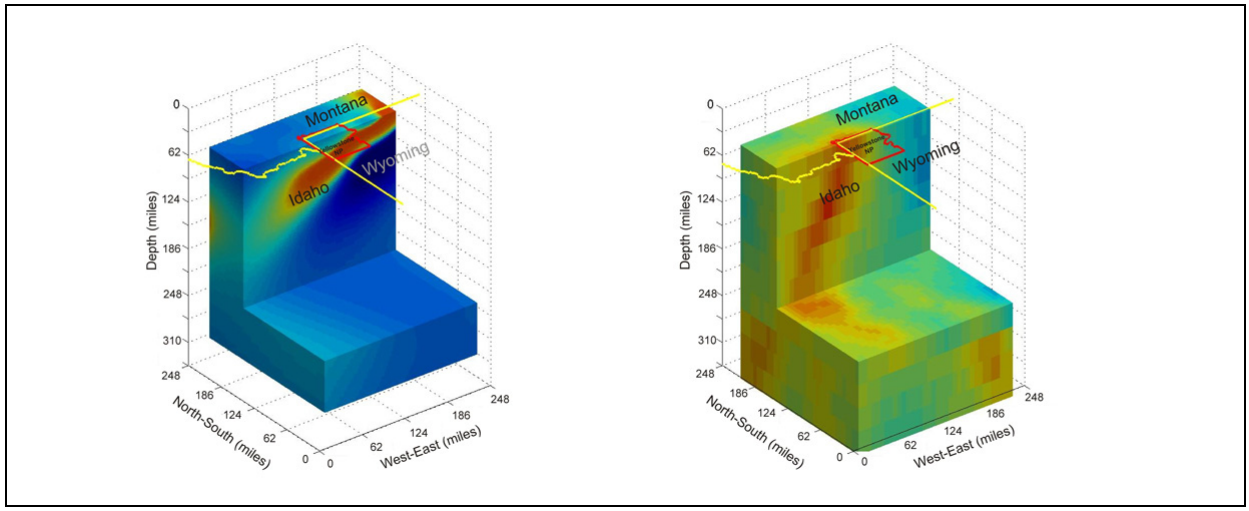

Figure 1. (left) 3D conductivity model obtained from 3D MT inversion over the Yellowstone hotspot area. (right) P-wave velocity model obtained from seismic tomography, presenting a rising column of partly molten rock originating in the mantle transition zone.

We refer the reader to Zhdanov et al. (2011a) for further details of the 3D MT inversion and a detailed discussion of its interpretation. The 3D Earth model itself was discretized to more 1.9 million cells. Here, we present a comparison of the 3D MT inversion over Yellowstone National Park (YNP) with a 3D p-wave velocity model (Figure 1). One can observe remarkable similarity between the images of the Yellowstone plume that were independently produced by seismic tomography and 3D MT inversion. The conductive body identified in the conductivity image is west dipping in a similar way to the low velocity body shown in the p-wave velocity image. Taking into account the different physical properties, one should not expect these images would coincide completely. Recent seismic studies have suggested relatively high attenuation in mantle, and this has been interpreted as a partially molten plume in which water is partitioned into the melt, and surrounded by a cooler and wetter mantle. The attenuation decrease at 200-250 km is considered as evidence that the plume is melting above this depth, and this corresponds well to the area of high conductivity in Figure 1.

Marine Magnetotellurics

In offshore hydrocarbon exploration, seismic reflection can provide detailed images of the top of salt, sedimentary layers, and basement formations. Yet, even with the introduction of wide azimuth towed streamer (WATS) and extra wide azimuth towed streamer (XWATS) seismic, common problems associated with subsalt seismic imaging include multiple reflections and mode conversions, loss of reflected energy from steeply dipping salt surfaces, and the lack of coherent features beneath salt structures. As discussed by Constable (2010), marine MT was experimented with in the 1990's for

deepwater and subsalt exploration, particularly in the Gulf of Mexico, where high costs of drilling justified the expenditure. During the 2000's, interest in marine MT was displaced by marine controlled-source EM (CSEM), even though the same receiver instruments were/are used.

In the example we present here, we focus our attention on marine MT data acquired over the Gemini prospect in the Gulf of Mexico. Located in 1 km of water approximately 200 km southeast of New Orleans, Gemini contains a salt body associated with a roho system that forced out salt both basinward and laterally, resulting in a complex 3D salt geometry. 3D seismic reflection data indicated that the salt resides between 1 and 5 km beneath the seafloor, although the deepest portions of the salt are not well resolved due to lower fidelity of the seismic data with depth. Ambiguity exists whether the Gemini salt body is still rooted to the deeper Louann salt layer, or merely bottoms out at a depth of 5 to 6 km. MT surveys were conducted in several cruises during 1997, 1998, 2001, and 2003, resulting in a grid of 42 marine MT sites (e.g., Constable et al., 1998; Key et al., 2006).

We refer the reader to Zhdanov et al. (2011b) for further details of the 3D MT inversion and a detailed discussion of its interpretation. The 3D Earth model itself was discretized into more than 1.6 million cells. Here, we present a comparison of 2D and 3D MT inversion from line H (Figure 2). The white contour in Figure 2 indicates the position of the salt dome estimated on the basis of seismic reflection data. We note, however, that the seismic outline of the salt dome shown in Figure 2 can be used only for a qualitative comparison because it depends on a selection of the seismic velocity model which could not be done objectively in this area. We observe also that the resistivity of salt recovered by 3D inversion is about 10 Ωm. Similar results were obtained by Hoversten et al. (2000), who justified this result because the "MT response saturates as the resistivity of a body becomes greater than 10–20 times that of the background. In the GOM [Gulf of Mexico], bulk salt resistivity values are more than 20 times the background sediment resistivity values and, for the skin depths of interest, the MT response is totally governed by the distortion of electric currents in the sediments around the resistive salt." The saturation of the MT response for resistive layers is well known by MT practitioners. It is easy to demonstrate, for example, that for a 1 km thick resistive layer buried 1 km deep in 1 Ωm sediments (somewhat similar to the Gemini salt), the difference between 10 and 100 Ωm resistivity values for the layer yields no appreciable differences in the MT response; hence the response has become saturated. The difficulty to resolve thin salt at a 4 km depth logically follows from this as well.

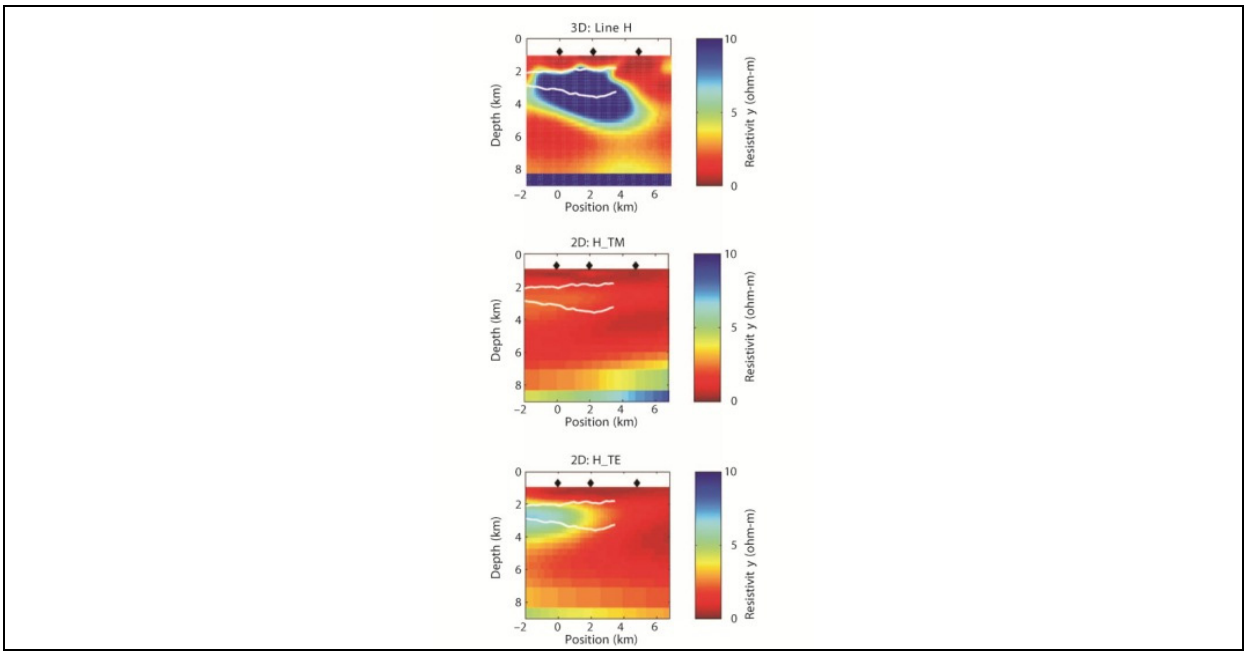

Figure 2. A comparison along line H from the marine MT survey of the Gemini prospect with the results obtained from 2D and 3D inversions. The top part shows the results of full 3D inversion, the middle part presents the result of 2D inversion of the TM-mode data, and the bottom part shows a similar result of 2D inversion of the TE-mode data obtained by Key et al. (2006). The white contour indicates the position of the salt dome estimated on the basis of seismic reflection data.

Audio-frequency magnetics (AFMAG)

It has long been recognized that magnetovariational (MV) data, being the ratio of the localized vertical magnetic field to the orthogonal horizontal magnetic fields, can provide information about the 3D conductivity distribution in the Earth (e.g., Berdichevsky and Zhdanov, 1984). The basic reasoning is that the vertical magnetic field is zero for plane waves vertically propagating into a 1D Earth. Non-zero vertical magnetic fields are thus directly related to 2D or 3D structures. This served as the basis for the original development of the audio-frequency magnetic (AFMAG) method (Ward, 1959) whereby two orthogonal coils were towed behind an airborne platform to determine the tilt angle of the plane of polarization of natural magnetic fields. The natural magnetic fields of interest originate from atmospheric thunderstorm activity and propagate over large distances with little attenuation in the Earth-ionosphere waveguide. These fields propagate vertically into the Earth as per MT fields. The tilt angle is zero over a 1D Earth, and hence the AFMAG method was effective when crossing conductors. However, the direction and amplitude of the natural magnetic fields randomly varies with time, meaning AFMAG data were not repeatable (Ward et al., 1966). By using MT processing techniques for ground-based orthogonal horizontal magnetic field measurement, Labson et al. (1985) demonstrated that repeatable tipper data could be recovered from measured magnetic fields.

The AFMAG method remained largely undeveloped until the commercialization of the Z-axis Tipper Electromagnetic (ZTEM) airborne system by Geotech. ZTEM measures the tipper components as the ratio of a vertical magnetic field measured from an airborne receiver to the horizontal components measured at a ground-based (reference) location. Similar to the ratio of electric to magnetic fields in MT data, the ratio of the magnetic fields effectively removes otherwise unknown source terms. The receiver coil is currently flown via helicopter or fixed-wing platform, meaning data can be rapidly acquired over large survey areas for relatively low cost compared to equivalent ground surveys. The time series of the magnetic fields are recorded at fixed sampling rates and the data are binned and processed to generate in-phase and quadrature transfer functions (i.e., tippers) in the frequency-domain as per Labson et al. (1985). The lowest frequency of the tipper depends on the speed of the aircraft, and the highest frequency depends on the sampling rate. Tippers are typically obtained at five frequencies from 30 Hz to 360 Hz, giving skin depths ranging between 600 m and 2000 m for terrain conductivities typically encountered in ZTEM surveys. Holtham and Oldenburg (2010) introduced 3D ZTEM inversion based on modifications of the 3D MT inversion of Farquharson et al. (2002). Similarly, our 3D ZTEM inversion is an analogue of the 3D MT inversion by Zhdanov et al. (2011a). One key difference between our 3D ZTEM inversion and that of Holtham and Oldenburg (2010) is that we employ a footprint approach for each receiver (e.g., Cox et al., 2010). This permits us to efficiently compute, store and manipulate the sensitivities for very large surveys. We also utilize focusing regularization (Zhdanov, 2002) which enables us to recover higher contrasts and sharper conductivity boundaries than with smooth regularization.

In the following example, we review a case study from the Pebble porphyry deposit where we compared 3D inversions of both ZTEM and SPECTREM airborne electromagnetic data (Pare et al., 2012). By way of introduction, Pebble is a calc-alkalic Cu-Au-Mo porphyry deposit located in the Bristol Bay region of southwest Alaska, approximately 320 km southwest of Anchorage and 27 km west-northwest of the village of Iliamna. Development of the Pebble Cu-Au-Mo mine is managed by Pebble Limited Partnership (PLP), a joint venture between Northern Dynasty Mines Ltd (50%) and Anglo American plc (50%). Since discovery in 1988, over 886,177 feet of drilling in 1,085 holes have been completed, making Pebble one of the most intensively studied, undeveloped mineral systems in the world. At a 0.30% Cu equivalent cut-off, the latest Pebble resource estimate includes 5.942 billion tonnes in the measured and indicated category containing 25.0 million tonnes of copper, 66.9 million ounces of gold and 1.5 million tonnes molybdenum; and 4.835 billion tonnes in the inferred category, containing 11.6 million tonnes of copper, 40.4 million ounces of gold and 1.0 million tonnes of molybdenum. This resource base makes Pebble the largest gold and sixth largest copper deposit in the world.

We inverted 250 line km of ZTEM data acquired at 200 m flight-line spacing along strike of the Pebble deposit . This corresponded to 5,472 stations with both Z/X (inline) and Z/Y (transverse) tipper components at five frequencies; 30 Hz, 45 Hz, 90 Hz, 180 Hz, and 360 Hz. The 3D Earth model was discretized into approximately 570,000 cells of 50 m inline by 50 m transverse discretization, where the vertical cell size varied from 10 m near the surface to 100 m at 2,000 m depth. The 3D inversion settings and constraints were assigned their default values (i.e., no specific geological constraints nor *a priori* geological information were provided). The depth of investigation for ZTEM was about

1,500 m below the surface. The 3D ZTEM inversion has recovered Pebble's main alteration pattern and the known structures ZF, ZC, ZE and ZG1. Generally speaking, the 3D ZTEM inversion recovered the geological features and structures with better accuracy than the 2D inversions of the same data. As expected, the 3D inversion with focusing regularization produced sharper contrasts and better lateral model continuity from line to line than the 2D inversions with smooth regularization.

Studying the 3D ZTEM inversion for lines L10060 highlights the following correlations (which we note are very similar to those observed in the 3D SPECTREM inversion):

- The highly conductive zones to the known illite-pyrite and advanced argillic alteration parts of the system (Figure 3);
- The weak conductive zone and resistive high beneath the Pebble West and East zones are characterized by sodic-potassic, K-silicate and deep sodic-calcic domains;
- The high conductive zone on line L10120 above the Pebble East zone and confined between the ZE and ZG1 faults is associated with the advanced argillic alteration that overprints the highest grades (Figure 3);
- The moderately conductive layer near the surface above the Pebble East zone and to the east appears to be related with the Tertiary cover;
- The main known structures (ZF, ZC, ZE and ZG1) are well resolved, and correlate with the breaking pattern of the 3D conductivity model; especially the ZG1 fault to the east of Pebble East.

It is interesting that a conductive zone is present at depth to the east of the ZG1 fault on line L10120. This feature is being investigated further and if real, could potentially be a deep extension of Pebble East. The geometry of the 3D ZTEM inversion also follows the general trend of the alteration and ore geometry. Similar to 3D SPECTREM inversion, the mineralization is not in direct correlation with the conductive zones resolved by the 3D inversions. The conductive zones are mostly coincident with alteration change. The high grade copper equivalent (CuEq) 0.6% is not consistently following the high conductive trend. As per the 3D SPECTREM inversion, this suggests that the sulphide content is not a major factor in the ZTEM response.

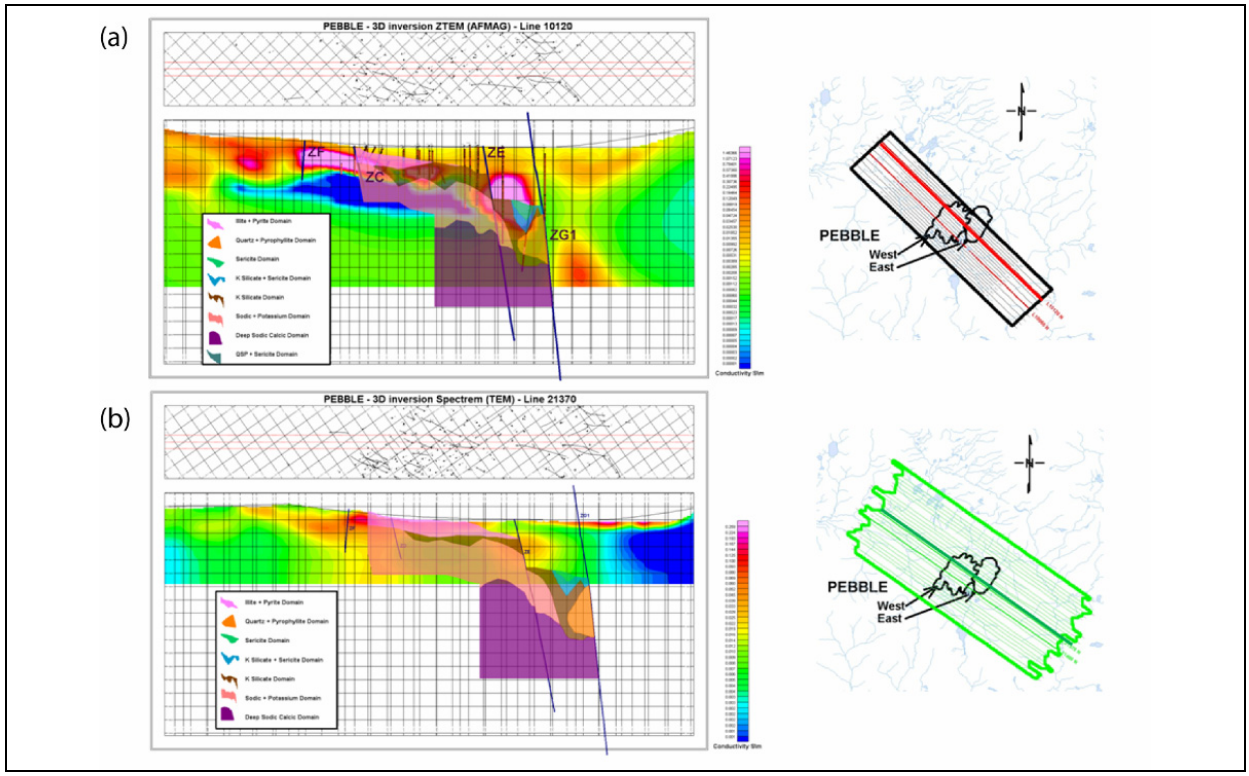

Figure 3. Comparison of (a) 3D ZTEM inversion for ZTEM line L10120 and (b) 3D SPECTREM inversion for SPECTREM line L21370, with alteration patterns superimposed.

Conclusions

Over the past decade, 3D modelling and inversion of natural source EM data has evolved so that we are now able to invert various forms of natural source EM data from land, marine and airborne systems for 3D Earth models from deposit to regional scales that can have millions of cells (i.e., mega-cell 3D models). We have provided examples from EarthScope MT data in the western US for understanding continental-scale structures, marine MT data in the Gulf of Mexico for subsalt oil and gas exploration, and ZTEM data over the Pebble Cu-Au-Mo porphyry deposit in Alaska. These examples demonstrate the variety of natural field EM methods, and 3D inversion thereof. However, given the inherent low resolution of natural field EM data, it lends itself to joint inversion with other geophysical data (e.g., gravity, gravity gradiometry, magnetics, and reflection seismic) and this is a subject of our on-going research.

Acknowledgements

The authors acknowledge TechnoImaging for support of this research and permission to publish.

Zhdanov, Gribenko, and Cuma acknowledge support of the University of Utah's Consortium for Electromagnetic Modeling and Inversion (CEMI) and Center for High Performance Computing (CHPC).

We acknowledge Professor Bob Smith at the University of Utah for his involvement in the analysis of the Yellowstone MT and seismic Earth models.

The Gemini MT results are included with permission and thanks to the Scripps Institute of Oceanography's Marine EM Laboratory. Particularly, we acknowledge Dr. Kerry Key and Professor Steve Constable for their involvement in the work presented.

The Pebble ZTEM results are included with permission and thanks to Pebble Partnership Ltd, Anglo American Exploration (Canada) Ltd, Northern Dynasty Mines Ltd, Spectrem Air Ltd, Geotech Ltd, and TechnoImaging LLC. Particularly, we acknowledge Pascal Pare, Jean Legault, Jaco Smit and Louis Polomé for their involvement in the work presented.

References

Airy, G. B., 1868, Comparison of magnetic disturbances recorded by the self-registering magnetometers at the Royal Observatory, Greenwich, with magnetic disturbances deduced from the corresponding terrestrial galvanic currents recorded by the self-registering galvanometers of the Royal Observatory: Philosophical Transactions of the Royal Society of London, 158, 465-472.

Berdichevsky, M. N., and Zhdanov, M. S., 1984, Advanced Theory of Deep Geomagnetic Sounding: Elsevier, Amsterdam.

Cagniard, L., 1953, Basic theory of the magneto-telluric method of geophysical prospecting: Geophysics, 18, 605-635.

Constable, S., 2010, Ten years of marine CSEM for hydrocarbon exploration: Geophysics, 75, 75A67-75A81.

Constable, S. C., Orange, A. S., Hoversten, G. M., and Morrison, H. F., 1998, Marine magnetotellurics for petroleum exploration: Part 1—A sea-floor equipment system: Geophysics, 63, 816–825.

Cox, L. H., Wilson, G. A., and Zhdanov, M. S., 2010, 3D inversion of airborne electromagnetic data using a moving footprint: Exploration Geophysics, 41, 250-259.

Farquharson, C. G., Oldenburg, D. W., Haber, E., and Shekhtman, R., 2002, An algorithm for the three-dimensional inversion of magnetotelluric data: SEG Expanded Abstracts, 21, 649-652.

Hatakayama, H., 1938, On the bay disturbance and the pulsation of the Earth current: Geophysical Magazine, 12, 189-210.

Hirayama, M., 1934, On the relations between the variations of Earth potential gradient and terrestrial magnetism: Journal of the Meteorological Society of Japan, 12, 16-22.

Holtham, E., and Oldenburg, D. W., 2010, Three-dimensional inversion of ZTEM data: Geophysical Journal International, 182, 168-182.

Hoversten, G. M., Constable, S. C., and Morrison, H. F., 2000, Marine magnetotellurics for base-of-salt mapping: Gulf of Mexico field test at the Gemini structure: Geophysics, 65, 1476–1488.

Key, K. W., Constable, S. C., and Weiss, C. J., 2006, Mapping 3D salt using the 2D marine magnetotelluric method: Case study from Gemini Prospect, Gulf of Mexico: Geophysics, 71, B17–B27.

Labson, V. F., Becker, A., Morrison, H. F., and Conti, U., 1985, Geophysical exploration with audiofrequency natural magnetic fields: Geophysics, 50, 656-664.

Lamont, J. V., 1862, Der Erdstrom und der Zusammen desselben mit dem Erdmagnetismus: Leopold-Voss-Verlag, Leipzig und Muenchen, 1862.

Pare, P., Gribenko, A. V., Cox, L. H., Čuma, M., Wilson, G. A., Zhdanov, M. S., Legault, J., Smit, J., and Polomé, L., 2012, n3D inversion of SPECTREM and ZTEM airborne electromagnetic data from the Pebble Cu-Au-Mo porphyry deposit, Alaska: Presented at ASEG 22nd Geophysical Conference and Exhibition, Brisbane.

Rikitake, T., 1950, Electromagnetic induction within the Earth and its relation to the electrical state of the Earth's interior: Bulletin of the Earthquake Research Institute, University of Tokyo, 28, 263-283.

Terada, T., 1917, On rapid periodic variations of terrestrial magnetism: J. Coll. Sci. Imp. Univ. Tokyo, 37, 56-84.

Tikhonov, A. N., 1950, On the determination of the electrical characteristics of deep layers of the Earth's crust: Doklady, 73, 295-297.

Ward, S., O'Donnell, J., Rivera, R., Ware, G., and Fraser, D., 1966, AFMAG - Applications and Limitations: Geophysics, 31, 576-605.

Zhdanov, M. S., 2002, Geophysical Inverse Theory and Regularization Problems: Elsevier, Amsterdam.

Zhdanov, M. S., Smith, R. B., Gribenko, A., Čuma, M., and Green, A. M., 2011a, Three-dimensional inversion of large-scale EarthScope magnetotelluric data based on the integral equation method – geoelectrical imaging of the Yellowstone conductive mantle plume: Geophysical Research Letters, 38, L08307, doi:10.1029/2011GL046953.

Zhdanov, M. S., Wan, L., Gribenko, A., Čuma, M., Key, K., and Constable, S., 2011b, Large-scale 3D inversion of marine magnetotelluric data: Case study from the Gemini prospect, Gulf of Mexico: Geophysics, 76, F77-F87, doi: 10.1190/1.3526299.